# ADVANCED STEEL CONSTRUCTION

*An International Journal*

**Volume 18 Number 3**

**September 2022**

**CONTENTS**

**Technical Papers**




Website: *http://www.hkisc.org*
ISSN 1816-112X
Science Citation Index Expanded, Materials Science Citation Index and ISI Alerting
*Cover: A Steel Footbridge in Hong Kong. Photo @LIU Yao-Peng*
*e-copy of IJASC is free to download at "www.ascjournal.com" in internet and mobile apps.*

ADVANCED STEEL CONSTRUCTION

VOL.18, NO.3 (2022)

ADVANCED STEEL CONSTRUCTION

*an International Journal*

*ISSN 1816-112X*

*Volume 18 Number 3* *September 2022*

ADVANCED STEEL CONSTRUCTION
an international journal

ISSN 1816-112X

Science Citation Index Expanded, Materials Science Citation Index and ISI Alerting

# Advanced Steel Construction
## an international journal



*Cover: A Steel Footbridge in Hong Kong. Photo @LIU Yao-Peng*
*e-copy of IJASC is free to download at "www.ascjournal.com" in internet and mobile apps.*

# General Information
## *Advanced Steel Construction, an international journal*

**Aims and scope**

The International Journal of Advanced Steel Construction provides a platform for the publication and rapid dissemination of original and up-to-date research and technological developments in steel construction, design and analysis. Scope of research papers published in this journal includes but is not limited to theoretical and experimental research on elements, assemblages, systems, material, design philosophy and codification, standards, fabrication, projects of innovative nature and computer techniques. The journal is specifically tailored to channel the exchange of technological know-how between researchers and practitioners. Contributions from all aspects related to the recent developments of advanced steel construction are welcome.



**Subscription inquiries and change of address.** Address all subscription inquiries and correspondence to Member Records, IJASC. Notify an address change as soon as possible. All communications should include both old and new addresses with zip codes and be accompanied by a mailing label from a recent issue. Allow six weeks for all changes to become effective.

**The Hong Kong Institute of Steel Construction**
HKISC
c/o Department of Civil and Environmental Engineering,
The Hong Kong Polytechnic University,
Hunghom, Kowloon, Hong Kong, China.
Tel: 852- 2766 6047 Fax: 852- 2334 6389
Email: *ceslchan@polyu.edu.hk* Website: *http://www.hkisc.org/*
**ISSN 1816-112X**
**Science Citation Index Expanded, Materials Science Citation Index and ISI Alerting**

ISSN 1816-112X

**Science Citation Index Expanded, Materials Science Citation Index and ISI Alerting**



# Advanced Steel Construction
*an international journal*

**VOLUME 18 NUMBER 3 September 2022**

**Technical Papers**

**Advanced Steel Construction** – Vol. 18 No. 3 (2022) 630–647
**DOI:**10.18057/IJASC.2022.18.3.1


# AN ANALYTICAL METHOD FOR EVALUATING THE DEFLECTION AND LOAD-BEARING AND ENERGY ABSORPTION CAPACITY OF ROCKFALL RING NETS CONSIDERING MULTIFACTOR INFLUENCE

Li-Ping Guo [1, 2], Zhi-Xiang Yu [1, 2, 3, *], Yun-Tao Jin [1, 2], Lin-Xu Liao [1, 2] and Li-Ru Luo [1, 2]

[1] *School of Civil Engineering, Southwest Jiaotong University, Chengdu, China*
[2] *Research Centre for Protection Structures Against Natural Hazards, Southwest Jiaotong University, Chengdu, China*
[3] *Shock and Vibration of Engineering Material and Structure Key Laboratory of Sichuan Province, Mianyang, China*
** (Corresponding author: E-mail: yzxzrq@swjtu.edu.cn)*

**ABSTRACT**

In this study, an analytical method for evaluating the structural performance, including maximum deflection, load-bearing, and energy absorption capacity of a steel wire-ring net, was proposed to effectively design the ring net of the flexible barrier systems. Puncture tests of the ring nets and two-point traction tests of the three-ring chains with various wire-ring specifications were conducted. Correlation analysis was used to test the results between ring nets and chains, revealing that three structural performance indicators of the test specimens were strongly related. The ring net's structural performance was affected specifically by ring chains on the shortest load transfer path. Accordingly, a three-ring chain with a flexible boundary corresponded to a fibre–spring element. A three-dimensional analytical model of the ring net was established. Explicit formulas for computing the three indicators of the ring net were derived. Comprehensive quasi-static and impact tests, using different shapes and sizes of punching devices, were conducted, providing valuable data to calibrate and validate this analytical method. The ability of the model in yielding consistent results when implemented at the structure scale was then assessed, based on the data of full-scale impact tests on a 1500kJ-energy rockfall barrier. Lastly, the effects of various factors, such as single ring geometry, the length–width ratio of the net, loading area size, boundary stiffness, and load rate, influencing the structural performance indicators of the ring net were investigated, respectively.

**ARTICLE HISTORY**

Received: 20 July 2021
Revised: 26 October 2021
Accepted: 29 October 2021

**KEYWORDS**

Flexible barrier systems;
Steel wire ring net;
Analytical model;
Puncture tests;
Destructive impact tests;
Structural performance



## 1. Introduction

Flexible net barriers are protection structures used to mitigate geological hazards, such as rockfall [1,2], landslide [3], debris flow [4,5], and avalanche [6]. A typical flexible barrier mainly comprises the interception structure, support structure, connection components, and foundation. The flexible net panel is the key interception component of the protection system. When subjected to a falling rock impact, the out-of-plane puncture is a common failure mode of the net panel[7]. Once the net fails, the entire protective system may lose its protective function [8] (**Fig. 1)**. Therefore, it is vital to study the puncture failure behaviour of the flexible net panel under the impact.

The maximum deflection [9], load-bearing capacity [10], and energy absorption capacity [11] are the three important indicators used to evaluate the flexible net panel's structural performance. Several experimental models have been developed over the past decades to investigate the structural performance of flexible net panels under out-of-plane loading. Quasi-static puncture tests were conducted on G.T.S mesh [12] and chain-link mesh [10]. The maximum deflection and the load-bearing capacity of the mesh are closely related to the loading area's size between the punch device and net panel. Further studies have shown that, with the same energy level, the smaller the loading area's size, the more prone to fail the mesh—the so-called "bullet effect" [13]. Rockfall impact tests conducted on ring nets with different boundary conditions have shown that boundary stiffness is also an important factor affecting its mechanical properties [14,15]. The more compliant the system, the larger the deformation ability and the higher impact resistance of the flexible barrier [16].

Various numerical approaches, using both FE [17] and DE [18] methods, for modelling rockfall protection systems with steel wire meshes have been proposed in the literature. A sophisticated numerical model [19,20] is well established for dynamic modelling of continuum problems with non-linear geometries, complex mechanical behaviour, and various contact conditions. However, such a process is time-consuming, especially if failure of the wire mesh and various load cases needs to be considered in practice.

A more efficient approach requiring fewer tests or lower computational costs is highly needed. Some researchers have also used theoretical methods to study the puncture resistance–mechanical properties of flexible nets [21,22]. A dimensionless model [23] and analytical model [24] for chain-link mesh laid the foundations to understand the bullet effect. Peila et al. [25] developed a macro-analytical model for designing wire ropes, steel posts, and anchor foundations in a rockfall protective barrier. However, the net is considered to act only as a structure distributing the force on the cables and the posts. Yu et al. [26,27] obtained an empirical expression for calculating the punching deformation of the ring net. Guo et al. [28] established a simplified model for the deformation and load-bearing capacity of the ring net, but it is only applicable to the square mesh, and cannot consider the influence of the boundary stiffness.

(a) Perspective view

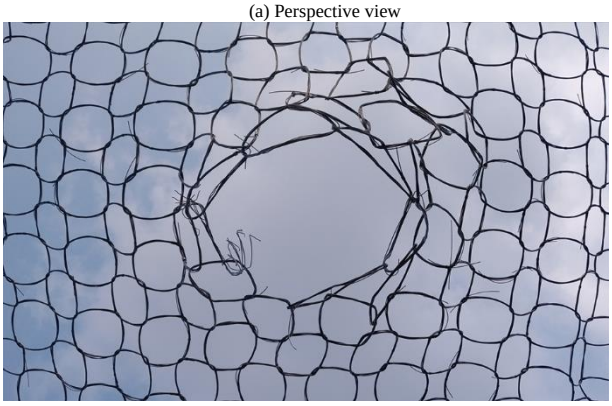

(b) Bottom view

**Fig. 1** Failure of ring net

The above studies basically focus on a few factors on the energy absorption capacity of the net panel. The structural performance indicators of the actual steel-wire ring net are affected by multiple factors such as the strength of materials, the geometric parameters, the boundary stiffness, and the load rate.

However, comprehensive destructive tests and related analytical models of the steel-wire ring nets are rarely reported, which seriously affects the engineering design and application of flexible protection technology.

Aiming at effectively evaluating the maximum deflection, load-bearing, and energy absorption capacity of the steel wire ring net in the flexible barrier systems, out-of-plane puncture tests of the ring nets and 2-point traction tests of the three-ring chains with various wire-ring specifications were conducted. Correlation analysis was used to test results between ring nets and ring chains, revealing that three structural performance indicators of the test specimens were strongly related (**Section 2**). Multiple factors influencing the structural performance indicators of the ring net were summarized. The fundamental principles of mechanics were investigated in **Section 3**. The ring net's structural performance is especially affected by ring chains on the shortest load path of the ring net under out-of-plane load. Therefore, a three-ring chain with a flexible boundary on the load transfer path of the ring net was equivalented to a fibre–spring element. Then, a three-dimensional analytical model of the ring net was established (**Section 4**). Model parameters were calibrated by comparing analytical results to experimental tests performed at the wire-ring net scale (**Section 5**). Additional quasi-static and impact tests, using different shapes and sizes of punching devices, were conducted, yielding valuable data to validate this analytical method. The ability of the model in yielding consistent results when implemented at the structure scale was then assessed, based on the data of full-scale impact tests on a 1500kJ-energy rockfall barrier. Lastly, the effects of multiple factors, such as single ring geometry, the length-width ratio of the net, loading area size, boundary stiffness, and load rate were studied (**Section 6**).

## 2. Model test

Different scales of single rings, ring chains, ring groups, and ring net panel specimens have been tested by [29–32], respectively. The above-mentioned studies could provide basic data for later research and reveal the mechanical behaviour of ring nets from different aspects. However, no studies are focusing on the relevance between test results of steel ring specimens with different scales, which would be insufficient to reveal the mechanical behaviour of the ring net in depth. Hence, this section focuses on investigating the relationships between ring nets and ring chains.

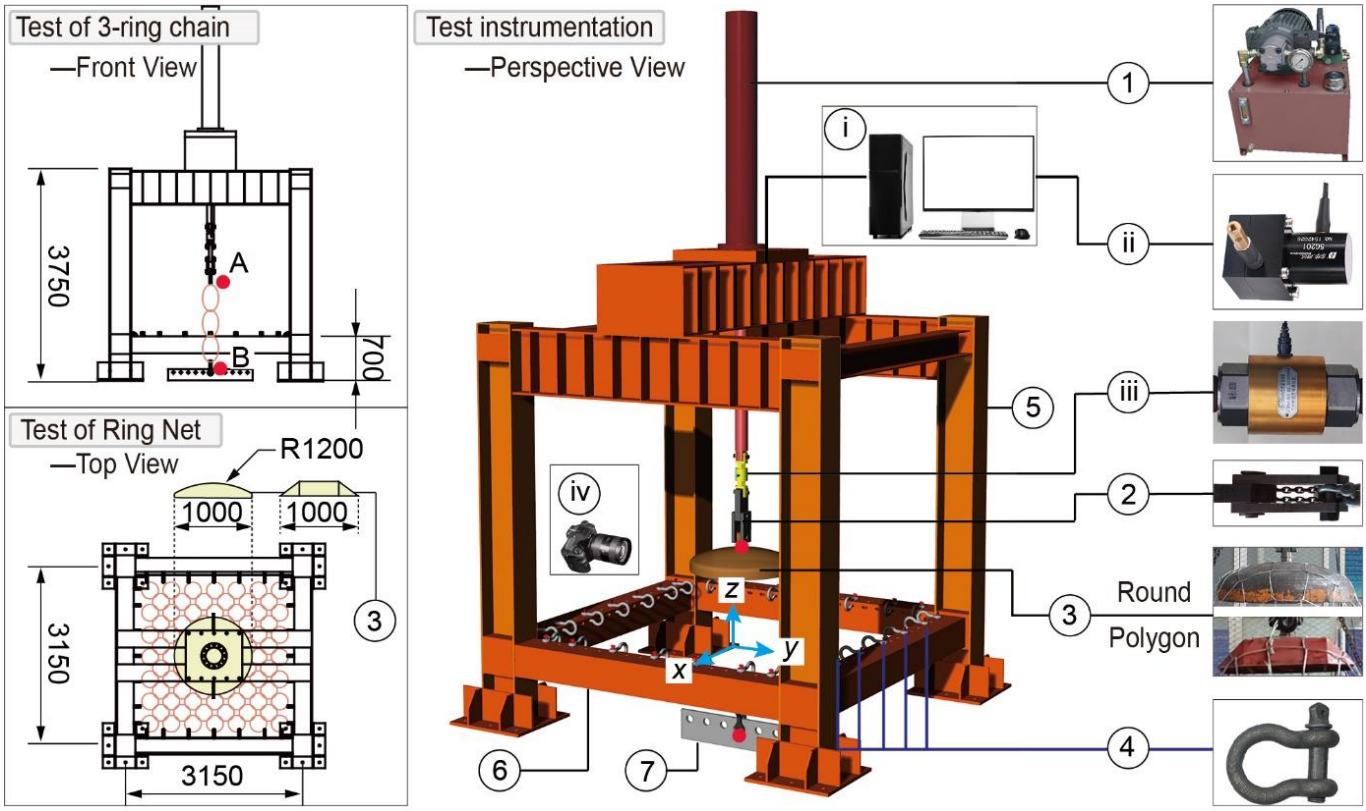


**Fig. 2** Experimental setup and instrumentation

### *2.1. Experimental setup and instrumentation*

The test site was located at the Rockfall Test Centre of Southwest Jiaotong University. The experiment setup was made of high-quality steel. The length and width of the steel frame were both 3.15 m, whereas the height was 3.75 m. The arrangement of the instrumentation is plotted in **Fig. 2**.

The test loading device included the following components and processes.

(1) A hydraulic loading system, comprising an electric motor and a hydraulic cylinder, is used to provide hydraulic power and pull the load device moving vertically with a speed of $7\pm1$mm/s.

(2) A connecting plate made of high-quality steel is used to connect the load sensor and the loading device.

(3) A polyhedral-shaped and hemispherical-shaped load sharing devices (press), respectively, correlate with the spherical block from the international standard [33] and the polyhedral block from [34] with different sizes of 600 mm and 1000 mm in diameter, are used to provide out-of-plane loading conditions to the ring net specimens.

(4) Shackles (8.5T～12.5T), symmetrically arranged along the lower beam, are used to anchor the net panel to the frame so that the boundary rings remained hinged.

(5) An I-shaped steel beam, with stiffener plates along the length direction, is used to transmit the load from the cylinder's hydraulic pressure to the ground.

(6) The lower beam, connected with shackles, is used to form the boundary conditions of the wire ring specimens. The horizontal plane of the ring net boundary was used as the datum plane for measuring out-of-plane displacement.

(7) Hinged support, anchored at the centre of the steel frame bottom, is used to provide hinged constraints for the ring chains' specimens.

The instrumentation included the following.

(i) A data logger with the capability to sample 24 transducers at 1000Hz simultaneously is used to collect the transducer data.

(ii) A displacement sensor with 0.3%fs precision and a 1500mm measuring range are used to measure and record the out-of-plane displacement data.

(iii) A force sensor system with 0.3%fs precision and two types of measuring ranges (500kN and 1500kN) is connected in series with the punching device to measure the real-time tension force directly.

(iv) A video camera, with a resolution of 5184 × 3456 pixels and a frame rate of 30 frames per second is utilised to monitor the motion of the punch device and the deflection of the flexible barrier ring net during the out-of-plane loading.

### *2.2. Puncture test of the ring net*

Firstly, out-of-plane puncture tests of the ring nets were conducted. To ensure the test's repeatability and the results' reliability, three identical ring nets are repeatedly tested for each specification. **Fig. 3** shows the ring net (RN) specification of RN07/3.0/300, which means the number of windings is $n_w=7$, the diameter of the high-strength steel wire is $d=3$ mm, and the average diameter of the single ring is $D=300$ mm. Each ring net comprised 85 single rings, and the length and width of the net were 3m. **Table 1** shows all test

specimens of the ring nets. The net with the number of windings $n_w = 3$ and $n_w = 4$ is made of a high-strength steel wire with a diameter of $d = 2.2$ mm, while the net with $n_w \geq 5$ is made of a steel wire with diameter $d = 3.0$ mm.

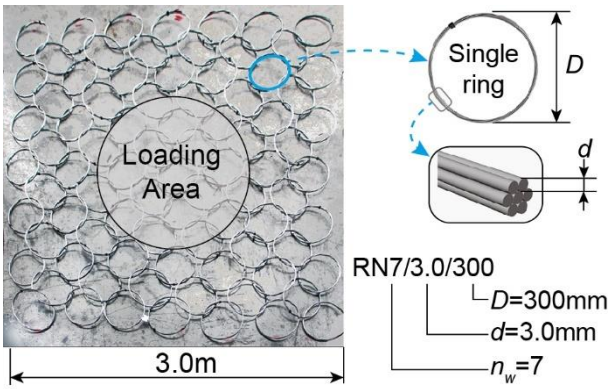


**Fig. 3** Ring net specimen

**Table 1**
Specimens of steel wire-ring net panel

| Test 1 | Specification | Each ring in specimens | | |
|---|---|---|---|---|
| | | $n_w$ | $d$ | $D$ |
| Punching test | RN03/2.2/300 | 3 | 2.2 | 300 |
| | RN04/2.2/300 | 4 | 2.2 | 300 |
| | RN05/3.0/300 | 5 | 3 | 300 |
| | RN07/3.0/300 | 7 | 3 | 300 |
| | RN09/3.0/300 | 9 | 3 | 300 |
| | RN12/3.0/300 | 12 | 3 | 300 |
| | RN16/3.0/300 | 16 | 3 | 300 |
| | RN19/3.0/300 | 19 | 3 | 300 |

The out-of-plane puncturing tests on the net panels were conducted following the procedure suggested in the international standard [33]. The test comprised loading a net panel perpendicularly to its plane using the hemispherical-shaped loading device with a speed of $7 \pm 1$ mm/s and which was located centrally. Wire-ring net specimens were punctured upwards until failure. The force–displacement curve of the central point of the panel was then obtained. **Fig. 4** presents three typical deflection states at the representative time recorded by the side-view camera combined with the signal from load and displacement sensors.

From this figure, two occurring stages are obvious: When $t = t_0$, the initial moment, each ring in the net panel is kept in a round, which can be considered as being in a zero-stress state. At this moment, the bottom plane of the loading device is flush with the boundary plane of the ring net, and the out-of-plane displacement is recorded as $z = h_0$. At $t = t_1$, the wire rings have undergone a bending process, deforming to a rounded triangle and quadrilateral. The out-of-plane displacement is recorded as $z = h_1$. At $t = t_2$, the bending deformation of the ring has been fully developed. Steel wires are straightened and broken. The ring net panel is no longer able to support any increase to the applied force. At this moment, the out-of-plane deformation reaches the maximum $z = h_2$.

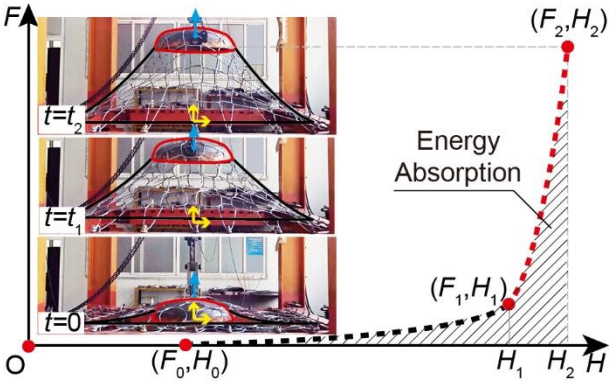


**Fig. 4** Punching tests of the ring nets

Corresponding to the pictures of the puncturing test, the traction force time-history curve shows obvious two-stage characteristics: In the first stage ( $t_0 \sim t_1$ ), the out-of-plane displacement increases obviously (accounting for 85 % of the maximum defection), whereas the force increases slowly (accounting for 15 % of the puncture resistance). The traction force and displacement were recorded as $F_1$ and $l_1$, respectively, at $t_1$. In the second stage ( $t_1 \sim t_2$ ), the displacement increases slowly (accounting for 15 % of the maximum deflection), whereas the force increases obviously (accounting for 85 % of the puncture resistance). The traction force and displacement were recorded as $F_2$ and $l_2$ respectively at $t_2$. The ring net failed at $t_2$, the out-of-plane deflection reached the maximum to $z = h_2$; and the tensile force reached the peak value of $F_2$.

The out-of-plane force and displacement signals were recorded in real-time by the load cell and the displacement sensor, respectively. The tension force doing work along the displacement direction was converted into internal energy and dissipated through the ring net.

### *2.3. Two-point traction test of the 3-ring chain*

On the load transfer path of the ring net under out-of-plane load, steel rings are connected with each other, and typical test specimens with different scales, including single ring, ring chain, and ring group, appear concurrently. Among them, the ring chain is not only relatively simple but can also reflect the contact relationship between the steel rings and can represent the mechanical behaviour of other scale specimens.

To quantitatively describe the initial conditions, stiffness changes, and failure criterion of the steel rings in the net panel, 2-point traction tests on the 3-ring chains with the same number and specifications of ring net pieces were conducted. Also, the ultimate bearing capacity, maximum deflection, and energy absorption capacity of the three-ring chains were analysed respectively. **Table 2** shows all the 3-ring chain specimens. The 3-ring chain (RC) specification of RC07/3.0/300 means the number of windings is $n_w = 7$, the diameter of the high-strength steel wire is $d = 3.0$ mm, and the average diameter value of the single ring is $D = 300$ mm.

**Table 2**
Specimens of three-ring chain

| Test 2 | Specimens of ring chains | Each ring in specimens | | |
|---|---|---|---|---|
| | | $n_w$ | $d$(mm) | $D$(mm) |
| Two-point traction test | RC03/3.0/300 | 3 | 2.2 | 300 |
| | RC04/3.0/300 | 4 | 2.2 | 300 |
| | RC05/3.0/300 | 5 | 3 | 300 |
| | RC07/3.0/300 | 7 | 3 | 300 |
| | RC09/3.0/300 | 9 | 3 | 300 |
| | RC12/3.0/300 | 12 | 3 | 300 |
| | RC16/3.0/300 | 16 | 3 | 300 |
| | RC19/3.0/300 | 19 | 3 | 300 |

The 2-point traction test of the 3-ring chain was conducted following the procedure suggested in the international standard [33]. Before the test, a slight tension is given to stabilise the system; then, the force is reduced again to zero and the rings are kept round before the test started. The 3-ring chain was tensioned by the hydraulic loading rig with a displacement speed of $7 \pm 1$ mm/s, until breaking.

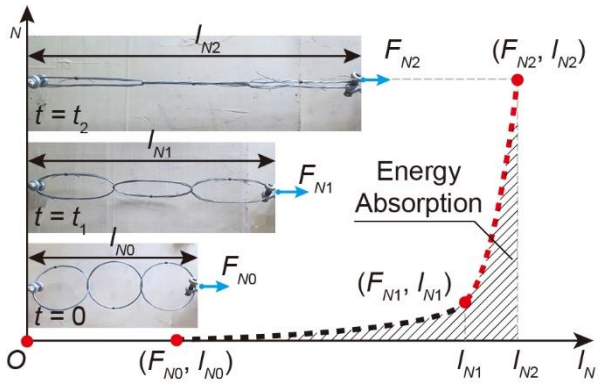


**Fig. 5** Two-point traction tests of the 3-ring chains

**Fig. 5** shows three typical photos recorded by the camera combined with the load–displacement curve. At the initial moment( $t=0$ ), each ring in the three-ring chain is kept round, and the length of the ring chain is $l=l_0$ . At $t=t_1$ , the bending deformation of the net ring is fully developed and depicts an oval shape, with the chain length being $l=l_1$ . At $t=t_2$ , the ring chain is straightened, part of the steel wires of the ring at the contact position is broken, and the chain can no longer support any increase in the applied force. At this moment, the length of the ring chain reaches the maximum $l=l_2$ .

Corresponding to the pictures of the 3-ring chain test, the traction force–displacement curve shows obvious two-stage characteristics. In the first phase ( $0\sim t_1$ ), the axial tension $F_N$ slowly increases from 0 to $F_{N1}$ (approximately 15% of the breaking load), and the length of the ring chain $l_N$ increases significantly from $l_{N0}$ to $l_{N1}$ (approximately 85% of maximum deflection). In the second phase ( $t_1\sim t_2$ ), the axial tension force $F_N$ of the net ring increases sharply from $F_{N1}$ to $F_{N2}$ (roughly 85% of breaking load), and the length of the ring chain $l_N$ increases from $l_{N1}$ to $l_{N2}$ (nearly 15% of maximum deflection).

The traction force and displacement signals were recorded in real-time by the load cell and the displacement sensor, respectively. The tension force doing work in the displacement direction was converted into internal energy and dissipated through the 3-ring chain.

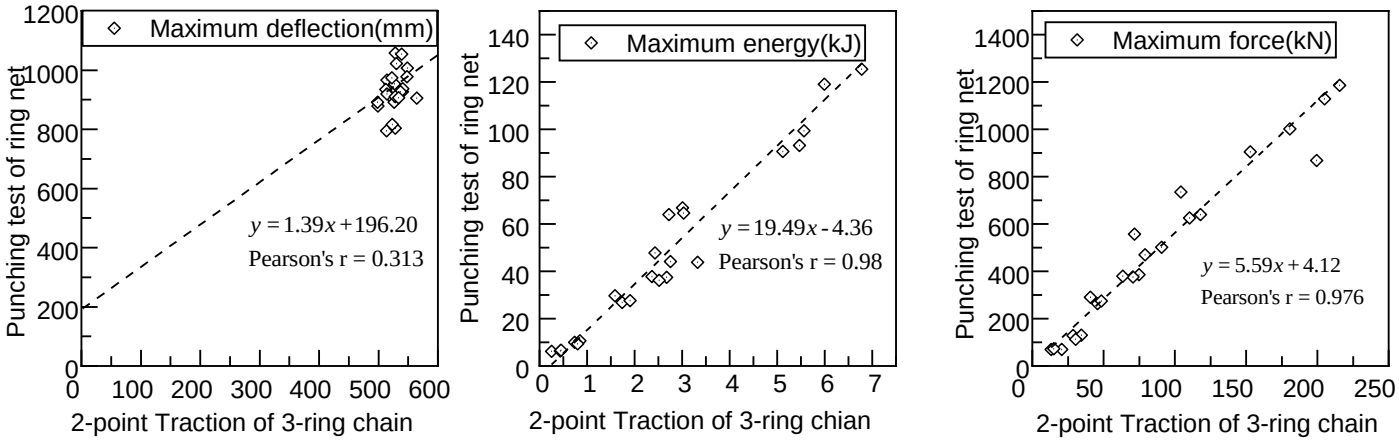


(a) Maximum deflection $t = t_2$ (b) Energy dissipation capacity $t = t_2$ (c) Load-bearing capacity $t = t_2$

**Fig. 6** Correlation between test results of 3-ring chain and ring net

*2.4. Correlation analysis*

The same displacement-controlled loading condition, with a displacement speed of $7\text{mm}\pm1\text{mm}$ , was used for both the 2-point traction test of the 3-ring chain and the puncturing test of the ring net. Similar two-stage characteristics occurred on the force-displacement curves in both destructive tests of the ring nets and the 3-ring chains. The steel-wire rings were both deformed from a circular shape in the initial state to a straightened shape in the ultimate limit state. Furthermore, all the specimens eventually broke first at the point of contact where the rings underwent severe bending. To quantitatively study the correlation between the 3-ring chain and the ring net test results, the maximum deflection, load-bearing, and energy absorption capacity, Pearson's correlation coefficient was used to study the correlation relationship between the two tests, as Eq. (1) describes,

$$r_{XY}=\frac{\sum_{i=1}^{n}\left(X_i-\bar{X}\right)\left(Y_i-\bar{Y}\right)}{\sqrt{\sum_{i=1}^{n}\left(X_i-\bar{X}\right)^2}\sqrt{\sum_{i=1}^{n}\left(Y_i-\bar{Y}\right)^2}} \tag{1}$$

where $n$ is the sample size, $X_i$ , $Y_i$ are the values for each set of samples, $\bar{X}$ is the average value of $X_i$ , and $\bar{Y}$ is the average value of $Y_i$ .

**Fig. 6** shows the correlation distribution between the 2-point traction test and the punching test results. Observably, there is no obvious correlation between the maximum deflection results, with a Pearson correlation coefficient of $r=0.313$ . However, the scattered plots are distributed in a small area, indicating that the breaking displacements are almost constant for all specimens of the 3-ring chain and ring net with different numbers of windings. The breaking force results of both tests showed a strong correlation, with the Pearson correlation coefficient of $r=0.976$ . The energy absorption results of the 3-ring chain and the ring net puncturing tests also show a strong correlation with the Pearson correlation coefficient of $r=0.980$ .

## 3. Fundamental concepts and principles of mechanics

*3.1. Tension-bending coupling effects on the steel ring*

Before breaking the steel wire rings in contact with each other, the wires underwent evident bending deformation in both puncturing and 2-point traction tests. Tension-bending coupling effects exist on the steel ring segment of the net. (**Fig. 7** ). The dimensionless relationship form of the axial force-bending moment combined tension and bending of a circular member [35][24] is shown in Eq. (2),

$$\frac{F_N}{F_y}=\frac{2}{\pi}\left\{\left(\frac{M}{M_y}\right)^{\frac{1}{3}}\sqrt{1-\left(\frac{M}{M_y}\right)^{\frac{2}{3}}}+\cos^{-1}\left[\left(\frac{M}{M_y}\right)^{\frac{1}{3}}\right]\right\} \tag{2}$$

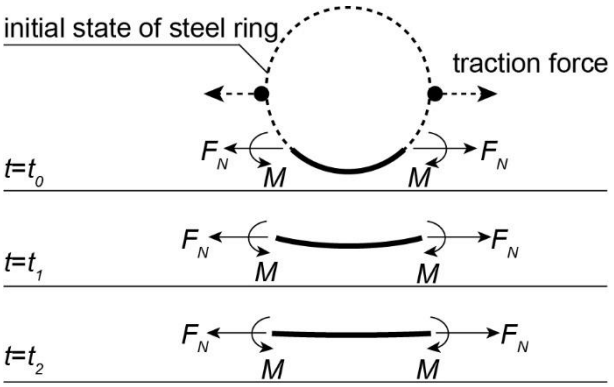


**Fig. 7** Deformation process of a steel ring segment

where $M$ is the applied moment, and $M_y=\sigma_y d^3/6$ is the moment capacity of the wire in pure bending (zero tension). $F_N$ is the applied axial force and $F_y=\sigma_y\pi d^2/4$ is the tensile bearing capacity of the wire in pure tensioning (zero bending). Eq. (2) demonstrates that bending deformation causes a potentially substantial reduction of the maximum axial force that the wire can sustain. On the left side of the equation, the normalised axial force $F_N/F_y$ represents the degree of the axial force of the steel wire, which is simpler than the expression related to the bending moment on the right side. The development degrees of the axial force and bending moment of the ring section show an opposite tendency. When the degree of axial force development reaches the maximum, the axial force of the steel rings reaches the maximum. More generally, the dimensionless parameter $\gamma_N$ could be defined below to express the development degree of the axial stress in the steel wire ring section (Eq. (3)).

$$\gamma_N=F_N/F_y=\sigma_N/\sigma_y \tag{3}$$

Once the normalised axial stress ratio reaches the maximum that the contacted rings could sustain, the damage will occur on steel rings in the net.


(a) Deformation pattern in loaded area

(b) Orthogonal internal force in load path

**Fig. 8** Deformed steel rings at ultimate limit state

*3.2. Load path of the ring net under out-of-plane load*

Under out-of-plane loading, slippage occurred between the steel rings on the load path of the ring net. Each ring deformed due to the tension and bending force (**Fig. 8**). As the load increased, the deformation tended to stabilise, which limits the further development of sliding. Once the internal force of the ring section was along its axis, an obvious square-shaped pattern appears from the deformed rings in the loaded area between the net panel and load device. The dimension of the deformed rings on the loaded area was measured after out-of-plane loading. Although the bending of the rings was significant, there was a tiny difference in circumference before (942 mm) and after (959 mm) deformation, indicating that the tensile deformation of the rings was almost negligible.

An approximately orthogonal internal force distribution pattern of the deformed rings is formed on the load transfer path of the ring net. $F_i$ and $F_j$ are the internal force vectors of the steel rings stretched in the radial direction, while $f_i$ and $f_j$ are the internal force vectors of the rings stretched along the circumferential direction of the load device. Observably, the horizontal component of the internal force in the steel rings along the circumferential direction can be self-balanced, and that the vertical component is almost zero. The horizontal component of the internal force of the rings in the radial direction is self-balanced, and the vertical component is balanced with the out-of-plane load. Therefore, it is the radial internal forces in the ring chains around the punching device that form the main part of the bearing capacity of the steel wire-ring net panel.

The circumferential ring chains could influence those structural performances by creating a small off-angle of the load path (**Fig. 8 (b)**). Constrained by the circumferential ring chains, a curved load path is observed on the ring net (Arc PQ), and the tangent at the end of the curve should be the actual direction of the force vector in the fibre–spring element (Line PB). There is an off-angle ($\angle$ BPQ) of the force vectors between the analytical model and the experimental deformed ring net. These phenomena can be described using a correction coefficient:

$$\lambda_\theta = \angle\mathrm{APB} / \angle\mathrm{APQ} \tag{4}$$

*3.3. Equilibrium of force system*

At ultimate limit states, the steel rings on the load path of the net panel are fully stretched, and the internal axial force vectors of the radial ring chains were balanced with the out-of-plane loading (**Fig. 9**). The effect of the circumferential ring chains can be considered a correction coefficient to the direction of axial force in straightened rings ($\lambda_\theta$). Further to the above analysis, considering the load-sharing device as a rigid block in 1D motion, the accelerating block can be transformed into an equivalent static system by adding the so-called d'Alembert inertia "force" ($\mathbf{I} = -m_{block}\mathbf{a}$). Thus, the space balance force system is formed between the out-of-plane load ($\mathbf{F}_{load}$), all internal axial force vectors of the rings, the block gravity, and the inertia force. As Eq. (5) describes,

$$\mathbf{F}_{load} + \mathbf{I} + m_{block}\mathbf{g} = -\sum \mathbf{F}[\mathbf{i}] \cdot \mathbf{z} \tag{5}$$

where $m_{block}$ is the mass of the block, $\mathbf{g} = 9.81\mathrm{m/s}^2$ is the gravitational acceleration, and $\mathbf{z}$ is the out-of-plane load direction of the rigid block. Keeping the same magnitude and direction of the force vector in the straightened rings, the complex force transfer path of the ring net can be replaced by tension-only fibres.

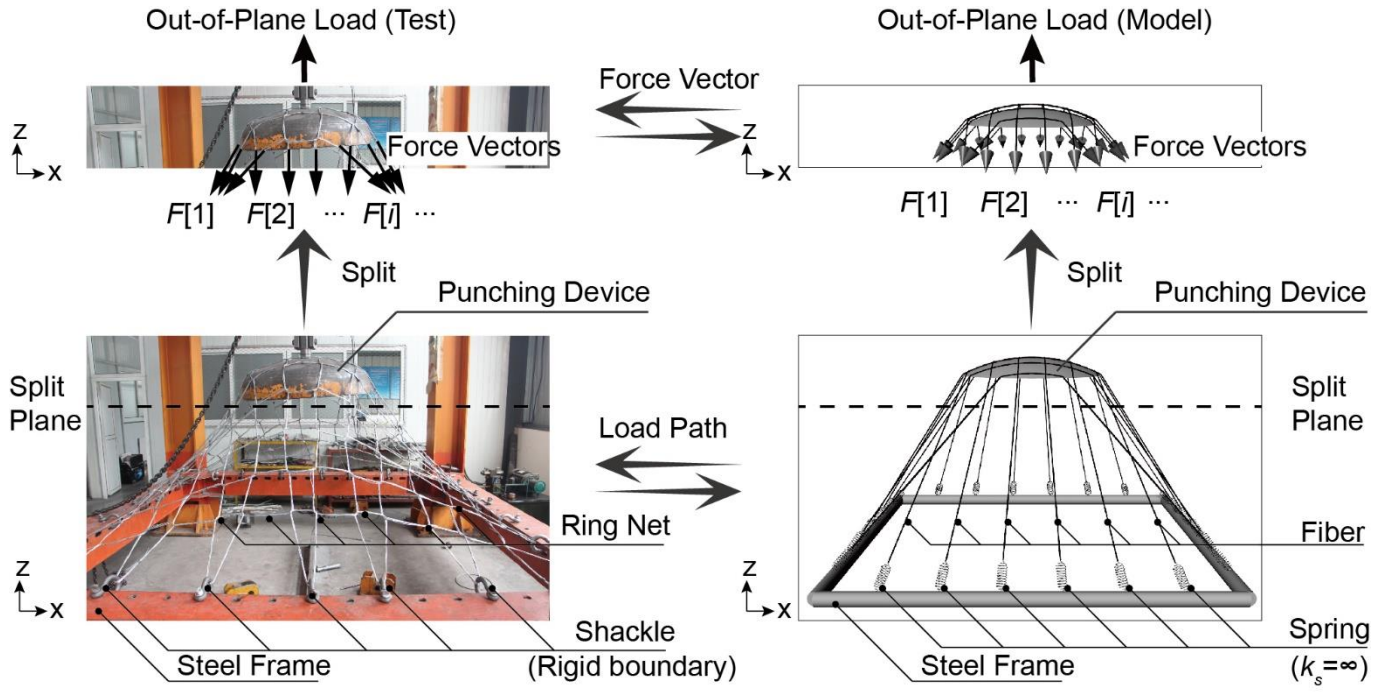


**Fig. 9** Equivalent principle between the analytical model and the ring net under out-of-plane load

Once the axial stress factor $\gamma_N$ of an equivalent fibre reaches its maximum value $\gamma_{N\max}$, the fibre is considered to have failed:

$$\gamma_N = \gamma_{N\max} \tag{6}$$

Rather than model the cables, posts, and foundations explicitly, the flexible boundary of the ring net can be represented by springs of some effective stiffness, as suggested by Spadari et al [36].

## 4. Analytical method

### *4.1. Key effects affecting structural behaviours*

The influence of multiple factors is comprehensively reflected when the ring net in the flexible barrier system is impacted by a falling block. The main factors are summarized as follows:

(1) Material characteristics: The primary material of the ring net is a high-strength steel wire. The yield stress $\sigma_y$ and diameter $d$ of the steel wire are the main material parameters affecting the performance of the ring net.

(2) Steel ring specifications: The ring net panel is made of steel wire rings. The number of windings $n_w$ and ring diameter $D$ are the main parameters affecting the performance of the ring net.

(3) Loaded area (block): According to the "bullet effect"[13], the load-bearing capacity and maximum deflection of the ring net are directly related to the block size $R_p$ and the diameter of the single ring $D$ , which affects the number of tensioned rings at the edge of the loaded area. Also, the shape and position of the block are essential factors affecting net panel performance **(Fig. 10 a)**.

(4) Geometry of the net panel: Rectangular ring net panel with different length–width ratios $\kappa$ ( $\kappa \geq 1$ ) could be used in actual engineering (**Fig. 10 b**). The ring net size should be determined by following the protective structure form and the spacing of the support structures. Once the width of the net is determined as $w$ , the length would be $\kappa w$ . More steel wire rings may participate in the deformation and stress process with an increase in the ring net size, thereby affecting the performance of the whole ring net.

(5) Boundary stiffness: Generally, the ring net is supported with a steel column by wire ropes, which makes the boundary of the ring net flexible. The deformation of the wire ropes can affect the overall out-of-plane stiffness of the ring net. A boundary stiffness factor ( $k_s$ ) can be used to evaluate the flexibility of the boundary and help calculate the deflection of the flexible ring net panel (**Fig. 10 c**).

(6) Load rate: The load rate of a flexible barrier in static and dynamic conditions differs. The variation in material strength with applied load rate should be considered in designing flexible barriers subjected to suddenly applied loads.

### *4.2. Fibre–spring element*

From a structural engineering perspective, the energy absorption capacity of the ring chains under external loads is the area beneath the load-displacement curve under the assumption of reaching the failure load. The total energy absorbed by the steel rings is composed of elastic and plastic energy.

The axial mechanical behaviour of equivalent fibres should reflect the macro force–displacement relation of the ring segment under traction and ensure that the failure criterion, including the maximum length, breaking load, and energy absorption, is consistent with the segment in the ring chain test. Therefore, the two-stage force-displacement curve (**Fig. 5**) of the 3-ring chain is converted into the axial force–displacement curve of the equivalent fibres (**Fig. 11**).

The 3-ring chains bear traction force $F_N$ , and the length of the 3-ring chain is $l_N$ with an initial length of $l_{N0}$ . The equivalent fibres bear axial force $F_f$, and the length is $l_f$ with an initial length of $l_{f0}$. For a steel ring with $n_w$ windings, the sectional area of both the ring chain and the equivalent fibres is $A$ , it can be calculated as follows:

$$A = \frac{n_w \pi d^2}{4}, \quad l_{N0} = 3D \tag{7}$$

The fibre force–displacement curve can be divided into two stages: In the first stage, the axial force of the equivalent fibre ($F_f$) increases from 0 to $\gamma_{N1}\sigma_y A$, and the length of the equivalent fibre ($l_f$) increases from $l_{f0}$ to $l_{f1}$, and the equivalent stiffness of the fibre is $k_{f1}$. In the second stage, the axial force $F_f$ increases from $\gamma_{N1}\sigma_y A$ to $\gamma_{N2}\sigma_y A$, and the fibre length ($l_f$) increases from $l_{f1}$ to $l_{f2}$. Also, the equivalent stiffness of the fibre is $k_{f2}$. The axial stress factor of the equivalent fibre $\gamma_{N1}$ and $\gamma_{N2}$ can be obtained from Eq. (8):

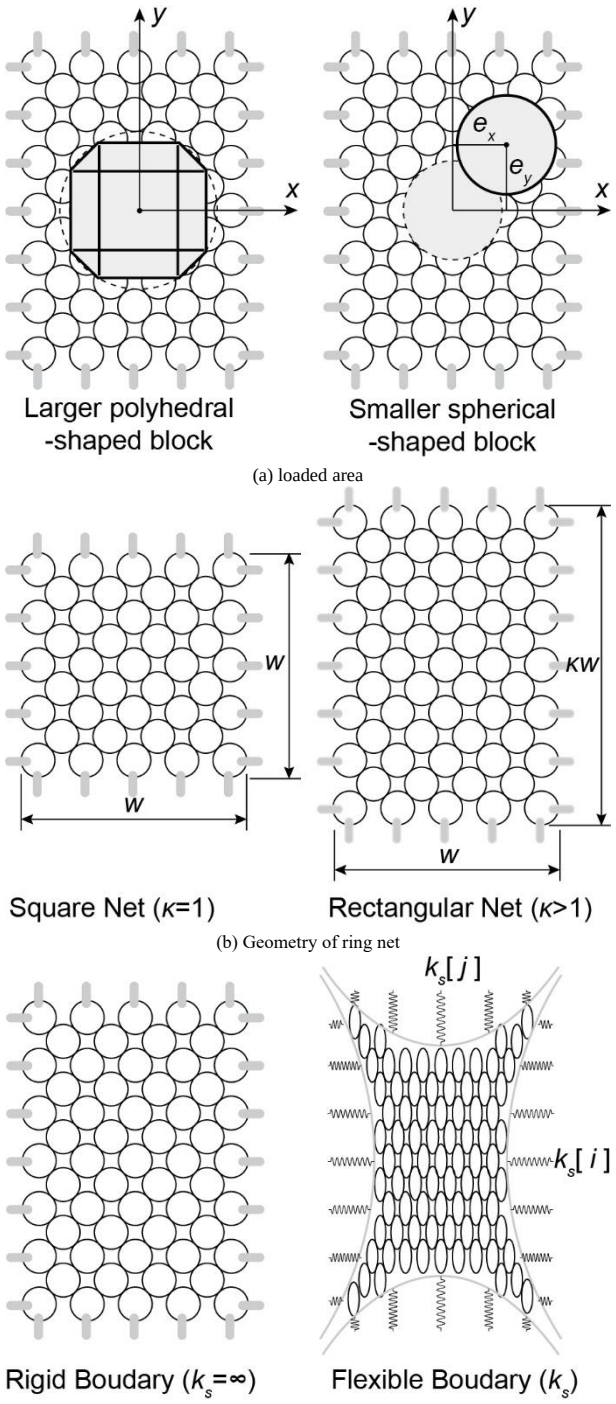


**Fig. 10** Multiple-factor influence on ring net performance

$$\gamma_{N1} = \frac{F_{N1}}{2\sigma_y A}, \quad \gamma_{N2} = \frac{F_{N2}}{2\sigma_y A} \tag{8}$$

The equivalent stiffness and $k_{f2}$ of the fibres can be calculated by Eq. (9).

$$k_{f1} = \frac{F_{N1} L_{N0}}{2(L_{N1} - L_{N0}) l_{f0}}, k_{f2} = \frac{(F_{N2} - F_{N1}) L_{N0}}{2(L_{N2} - L_{N1}) l_{f0}} \tag{9}$$

Here, the differential force–displacement relationship of the equivalent fibre is defined by Eq. (10):

$$\frac{\mathrm{d}F_f}{\mathrm{d}l_f} = \begin{cases} k_{f1} & ,0 < \gamma_N \leq \gamma_{N1} \\ k_{f2} & ,\gamma_{N1} < \gamma_N \leq \gamma_{N2} \end{cases} \tag{10}$$

with an initial condition of $F_f = 0$ , $l_f = l_{f0}$ .

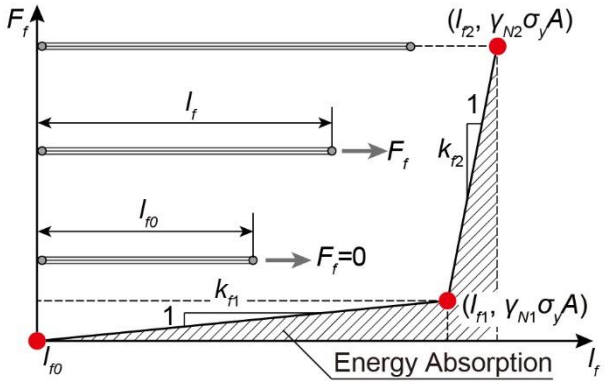


**Fig. 11** Equivalent force-displacement curve of the fibre

The equivalent springs bear axial force $F_s$, and the length is $l_s$. Then, the differential force-displacement relationship of equivalent spring with a constant stiffness $k_s$ is defined by Eq. (11):

$$\frac{\mathrm{d}F_s}{\mathrm{d}l_s} = k_s \tag{11}$$

with an initial condition of $F_s = 0$, $l_s = l_{s0}$.

Since the fibre–spring element comprises equivalent fibre and spring in series, the axial force $F$ of the element is equal to the equivalent fibre force $F_f$ and the equivalent spring force $F_s$. The current length of the element $L$ is the sum of the fibre length $l_f$ and the spring length $l_s$, as Eq. (12) describes.

$$\begin{cases} F = F_s = F_f \\ L = l_s + l_f \end{cases} \tag{12}$$

where $F_f = \gamma_N \sigma_y A$

Combining Eqs. (10), (11), and (12), the force–displacement relationship of the fibre–spring model can be written as follows:

$$\frac{\mathrm{d}F}{\mathrm{d}L} = \begin{cases} K_1 = 1/\left(1/k_{f1} + 1/k_s\right), & 0 < \gamma_N \le \gamma_{N1} \\ K_2 = 1/\left(1/k_{f2} + 1/k_s\right), & \gamma_{N1} < \gamma_N \le \gamma_{N2} \end{cases} \tag{13}$$

With an initial condition of $F = 0$, $L = L_0 = l_{s0} + l_{f0}$. The overall stiffness of the fibre–spring element also has two-stage characteristics. When the development degree of the axial stress ranges in $0 \le \gamma_N \le \gamma_{N1}$, the fibre–spring element stiffness is $K_1$, and the overall stiffness of the fibre–spring element of the fibre–spring element is $K_2$ when the development degree of axial stress ranges in $0 \le \gamma_{N1} \le \gamma_{N2}$.

With the elongation of the fibre–spring element under axial loading, the work is converted to energy in the fibre–spring element. The relationship between the increment of the work *E* done by external forces and the increment of the element length can be written as follows:

$$\frac{\mathrm{d}E}{\mathrm{d}L} = \begin{cases} K_1\left(L - L_0\right), & 0 < \gamma_N \le \gamma_{N1} \\ K_1\left(L_1 - L_0\right) + K_2\left(L - L_1\right), & \gamma_{N1} < \gamma_N \le \gamma_{N2} \end{cases} \tag{14}$$

With an initial condition of $E = 0$, $L = L_0 = l_{s0} + l_{f0}$. Where $L_1$ is the length of the fibre–spring element when $\gamma_N = \gamma_{N1}$, which can be calculated by Eq. (15)

$$L_1 = L_0 + \frac{\gamma_{N1}\sigma_y A}{K_1} \tag{15}$$

When the axial stress level $\gamma_N$ reaches its maximum $\gamma_{N\max}$, the fibre–spring element fails immediately.

### *4.3. Analytical model*

An equivalent analytical model of the ring net can be established as shown in **Fig. 12**. The fibre–spring elements are distributed at the edge of the loaded area. Under out-of-plane loading, the equivalent fibre and spring undergo axial deformation concurrently, forming the out-of-plane deflection of the ring net. For the present, the analytical model shall be restricted to a three-dimensional Cartesian coordinate, pictured as a set of three orthogonal $x$, $y$, and $z$ axes.

As mentioned in **Section 3.2**, the deformed rings in the loaded area of the net panel have a square-shaped pattern, and the difference in circumference before and after deformation was almost negligible. It is assumed that the steel rings distributed in the loaded area deform to a regular rectangle after bending and straight deformation, and the dimensions of the deformed rings are determined by the geometric boundary (the length $\kappa w$ and width $w$) of the net panel, that is

$$2\left(1+\kappa\right)a = \pi D \tag{16}$$

In the analytical model, the two sets of endpoints of the fibre–spring elements are located at the edge of the loading area and the geometric boundary of the ring net. Considering hemispherical-shaped and polygonal-shaped blocks, the external contour lines of the blocks are divided by deformed rectangular rings, producing a series of intersection points along the upper edge of the loaded area. The number of all fibre–spring elements is determined by these points. For brevity and focus, greater emphasis was placed on modelling the ring net panel subjected to out-of-plane loading by a hemispherical-shaped block in this study.

Let $m$ be the total number of all fibre–spring elements, $m_1$ be the number of elements along the positive *x*-axis, and $m_2$ be the number of elements along the positive *y*-axis, then

$$\begin{cases} m_1 = \mathrm{Round}\left[R_p / a\right] \\ m_2 = \mathrm{Round}\left[R_p / \left(\kappa a\right)\right] \end{cases} \tag{17}$$

where Round[·] is a rounding function. Considering the bi-axial symmetry of the analytical model, the total number of all fibre–spring elements $m$ can be calculated by

$$m = 2\left(m_1 + m_2\right) \tag{18}$$

A set of endpoints $\mathrm{P}_1$, $\mathrm{P}_2$ … $\mathrm{P}_i$ … $\mathrm{P}_{m1}$, connecting with equivalent fibres of the fibre–spring elements are distributed along the upper edge of the load device, and another set of endpoints, $\mathrm{Q}_1$, $\mathrm{Q}_2$ … $\mathrm{Q}_i$ … $\mathrm{Q}_{m1}$, connecting with equivalent springs of the fibre–spring elements, are distributed along the lower boundary of the ring net. For a random position of the loaded area centre with different shifts ($e_x$, $e_y$) along the x-axis and y-axis of the net panel (**Fig. 10 a**), the coordinates of $\mathrm{P}_i$ can be expressed as

$$\begin{cases} x_{\mathrm{P}}[i] = a(i - 1/2) + e_x \\ y_{\mathrm{P}}[i] = \sqrt{R_{\mathrm{P}}^2 - a^2(i-1/2)^2} + e_y \\ z_{\mathrm{P}}[i] = z \end{cases} \tag{19}$$

The coordinates of $\mathrm{Q}_i$ can be expressed as

$$\begin{cases} x_{\mathrm{Q}}[i] = \kappa w(i - 1/2)/\left(2m_1 + 1\right) + e_x \\ y_{\mathrm{Q}}[i] = w/2 + e_y \\ z_{\mathrm{Q}}[i] = 0 \end{cases} \tag{20}$$

where $i = 1, 2, \ldots m_1$, and all of the coordinate value in Eqs. (19) and (20) should be positive, that is $x_{\mathrm{P}}[i] \ge 0$, $y_{\mathrm{P}}[i] \ge 0$, $z_{\mathrm{P}}[i] \ge 0$, $x_{\mathrm{Q}}[i] \ge 0$, $y_{\mathrm{Q}}[i] \ge 0$ and $z_{\mathrm{Q}}[i] \ge 0$.

Along the x-axis, Each direction vector of the internal force of the fibre–spring element can be expressed as

$$\mathbf{PQ} = \left(x_{\mathrm{Q}}[i] - x_{\mathrm{P}}[i], y_{\mathrm{Q}}[i] - y_{\mathrm{P}}[i], -z\right) \tag{21}$$

The length of each fibre–spring element is defined by:

$$L[i] = \left|\mathbf{PQ}\right| \tag{22}$$

and the initial length of $i^{th}$ fibre–spring element is defined by:

$$L_0[i] = \left|\mathbf{PQ}\right|_{z=0} \tag{23}$$

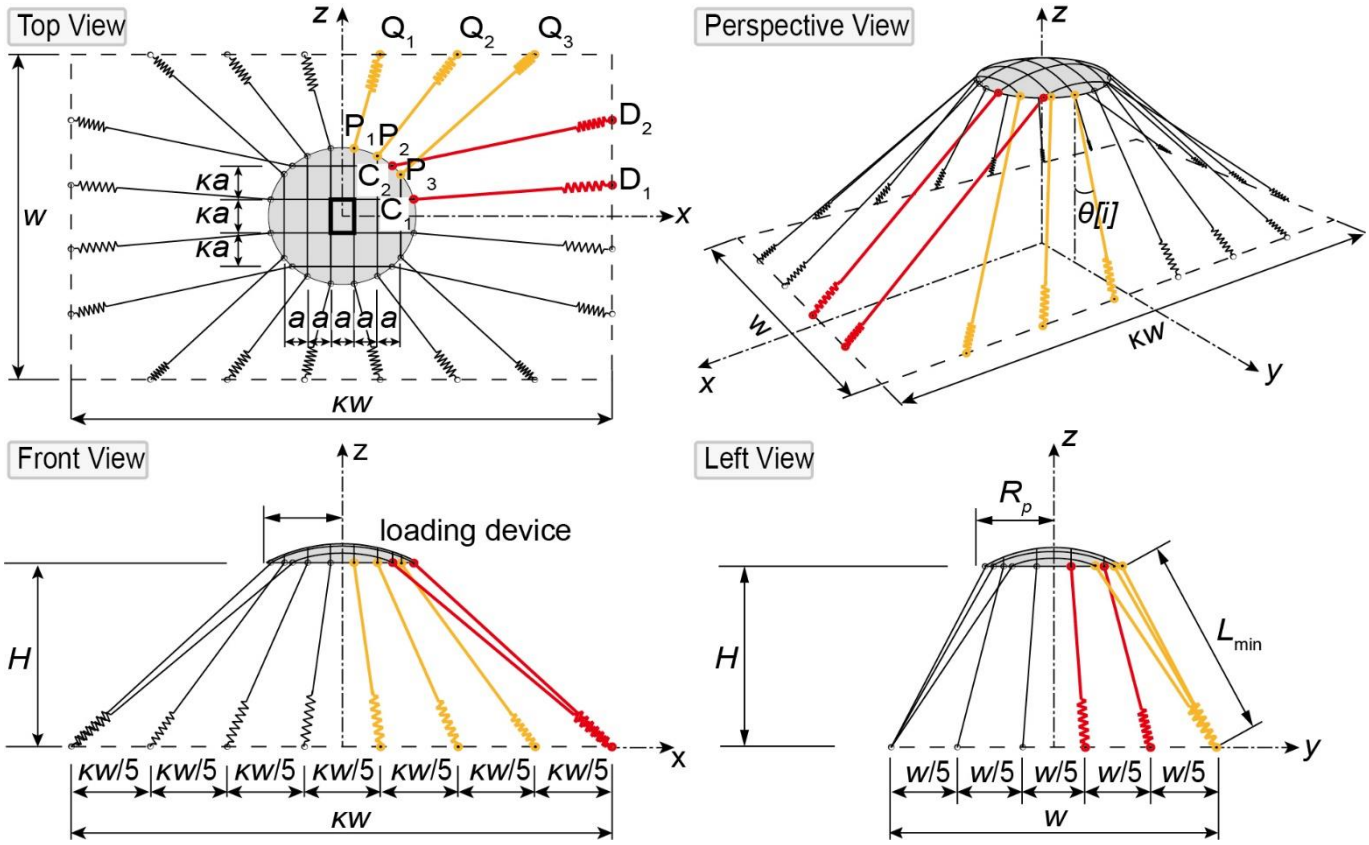


**Fig. 12** Geometric parameters of the analytical model

At any moment, the equivalent fibre length $l_f$ and the spring length $l_s$ in the fibre–spring element can be calculated by Eqs. (24) and (25), respectively.

When the axial stress level ranges in $0<\gamma_N\le\gamma_{N1}$,

$$\begin{cases} l_s[i]=\dfrac{k_{f1}[i]\left(L[i]-l_{f0}[i]\right)+k_s l_{s0}}{k_s+k_{f1}[i]} \\ l_f[i]=\dfrac{k_s\left(L[i]-l_{s0}\right)+k_{f1}[i]l_{f0}[i]}{k_s+k_{f1}[i]} \end{cases} \tag{24}$$

and when axial stress level ranges in $\gamma_{N1}<\gamma_N\le\gamma_{N2}$

$$\begin{cases} l_s[i]=\dfrac{k_{f2}[i]\left(L[i]-l_{f1}[i]\right)+k_s l_{s1}[i]}{k_s+k_{f2}[i]} \\ l_f[i]=\dfrac{k_s\left(L[i]-l_{s1}[i]\right)+k_{f2}[i]l_{f1}[i]}{k_s+k_{f2}[i]} \end{cases} \tag{25}$$

where $l_{f1}$ and $l_{s1}$ are the length of the equivalent fibre and spring in the fibre–spring element when $\gamma=\gamma_{N1}$. The internal force of the $i^{\text{th}}$ fibre–spring element can be obtained by Eq. (26).

$$F[i]=\begin{cases} K_1[i]\left(L[i]-L_0[i]\right), 0<\gamma_N\le\gamma_{N1} \\ K_1[i]\left(L_1[i]-L_0[i]\right) \\ +K_2[i]\left(L[i]-L_1[i]\right), \gamma_{N1}<\gamma_N\le\gamma_{N2} \end{cases} \tag{26}$$

Integrating Eq. (14), the energy absorbed by the $i$-th fibre–spring element during the loading process can be obtained by:

$$E[i]=\begin{cases} K_1[i]\left(L[i]-L_0[i]\right)^2/2 & ,0<\gamma_N\le\gamma_{N1} \\ K_1L[i]\left(L_1[i]-L_0[i]\right)+K_1\left(L_0^2[i]-L_1^2[i]\right)/2 & ,\gamma_{N1}<\gamma_N\le\gamma_{N2} \\ +K_2\left(L[i]-L_1[i]\right)^2/2 & \end{cases} \tag{27}$$

As the symmetry of the model, the points, $C_1$, $C_2$ ... $C_j$ ... $C_{m2}$, connecting with equivalent fibres of the fibre–spring elements in y-axis are distributed along the upper edge of the load device, and another set of endpoints, $D_1$, $D_2$ ... $D_j$ ... $D_{m2}$, connecting with equivalent springs in the *y*-axis of the fibre–spring elements, are distributed along the lower boundary of the ring net. Similarly, the coordinates of $C_j$ can be expressed as:

$$\begin{cases} x_C[j]=\sqrt{R_p^2-(\kappa a)^2\left(j-1/2\right)^2}+e_x \\ y_C[j]=\kappa a\left(j-1/2\right)+e_y \\ z_C[j]=z \end{cases} \tag{28}$$

The coordinates of $D_j$ can be expressed as:

$$\begin{cases} x_D[j]=\kappa w/2+e_x \\ y_D[j]=w\left(j-1/2\right)/\left(2m_2+1\right)+e_y \\ z_D[j]=0 \end{cases} \tag{29}$$

where $j=1,2,...m_2$, and all of the coordinate value in Eqs. (28) and (29) should be positive, viz. $x_C[j]\ge 0$, $y_C[j]\ge 0$, $z_C[j]\ge 0$, $x_D[j]\ge 0$, $y_D[j]\ge 0$ and $z_D[j]\ge 0$.

Along the *y*-axis, each direction vector of the internal force of the fibre–spring element can be obtained by

$$\mathbf{CD}=\left(x_D[j]-x_C[j], y_D[j]-y_C[j], -z_C\right) \tag{30}$$

The length of each fibre–spring element can be calculated by

$$L[j]=|\mathbf{CD}| \tag{31}$$

The initial length of each vector is defined by

$$L_0[j]=|\mathbf{CD}|_{z=0} \tag{32}$$

The internal force value $F[j]$ and energy absorbed $E[j]$ of each element can be calculated by Eqs. (13) and (14), respectively. Once the axial force of any element in the analytical model develops to the maximum, the ring net panel is considered to fail.

$$\max\left\{|F[i]|,|F[j]|\right\}=\gamma_{N\max}\sigma_y A \tag{33}$$

When the load device moves to a certain height, it can be proved that the shorter the initial length $L_0[i]$ of the fibre–spring elements, the larger the axial

force $F[i]$ of the fibre–spring element. The proof process is as follows:

when $0 < \gamma_N \le \gamma_{N1}$:

$$F = K_1\left(L - L_0\right) = k_s k_{f1} \frac{\sqrt{\left(l_{f0} + l_{s0}\right)^2 + z^2} - \left(l_{f0} + l_{s0}\right)}{k_{f1} + k_s}$$

where $L_0 = l_{f0} + l_{s0}$ and $l_{s0}$=const , then:

$$\frac{\partial F}{\partial L_0} = \frac{\partial F}{\partial l_{f0}} = -k_s k_{f1}\left(\sqrt{L_0^2 + z^2} - L_0\right)\frac{k_{f1} + k_s + k_s\sqrt{L_0^2 + z^2}/l_{f0}}{\left(k_{f1} + k_s\right)^2\sqrt{L_0^2 + z^2}} < 0$$

Similarly, it can be obtained that $\partial F/\partial L_0 < 0$ when $\gamma_{N1} < \gamma_N \le \gamma_{N2}$.

This indicates that $F$ is a decreasing function of $L_0$. When the out-of-plane deflection reaches $z$, the smaller the initial length of the fibre–spring element, the larger the axial force $F[i]$. The maximum axial force $F[i=1]$ appears at the fibre–spring element $L_0[i]$ with a minimum initial length, and the failure occurs first on it, that is

$$L_0[i] < L_0[j] \Rightarrow F[i] < F[j] \tag{34}$$

The minimum initial length of the first failed element equals

$$L_0\big|_{i=1} = \min\left\{L_0[i], L_0[j]\right\} \tag{35}$$

For a ring net panel under out-of-plane loading, the maximum internal force of the shortest fibre–spring element ( $i=1$ ) fast develops and is the first to fail, which can be represented as follows:

$$F\big|_{i=1} = \gamma_{N2}\sigma_y A \tag{36}$$

Substituting Eq. (36) into Eq. (26), the maximum length of the shortest element that fails at first can be calculated by

$$L_{\max}\big|_{i=1} = L_0\big|_{i=1} + \sigma_y A\left(\frac{\gamma_{N1}}{K_1\big|_{i=1}} + \frac{\gamma_{N2} - \gamma_{N1}}{K_2\big|_{i=1}}\right) \tag{37}$$

where $L_0$ is the fibre–spring element length at $z=0$ and $L_{\max}$ at $z=H$, $H_{\text{net}}$ represents the maximum out-of-plane deflection of the ring net. The three sides of $H_{\text{net}}$, $L_{\max}$, and $L_0$ forms a right triangle. According to the Pythagorean theorem, the maximum out-of-plane deflection $H_{\text{net}}$ can be written as

$$H_{\text{net}} = z = \sqrt{L_{\max}^2\big|_{i=1} - L_0^2\big|_{i=1}} \tag{38}$$

Substituting Eq. (38) into Eq. (19), then the internal force vectors of $F[i]$ and $F[j]$ of each fibre–spring element, and the energy of $E[i]$, $E[j]$ absorbed can be calculated by Eqs. (26) and (27) respectively. Finally, the load-bearing capacity of the steel ring net $F_{\text{net}}$ can be derived by projecting all force vectors in the z-axis:

$$F_{\text{net}} = 4\left\{\sum_{i=1}^{m_1} F[i]\cos\left(\lambda_\theta\theta[i]\right) + \sum_{j=1}^{m_2} F[j]\cos\left(\lambda_\theta\theta[j]\right)\right\} \tag{39}$$

where $\theta$ is the angle between the direction of the internal force vector of the fibre–spring element and the z-axis, and

$$\cos\theta[i] = \frac{H}{L[i]}, \cos\theta[j] = \frac{H}{L[j]} \tag{40}$$

Considering the influence of circumferential ring chains, the correction coefficient $\lambda_\theta$ has been calibrated through the test results (**Section 5.2**). Because of the scalar nature of energy, the energy absorption capacity of the ring net can be obtained by simply adding together values of energy dissipated by all fibre–spring elements, as Eq. (41) describes

$$E_{\text{net}} = 4\left\{\sum_{i=1}^{m_1} E[i] + \sum_{j=1}^{m_2} E[j]\right\} \tag{41}$$

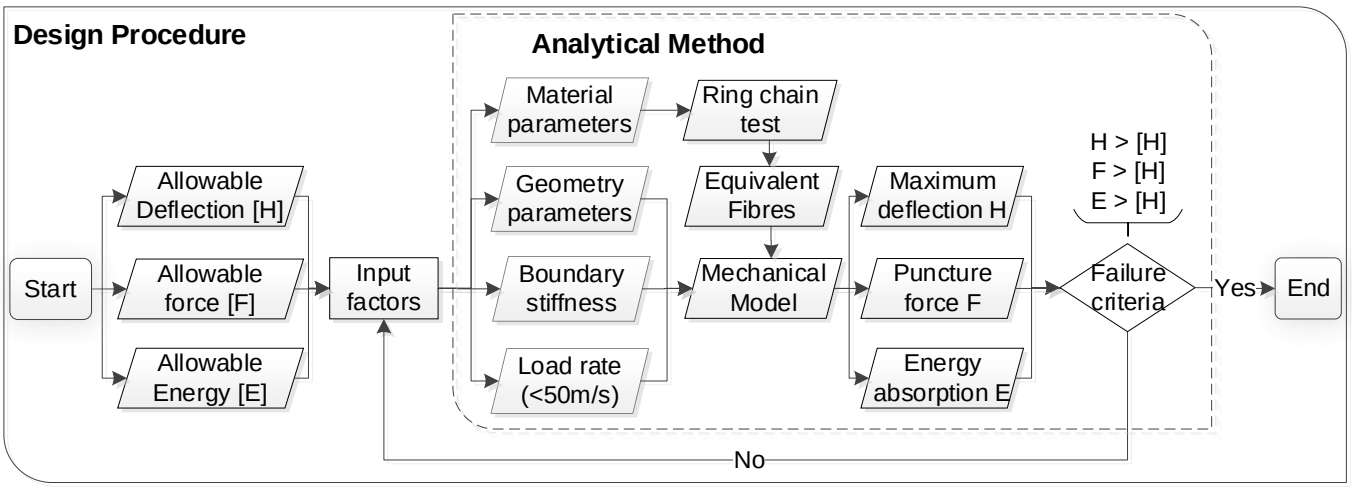


**Fig. 13** Flowchart of the design procedure

*4.4. Design procedure of the ring net*

Through the analytical method, on the one hand, while it can be used to quantitatively analyse and evaluate the structural performance indicators of maximum out-of-plane deflection, load-bearing capacity, and energy absorption capacity of the ring net under multiple influence factors, it is convenient for designing the ring net in a specific engineering project.

The flowchart of the design procedure is depicted in **Fig. 13**. The design approach first entails an assessment of site conditions: characterization of the location, protective area, and allowable deflection of the flexible barrier and evaluation of the potential loads and gravitational energy that the ring net must withstand. Following this assessment, the geometry of the steel rings, loaded area, and the net panel are determined. The force-displacement relationship of the equivalent fibre is obtained through a three-ring chain test. The remaining parameters, such as the strength of the material, and boundary stiffness, are initially set as reference values. Then, a prototype of the ring net is developed. Using the analytical method, the maximum deflection, load-bearing, and energy absorption capacity of the prototype are quantified to check whether its structural performance meets the protection requirements. If any of the calculated values is less than the allowable value, the influencing factors are adjusted, and the iteration process is activated until the correct design parameters are obtained.

## 5. Model parameters and calibration

In this section, the normalised axial stress ratio, the correction coefficient of the direction of force vectors, and stiffness of the equivalent springs for the analytical model are analysed and calibrated.

*5.1. Normalised axial stress ratio*

The experimental and literature results of the three-ring chain under quasi-static tension are used to calibrate the normalised axial stress ratio. Taking the specification of the ring chain as abscissa, the maximum axial stress ratio $\gamma_{\text{Nmax}}$ as ordinate, and the scatter diagram is shown in **Fig. 14**. Observably, with an

increase in the number of windings of the ring net, both the experimental and literature results of the maximum axial stress ratio of the steel wire tend to increase. To quantify the relationship between the axial stress level of the steel wire and the number of windings of the ring, a linear fitting was performed on the scattered points, and a confidence band with a confidence level of 95% was drawn. Since $n_w$ and $\gamma_{\mathrm{Nmax}}$ are dimensionless numbers, the relationship between the maximum axial stress levels $\gamma_{\mathrm{Nmax}}$ and $n_w$ can be directly expressed by

$$\gamma_{\mathrm{N}} = C_1 + C_2 n_w \tag{42}$$

Keeping $\gamma_{\mathrm{N}}$ in the confidence band, different $C_1$ and $C_2$ were tested until the strongest consistency between the experimental and calculated structural performance indicators of the ring net was achieved (**Fig. 17**), when $C_1$ = 0.3, $C_2$ = 0.01.

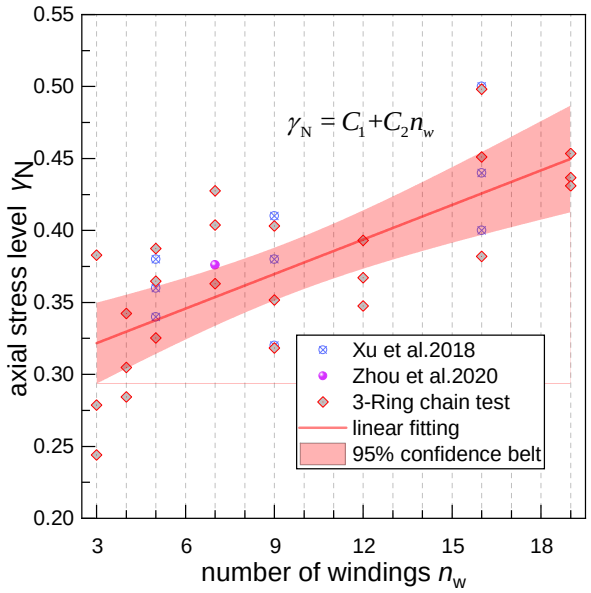


**Fig. 14** Maximum normalized axial stress ratio in literature and ring chain tests **[30,32]**

### *5.2. Correction coefficient* $\lambda_\theta$

Puncture test results with rigid boundary and flexible boundary were conducted to calibrate the correction coefficient. The angles between the actual load path and the z-axis and between the fibre–spring element and the z-axis at the limit state were measured. **Table 3** shows the ranges of ∠ APB and ∠ APQ in the tests and the average correction coefficients.

**Table 3**
Statistical result of the off-angle in puncture tests

| Puncture test | ∠APB | ∠APQ | Average $\lambda_\theta[i]$ |
|---|---|---|---|
| Test2 (RN3-4) | 27°~33° | 43°~46° | 0.73 |
| Test2 (RN5-19) | 29°~36° | 44°~51° | 0.71 |
| Test-Po10R7 | 31°~33° | 45°~48° | 0.69 |
| Test-Ro06R5 | 26°~31° | 45°~48° | 0.6 |
| Test-Po06R7 | 22°~27° | 44°~47° | 0.58 |
| Test-RN5Rope | 21°~25° | 36°~39° | 0.61 |

Accordingly, correction coefficients between 0.5 and 0.75 were tested until $\lambda_\theta = 0.65$, where the calculated results properly agreed with the test results. Notably, assuming the angle ∠ APQ is 45 degrees, a correction coefficient $\lambda_\theta$ of 0.65 means that the force component along the z-axis would increase by 1.23 times that of the original fibre–spring element caused by the angle deviation ( ∠ BPQ). A detailed description of the Test-Ro06R5, Test-Po06R7, Test-Po10R7, and Test-RN5Rope tests can be found in **Section 6**.

### *5.3. Boundary stiffness*

In general, the boundary conditions of the ring net specimens in the quasi-static puncture tests differ in the actual rockfall barrier. In the puncture test, the ring net is connected with rigid shackles mounted to the steel frame so that the boundary can be regarded as a "rigid boundary", i.e.

$$k_s = \infty \tag{43}$$

The ring net is usually connected to the support post by deformable wire ropes in the actual flexible barrier. According to the studies by [21], steel wire rope in a flexible barrier undergoes a nonlinear deflection process subjected to out-of-plane loads. If the drag force in steel rings is equivalent to the distributed load, the deformed wire rope geometry can be reduced to a parabola equation, which can explicitly be written as

$$y_r = \frac{4v_r}{l_{r0}^2}\left(l_{r0}x_r - x_r^2\right) \tag{44}$$

where $l_{r0}$ and $v_r$ are the lengths of the parabola along the $x_r$ -axis and $y_r$ -axis, respectively (**Fig. 15**). The maximum deflection $v_r$ of the rope can be obtained by

$$v_r = \sqrt[3]{\frac{3q_e l_{r0}^4}{64E_r A_r}} \tag{45}$$

where $E_r$ is the elastic modulus, and $A_r$ is the cross-sectional area of the rope. The flexible boundary (rope) is equivalent to several springs with a stiffness of $k_s$. Since the springs are connected in series with fibres to form the fibre–spring elements, the equivalent distributed load $q_e$ along the wire rope depends on the number and magnitude of the internal force in the equivalent fibres. Let $m_r$ be the number of fibre–spring elements, the maximum axial force in the fibres is $\gamma_{N\max}\sigma_y A$. Then, $q_e$ can be obtained by

$$q_e = \lambda_q \cdot \frac{m_r \gamma_{N\max}\sigma_y A}{l_{r0}} \tag{46}$$

When failure occurs on the ring net panel, the axial stress ratio of the fibre–spring element on the shortest load path reaches its maximum $\gamma_{N\max}$, but not all elements reach $\gamma_{N\max}$, so a reduction coefficient $\lambda_q$ is introduced in Eq. (46) to calculate the actual equivalent distributed load on the wire rope. Integrating Eq. (44), the arc length of the deformed rope can be obtained by

$$l_r = \sqrt{\frac{l_{r0}^2}{4} + 4v_r^2} + \frac{l_{r0}^2}{8v_r}\sinh^{-1}\left(\frac{4v_r}{l_{r0}}\right) \tag{47}$$

The internal force of the wire rope can be calculated by,

$$T_r = T_{r,x}\sqrt{1+\left(\frac{q_e l_{r0}}{2T_{r,x}}\right)^2} \tag{48}$$

where $T_{r,x}$ is the horizontal component of $T_r$,

$$T_{r,x} = \frac{E_r A_r}{l_{r0}}\left(l_r - l_{r0}\right) \tag{49}$$

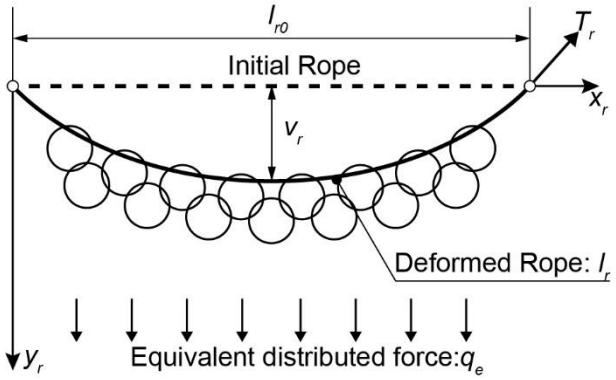


**Fig. 15** Deformed wire rope under the traction of the rings

In addition, to further increase the energy absorption capacity of the flexible barrier system, energy dissipating devices are often connected in series at both ends of the wire rope. Such devices usually become effective when the activation

force is attained during the loading process; the brake then maintains this maximum characteristic force $F_{energy}$ and dissipates energy until the maximum brake elongation $\Delta l_{b,\max}$ is developed. Once such a maximum brake stroke is reached, the device loses the capacity to react, and the force in the cable starts to increase again until it fails. The maximum length of the wire rope connected with an energy-dissipating device can reach

$$l_{r,b} = l_{r,\max} + \Delta l_{b,\max} \tag{50}$$

Here, Eq. (47) can be rewritten as follows:

$$l_{r,b} = \sqrt{\frac{l_{r0}^2}{4} + 4v_{r,b}^2} + \frac{l_{r0}^2}{8v_{r,b}} \sinh^{-1}\left(\frac{4v_{r,b}}{l_{r0}}\right) \tag{51}$$

According to Eq. (34), the shortest fibre–spring element first breaks when its axial force equals $\gamma_{N\max}\sigma_y A$; the equivalent spring in this element reaches the maximum elongation. To ensure a consistent maximum deflection $v_r$ with the deformed rope, the stiffness of the springs can be derived by:

$$k_s = \begin{cases} \gamma_{N,\max}\sigma_y A / v_r, & \text{without braker} \\ \gamma_{N,\max}\sigma_y A / v_{r,b}, & \text{with braker} \end{cases} \tag{52}$$

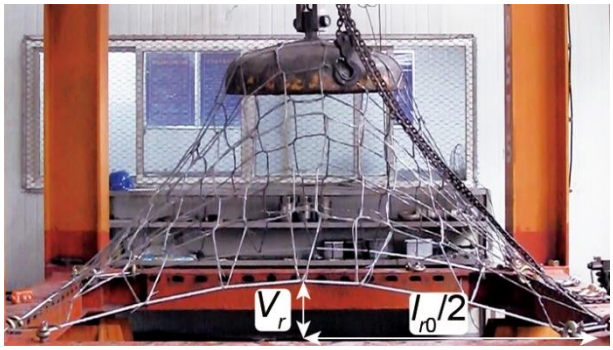


(a) Deformation of the wire rope

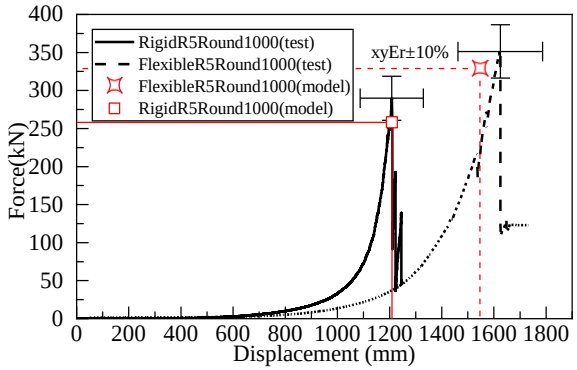


(b) Load-deflection curve

**Fig. 16** Punching test of the ring net with flexible boundary

To calibrate the reduction coefficient $\lambda_q$ of the distributed load along the wire rope, a quasi-static puncture test on a ring net connected with a wire rope was conducted (Test-RN5Rope) (**Fig. 16 a**). The test equipment and instruments conform to **Section 2**. The specification of the net specimen is R5/3.0/300. The size of the square panel is 3.0 m. The wire rope has a diameter of 18 mm, an initial length of 3.0 m at each side of the net boundary, and Young's modulus of 60 GPa [10,12,31].

**Fig. 16 a** shows the deflection of the wire rope and ring net at the limit state. Observably, the deformation patterns of the steel rings in the ring net are similar between puncture tests with rigid and flexible boundaries. The deformed wire rope has a parabolic shape. Due to the non-linear deformation of the wire rope itself, the maximum out-of-plane deflection, load-bearing, and energy dissipated of the ring net with a flexible boundary have been significantly increased compared with the rigid boundary.

Under out-of-plane loading centrally by a hemispherical-shaped press with a diameter of 1.0 m, the wire-ring net specimens were punctured upwards till failure. Since no energy dissipating device is connected with the wire rope, the maximum deflection $v_r$ of the wire rope in Eq. (45) is used to compute the equivalent stiffness.

The reduction coefficient $\lambda_q$ from 0 to 1 was tested until $\lambda_q = 0.25$, where the calculated results of the maximum deflection, load-bearing, and energy absorption capacity properly agreed with the test results (**Fig. 16 b**).

## 6. Verification and discussion

In this section, quasi-static puncture and dynamic destructive tests of the steel ring net panels were conducted. Then, a 1500-kJ full-scale test of the rockfall barrier is presented to validate the potential predicting capability of the analytical model extended to actual flexible barriers.

**Table 4**
Test specimens and loaded areas

| Test | Loaded area | | Ring net size | |
|---|---|---|---|---|
| | Shape | Size | Specimens | Length × width |
| Test-Po10R7 | Polygon | 1.0m | R7/300/3.0 | 3.0m×3.0m |
| Test-Po06R7 | Polygon | 0.6m | R7/300/3.0 | 3.0m×3.0m |
| Test-Ro10R7 | Round | 1.0m | R7/300/3.0 | 3.0m×3.0m |
| Test-Ro10R5 | Round | 1.0m | R5/300/3.0 | 3.0m×3.0m |
| Test-Ro06R5 | Round | 0.6m | R5/300/3.0 | 3.0m×3.0m |

### *6.1. Model validation by quasi-static testing data*

Five quasi-static puncture tests were conducted on the ring net with different specifications, loaded area sizes, and shapes. **Table 4** shows the major information on the test specimens and loaded areas.

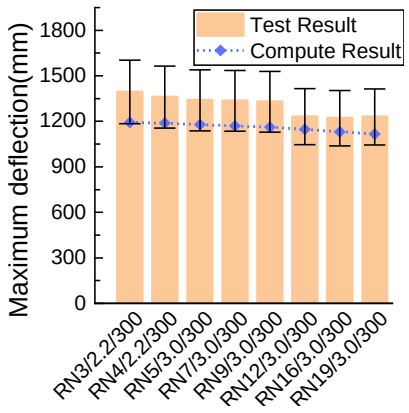


(a) Maximum deflection

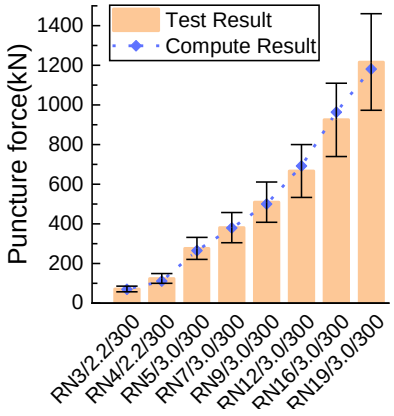


(b) Load-bearing capacity

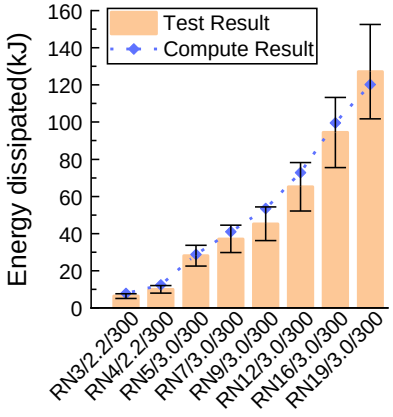


(c) Energy dissipation capacity

**Fig. 17** Comparison between the calculation results and punching test results for maximum force and deflection

*6.1.1. Validation of steel ring specification*

To verify the capability of the model for predicting the effect of ring specification, puncture test results of the ring nets with different numbers of winding and steel wire diameters were compared with computational results (**Fig. 17**). With the increase in the number of ring windings, the maximum deflection of the ring nets shows a slightly decreasing trend, while the braking force and energy absorption shown a significantly increasing trend. The maximum relative errors between the experimental and computational results of the deflection, load-bearing, and energy absorption capacity of the ring net are 14.4%, 10.4%, and 14.8%, respectively. The result comparison presented demonstrates the accuracy and reliability of the analytical model developed in this study. Emphatically, adding to the factors affecting the performance of the steel ring net considered in this study, the slippage between the steel wires and the clip, the initial stress of the steel wire section, and the error of the steel ring diameter will also affect the structural performance indicators of the ring net. There are accidental errors in the manufacturing and installation procedures of the ring net, which make the test results more discrete. It is difficult to further improve the calculation accuracy of the flexible ring net.

*6.1.2. Validation of the loaded area*

To validate the capability of the model for predicting the effect of loading area shape, two puncture tests were conducted on R7/3.0/300 net panels loaded by 1000 mm spherical-shaped and polyhedral-shaped presses, respectively. The outer contour of the polyhedral-shaped press has a circumscribed circle with a diameter of 1000 mm. The test results were compared with the analytical model(**Fig. 18 a, b**). Since the polyhedral-shaped press is slightly smaller than the spherical-shaped press, the maximum deflection of the ring net loaded by the 1000 mm polyhedral-shaped press is more significant than the other one. Notably, compared with the spherical press, although the steel wire rings at polyhedral-press edges have undergone an extra bending deformation (curvature radius of $(1/\rho_1)$, the bending degree is relatively more minor compared to the wire at the contact position between the steel rings (curvature radius of $1/\rho_2$). The steel rings first failed at the edge of the loading area instead of the polyhedral edge. Therefore, unless there is a very sharp edge of the polyhedral-shaped press, making the most unfavourable loading condition for steel rings, the effect of the press shape on the structural performance of the ring net is not significant.


(a) Polygonal-shaped press with size of 1000mm

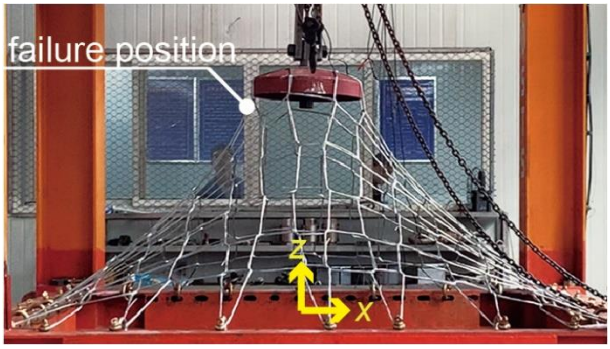


(c) Hemispherical-shaped press with size of 600mm

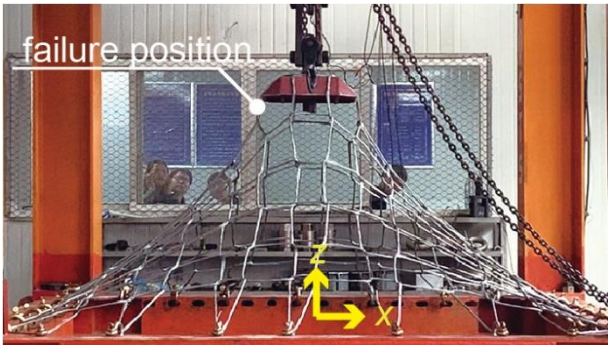


(e) Polygonal-shaped press with size of 600mm

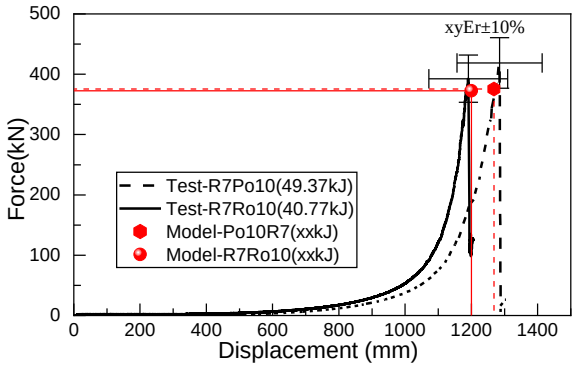


(b) Force-displacement curve of Po10R7 and He10R7

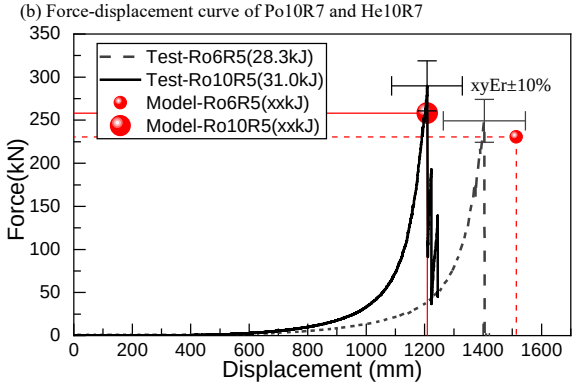


(d) Force-displacement curve of He06R5 and He10R5

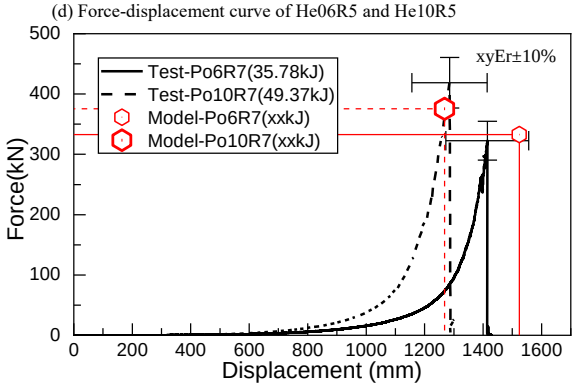


(f) Force-displacement curve of Po06R7 and Po10R7

**Fig. 18** Puncture tests on the ring net loaded by different block shape and size

To validate the capability of the model for predicting the effect of the loading area size, puncture tests on an R5/3.0/300 net panel loaded by hemispherical-shaped presses with 600 mm and 1000 mm diameters were conducted (**Fig. 18 c**). Considering another factor, the number of windings $n_w$, puncture tests on R7/3.0/300 net panels loaded by polygonal-shaped presses with 600 mm and 1000 mm sizes were conducted (**Fig. 18 e**).

The test results were compared with the analytical model (**Fig. 18 d** and **Fig. 18 f**). Concurrently, because of the smaller number of fibre–spring elements in the net loaded by a smaller press size of 600 mm, the load-bearing capacity of the ring net is lower than, which is loaded by a larger press size of 1000 mm. Since the initial length of the shortest fibre–spring element under 600 mm press loading exceeds the net under 1000 mm press loading, the maximum deflection of the former net exceeds the latter. Observably, the analytical model can reflect the effect tendency of the load area size, and the relative errors in maximum deflection and load-carrying capacity between the test results and calculated results by the analytical model are within $10\%$. Thus, the analytical model can describe the maximum deflection, load-bearing capacity, and of the ring net with different shapes and sizes of the loaded areas.

*6.2. Model validation by dynamic testing data*

In actual flexible protection barriers, the ring net is usually subjected to falling rock impact. The load rate of a flexible barrier in static and dynamic conditions differs. The variation in material strength with applied load rate should be considered in designing flexible barriers subjected to suddenly applied loads. From a dynamic plasticity viewpoint, the difference in material behaviour under impact loading and quasi-static loading is that the dynamic strength or yield stress increases as the strain rate increases. The approximate increases in the strain rate are $\dot{\varepsilon} \simeq 1\mathrm{s}^{-1}$ and $10^{-4}\mathrm{s}^{-1} \le \dot{\varepsilon} \le 10^{-1}\mathrm{s}^{-1}$ in quasi-static and drop tests, respectively [37]. Generally, the production material of the wire-ring net in the flexible barrier is a high-strength steel wire with a yield strength exceeding 1770 MPa. The strain rate dependency of the yield stress for high strength wires can be neglected for the strain rates involved in the rockfall problems, typically ranging in $10^{-4}\mathrm{s}^{-1}$ : $10^{2}\mathrm{s}^{-1}$ [20]. In this range of strain rates, high-strength steel alloys experience only modest degrees of strain-rate sensitivity [38]. In this section, destructive impact tests on two square ring nets have been conducted and compared with the analytical results. The model's ability in yielding consistent results when implemented at the structure scale has also been assessed, based on the data of full-scale impact tests on a 1500kJ-energy rockfall barrier.

*6.2.1. Validation at net panel scale*

Firstly, relevant research results of the ring nets impacted by different specifications, loaded areas are summarised. The net specimens are 3m × 3m in size. The maximum deflection, equivalent load, and energy absorption of the ring nets are compared with the calculation results (**Table** 5). Notably, all the ring nets studied in the literature were neither punctured nor were apparent failures found in the steel rings. Their maximum safe bearing capacity remained partially developed. Therefore, the maximum deflection, load-bearing, and energy absorption capacities predicted by the analytical model exceeded the test results obtained from the references. The positive differences between the calculated and referenced values imply that these ring nets still have a residual bearing capacity after being impacted.

To further verify the capability of the analytical model for predicting the maximum deflection, load-bearing, and energy absorption capacity of the ring net under the impact, two destructive impact tests of R5/3.0/300 and R7/3.0/300 ring nets were performed **Fig. 19**. The net specimen tested has a rectangular shape with a size of 3.9 m. Rigid shackles were used to connect the ring net to the steel frame structure. The length and width of the frame were both 4.65 m, and the height was 4.12 m. A spherical-shaped block with a mass of 760 kg and a diameter of 0.8 m was lifted to 13 m to produce kinetic energy equal to 97.2 kJ. Using a high-speed camera with a sampling frequency of 1000 fps, the vertical displacement–time curve of the block was tracked directly from the high-speed video using image tracking software [39]. The block's velocity was obtained by taking the derivative of a displacement with respect to time. The block's acceleration is recorded by an acceleration sensor installed inside its inner space. All measurements were made using calibration factors (mm/pixel) for each set of frames based on the width of the block. However, small oscillations in the block's position (due to image resolution and vibrations) were amplified by the differentiation step, inducing oscillating velocities. Consequently, the velocity plot was smoothed to avoid noisy data caused by the adjacent averaging method.

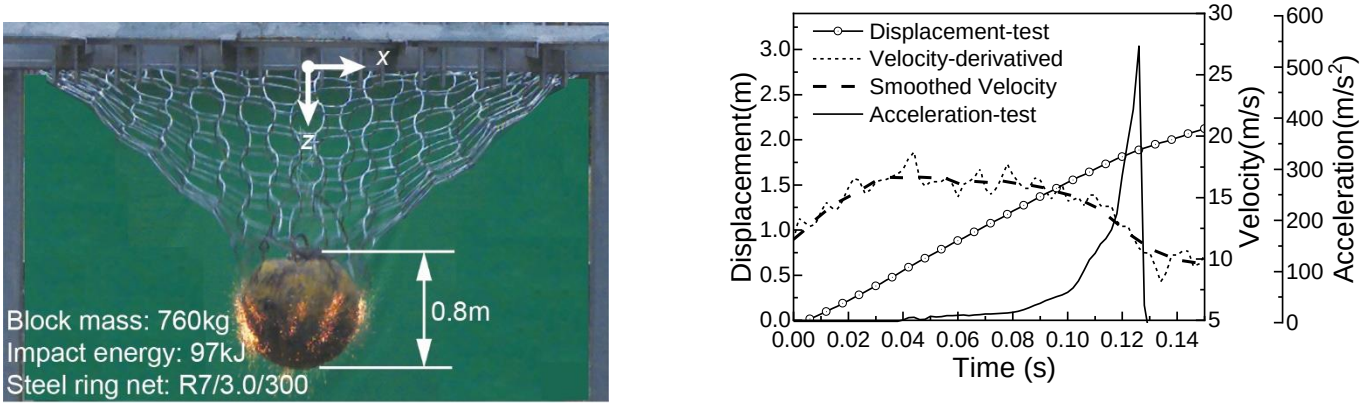


(a) Failure of the ring net under impact load

(b) Displacement, velocity, and acceleration time history curve

**Fig. 19** Destructive impact test on the ring net

The maximum deflection was obtained directly from the photographs using a reference length. The equivalent load-bearing capacity was calculated as the product of the block mass by its maximum deceleration when the failure occurred. The energy absorption capacity was calculated as the difference in the mechanical energy (including both kinetic energy and potential energy) of falling blocks before and after contact with the ring net. Experimental results from both previous works and the destructive impact test of the ring net are modelled and compared with the calculated results in

**Table** 5. Observably, the analytical model can satisfactorily predict failure and provide the maximum deflection, load-bearing, and energy absorption capacity of the ring net. The comparisons also add to the evidence that the load rate effect of the ring nets, made by high-strength steel wires, can be neglected in the rockfall problems.

**Table 5**
Dynamic testing results of the ring net panels

| Specimens of ring nets | Fail (Yes/No) | Ring net size | Loading area diameter | Deflection | | Equivalent force | | Energy dissipated | | Reference/Year |
|---|---|---|---|---|---|---|---|---|---|---|
| | | | | test | model | test | model | test | model | |
| | | length×width | m | m | m | kN | kN | kJ | kJ | |
| R5/3/300 | Yes | 3.9m×3.9m | 0.8 | 2.01 | 1.89 | 274 | 263 | 43.3 | 46.87 | Destructive Impact Test |
| R7/3/300 | Yes | 3.9m×3.9m | 0.8 | 1.98 | 1.87 | 402 | 378 | 59.3 | 66.67 | |
| R7/3/300 | No | 3.9m×3.9m | 0.8 | 1.36 | 1.87 | 160 | 378 | 24 | 66.67 | (Grassl et al. 2002) |
| R7/3/300 | No | 3.9m×3.9m | 0.8 | 1.4 | 1.87 | 282 | 378 | 45 | 66.67 | |
| R5/3/300 | No | 3.9m×3.9m | 0.8 | 1.49 | 1.89 | 165 | 263 | 24.3 | 46.87 | (Volkwein 2004) |
| R7/3/300 | No | 3.9m×3.9m | 0.8 | 1.37 | 1.87 | 155 | 378 | 24.3 | 66.67 | |
| R12/3/300 | No | 3.9m×3.9m | 0.8 | 1.33 | 1.84 | 128 | 691 | 24.3 | 118.47 | |
| R7/3/300 | No | 3.9m×3.9m | 0.8 | 1.45 | 1.87 | 303 | 378 | 44.5 | 66.67 | |
| R12/3/300 | No | 3.9m×3.9m | 0.8 | 1.44 | 1.84 | 222 | 691 | 44.5 | 118.47 | |
| R5/3/300 | No | 3.9m×3.9m | 0.8 | —— | 1.89 | 169 | 221.57 | 24.3 | 38.13 | (Escallón 2013) |

*6.2.2. Validation at structure scale*

A full-scale impact test and numerical simulation of a rockfall barrier with a maximum energy level of 1500 kJ are used to explore the capability of the analytical model when applied to evaluate the maximum structural performance of the net force. One can refer to [30,40] for a complete description of the test procedure and numerical model of the barrier.

A full-scale impact test on the flexible ring net barrier is shown in **Fig. 20**. The ring chains on the shortest load path of the ring net are fully stretched, and the internal axial force vectors of the rings were balanced with the out-of-plane loading. Large deflection for both the ring net and the flexible boundary is developed in coordination. Steel rings showing the largest deformation on the shortest load path are consistent with deformed ring chains. These rings play an indispensable role in the structural performance of the net.

Under the impact of the 4002 kg block with 1500 kJ kinetic energy, the ring net with a flexible boundary has successfully intercepted the block, and no apparent damage occurred on steel rings. The maximum diameter of the polyhedral block is 1.374 m. The specification of the ring net is R12/3.0/300 with a length of 10 m and a width of 5.5 m. The support rope has a diameter of 22 mm and a broken force of 305 kN. Both ends of the support rope along the span direction are connected in series with two energy dissipaters with a maximum elongation of 1.0 m and a maximum characteristic force of 75 kN.

The same finite element model of the rockfall barrier was developed. Keeping the same shape and size of the block, the ring net was punctured when the initial impact energy of the block increased to 2000 kJ. The steel rings at the shortest load path broke first, and the maximum normalized axial stress ratio of straightened steel rings in the whole barrier structure is 0.404, which agrees with the axial stress ratio of 0.42 measured through breaking load in the three-ring chain test with the same specification of R12/3.0/300. **Fig. 20** shows the ultimate limit state of the rockfall barrier. There are two specific load paths in the net. The steel rings deformed slightly in load path 1, indicating that a small internal force developed in these rings. The steel rings deformed significantly in the shortest load path 2, which should be viewed as the primary contribution of the load-bearing capacity of the ring net.

The performance curve (force–elongation curve) of the rockfall barrier is shown in **Fig. 20**. Both the maximum structural performance of the experimental and numerical results are compared with the analytical model. Observably, in the rockfall barrier, the ring net's load-bearing capacity calculated by the analytical model is in good consistent with the numerical simulation results. As the analytical model does not consider the rotation of the steel posts and specific arrangement of non-impact spans of the barrier, the maximum deflection is smaller than the numerical calculation results, and the maximum energy absorption is slightly smaller than the numerical results. The relative error between the analytical model and the test results in this work is below $15\%$. Expectedly, the current accuracy can meet engineering needs.

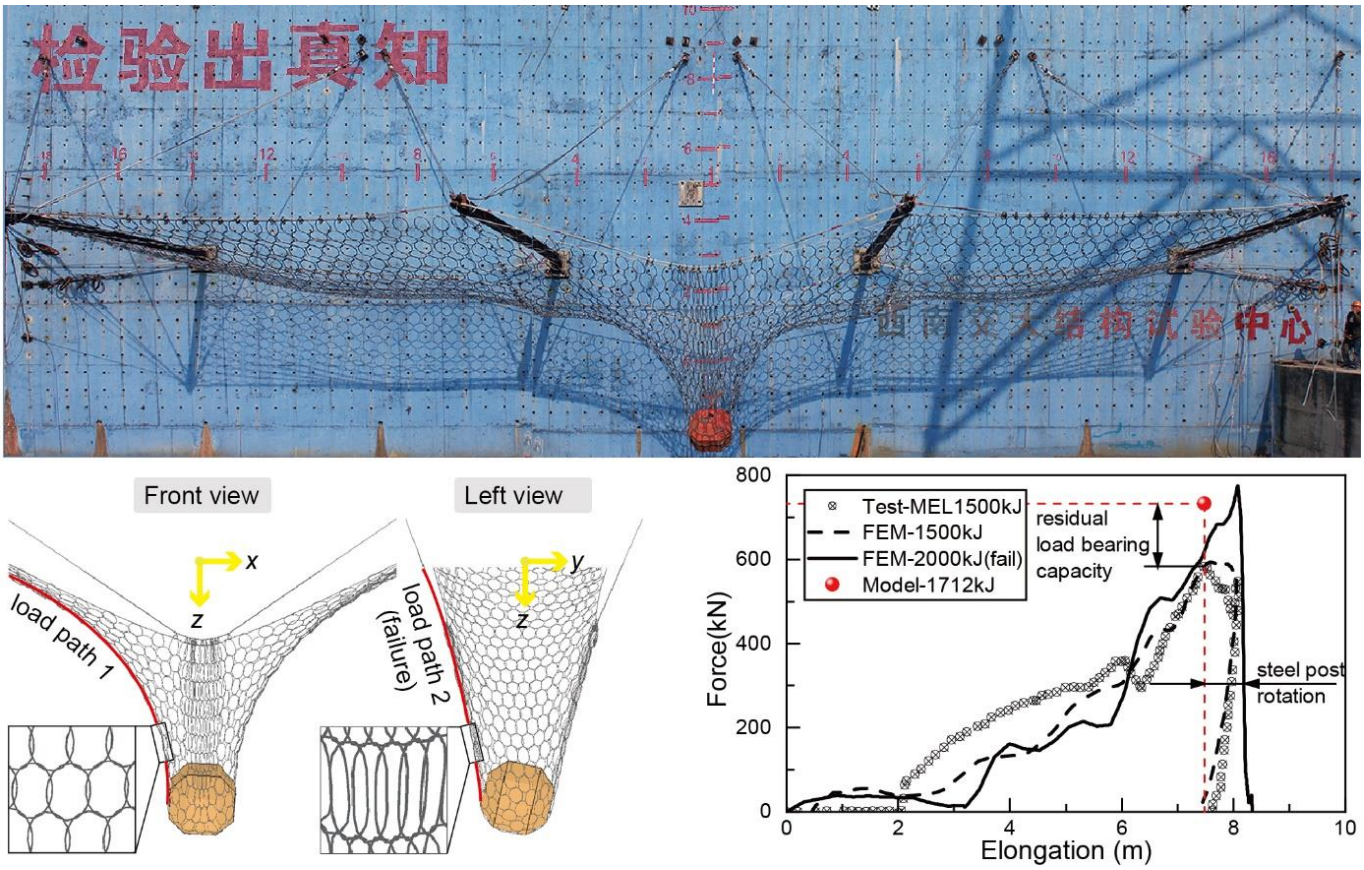


**Fig. 20** Full-scale impact test and numerical simulations on a 1500kJ rockfall barrier

*6.3. Effect of multiple factors*

The deflection, load-bearing, and energy absorption capacity are important structual performance indicators for the design and selection of ring nets. To extend the results of the standard net characterization (i.e. laboratory puncture test) to more general field conditions. The effects of multiple factors, such as the number of windings of steel ring $n_w$, wire diameter $d$, loading area size $R_p$, single ring diameter $D$, the length-width ratio $\kappa$, the boundary stiffness $k_s$, and the load position are discussed in the following.

**Table 6** shows the reference values and ranges of each factor. Notably, to make the parametric analysis results reliable, the load position is set to the net's centre. The reference value of $k_s$ = 5000kN/mm is set to be quite large to maintain consistency with the experimental rigid boundary condition. The maximum deflection $H$, load-bearing capacity $F$, and energy absorption capacity $E$ of the ring net influenced by various factors are plotted collaboratively with trend lines (**Fig. 21**).

(1) Effect of number of windings $n_w$

In this perspective, $n_w$ of the wire-ring is varied ranging from 3 to 15 with an incremental step of 2. The other parameters are the same as those in the reference test reported in **Table 6**.

The structural performance indicators of the ring net obtained for seven different values of $n_w$ (3, 5, 7, 9, 11, 13, 15) is reported in **Fig. 21 a**. The maximum out-of-plane deflection slightly decreases with the increasing number of windings $n_w$. **Fig. 21 a** shows a strong linear correlation between the maximum out-of-plane deflection $H$ and the number of windings. The load-bearing capacity $F$ and the energy absorption $E$ increase obviously with the increasing number of windings, indicating that the $n_w$ limitedly influences the maximum deflection of the ring net, but significantly influences the load-bearing and energy absorption capacity of the ring net.

(2) Effect of wire diameter $d$

In this perspective, the dimension $d$ of the wire is varied ranging from 0.6 mm to 4.8 mm with an incremental step of 0.6 mm. The other parameters are the same as those in the reference test reported in **Table 6**. The structural performance indicators of the ring net obtained for seven different values of $d$ (1.2 mm, 1.8 mm, 2.4 mm, 3.0 mm, 3.6 mm, 4.2 mm, 4.8 mm) is reported in **Fig. 21 b**. With the increase in wire diameter $d$, the maximum deflection $H$ of the

ring net decreases linearly, while the load-bearing capacity $F$ and energy absorption capacity $E$ increase, and the rate of increase increases continuously, indicating that the steel wire diameter limitedly influences the maximum deflection of the ring net but more significantly influences the bearing capacity and energy absorption than the number of windings (**Fig. 21 a**).

**Table 6**
Main parameters of multiple factors

| Parameter type | parameter | unit | range | reference value |
|---|---|---|---|---|
| Influential Parameters | Number of windings ($n_w$) | 1 | 3~15 | 9 |
| | Diameter of single steel wire ($d$) | mm | 1.2~4.8 | 3.0 |
| | Radius of punching device ($R_p$) | mm | 200~800 | 500 |
| | Diameter of steel ring ($D$) | mm | 120~480 | 300 |
| | Length–width ratio ($\kappa$) | 1 | 1.0~2.2 | 1.0 |
| | Boundary stiffness ($k_s$) | N/mm | $2^{-5}$~$2^{25}$ | $5\times10^6$ |
| System performance | Out-of-plane deformation capacity ($H$) | m | —— | 1.18 |
| | Out-of-plane load capacity ($F$) | kN | —— | 504.60 |
| | Energy dissipation capacity ($E$) | kJ | —— | 57.16 |

(3) Effect of steel ring diameter $D$

In this perspective, steel ring diameter $D$ is varied ranging from 0.2 m to 0.8 m with an incremental step of 0.06 m. The other parameters are the same as those in the reference test reported in **Table 6**. The structural performance indicators of the ring net obtained for seven different values of $D$ (0.12 m, 0.18 m, 0.24 m, 0.30 m, 0.36 m, 0.42 m, 0.48 m) is reported in **Fig. 21 c**. The maximum out-of-plane deflection $H$ slightly increases with the increasing diameter of steel rings. **Fig. 21 c** shows a strong linear correlation between the maximum out-of-plane deflection and the diameter of steel rings. The load-bearing capacity $F$ and energy absorption capacity $E$ decrease with increasing steel ring diameter, indicating that the steel ring diameter limitedly influences the maximum deflection of the ring net, but significantly influences the load-bearing capacity and energy consumption of the ring net.

(4) Effect of loading area size $R_p$

In this perspective, loading area size $R_p$ is varied ranging from 0.2 m to 0.8 m with an incremental step of 0.1 m. The other parameters are the same as those in the reference test reported in **Table 6**. The structural performance indicators of the ring net obtained for seven different values of $R_p$ (0.2 m, 0.3 m, 0.4 m, 0.5 m, 0.6 m, 0.7 m, 0.8 m) is reported in Fig. **Fig. 21 d**. As the size of the loading area $R_p$ increases, the maximum deflection $H$ of the net decreases linearly, and the bearing capacity $F$ gradually increases, showing a quadratic relationship between them. The larger the loading area, the shorter the initial length of the equivalent fibres along the edge, so the maximum deflection $H$ could be reduced; however, as the loading area increases, the number of force vectors balanced with the out-of-plane loading of the ring net increases, resulting in a larger load-bearing capacity of the ring net. Conversely, the smaller the size of the loading area $R_p$, the lower the load-bearing capacity $F$. Thus, the ring net could be more prone to damage with a smaller loading area. This result agrees with the "bullet effect" of the flexible intercepting structure reported in the literature [36,41]. The energy absorption of the ring net first increases and then decreases with the increase in the number of windings of the steel rings. This is because the energy absorption capacity of the ring net positively correlates with deflection and load-bearing capacity. As the loading area increases, the influence of the maximum deflection reduction of the ring net on energy consumption gradually exceeds that of the load-bearing capacity increment on energy absorption capacity.

(5) Effect of length–width ratio $\kappa$

In this perspective, length–width ratio $\kappa$ of the ring net is varied ranging from 1.0 to 2.2 with an incremental step of 0.2. The other parameters are the same as those in the reference test reported in **Table 6**. The structural performance indicators of the ring net obtained for seven different values of $\kappa$ (1.0, 1.2, 1.4, 1.6, 1.8, 2.0, 2.2) is reported in **Fig. 21 e**. Keeping the width of the rectangular ring net constant (3.0 m), as the length-width ratio increases, the maximum deflection of the ring net slowly increases with a linear trend, while the load-bearing capacity and energy consumption capacity of the ring net significantly decrease and eventually stabilise, showing an exponential trend (**Fig. 21 e**). The length-width ratio linearly correlates with the maximum deflection of the ring net and exponentially correlates with load-bearing capacity and energy absorption. The length-width ratio of the rectangular net is a key factor affecting the load-bearing and energy-consumption performance of the ring net. When the length-width ratio tends to 1, the ring net can fully perform its protective function.

(6) Effect of boundary stiffness $k_s$

In this perspective, boundary stiffness $k_s$ of the ring net is varied ranging from $2^{-5}$ N/mm to $2^{25}$ N/mm with increasing by multiples of 2. The other parameters are the same as those in the reference test reported in **Table 6**. For clarity, the structural performance indicators of the ring net obtained for eighteen different values of $k_s$ ($2^8 N/mm$ to $2^{25} N/mm$) is reported in **Fig. 21 f**. As the boundary stiffness increases, the maximum deflection and energy absorption capacity decrease exponentially, and the load-bearing capacity of the ring net decreases in the shape of an inverse logistic curve. Since the fibres are connected in series with the equivalent spring, the stiffness of the fibre–spring element in the analytical model increases as the boundary stiffness $k_s$ increases, inducing a smaller elongation of the element and smaller deflection of the net when the failure occurs.

When the boundary stiffness is below 0.256 kN/mm, the load-bearing capacity remains constant because once the boundary stiffness is reduced to a certain level, the direction of the internal force vectors of the fibre–spring elements are almost parallel to the loading direction. However, the maximum axial force of the fibre–spring element remains constant $\gamma_{N\max}\sigma_y A$.

When the boundary stiffness exceeds 0.256 kN/mm and is below 5000 kN/mm, the structural performance indicators of the net are very sensitive to the boundary stiffness. As the boundary stiffness increases, the maximum deflection and energy absorption capacity decrease exponentially, and the reduction rate of the load-bearing capacity increases first and then decreases to zero.

When the boundary stiffness exceeds 5000 kN/mm, the net boundary is considered a rigid boundary, and the structural performance indicators of the net tend to be stable.

**Fig. 21 f** shows that the maximum deflection, load-bearing, and energy absorption capacity of the ring net with a rigid boundary are the smallest under the centrally loading conditions — considered as the lower bound of the structural performance of the ring net with flexible boundary. In practical rockfall barriers, wire ropes are often used as the flexible boundary of the ring net, and energy-dissipating devices with a certain elongation capacity are attached to the ends of the wire ropes. From the analytical method viewpoint, these technical measures significantly reduce the boundary stiffness and increase the maximum deflection of the net while concurrently adjusting the direction of the fibre–spring elements to be parallel with the out-of-plane loading direction to increase the load-carrying capacity. Further, greater deflection and load-bearing capacity will increase the energy absorption capacity of the ring net.

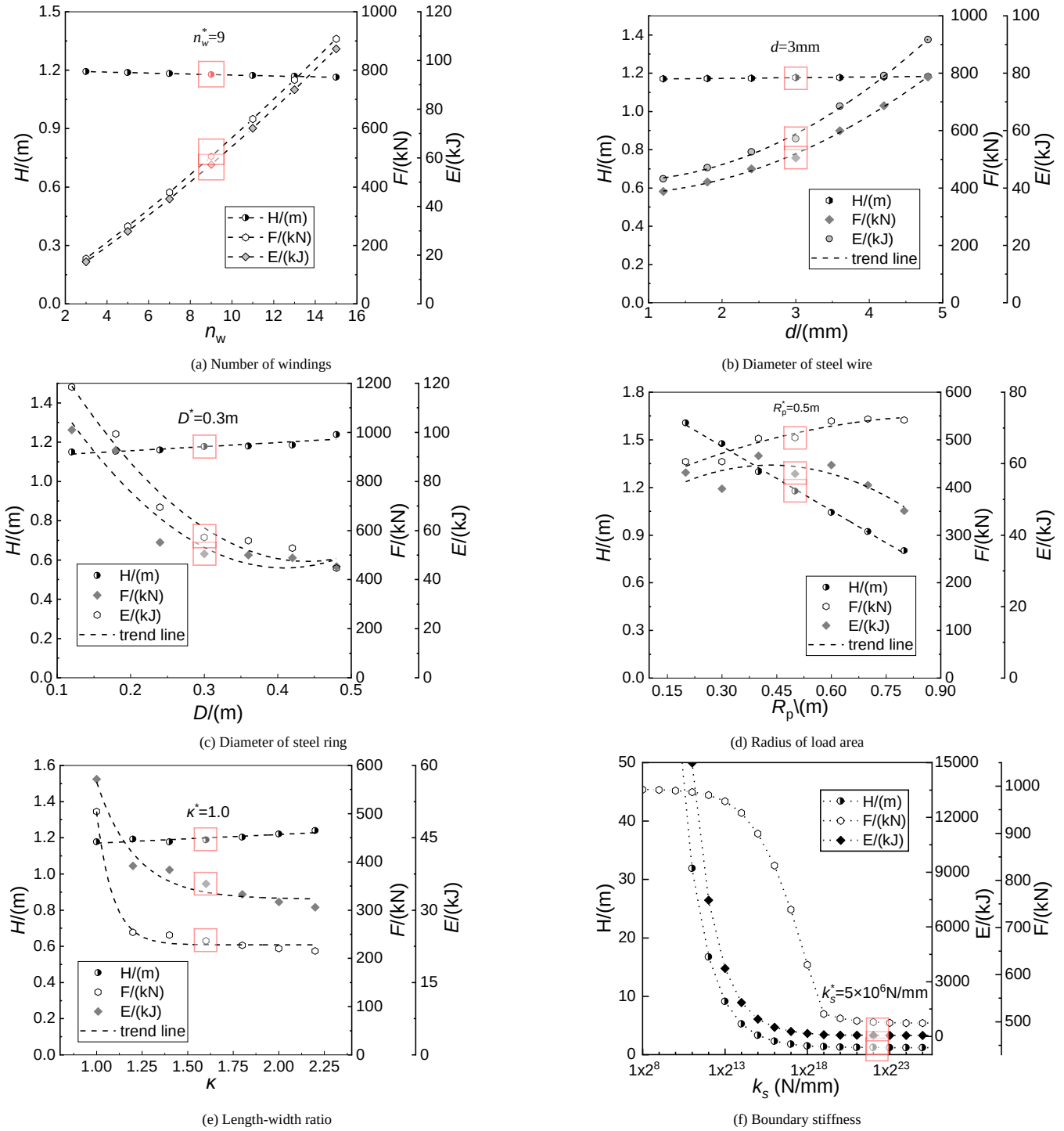


**Fig. 21** Structural performance indicators of ring nets influenced by multiple factors

(7) Effect of the load position

The effect of a generic loaded position ( $e_x$,$e_y$ ) on the structural performance indicators of the ring net panel can be observed in the contour plots of **Fig. 22**. The square net panel size is 3 m, with a steel ring specification of R9/3.0/30. The spherical press diameter is 1 m. As described in Eq. (34), the shorter the initial length of the fibre–spring element, the greater the axial force at a certain out-of-plane deflection. The structural performance of the net panel is controlled by the shortest fibre–spring element on which failure occurs first.

**Fig. 22** shows that, when the loading position is located at the geometry centre of the net panel, the structural performance indicators of the ring net reach their maximum. When the load is applied close to the net's boundary, the length of the fibre–spring elements at the shortest load path decreases. Therefore, the deflection, load-bearing, and energy consumption capacity decrease to varying degrees.

Due to the symmetry of the ring net in the *xy* plane, the structural performance indicators also show symmetrical properties with the shift of loading position. When the loading position is on the symmetrical axes, the ring net has at least two shortest load paths when it fails. When the loading area deviates from the symmetrical axes, the ring net has only one shortest load path when it fails, and there are fewer fibre–spring elements broken simultaneously. When the loading position is located on the four symmetrical axes, the structural performance indexes slowly decrease with an increase in the eccentric distance of the loading position centre. However, all structural performance indicators fall rapidly when the loading position deviates from the symmetric axes.

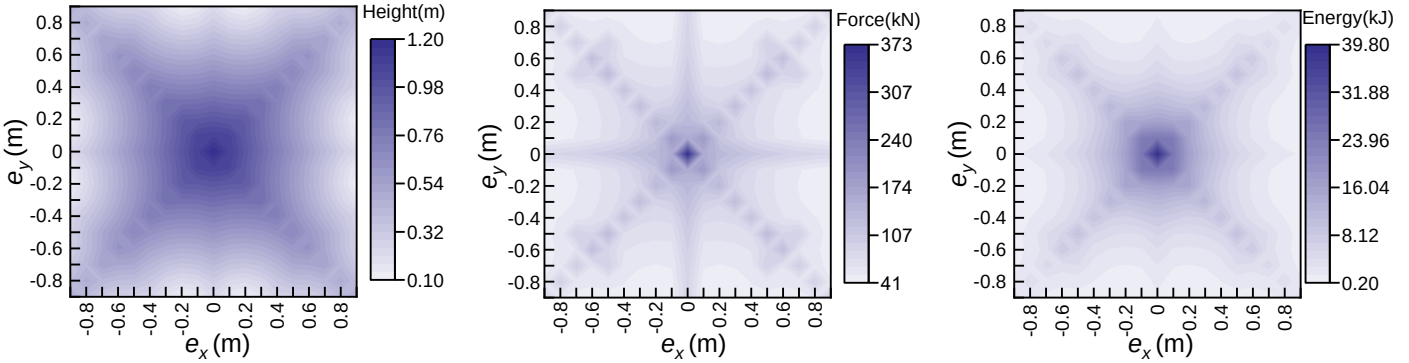


**Fig. 22** Effect of the load position

## Conclusion

This work investigates the maximum deflection, load-bearing, and energy absorption capacity of steel wire-ring nets considering multiple factors' influence. The experimental results indicate that the ring net's structural performance was affected specifically by ring chains on the shortest load path. Before breaking, the steel wire of each ring underwent coupled tension–bending deformation. Further correlation analyses have shown that three structural performance indicators between ring nets and ring chains were strongly related. Accordingly, the ring chains on the load path of the ring net were equivalent to the fibre–spring elements. A three-dimensional analytical model was established. Explicit expressions were derived, which is convenient for engineering design and application. Comprehensive quasi-static and dynamic destructive tests on thirty-two ring nets are conducted to validate the proposed approach. The relative error between the calculation results and the test results was less than 15%, verifying the model's reliability.

Subsequently, the analytical model was used to perform a parametric analysis aimed at quantifying the influence of the fundamental parameters characterizing the field conditions. The main results are summarized as follows:

**The number of windings** controls the load-bearing and energy absorption capacity of the ring net. However, it has a negligible effect on the panel's maximum deflection.

**The steel wire diameter** influences the bearing capacity and energy absorption of the ring net more significantly than the number of windings but limitedly influences the maximum deflection $H$. The maximum deflection $H$ of ring net decreases linearly with the increase in wire diameter $d$. The load-bearing and energy absorption increase with the wire diameter near exponential growth.

**The wire-ring diameter** is one key factor influencing the total number of fibre–spring elements in the analytical model (Eqs. (16) and (17)). It significantly influences the load-bearing and energy absorption capacity, but slightly influences the maximum deflection of the ring net.

**The loaded area size** is another key factor influencing the total number of fibre–spring elements (Eq. (17)). The larger the loading area, the shorter the initial length of the equivalent fibres along the edge, so the maximum deflection $H$ could be reduced. However, as the loading area increases, the number of force vectors balanced with the out-of-plane loading of the ring net increases, resulting in a larger load-bearing capacity of the ring net. Under the influence of maximum deflection and load-bearing capacity, The energy absorption of the ring net first increases and then decreases with the increase in the number of windings of the steel rings.

**The loaded area shape** affects the deformation characteristics of the steel wires at the edges of the loaded area. Compared with the spherical press, the steel wire rings at polyhedral-press edges have undergone an extra bending deformation in the puncture test of the ring net. However, unless there is a very sharp edge of the polyhedral-shaped press, making a more unfavourable condition than contact points between the steel rings, the effect of the loaded area shape on the structural performance of the ring net is not significant.

**The load position** affects the symmetrical properties of the steel rings distributed on the shortest load paths. When the loading area deviates from the symmetrical axes, the ring net has only one shortest load path when it fails, and there are fewer fibre–spring elements broken simultaneously. All of the maximum deflection, load-bearing, and energy absorption capacity reached the highest value when the loaded area is located at the centre of the ring net.

**The length–width ratio** controls the maximum deflection and symmetrical properties of the ring net. Keeping the width of the rectangular ring net constant, as the length-width ratio increases, the deflection of the ring net slowly increases with a linear trend, while the load-bearing and energy absorption capacity of the ring net significantly decrease and eventually stabilise, showing an exponential trend. When the length-width ratio tends to 1, the ring net can fully perform its protective function.

**The boundary stiffness** plays a crucial role in the structural performance of the ring net. When the boundary stiffness exceeds 0.256 kN/mm and is below 5000 kN/mm, the structural performance indicators of the net are very sensitive to the boundary stiffness. Once the boundary stiffness is below 0.256 kN/mm, the load-bearing capacity remains constant. When the boundary stiffness exceeds 5000 kN/mm, the net boundary is considered a rigid boundary, and all of the structural performance indicators of the net tend to be stable. The maximum deflection, load-bearing, and energy absorption capacity of the ring net with a rigid boundary are the lower bound of the structural performance of the ring net with a flexible boundary.

**The Load rates** of a flexible barrier in quasi-static and dynamic conditions differ. However, for the strain rates involved in rockfall problems, the approximate increases in the strain rates range from $10^{-4}s^{-1}$ to $10^{2}s^{-1}$. In this range of strain rates, ultra-high-strength steel wires experience only modest degrees of strain-rate sensitivity and the strain rate effect of the material can be neglected.

In practice, all indicators of maximum deflection, load-bearing, and energy absorption capacity of the ring net should be carefully set to satisfy engineering requirements during designing. The more sensitive factor should be primarily adjusted to realize fast and effective control of ring net structural performance indicators.

## Acknowledgements

The work in this study was supported by the National Key Research and Development Program of China under Grant No.2018YFC1505405, the Natural Science Foundation of China under Grant No.51678504, the Department of Science and Technology of Sichuan Province under Grant No.2018JY0029 & No.2019YJ0221, the Science and Technology Research and Development Program of China Railway Corporation under Grant No.2018KY10, the Shock and Vibration of Engineering Material and Structure Key Laboratory of Sichuan Province under Grant No.18kfgk07, the Applied Basic Research Projects of Sichuan Province under Grant No.2020YJ0263 and the Fundamental Research Funds for the Central Universities under Grant No.2682019ZT04.

## References

[1] Gentilini C., Gottardi G., Govoni L., Mentani A. and Ubertini F., "Design of falling rock protection barriers using numerical models", Engineering Structures, 50, 96-106, 2013. https://doi.org/10.1016/j.engstruct.2012.07.008

[2] Volkwein A. and Gerber W., "Stronger and lighter-evolution of flexible rockfall protection systems", London Symposium Report: Taller, Longer, Lighter (IABSE-IASS 2011), Zurich, Switzerland, 1-5, 2011.

[3] Kwan J.S.H., Chan S.L., Cheuk J. C. Y. and Koo R. C. H., "A case study on an open hillside landslide impacting on a flexible rockfall barrier at Jordan Valley, Hong Kong", Landslides, 11(6), 1037–1050, 2014. https://doi.org/10.1007/s10346-013-0461-x

[4] Wendeler C. and Volkwein A., "Laboratory tests for the optimization of mesh size for flexible debris-flow barriers", Natural Hazards and Earth System Sciences, 15(12), 2597-2604, 2015. https://doi.org/10.5194/nhess-15-2597-2015

[5] Liu, C., Yu Z.X. and Zhao S.C. "Quantifying the impact of a debris avalanche against a flexible barrier by coupled DEM-FEM analyses", Landslides, 17, 33-47, 2019. https://doi.org/10.1007/s10346-019-01267-8

[6] Margreth S. and Roth A., "Interaction of flexible rockfall barriers with avalanches and snow pressure", Cold Regions Science and Technology, 51(2), 168-177, 2008. https://doi.org/10.1016/j.coldregions.2007.03.008

[7] Zhao S.C., Yu Z.X., Zhao L., Qi X. and Wei T., "Damage mechanism of rockfall barriers under strong impact loading", Engineering Mechanics (in Chinese), 33(10), 24-34, 2016.

[8] von Boetticher A. and Volkwein A., "Numerical modelling of chain-link steel wire nets with discrete elements", Canadian Geotechnical Journal, 56(3), 398–419, 2018. https://doi.org/10.1139/cgj-2017-0540

[9] Sasiharan N., Muhunthan B., Badger, T. C., Shu S. and Carradine D. M., "Numerical analysis of the performance of wire mesh and cable net rockfall protection systems", Engineering Geology, 88(1), 121-132, 2006. https://doi.org/10.1016/j.enggeo.2006.09.005

[10] Castro-Fresno D., del Coz Diaz J. J., López L. A. and García Nieto P. J., "Evaluation of the resistant capacity of cable nets using the finite element method and experimental validation."

Engineering Geology, 100(1), 1–10, 2008. https://doi.org/10.1016/j.enggeo.2008.02.007
[11] Tahmasbi S., Giacomini A., Wendeler C. and Buzzi O., “Towards a novel and efficient method to determine the failure energy of rockfall chain-link meshes”, Computers and Geotechnics, 119, 103299, 2020. https://doi.org/10.1016/j.compgeo.2019.103299
[12] Bertrand D., Trad A., Limam A. and Silvani C., “Full-Scale Dynamic Analysis of an Innovative Rockfall Fence Under Impact Using the Discrete Element Method: from the Local Scale to the Structure Scale”, Rock Mechanics and Rock Engineering, 45(5), 885–900, 2012. https://doi.org/10.1007/s00603-012-0222-5
[13] Volkwein A., Roth A., Gerber W. and Vogel A. “Flexible Rockfall Barriers Subjected to Extreme Loads”, Structural Engineering International, 19(3), 327–332, 2009. https://doi.org/10.2749/101686609788957900
[14]Grassl H. G., Volkwein A., Anderheggen E. and Ammann W., “Steel-net rockfall protection-experimental and numerical simulation”, WIT Transactions on The Built Environment, 63, 143–153, 2002.
[15] Volkwein A., “Numerische Simulation von flexiblen Steinschlagschutzsystemen”, Doctoral Thesis, ETH Zürich, Switzerland, 2004.
[16] Buzzi O., Spadari M., Giacomini A., Fityus S. and Sloan S. W., “Experimental Testing of Rockfall Barriers Designed for the Low Range of Impact Energy”, Rock Mechanics and Rock Engineering, 46(4), 701–712, 2013. https://doi.org/10.1007/s00603-012-0295-1
[17] Yu Z.X., Liu, C., Guo L.P., Zhao L. and Zhao S.C., “Nonlinear Numerical Modeling of the Wire-Ring Net for Flexible Barriers”, Shock and Vibration, 7934696, 2019. https://doi.org/10.1155/2019/3040213
[18] Nicot F., Cambou B. and Mazzoleni G., “From a constitutive modelling of metallic rings to the design of rockfall restraining nets”, International Journal for Numerical and Analytical Methods in Geomechanics, 25, 49-70, 2001. https://doi.org/10.1002/1096-9853(200101)25:1<49::AID-NAG117>3.0.CO;2-N
[19] Gentilini C., Govoni L., de Miranda S., Gottardi G. and Ubertini F., “Three-dimensional numerical modelling of falling rock protection barriers”, Computers and Geotechnics, 44, 58-72, 2012. https://doi.org/10.1016/j.compgeo.2012.03.011
[20] Escallón J. P., Wendeler C., Chatzi E. and Bartelt P., “Parameter identification of rockfall protection barrier components through an inverse formulation”, Engineering Structures, 77, 1-16, 2014. https://doi.org/10.1016/j.engstruct.2014.07.019
[21] Brighenti R., Segalini A. and Ferrero A.M., “Debris flow hazard mitigation: A simplified analytical model for the design of flexible barriers”, Computers and Geotechnics, 54, 1-15, 2013. https://doi.org/10.1016/j.compgeo.2013.05.010
[22] Ferrero A. M., Segalini A. and Umili G., “Experimental tests for the application of an analytical model for flexible debris flow barrier design”, Engineering Geology, 185, 33-42, 2015. https://doi.org/10.1016/j.enggeo.2014.12.002
[23] Spadari M., “Experimental and numerical investigations on barriers for rockfall hazard mitigation”, Doctoral Thesis, University of Newcastle, 2013.
[24] Hambleton J. P., Buzzi O., Giacomini A., Spadari M. and Sloan S. W., “Perforation of Flexible Rockfall Barriers by Normal Block Impact”, Rock Mechanics and Rock Engineering, 46(3), 515–526, 2013. https://doi.org/10.1007/s00603-012-0343-x
[25] Peila D., Pelizza S. and Sassudelli F., “Evaluation of Behaviour of Rockfall Restraining Nets by Full Scale Tests”, Rock Mechanics and Rock Engineering, 31(1), 1-24, 1998. https://doi.org/10.1007/s006030050006
[26] Yu Z.X., Qiao Y.K., Zhao L., Xu H., Zhao S.C. and Liu Y.P., “A simple analytical method for evaluation of flexible rockfall barrier Part 1: working mechanism and analytical solution”, Advanced Steel Construction, 14(2), 115–141, 2018a. https://doi.org/10.18057/IJASC.2018.14.2.1
[27] Yu Z.X., Qiao Y.K., Zhao L., Xu H., Zhao S.C. and Liu Y.P., “A simple analytical method for evaluation of flexible rockfall barrier Part 2:application and full-scale test”, Advanced Steel Construction, 14(2), 142-165, 2018b. https://doi.org/10.18057/IJASC.2018.14.2.2
[28] Guo L.P., Yu Z.X., Luo L.R., Qi X. and Zhao S.C., “An analytical method of puncture mechanical behavior of ring nets based on the load path equivalence”, Engineering Mechanics (in Chinese), 37(5), 129–139, 2020. https://doi.org/10.6052/j.issn.1000-4750.2019.07.0345
[29] Trad A., Limam A., Bertrand D. and Robit P., “Multi-scale Analysis of an Innovative Flexible Rockfall Barrier”, Rockfall Engineering, John Wiley & Sons, Ltd, 303-342, 2013. https://doi.org/10.1002/9781118601532.ch9
[30] Xu H., Gentilini C., Yu Z.X., Qi X. and Zhao S.C., “An energy allocation based design approach for flexible rockfall protection barriers”, Engineering Structures, 173, 831-852, 2018. https://doi.org/10.1016/j.engstruct.2018.07.018
[31] Mentani A., Giacomini A., Buzzi O., Govoni L., Gottardi G. and Fityus S., “Numerical Modelling of a Low-Energy Rockfall Barrier: New Insight into the Bullet Effect”, Rock Mechanics and Rock Engineering, 49(4), 1247–1262, 2016. https://doi.org/10.1007/s00603-015-0803-1
[32] Zhu Z. H., Yin J. H., Ouyang C., Tan D. Y. and Qin J.Q., “Modeling a Flexible Ring Net with the Discrete Element Method”, Journal of Engineering Mechanics, 146(2), 04019120. 2020. https://doi.org/10.1061/(ASCE)EM.1943-7889.0001707
[33]Steel wire ring net panels–Definitions and specifications. ISO 17745:2016, 16, 2016.
[34] Falling Rock Protection Kits, European Assessment Document–EAD 340059-00-0106 EOTA, 2018.
[35] Jirasek M. and Bazant Z. P., Inelastic Analysis of Structures, John Wiley & Sons, England, 2001.
[36] Spadari M., Giacomini A., Buzzi O. and Hambleton J. P., “Prediction of the Bullet Effect for Rockfall Barriers: a Scaling Approach”, Rock Mechanics and Rock Engineering, 45(2), 131–144, 2012. https://doi.org/10.1007/s00603-011-0203-0
[37] Cristescu N.D., Dynamic Plasticity, World Scientific Publishing Co. Pte. Ltd., University of Florida, USA, 2007.
[38] Boyce B. L. and Dilmore M.F., “The dynamic tensile behavior of tough, ultra-high-strength steels at strain-rates from 0.0002s−1 to 200s−1”, International Journal of Impact Engineering, 36(2), 263–271, 2009. https://doi.org/10.1016/j.ijimpeng.2007.11.006
[39] Xcitex. Xcitex - ProAnalyst Motion Analysis Software. Proanalyst. (2021).
[40] Yu Z.X., Zhao L., Liu Y.P., Zhao S.C., Xu H. and Chan S.L., “Studies on flexible rockfall barriers for failure modes, mechanisms and design strategies: a case study of Western China”, Landslides, 16(2), 347–362, 2019. https://doi.org/10.1007/s10346-018-1093-y
[41] Buzzi O., Leonarduzzi E., Krummenacher B., Volkwein A. and Giacomini A., “Performance of High Strength Rock Fall Meshes: Effect of Block Size and Mesh Geometry”, Rock Mechanics and Rock Engineering, 48(3), 1221–1231, 2015. https://doi.org/10.1007/s00603-014-0640-7

**Advanced Steel Construction** – Vol. 18 No. 3 (2022) 648–657
**DOI:**10.18057/IJASC.2022.18.3.2


# COLD FORMED STEEL SHEAR WALL RACKING ANALYSIS THROUGH A MECHANISTIC APPROACH: CFS-RAMA

Jammi Ashok * and S. Arul Jayachandran

*Indian Institute of Technology, Madras, India*
** (Corresponding author: E-mail: ashokjammi10994@gmail.com)*

**ABSTRACT**

Cold-formed steel shear wall panels are an effective lateral load resisting system in cold-formed steel or light gauge constructions. The behavior of these panels is governed by the interaction of the sheathing - frame fasteners and the sheathing itself. Therefore, analysis of these panels for an applied lateral load (monotonic/cyclic) is complex due to the inherent non-linearity that exists in the fastener-sheathing interaction. This paper presents a novel and efficient, fastener based mechanistic approach that can reliably predict the response of cold-formed steel wall panels for an applied monotonic lateral load. The approach is purely mechanistic, alleviating the modelling complexity, computational costs and convergence issues which is generally confronted in finite element models. The computational time savings are in the order of seven when compared to the finite element counterparts. Albeit its simplicity, it gives a good insight into the component level forces such as on studs, tracks and individual fasteners for post-processing and performance-based seismic design at large. The present approach is incorporated in a computational framework - CFS-RAMA. The approach is general and thereby making it easy to analyze a variety of configurations of wall panels with brittle sheathing materials and the results are validated using monotonic racking test data published from literature. The design parameters estimated using EEEP (Equivalent Energy Elastic Plastic) method are also compared against corresponding experimental values and found in good agreement. The method provides a good estimate of the wall panel behavior for a variety of configurations, dimensions and sheathing materials used, making it an effective design tool for practicing engineers.

**ARTICLE HISTORY**

Received: 10 June 2021
Revised: 13 December 2021
Accepted: 13 December 2021

**KEYWORDS**

Cold formed steel;
Shear wall panel;
Mechanistic approach;
Brittle sheathing;
Monotonic racking;
Equivalent energy elastic plastic



## 1. Introduction

Cold Formed steel (CFS) framed construction is one of the most resilient system in residential, commercial and institutional constructions. The use of cold formed steel as secondary non-load-bearing components like partition walls and curtain walls has been for long time in construction industry. But with the increase in research on these members/systems as primary load-bearing members and thereby inclusion in the codes of practice, it is gaining appreciable response for adoption in construction sector. Cold formed steel sheathed wall panels (CFSSW) form the gravity and lateral load resisting systems in these constructions. They consist of framing, sheathing, fasteners and hold downs. The framing consists of studs which are cold formed steel lipped channel sections arranged vertically and tracks are un-lipped channel sections, which hold the studs together at top and bottom locations. Together they form a framing system. Sheathing serves as skin for the steel framing and also braces the studs in-plane and out-of-plane directions due to being attached through fasteners at discrete locations. Figure.1 shows the schematic layout of a cold formed steel shear wall panel.

The response of CFSSW panels to applied lateral load well into the non-linear range is of importance for designers to elicit proper design guidelines for Performance-Based Seismic Design (PBSD). The CFSSW panels can be broadly classified into 3 types namely, brittle sheathed panels, ductile sheathed (steel sheet) panels and strap braced panels based on the type of sheathing material used and failure modes observed. The design guidelines for ductile sheathed and strap braced wall panels is well established in AISI S213[1], owing to the extensive experimental campaign by [2, 3, 4]. But the design of brittle sheathed wall panels such as those sheathed with Gypsum boards, calcium silicate boards, fiber cement boards, Oriented Strand Boards (OSB) and so on, require special attention due to their highly non-linear material characteristics. The lateral response of these panels depends mainly on the behavior of the screws connecting the frame to sheathing. This fact is corroborated by the extensive experimental research in the past two decades on these panels with different configurations and sheathing materials. There had been significant effort by researchers across the globe to develop models for assessing the response of wall panels based on the response of individual fasteners, assessed experimentally. These models usually employ finite element analysis to capture the behavior of CFSSW panels. Therefore although accurate, they are prone to complex modelling and convergence issues by practicing engineers.

There had also been some mechanistic and empirical approaches developed to predict the ultimate load and displacement or peak load and displacement of CFSSW panels subjected to monotonic lateral load. However, these are limited in their scope of application due to the inherent assumptions and empiricism. Moreover they do not predict the entire load deformation history. But, the entire non-linear load deformation is necessary to calibrate equivalent single degree of freedom models to incorporate in full scale building models for response prediction of CFS structures.

This paper presents a simplified, robust and yet reliable mechanistic approach which utilizes the data from the fastener shear tests and predicts the entire non-linear load deformation history of the CFSSW panel. This is a step taken towards enabling analysis of different configurations of wall panels alleviating the necessity for full scale wall panel tests which are in themselves costly and difficult to perform. Modelling effort made by past researchers is reviewed and proposed approach is discussed, followed by implementation of the proposed approach in predicting response of four different configurations of CFSSW with different rigid panels from literature. Also the results and post-processing capabilities are presented, followed by conclusions and future work.

### *1.1. Background research on response prediction of CFSSW panels - analytical and numerical methods*

To a large extent the behavior of CFSSW panels closely resembles the behavior of sheathed wood shear wall panels (WSW). It has been a legacy in wood-framed structures, to analyze the behavior of wood shear walls using the screw load-displacement data obtained by simple screw tests. Early efforts by Tuomi and McCutcheon [5], Easley et al. [6], Mc-Cutcheon [7] were to derive simple analytical formulas to predict load-displacement history of WSW under monotonic lateral loads, based on the screw tests and using an energy approach. Although these closed form equations captured the load-deformation behavior accurately up to a moderate load levels, the simplified assumptions in behavior of wall panel and in approximating the screw load deformation data to a function, prevented them to capture the behavior fully into the non-linear range. Itani et.al [8], Dolan and Foschi [9], White and Dolan [10] adopted finite element models to analyze the behavior of these WSW panels. In this regard two computer programs were developed by the researchers namely, SHWALL and WALSEIZ, used for assessing lateral behavior of WSW panel. The models model the frame with beam element, sheathing with 4 node plate element and sheathing to framing connector as non-linear spring. Although, these models are comprehensive and accurate, it is often difficult for a practicing engineer to adopt such methodologies in design practice. Moreover, they are computationally too expensive while modelling whole building for non-linear dynamic analysis [11]. Gupta and Kuo [12] on the other hand followed the similar methodology as [5] and [7], but their aim was not to arrive at simple closed form solutions, rather to develop an analytical procedure based on strain energy approach to arrive at equilibrium equations. This method could assess the wall panel behavior with good accuracy and because of its simplicity it is proposed to be adoptable for non-linear dynamic studies.

The culmination of all these efforts was the development of CASHEW computer program [13, 14] by Folz and Filiatrault under the CUREe-Caltech Woodframe project. This program highlights the efficacy of cyclic analysis in light of full non-linear dynamic analysis and adopted a unified approach for both monotonic and cyclic analysis of WSW panels. This was done using the monotonic experimental data obtained from screw tests and modelling the screws as nonlinear orthogonal spring pair. Once the monotonic curve is obtained, the hysteresis behavior is obtained by using CUREE protocol and piece wise linear path defining rules. The results matched well with experiments. The backbone of all these modelling efforts was to characterize the screw behavior from screw component level tests and incorporate them in the numerical or analytical formulations. Now, in CFS research, the early efforts were by Fülöp and Dubina [15]. They performed screw connections tests in order to establish design criteria on seam and frame-sheathing connections in corrugated CFS wall panels. In an attempt to numerically model the wall panels using finite elements, they incorporated screw connection test data into the FE model. They found striking similarity between the experimental and simulated results. Xu and Martinez [16] have proposed a simple method to estimate the ultimate strength and associated lateral displacement of CFSSW panels. This method draws an analogy between eccentrically loaded bolt group and laterally loaded CFSSW panels and adopts Brandt's inelastic method for evaluating ultimate strength. The results were compared with contemporary experimental data and were found to be in good agreement. But this method doesn't predict the entire load-deformation history. Moreover, as reported by the authors the method predicts lateral strength more accurately than lateral displacement. The same authors developed a simplified numerical approach by modelling the CFSSW panel as equivalent sixteen noded orthotropic shell element [17] and incorporated it in SAP2000 software for assessing performance of a mid-rise CFS building under lateral loads. Although this method reduces the computational cost by modelling the whole panel as 16 node shell elements, the shear forces in the panels and internal forces in the studs are overestimated. Fiorino et.al[18] have performed several tests on screw connections with wood and gypsum sheathing for assessing the effect of different parameters like loading rate, sheathing orientation, sheathing edge distance and so on.

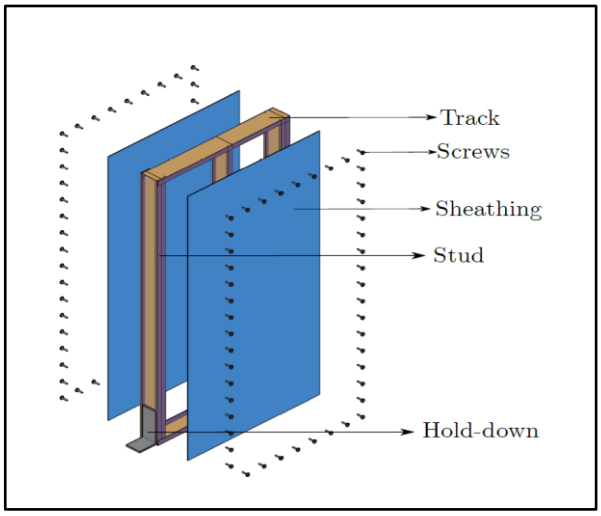


**Fig. 1** Layout of CFS shear wall panel

With the data from screw tests schematized into relationship proposed by Richard and Abbott, they have also presented an analytical method for predicting the lateral load-displacement curve of CFSSW panel sheathed with oriented strand board on one side and gypsum board on other side [19]. The results were in good agreement with experiments. Buonopane et.al [20] have modelled the behavior of CFSSW panel in OpenSees [21] by a similar approach as in WSW panels. The studs and tracks are modelled as displacement based beam column elements, the sheathing as *RigidDiaphram*. The fasteners are modelled as *CoupledZeroLength* element with *pinching4* material with parameters

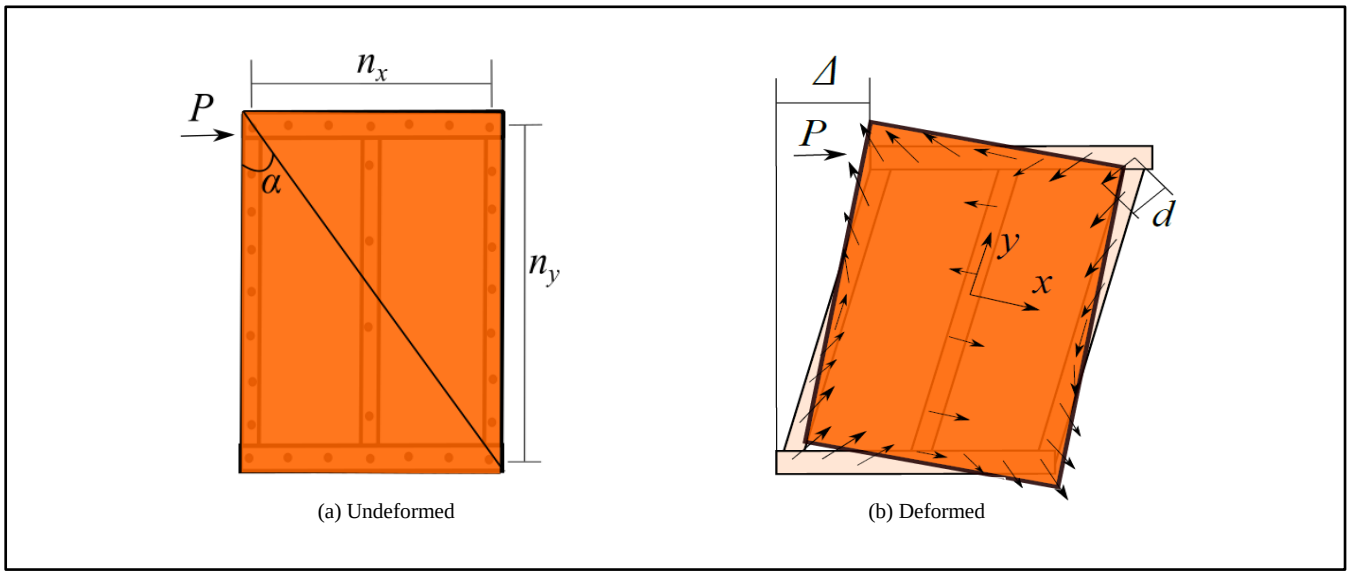


(a) Undeformed (b) Deformed

**Fig. 2** Response of wall panel under lateral load action

calibrated to cyclic screw connection tests. The model reasonably captured the key characteristics of the cyclic load-displacement response. These models are efficient, in that, they fall between detailed finite element models and simple frame models and the only experimentally derived input is parameters of pinching4 material that are obtained from fastener cyclic tests. Also, these models give significant insight into fastener forces, stud forces and so on. However the model under predicts the cumulative energy dissipated with increase in number of cycles. Karabulut and Soyoz [22] modelled the CFSSW panel in SAP2000 by characterizing the screw test data to a revised Richard and Abbott model and modelling the fasteners as non-linear connectors.

The results matched well with experiments. However, revising the Richard and Abbott model for every type of sheathing to framing connections is cumbersome on trial and error basis.

The above study shows that procedures proposed in the literature involve either numerical simulation which is prone to convergence issues and cumbersome modelling in FEM software or simplified methods where there is a tradeoff between strength and deformation predictions. Therefore there is necessity for a simplified methodology to reliably analyze the lateral load displacement response of CFSSW panels, which can be easily adopted by researchers and practicing engineers for arriving at reliable prediction of strength and deformation capacities. This paper presents a purely mechanics based approach which is simple to implement, nevertheless reliable in it's prediction of the entire lateral load displacement response of the CFSSW panels with rigid sheathing materials such as OSB, calcium silicate board, gypsum wall board and so on. The methodology is implemented and verified against the experimental data for four different geometric and material configurations representing typical variations in CFSSW panels, adopted from the literature and the results are found to be in good agreement.

## 2. Methodology

The methodology adopted in the present approach is based on geometric

relations between the CFS frame top displacement and the screw deformations and screw resistance developed thereof. The entire load-deformation history of CFSSW panel with rigid sheathing is discussed in two parts:

- Response till peak load
- Post-peak response

The idea behind such demarcation is primarily the change in deformation mode of the sheathing and subsequent change in geometric relations, as will be explained further.

### *2.1. Response till peal load*

When a lateral load is applied to a wall panel, the steel stud frame distorts into parallelogram and the sheathing undergoes rigid body rotation. There is no significant deformation observed in the sheathing and is considered to remain rectangular. This relative displacement between the framing and sheathing causes shear force to be acting on the fasteners. The shear resistance provided the fasteners equilibrates the external load acting on the wall panel. The fundamental relationships in deriving the resistance provided by the fasteners had been adopted from Tuomi and McCutcheon [5] and McCutcheon [7]. However, the latter has adopted energy approach to solve for the resistance developed, but an equilibrium approach has been adopted in this study. The following are the assumptions made in this approach:

1. Frame distorts as a parallelogram and the sheathing retains its initial rectangular shape.
2. Sheathing undergoes rigid body rotation about its geometric center.
3. Sheathing is continuous from top of the frame to bottom.
4. The overall response of the wall panel is dictated by the response of the individual fasteners only and the shear deformation of the sheathing itself is negligible and hence the shear resistance developed thereof.
5. The screws are spaced evenly and symmetrically at the perimeter of the wall panel and in the field.

Assumption 4 is justified from the previous research[20][23] i.e. the stiffness at local fastener location is considerably lower compared to the overall diaphragm shear stiffness of the brittle sheathing panels(generally used for CFSSW such as wood based panels), for it leverage on the shear resistance of sheathing material. Therefore the global wall behavior is essentially dictated by local fastener behavior. Considering assumptions 1, 2 and 4, ductile sheathing materials such as steel sheets, are not in the scope of this paper. However simpler mechanics based methods that take tension field action into account are proposed earlier [24].

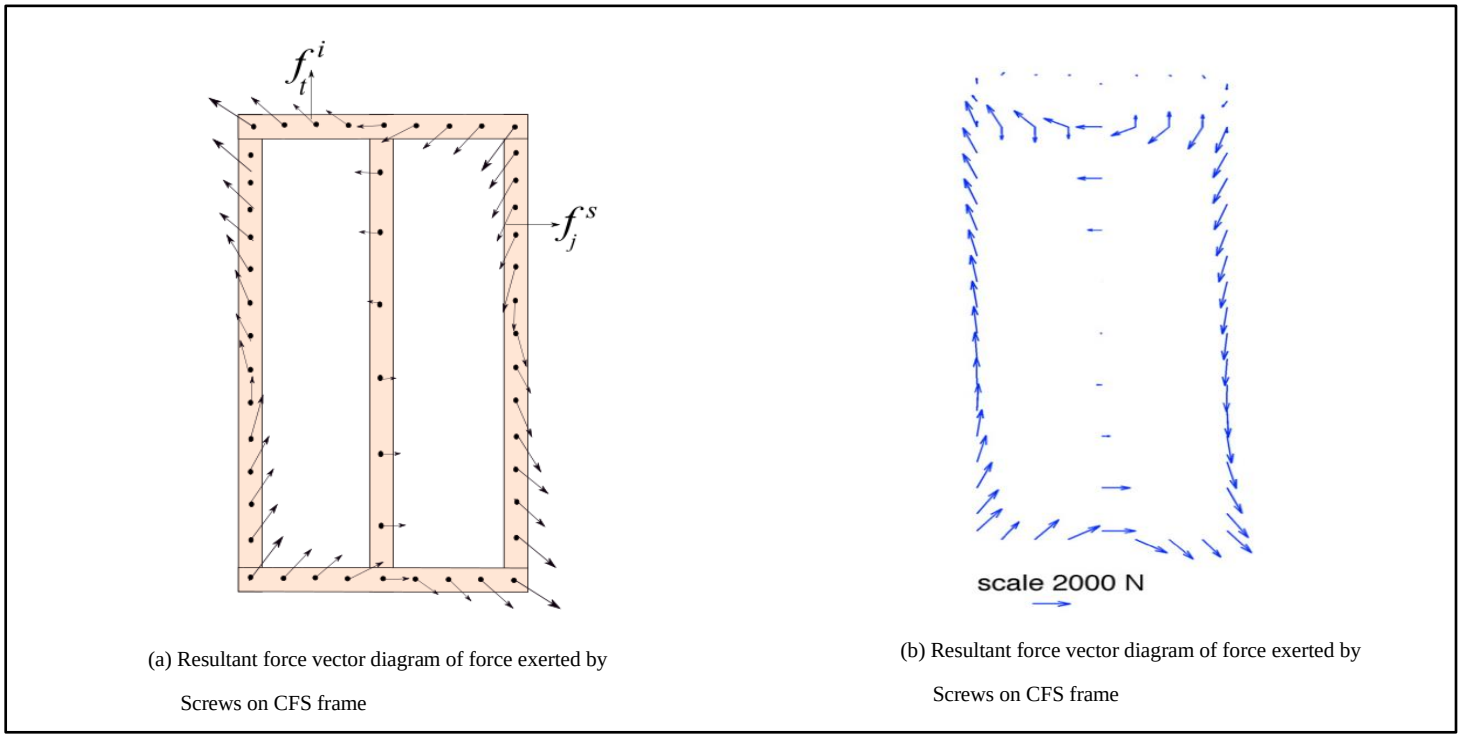


(a) Resultant force vector diagram of force exerted by Screws on CFS frame

(b) Resultant force vector diagram of force exerted by Screws on CFS frame

**Fig. 3** Forces on wall panel at discrete fastener locations

Fig.2 shows the undeformed and deformed configurations of the wall panel. It is found from several experiments by past researchers that the corner screws deform the most. These deformations are approximately along the sheathing diagonals. Calculations by [7] show that, moderate change in this direction doesn't alter the performance of wall panels significantly. So for mathematical simplicity, it can be approximated that corner screws deform along sheathing diagonals as shown in fig.2. With this approximation, the deformation of all other screws can be expressed in terms of corner screw deformation (eq. 1 to 4). Let 'd' be the corner screw deformation along the sheathing diagonal, which makes an angle 'α' with the vertical side fig.2(a). The individual screw deformation is denoted by 'δ', with horizontal and vertical components as '$\delta_X$' and '$\delta_Y$' respectively. Now, from McCutcheon [7] the following relations can be established.

For the top edge:

$$\delta_x = d\ sin\ (\alpha) \tag{1a}$$

$$\delta_y = -\left(2\frac{i}{n_x} - 1\right) d \cos(\alpha) \tag{1b}$$

For the bottom edge:

$$\delta_x = -d\ sin\ (\alpha) \tag{2a}$$

$$\delta_y = -\left(2\frac{i}{n_x} - 1\right) d \cos(\alpha) \tag{2b}$$

For the left edge:

$$\delta_x = -\left(2\frac{j}{n_y} - 1\right) d \sin(\alpha) \tag{3a}$$

$$\delta_y = d\ cos\ (\alpha) \tag{3b}$$

For the right edge:

$$\delta_x = \left(2\frac{j}{n_y} - 1\right) d \sin(\alpha) \tag{4a}$$

$$\delta_y = -d\ cos\ (\alpha) \tag{4b}$$

Where,
$n_x$ is the number of screw spacings on tracks,

$n_y$ is the number of screw spacings on studs,

i = 0,1,2,…. $n_x$

j = 0,1,2,…. $n_y$

Now, since the screws transfer the shear forces between the stud frame and the sheathing, the stud frame also experiences force in the same direction of the deformation of screws. These force vectors are shown in fig.3 (a). This fact is corroborated by observing the vector force diagram obtained using

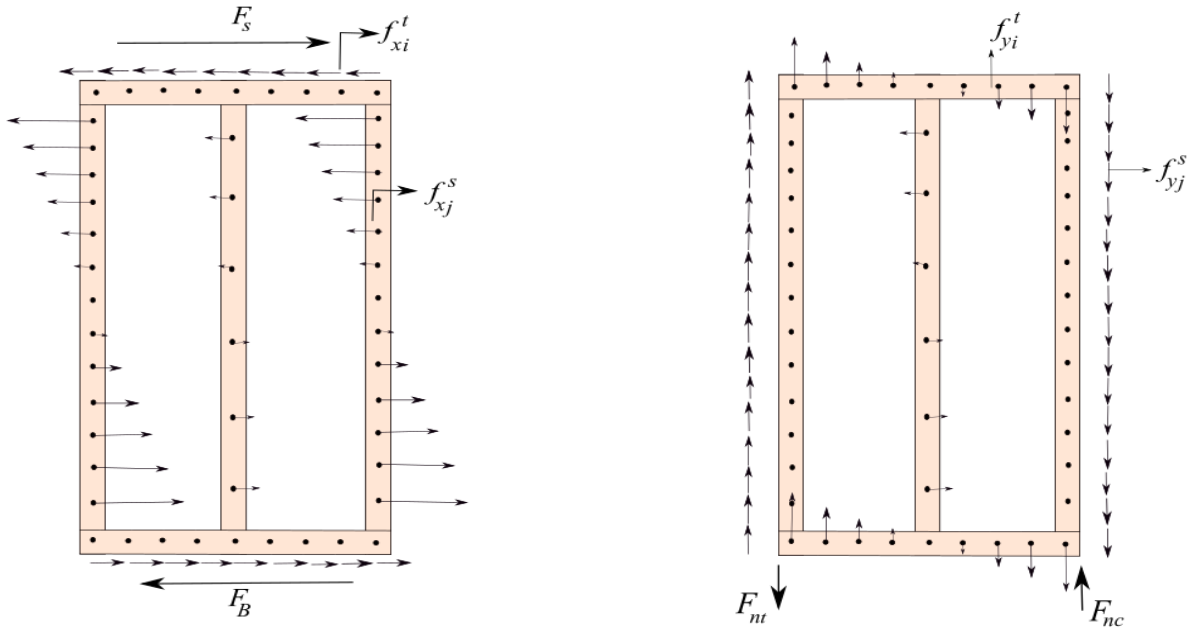


(a) Horizontal components of fastener forces at each screw location

(b) Vertical components of fastener forces at Each screw location

**Fig. 4** Force components on wall panel at discrete fastener locations

Computational analysis in OpenSees software by Buonopane et.al [20]. Therefore directions of the resultant vectors as per the proposed theory are similar to that of validated computational models. Now, resolving these vectors into horizontal and vertical components as shown in fig.4 (a) and (b). '$f_{xi}^t$' and '$f_{yj}^s$' are the horizontal components of screw force vector at i[th] location on the track and j[th] location on the stud respectively (fig.4 (a)). '$f_{yi}^t$' and '$f_{yj}^s$' are the vertical components of screw force vector at i[th] location on the track and j[th] location on the stud respectively (fig.4 (b)). $F_s$ is the external shear force acting and $F_B$ is the base shear developed. $F_{nt}$ and $F_{nc}$ are the reactions developed at the tension side and compression side of the wall panel respectively.

The proposed method adopts an algorithm, wherein the applied wall-panel top track lateral displacement (Δ) is given as the input. This lateral displacement (Δ) is related to the horizontal and vertical components of screw displacements using the simple geometric relationships as given in eq.1 through 4. From the resultant displacement, the resultant force developed at individual screw location is evaluated by characterizing the screw load displacement data to a 4[th] degree polynomial. Thereafter, by principles of equilibrium, the resistance developed in the wall panel is evaluated.

The global displacement of the top track 'Δ' is related to corner screw displacement 'd' as,

$$d = \frac{1}{2}\Delta \sin(\alpha) \tag{5}$$

$$\delta_k = (\delta_{kx}^2 + \delta_{ky}^2)^{\frac{1}{2}} \tag{6}$$

Therefore, from eq.1, 2, 5 and 6, the resultant screw deformation at i[th] location on the top and bottom tracks is,

$$\delta_i^t = \frac{1}{2}\Delta \sin\alpha \left[\left(2\frac{j}{n_y} - 1\right)^2 sin^2\alpha + cos^2\alpha\right]^{\frac{1}{2}} \tag{7}$$

Similarly, from eq.3, 4, 5 and 6, the resultant screw deformation at j[th] location on the left and right tracks is,

$$\delta_i^t = \frac{1}{2}\Delta \sin\alpha \left[\left(2\frac{j}{n_y} - 1\right)^2 sin^2\alpha + cos^2\alpha\right]^{\frac{1}{2}} \tag{8}$$

Therefore, in eq.7 and 8, the individual screw displacement is expressed in terms of global wall lateral displacement. Now these screw displacements have to be related to screw force. Now we have to relate the screw deformation to screw force. This is established mainly by fitting a curve to the screw test data, so that screw force can be expressed as a function of screw displacement. Therefore at any instant the screw force is dependent only on the instantaneous screw displacement and is independent of the displacement history. As the general screw load displacement data follows a polynomial curve [25], a 4[th] degree polynomial is chosen to represent screw force as a function of screw displacement. Sometimes even 3rd degree polynomial also suffices, but in order to maintain consistency in implementation, a 4[th] degree polynomial is chosen. The assumed polynomial is written in the form,

$$f(x) = ax^4 + bx^3 + cx^2 + dx + e \tag{9}$$

The coefficients [a,b,c,d,e] vary for different screw and sheathing combinations. But once the coefficients are evaluated for a particular configuration, by appropriate curve fitting techniques, then force developed in the screws can be established in terms of screw displacement as a continuous function. Therefore, from eq.9 the force developed in each individual screw '$f_k$' can be expressed in terms of individual screw displacement '$\delta_k$' as,

$$f_k(\delta_k) = a\delta_k^4 + b\delta_k^3 + c\delta_k^2 + d\delta_k + e \tag{10}$$

Therefore, in a displacement controlled loading, when the wall panel is laterally displaced by 'Δ', from eqs.7 and 8 we know the screw deformations ($\delta$) in terms of 'Δ'. In eq.10, we have related screw deformations ($\delta$) to force generated in the screws '$f_k$'. Now the force developed at each discrete screw location has to be related to total shear resistance developed by the panel '$F_s$'. This can be evaluated by considering the free body diagram of the wall panel with horizontal components of the screw forces as shown in fig.5. Considering

the upper part of X - X, for the panel to be in equilibrium the lateral force should be equal to sum of the horizontal components of the screw forces located on upper part of the X - X. This can be written as,

$$F_s = \sum_{i=1}^{n_x} f_{xi}^{ut} + \sum_{j=1}^{\frac{n_y}{2}} f_{xj}^{urs} + \sum_{j=1}^{\frac{n_y}{2}} f_{xj}^{uls} \quad (11)$$

Similarly for the lower part of X - X, the base shear '$F_B$' should be equal to sum

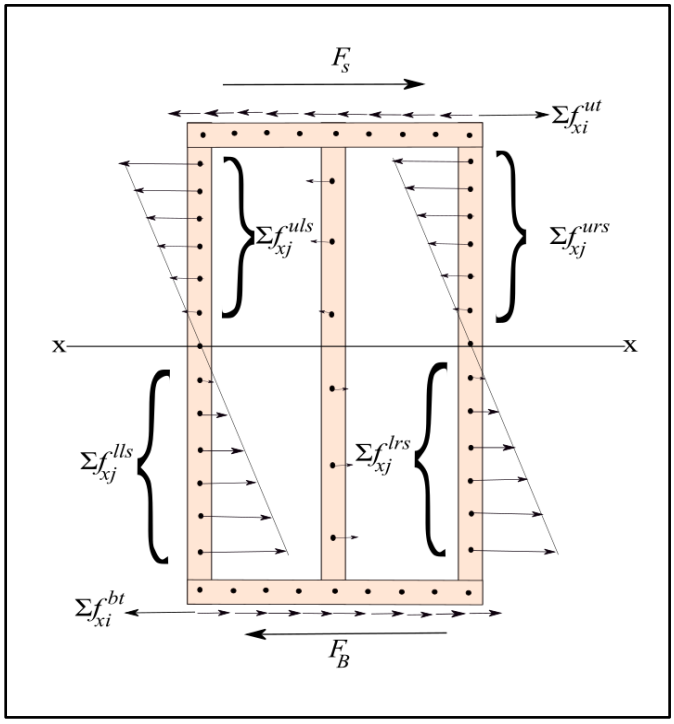


**Fig. 5** Free body of frame showing horizontal components of the screw forces

of the horizontal components of the screw forces located on lower part of the X - X. This can be written as,

$$F_B = \sum_{i=1}^{n_x} f_{xi}^{bt} + \sum_{j=\frac{n_y}{2}}^{n_y} f_{xj}^{lrs} + \sum_{j=\frac{n_y}{2}}^{n_y} f_{xj}^{lls} \quad (12)$$

Where in eq.11 and eq.12,

$f_{xi}^{ut}$ – Horizontal component of screw force located at the i[th] position on the upper track,

$f_{xj}^{urs}$- Horizontal component of screw force located at j[th] position on the upper right stud.

$f_{xj}^{urs}$- Horizontal component of screw force located at j[th] position on the upper left stud

$f_{xj}^{bt}$- Horizontal component of screw force located at j[th] position on the bottom track

$f_{xj}^{lrs}$- Horizontal component of screw force located at j[th] position on the lower right stud

$f_{xj}^{lls}$- Horizontal component of screw force located at j[th] position on the lower left stud

Therefore, evaluating $F_B$ for every displacement step gives the resistance developed in the panel. The eq.1a to 8 are implemented and were found to reliably capture the behavior of the CFSSW panel till peak load. After the peak load, the evaluated resistance would be over-estimated. This is because of the inherent assumptions like small displacements of screws that are made in deriving the above relationships. But in reality the panel undergoes large deflection beyond peak load. This is explained in the following section.

### *2.2. Post peak response*

It has been reported by many researchers [26, 27, 28, 29] that after failure of wall-panel that sheathing was observed to have underwent overturning movement. That means the center of rotation has shifted from geometric center of the sheathing towards the corner. This is also corroborated by the evaluation of instantaneous center of rotation for calculating the ultimate load in the analytical approach proposed by Xu and Martinez [16]. The instantaneous center of rotation was offset from the center of screw group at the ultimate strength level. Therefore, for evaluating the response after the peak load, the center of rotation is assumed to have shifted from center of panel to corner of the panel as shown in fig.6. 'O' is the center of rotation till peak load and 'O' is the center of rotation beyond peak load. Now the geometric relationship between post peak global lateral displacement '$\Delta_{pp}$' and the individual screw displacement '$\delta$' can be expressed directly as,
For track screws,

$$\delta_i = \delta_{peak} + \frac{\Delta_{pp}}{p_i} \quad (13)$$

Where,

$\delta_i$ is the displacement of i[th] screw on the track,

$p_i$ is the position of i[th] screw from the corner $O'$,

$\delta_i$ is the displacement of i[th] screw on the track,

$\Delta_{pp}$ is the post peak displacement of the wall panel,

s is the screw spacing on the track.

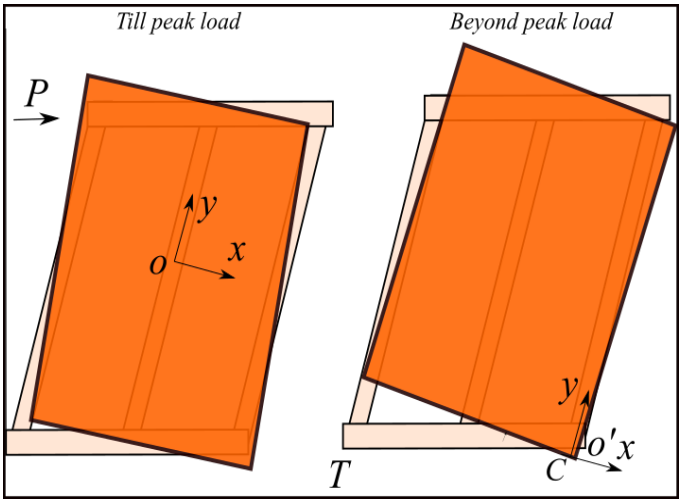


**Fig. 6** Peak and post peak deformation patterns (exaggerated)

This process is repeated for every global lateral displacement step and force developed is evaluated in the same way as described in the previous section, eq.10 to 12. From eq.13, it can be seen that the corner screw displacements keep on monotonically increasing leading to either edge tearing of the panel at the tension side (T) or the board crushing on the compression side (C) of the board, incapacitating the screws at these locations to offer shear resistance. So, in the algorithm, the screws that cross their ultimate displacement limit are traced and their resistance is made zero. Similar criteria applies to the screws on studs also. Finally the program stops when more than 40% screws are failed on the tracks indicating the onset of instability and attainment of ultimate resistance. The whole approach can be summarized as shown in fig.7.

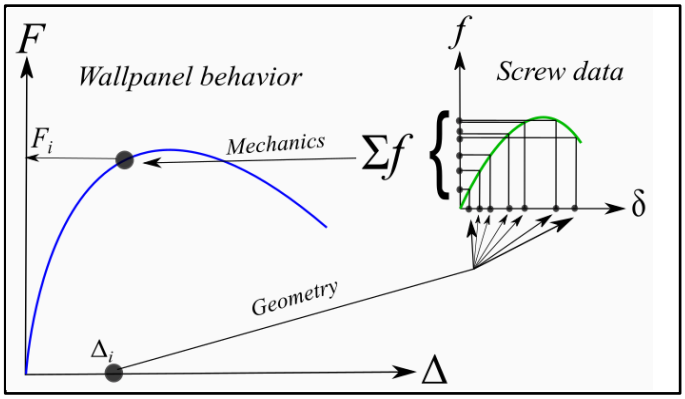


**Fig. 7** Summary of the approach

It is to be noted that the eq.11 is presented for one sheathing panel. But if multiple panels are used, this approach has to be applied on each individual sheathing panel and the resultant lateral resistance is simply a sum of lateral resistance of each individual panels. The multiple panels may be placed either

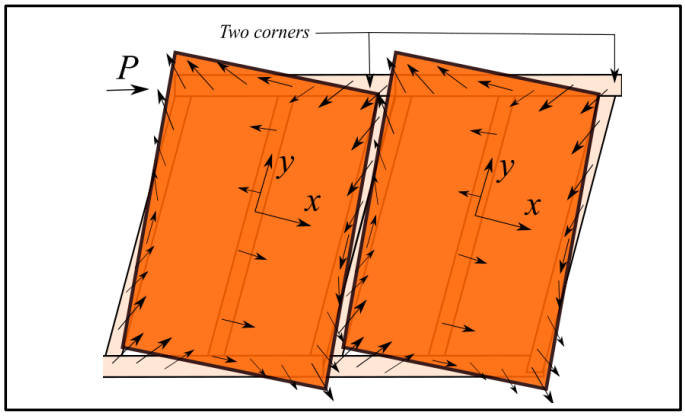


**Fig. 8** Wall panel with two sheathing boards

on one side or on both sides, still the approach is valid. The basic geometric relations (eq.1 to eq.8) remain valid irrespective of number and size of the wall panel. However, while applying eq.5, to multiple wall panels, as many corner screws as that of sheathing boards have to be considered. For example, as shown in fig.8, there are two sheathing boards and hence two corner screws have to be considered. The displacement of other screws in a particular sheathing board have to be expressed in terms of corresponding corner screws and finally the resultant force can be obtained by simple linear addition of '$F_s$' (eq.11) of each individual panel.

Thus, the proposed algorithm for assessing the response of CFSSW panels has been described. The approach is purely mechanistic, involving only principles of mechanics and geometric relations. There are no numerical methods involved, thereby alleviating the complex modelling and convergence issues confronted thereof. The proposed method is incorporated into a computational framework CFS-RAMA (Racking Analysis through Mechanistic Approach), which can be used for any configuration of wall panels with rigid sheathing. The following section describes the results obtained from this computer program.

## 3. Implementation and results

In the past two decades there has been a significant increase in the experimental research on lateral behavior of CFSSW panels. Many researchers have done experimental studies on different sheathing materials and different configurations of CFSSW panels. There are also experimental studies on component level screw tests in order to investigate the sheathing to screw interaction behavior for different sheathing materials, thickness, screw sizes, sheathing orientation, edge distance, loading protocols and so on. The present study extracts the data from four different configurations of CFSSW panels across the literature, whose screw tests and full scale wall panel tests are performed and reported [30]. The four configurations are chosen such that, they account the wide variety of configurations used in the industry. The implementation details and the results are presented in this section. The screw and full scale wall panel test data has been collected from the experiments of the following researchers in the literature,

1. Padilla-Llano et.al. [31, 32]
2. Nithyadharan and Kalyanaraman [33, 26]
3. L.Fiorino et.al. [18]

**Table 1**
Configurational details

| Config. No. | Name | Sheathing type | Overall dimensions (mm) | Description |
|---|---|---|---|---|
| C-1 | Padilla-Llano et.al [31, 32] | 1067x2413mm, 11mm thick Oriented strand board one on one side | 1067 x 2413 | The sheathing is attached to frame (1.37 mm thick) using #8 flat head fasteners |
| C-2 | Nithyadharan and Kalyanaraman [33, 26] | 1200 x 2400, 10mm thick Calcium silicate boards, one each on both sides | 1200 x 2400 | The calcium-silicate boards have been attached to the frame using 4mm screws, paced at 150mm c/c on the perimeter and 300mm c/c in the field studs. |
| C-3 | Nithyadharan and Kalyanaraman [33, 26] | 600 x 2400, 10mm thick Calcium silicate boards, 2 no's placed adjacent to each other on both sides | 1200 x 2400 | The boards were placed side by side on both sides and are attached to framing with screw spacing of 150 mm. |
| C-4 | L.Fiorino et.al [18] | Exterior panel: 1200 x 2500 mm, 9mm thick OSB, 2 no's placed side by side. Interior panel: 1200 x 2500, 12.5mm thick GWB, 2 no's placed side by side | 2400 x 2500 | The sheathing panels are placed side by side and are screwed to the frame at 150mm spacing on the perimeter and 300mm spacing on the field. |

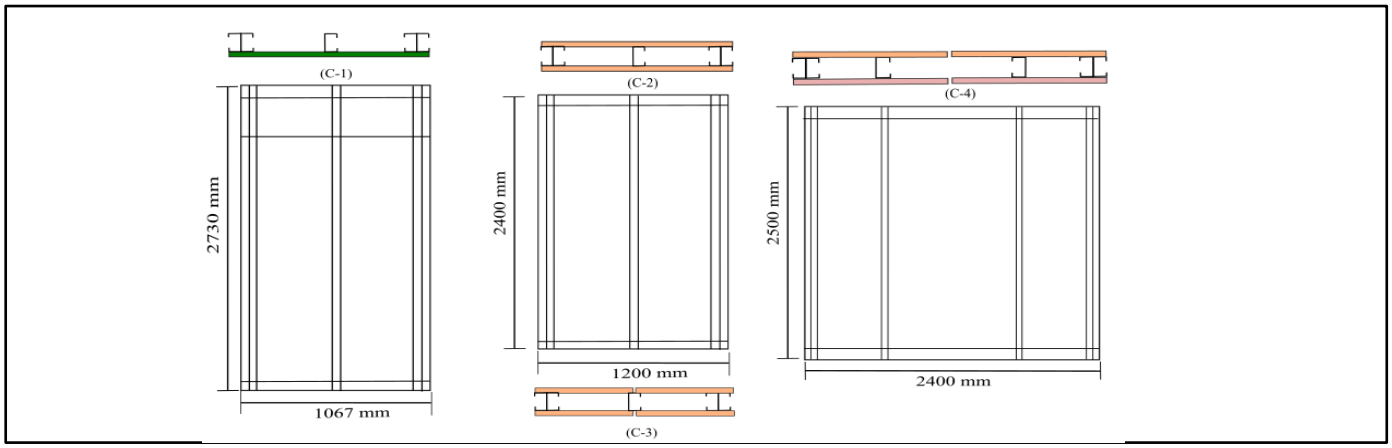


**Fig. 9** Configurations considered for validation

The configurational details of these panels are outlined in the table.1. It can be observed that the materials used for sheathing and dimensions of the wall panel vary significantly from experiment to experiment. The dimensions and layout of these panels can be seen in fig.9.

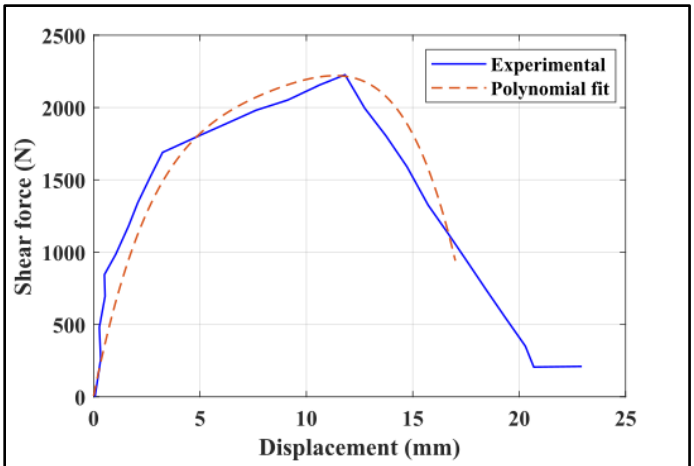


(a) Polynomial fitted to screw test data from Padilla-Liano et.al [31,32]

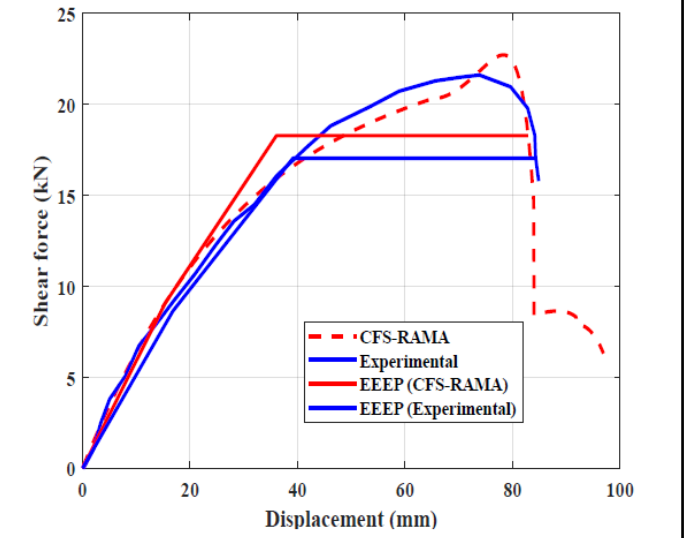


(b) Comparison of experimental data vs obtained response for C-1

**Fig. 10** Configuration-1, polynomial fitting and wall panel response

### 3.1. Configuration-1

The screw test data and the corresponding wall panel experimental data under monotonic loading has been extracted from Peterman et al [32] and Padilla-Llano et al. [30]. The configuration of the panel is as shown in fig.9(C-1) and table. 1. The wall panel is 2740mm high and 1220mm wide framed using back-to-back 600S162-54 CFS members. The framing is interconnected through #10 screws. This is a ledger frame with 1200T200-97 track that connects the wall to the floor diaphragm and is fastened to the vertical members at the top of the wall. On one side of the frame, OSB panel is attached and the ledger track on the opposite side. Two Simpson Strong-Tie S/HDU6 hold downs are connected to the bottom of the chord studs using #14 hex-head fasteners. Two 15.875mm (5/8in.) bolts serve as shear anchors. The single screw test data has been adopted from Peterman et al [32]. They have performed a series of screw tests in order to characterize the hysteretic behavior of stud to sheathing connection subjected to in-plane shear.

In order to implement the proposed method, the screw test data for 11mm OSB and 1.37mm studs has been extracted. A 4th degree polynomial is fit for the screw data using least squares and also equating the area under the curve. The fitted polynomial is shown in fig.10 (a). The proposed method is applied and the results obtained are shown in fig.10 (b). The Equivalent Energy Elastic Plastic (EEEP) plots are also shown. It can be seen that the proposed method captured the response of this configuration with fair accuracy. Moreover, the post peak response also matches well with the experiments. This validates the algorithm adopted for post peak load response. The peak load is overestimated but the ultimate loads and displacements are well captured. Therefore, this method can be used to predict the response of wall panels with similar configurations.

### 3.2. Configuration-2

The screw test data and corresponding wall panel test data for this configuration has been adopted from Nithyadharan and Kalyanaraman, see C-2 in table.1 and fig.9. Nithyadharan and Kalyanaraman have performed screw tests [33] and corresponding wall panels tests [26] on calcium silicate boards of different thickness. The screw test data corresponds to 3.9mm diameter screw drilled to 10mm thick calcium silicate board with edge distance of 25mm. The dimensions of the wall panel are 1200mm x 2400mm. In this configuration, 10mm thick calcium silicate boards of dimensions 1200mm x 2400mm are attached, one on each side of the steel framing. The screws are equally spaced at 150mm on the perimeter and 300mm on the interior studs. The proposed method is applied on this configuration and the results obtained are found to be in close comparison with experimental data, as shown in fig.11. Fig.11 (a) shows the 4$^{th}$ degree polynomial fitting and Fig.11 (b) compares the full scale wall panel test data with the obtained response. It can be seen that peak and post peak responses are also captured well. The initial stiffness and the peak load are also captured accurately. Therefore it can be concluded that the proposed method is well suited for similar configurations of wall panels.

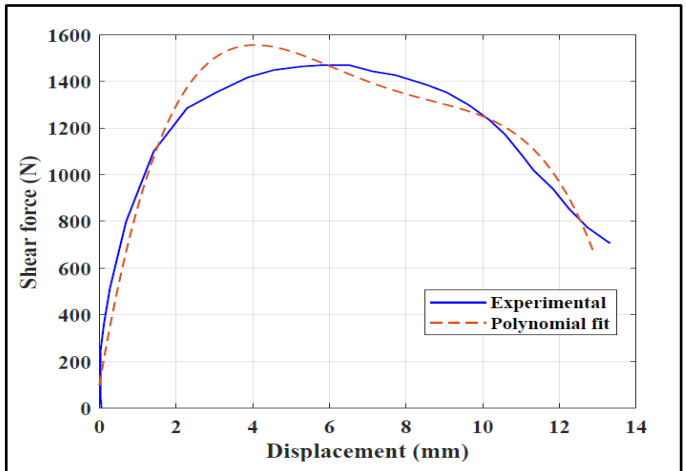


(a) Polynomial fitted to screw test data from Nithyadharan et.al [26]

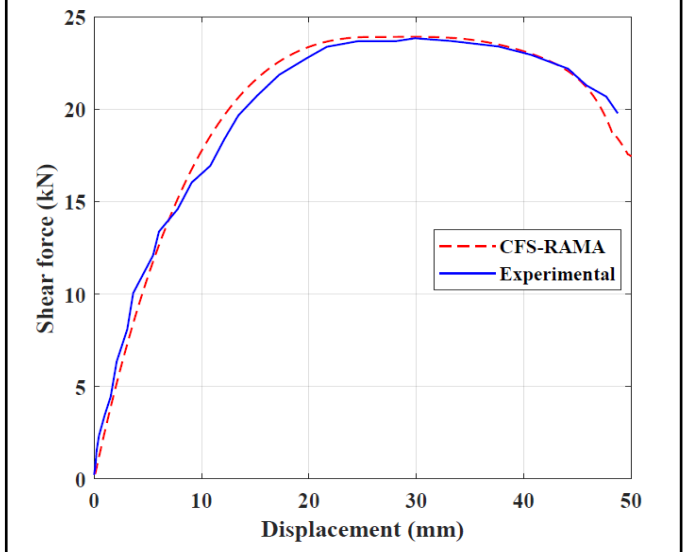


(b) Comparison of experimental data vs obtained response for C-2

**Fig. 11** Configuration-2, polynomial fitting and wall panel response

### 3.3. Configuration-3

The screw test data and corresponding wall panel test data for this configuration has also been adopted from Nithyadharan and Kalyanaraman, see C-3 in table.1 and fig.8. However, the screw test data in this case corresponds to 3.9mm diameter screw drilled to 10mm thick calcium silicate board with edge

distance of 10mm [33]. This configuration consists of 2 no's of 600mm x 2400mm calcium boards placed side by side on both sides of the wall framing. The overall dimension is 1200mm x 2400mm. The sheathing panels are attached to the frame with screws with spacing 150mm all around. The proposed method is applied to this configuration and the results are shown in fig.12. It can see that the results are in good agreement with the experimental values. But the initial stiffness is a little overestimated and also the peak load is little underestimated. This may be due to the contact between the adjacent sheathing boards and crushing against each other. Also the screw test data may not represent the average experimental values. However, this method reasonably assess the behavior of such configurations.

### *3.4. Configurartion-4*

The screw test data and corresponding wall panel test data for this configuration has also been adopted from L.Fiorino. [18], see C-4 in table.1 and fig.9. This configuration consists of 2 no's of 1200mm x 2500mm, 9 mm thick OSB sheathing on the exterior side, placed adjacent to each other and 2 no's of 1200mm x 2500mm, 12.5 mm thick GWB sheathing on the interior side, placed adjacent to each other. The overall wall panel dimensions are 2400mm x 2500mm. The proposed method is applied to this configuration and the results are shown in fig.13. It can be seen that the results match well with the experimental data. The peak and post peak responses are captured well. This implies that this method can be used for estimating the response of wall panels of this configuration.

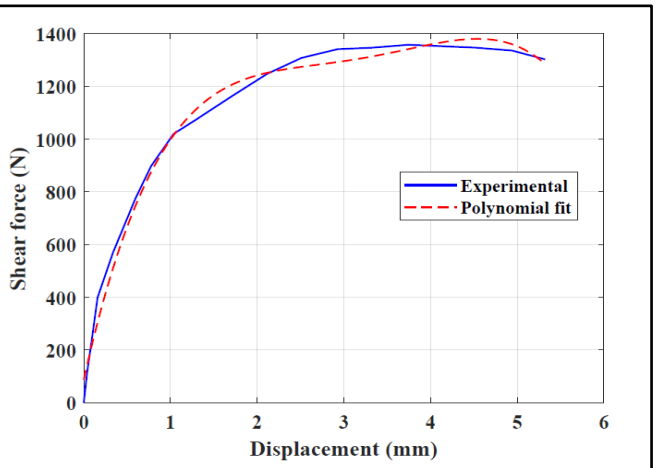


(a) Polynomial fitted to screw test data from Nithyadharan et.al [26]

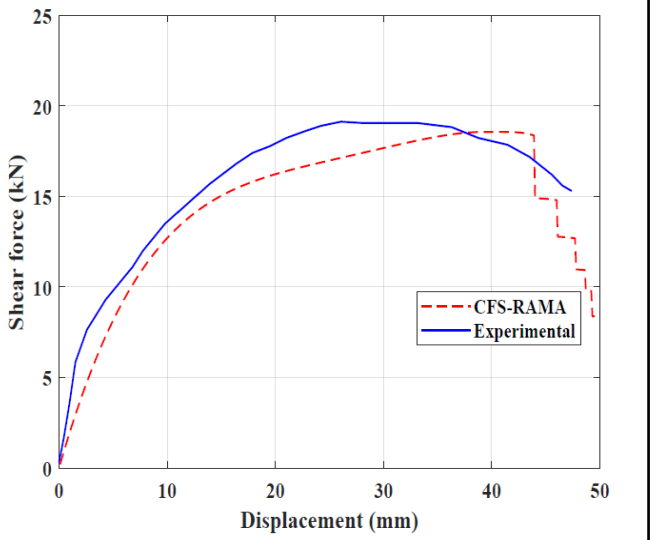


(b) Comparison of experimental data vs obtained response for C-3

**Fig. 12** Configuration -3, polynomial fitting and wall panel response

The design parameters of the four test configurations are estimated using EEEP method [34] and compared against their experimental counterparts. The results are summarized in Table.2. Therefore it can be seen that the proposed method reliably captures the behavior of the CFSSW panels under monotonic lateral load. The method is tested against various configurations of sheathing boards and wall panel dimensions and the results were satisfactory. The proposed method is simple and can be easily adopted in engineering practice. It can be conveniently programmed in spreadsheets also. The only input is the experimental data from component level screw tests.

### *3.5. Ductility*

The ductility of shear wall panels comes from the sheathing – frame connections. The response reduction factor (R) given in ASCE 7-16 is 6 for CFS shear walls with steel sheet and wood based sheathing, and 2.5 for shear walls with other brittle sheathing materials. This shows the energy dissiparion capability of these systems based on their ductility is reliable for earthquake resistant design. However, it is to be noted that the ductility of CFSSW panels is completely dependent of the sheathing and not on the frame. The frame can possibly trigger a brittle mode of failure by chord studs buckling under compression. But this can be avoided by properly designing the chord studs using capacity design principles. Another key component that enbles the development of full shear strength is the hold downs. The hold downs are to be designed to resist the tensile force developed in the chord studs at the point of peak shear resistance.

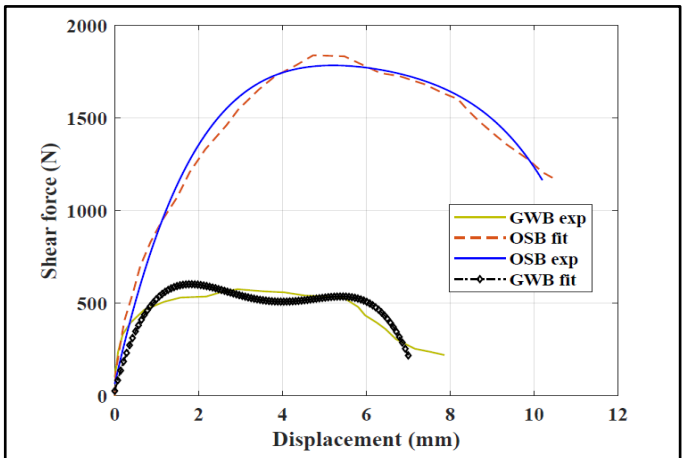


(a) Polynomial fitted to screw test data from Della Corte et.al [18]

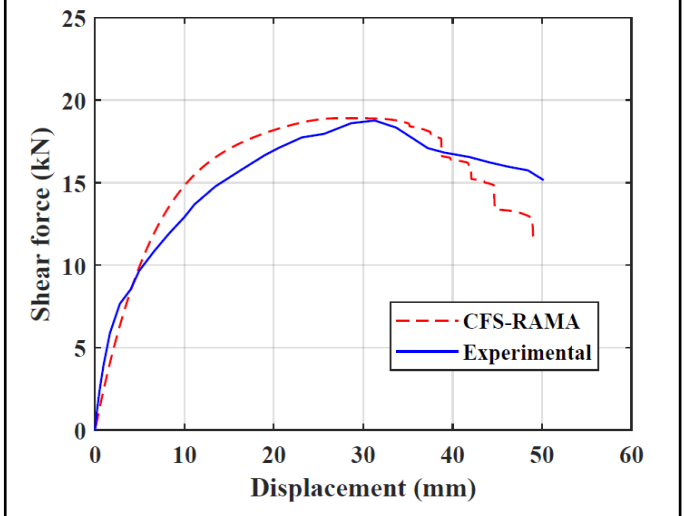


(b) Comparison of experimental data vs obtained response for C-4

**Fig. 13** Configuration-4, polynomial fitting and wall panel response

### *3.6. Industrial application*

The proposed method can be standardized if the sheathing manufacturers can perform in-house screw tests. The whole screw test data can be transferred to the customers just in the form of the 4th degree polynomial coefficients [a b c d e] (Refer eq.10) for a given sheathing material thickness and screw dia. Therefore the sheathing manufacturers can standardize the polynomial coefficients and just specify them for each sheathing thickness and corresponding screw diameter, then the monotonic pushover curve for any configuration of CFSSW panel can be assessed by the designers with the

proposed method. Therefore the method can be readily used in the analysis of CFSSW panels.

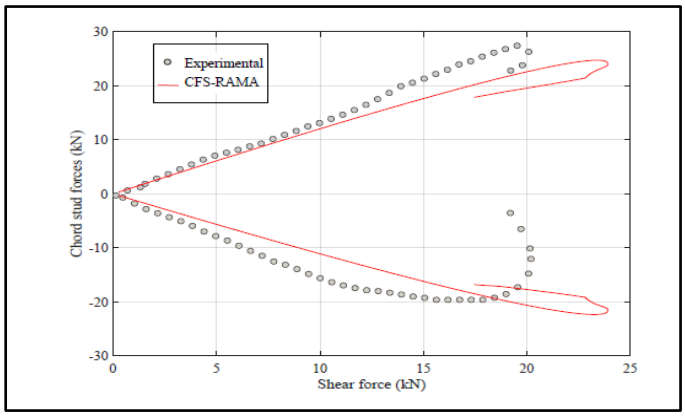


**Fig. 14** Chord stud forces on the tension and compression side of C-2 wall panel

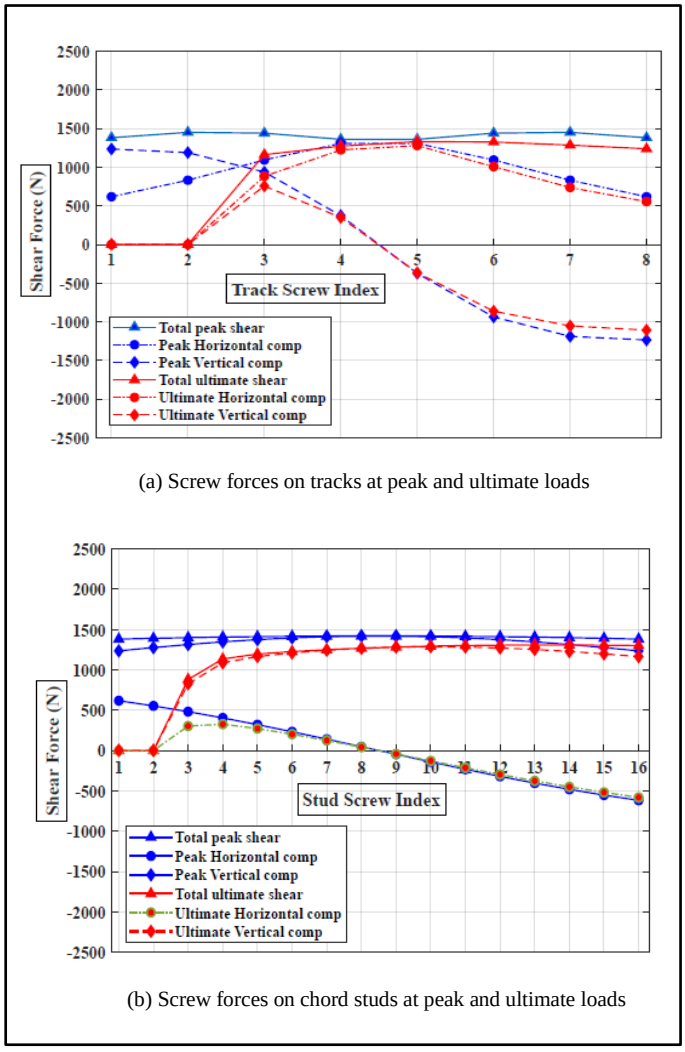


(a) Screw forces on tracks at peak and ultimate loads

(b) Screw forces on chord studs at peak and ultimate loads

**Fig. 15** State of fasteners at peak and ultimate loads of C-2 wall panel

The proposed approach also gives a significant insight to the forces developed in the chord studs and also state of the fasteners at any given point on the load-displacement curve of the wall panel. Fig.14 (a), (b) shows the state of fasteners at the peak and ultimate load points on tracks and studs of the C-2 wall panel. Also from fig.4 (b), the force developed in the chord studs and hold downs can be easily established. Fig.15 shows the axial load developed in the tension and compression side chord studs and compares with experimental values proposed by Nithyadharan and Kalyanaraman [27]. The predicted peak axial load value is, ±23kN which is close to experimental value of, ±20kN. This difference may be attributed to highly non-linear load sharing that happens between chord studs and sheathing, through screws connecting them near the region of peak load. So, the proposed method fits in the Performance Based Seismic Design (PBSD) paradigm by enabling the designer to assess the fastener states at any point on the load-displacement curve of the wall-panel, thereby incorporating performance parameters.

## 4. Limitations

The predictive capabilities of the proposed method for different sheathing materials and different wall configurations are demonstrated in the preceding section. However the method has few limitations which can be addressed by further research to improve its accuracy and generality of application. They are:

1. The proposed method is valid only under the rigid sheathing board assumption and does not include the shear deformation of the sheathing material. However for most of the rigid sheathing materials currently being used, this assumption does not affect the accuracy of prediction. This has been demonstrated for wood based sheathing materials such as OSB and also other sheathing materials like calcium silicate board and gypsum wall board. However this method cannot be applied for ductile sheathing materials like steel sheet and so on. However similar mechanic based methods have been proposed for steel sheet sheathed wall panels.
2. The proposed method does not include the slippage of bottom tracks and uplift of hold downs. The underestimation of ultimate displacements may be attributed to this exclusion. However this can be included using some empirical relationships standardized from test data.
3. When two sheathing boards are used on the same side of the wall panel, adjacent to each other some interaction takes place between them, this method does not account for that interaction. However, in spite of that, the error in prediction is within tolerance

## 5. Conclusion

The present paper presents a simplified mechanistic displacement based approach which can reliably capture the lateral behavior of CFSSW panels with rigid sheathing materials, subjected to monotonic lateral load. The approach involves relating the global wall panel lateral displacement to individual screw displacements using geometric relations. The individual screw displacements are related to screw forces by fitting a 4th degree polynomial to the screw test data. The individual fastener forces are related to wall panel resistance using simple mechanics. This alleviates the detailed finite element modelling and convergence issues confronted thereof. There is no numerical solution technique as such used for solving the equilibrium equations. The approach is rather direct. The formulation has been explained in detail and also validated against four different wall configurations from the literature. The details of the wall panel configurations has been outlined and the comparison between the experimental and calculated response has been presented. The configurations vary significantly viz. the sheathing materials, the dimensions of the wall panel and the thickness of the sheathing materials. The design parameters estimated using EEEP method are also compared against corresponding experimental values and found in good agreement. The method seems to give a reliable estimate of the wall panel behavior for a variety of configurations, dimensions and sheathing materials used. The error is within tolerance and conservative. The predicted values of yield and peak displacement of configuration-3 are significantly higher compared to their experimental counterparts possibly due to sheathing-sheathing interaction on the same side. The proposed method has been demonstrated to be robust and reliable for assessing the lateral load behavior of CFSSW panels with rigid sheathing under monotonic loading. The use of the proposed method in practical shear panel design is highlighted.

**Table 2**
Comparing the EEEP design parameters for all the configurations

| | Yield Strength ($f_y$) (kN) | Yield Displacement ($\Delta_y$) (mm) | Stiffness ($K_e$) (kN/mm) | Peak Strength ($f_p$) (kN) | Peak Displacement ($\Delta_p$) (mm) | Ultimate Load ($f_u$) (kN) | Ultimate Displacement ($\Delta_u$) (mm) |
|---|---|---|---|---|---|---|---|
| Config.1 Experimental | 16.1 | 6 | 2.7 | 18.8 | 31.3 | 15.1 | 50.2 |
| Config.1 Proposed method | 19.7 | 8.8 | 2.2 | 18.9 | 29.3 | 15.1 | 43.2 |
| Error Proposed – experimental | 3.5 | 2.8 | -0.4 | 0.1 | 2 | 0 | -7 |
| Config.2 Experimental | 21.8 | 8.3 | 2.6 | 23.8 | 29.9 | 19.8 | 48.7 |
| Config.2 Proposed method | 23.3 | 10.3 | 2.3 | 23.9 | 29.7 | 19.1 | 48 |
| Error Proposed – experimental | 1.5 | 2 | -0.3 | 0.1 | 0.2 | -0.7 | -0.7 |
| Config.3 Experimental | 17 | 5.7 | 2.9 | 19.1 | 26.1 | 15.3 | 47.4 |
| Config.3 Proposed method | 19.1 | 11.3 | 1.7 | 18.6 | 40.7 | 14.9 | 45.3 |
| Error Proposed – experimental | 2.1 | 5.6 | -1.2 | -0.5 | 14.6 | -0.4 | -2.1 |
| Config.4 Experimental | 20.1 | 39.1 | 0.5 | 21.6 | 73.8 | 17 | 84.3 |
| Config.4 Proposed method | 21.3 | 36.1 | 0.6 | 22.7 | 78.3 | 18.3 | 82.9 |
| Error Proposed - experimental | 1.2 | -3 | 0.1 | 1.1 | 4.5 | 1.3 | -1.4 |

## References


[1] AISI-S213-07/S1-09, North American standard for cold-formed steel framing-lateral design, Washington DC: American Iron and Steel Institute. (2007 edition with supplement No.1).
[2] R. Serrette, J. Encalada, G. Hall, B. Matchen, H. Nguyen, A.Williams, Additional shear wall values for light weight steel framing, American Iron and Steel Institute (AISI) Specifications, Standards, Manuals and Research Reports 47 (1997).
[3] C. Yu, Y. Chen, Detailing recommendations for 1.83 m wide cold formed steel shear walls with steel sheathing, Journal of Constructional Steel Research 67 (2011) 93–101.
[4] N. Balh, J. DaBreo, C. Ong-Tone, K. El-Saloussy, C. Yu, C. Rogers, Design of steel sheathed cold-formed steel framed shear walls, Thin-Walled Structures 75 (2014) 76–86.
[5] R. L. Tuomi, W. J. McCutcheon, Racking strength of light-framed nailed walls, Journal of Structural Engineering, ASCE 104 (1978) 1131–1140.
[6] J. Easley, M. Foomani, R. Dodds, Formulas for wood shear walls, Journal of Structural Engineering, ASCE 108 (1982) 2460–2478.
[7] W. J. McCutcheon, Racking deformations in wood shear walls, Journal of Structural Engineering, ASCE 111 (1985) 257–269.
[8] R. Y. Itani, K. Chung, A. M. Cheung, Nonlinear analysis of sheathed wood diaphragms, Journal of Structural Engineering, ASCE 110 (1985) 2137–2147.
[9] J. D. Dolan, R. O. Foschi, Structural analysis model for static loads on timber shear walls, Journal of Structural Engineering, ASCE 117(3) (1991) 851–861.
[10] M. W. White, J. D. Dolan, Nonlinear shear wall analysis, Journal of Structural Engineering, ASCE 121(11) (1995) 1629–1635.
[11] A. K. Gupta, G. P. Kuo, Modelling a wood framed house, Journal of Structural Engineering, ASCE 113(2) (1987) 260–278.
[12] A. K. Gupta, G. P. Kuo, Wood framed shear walls with uplifting, Journal of Structural Engineering, ASCE 113(2) (1987) 241–259.
[13] B. Folz, A. Filiatrault, A computer program for the cyclic analysis of shear walls in woodframe structures, CUREE W-08 (2002).
[14] B. Folz, A. Filiatrault, Cyclic analysis of wood shear walls, Journal of Structural Engineering, ASCE 127(4) (2001) 433–441.
[15] L. A. Fülöp, D. Dubina, Design criteria for seam and sheeting-to framing connections of cold-formed steel shear panels, Journal of Structural Engineering, ASCE 132(4) (2006) 582–590.
[16] L. Xu, J. Martinez, Strength and stiffness determination of shear wall panels in cold-formed steel framing, Thin Walled Structures 44 (2006) 1084–1095.
[17] L. Xu, J. Martinez, Simplified nonlinear finite element analysis of buildings with CFS shear wall panels, Journal of Constructional Steel Research 67 (2011) 565–575.
[18] L. Fiorino, D. G. Corte, R. Landolfo, Experimental tests on typical screw connections for Cold-formed steel housing, Engineering structures 29 (2007) 1761–1773.
[19] G. D. Corte, Lateral response of sheathed cold-formed shear walls an analytical approach, International Specialty Conference on Cold- Formed Steel Structures. 3 (2006).
[20] G. Buonopane, S, B. Bian, H. Tuna, T, W. Schafer, B, Computationally efficient fastener-based models of cold-formed steel shear walls with wood sheathing, Journal of Constructional Steel Research 110 (2015) 137–148.
[21] F. McKenna, G. Fenves, M. Scott, Open system for earthquake engineering simulation, University of California, Berkeley, CA. (2000).
[22] B. Karabulut, S. Soyoz, Experimental and analytical studies on different configurations of cold-formed steel structures, Journal of Constructional Steel Research 133 (2017) 535–546.
[23] L. C. Vieira, B.W. Schafer, Lateral stiffness and strength of sheathing braced cold-formed steel stud walls, Engineering Structures 37 (2012) 205–213.
[24] Chen, C.Y., Okasha,A. F., and Rogers, C. A. (2006). Analytical predictions of strength and deflection of light gauge steel frame/wood panel shear walls. Int. Conf. on Advances in Engineering Structures, Mechanics and Construction, Univ. of Waterloo, Waterloo, ON, Canada, 381–391.
[25] Y. L. Liew, E. F. Gad, C. F. Duffield, Modularized closed-form mathematical model for predicting the bracing performance of plasterboard clad walls, Structural Engineering and Mechanics 20(1) (2005) 45–47.
[26] C. S. McCreless, T. S. J. Tarpy, Experimental investigation of steel stud shear wall diaphragms, International Specialty Conference on Cold-Formed Steel Structures. 9 (1978).
[27] M. Nithyadharan, V. Kalyanaraman, Behavior of cold-formed steel shear wall panels under monotonic and reversed cyclic loading, Thin-Walled Structures 60 (2012) 12–23.
[28] J. Ye, X. Wang, H. Jia, M. Zhao, Cyclic performance of cold-formed steel shear walls sheathed with double-layer wall boards on both sides, Thin-Walled Structures 92 (2015) 146–159.
[29] C.-L. Pan, M.-Y. Shan, Monotonic shear tests of cold-formed steel wall frames with sheathing, Thin-Walled Structures 49 (2011) 363–370.
[30] A. Rohatgi, Webplotdigitizer (2020). URL: https://automeris.io/ WebPlotDigitizer.
[31] D. A. Padilla-Llano, C. Ding, C. D. Moen, M. R. Eatherton, Advancing seismic simulation of cold- formed steel framed buildings, American Iron and Steel Institute, AISI Report RP15-3 (2015).
[32] K.D.Peterman, N.Nakata, B.W.Schafer, Hysteretic characterization of cold-formed steel stud-to-sheathing connections, Journal of Constructional Steel Research 101 (2014) 254–264.
[33] Nithyadharan, Kalyanaraman, Experimental study of screw connections in CFS-calcium silicate board wall panels, Thin Walled Structures 49 (2011) 724–731.
[34] A. E. Branston, Development of a design methodology for steel frame / wood panel shear walls, Ph.D. Thesis, Department of Civil Engineering and Applied mechanics McGill University (2004).

**Advanced Steel Construction** – Vol. 18 No. 3 (2022) 658–669
**DOI:**10.18057/IJASC.2022.18.3.3


# ENERGY DISSIPATION OF STEEL-CONCRETE COMPOSITE BEAMS SUBJECTED TO VERTICAL CYCLIC LOADING

Jing Liu [1], Fei Lyu [2,*], Fa-Xing Ding [2,*] and Xue-Mei Liu [3]

[1] *School of Civil Engineering, Hunan City University, Yiyang, Hunan Province, 413000, P. R. China*
[2] *School of Civil Engineering, Central South University, Changsha, Hunan Province, 410075, P. R. China*
[3] *Department of Infrastructure Engineering, The University of Melbourne, Parkville, VIC 3010, Australia*
** (Corresponding author: E-mail: lyufei@csu.edu.cn; dinfaxin@csu.edu.cn )*

## ABSTRACT

The finite element (FE) software ABAQUS was used to establish a 3D FE model and perform a pseudo-static analysis of steel–concrete composite beams. With the validated model, the influences of several key parameters, including shear connection degree, force ratio, and transverse reinforcement ratio, on seismic behavior were investigated and discussed. In addition, the working performance of studs was analyzed. The FE analysis results show that the steel girder is the main energy dissipation component of the composite beam, and the energy dissipation of the steel girder is more than 80% of the total energy. The next is longitudinal reinforcement, followed by a concrete slab, the minimum proportion is the studs. Results show that the energy dissipation ratio of studs is less than 1% under the condition of the parameters. However, an increase in shear connection is beneficial to improve the energy dissipation of steel girders and rebars. Shear connection, force ratio, and steel girder width–thickness ratio are the major factors that influence bearing capacity and seismic behavior. Transverse reinforcement, section form, and stud diameter are the secondary factors. Finally, a seismic design for composite beams was established.

## ARTICLE HISTORY

Received: 2 June 2021
Revised: 14 December 2021
Accepted: 21 December 2021

## KEYWORDS

Steel–concrete composite beam;
Shear connection degree;
Plastic energy consumption;
Hysteretic behavior



## 1. Introduction

Steel–concrete composite beams have been applied large-scale to civil structures, such as bridges and buildings, in recent years because of their high capacity, small section size, lightweight, and convenient construction. These benefits accrue from the combination of advantages of different constituent materials and the elimination of shortcomings of steel and concrete [1]. However, the composite steel beam–reinforced concrete (RC) slab behaviors are not customary to be considered in the design. The reason is partially because the composite beam have been mainly used in high-rise building applications at early stages so that the steel beam is designed relatively deep. The contribution of RC slab to the beam stiffness and strength is, therefore, insignificant [2]. Nevertheless, research works of understanding of steel beam-RC slab co-work mechanism promoted the application of composite beams on low-to-moderate height structures in recent years. In this case, the composite action between RC slab and steel girder may have a considerable influence on its hysteretic behaviors [3]. To date, most of the experimental and analytical study of composite beams focused on its static performance and fatigue life at which failure of the shank of the shear stud occurs [4-8]. The study on the seismic property of composite beams remains underdeveloped. Hence, to explore further the co-work mechanism of the composite beam under seismic load is of great importance to complement current design codes so that the steel beam-RC slab behaviors can be rationally considered in the aseismic design.

Recently, scholars from various countries have conducted extensive experiments to explore on the seismic property of steel–concrete composite beams. Reference [9-12] presented detailed experimental investigations of simply supported composite beams under vertical cyclic load (Fig. 1) and discussed the influences of several key parameters, such as the shear connection degree, width–thickness ratio, and transverse reinforcement ratio, of steel girders, on seismic behavior. This testing scheme is relatively rarely presented but meaningful for the following reasons: (1) In the aseismic design, a strong column–weak beam means that the plastic hinge appeared at the beam end for frame structure, which improved the ductility of the structure and prevented the collapse of buildings when subjected to severe shaking. Moreover, beams should have adequate shear and bending load capacity to develop plastic hinges under earthquake action. In general, the quasi-static test of the strong column-weak beam should be conducted, but the fabrication of specimens and experiments is costly and complicated. Thus, for simplicity, the experimental study of seismic performance of simply supported composite beams bearing the quasi-static cycle loading can be performed as a reasonable alternative. (2) The non-uniform settlement of buildings induced the bending moment and shear force that appeared at the beam end, which is highly similar when a vertical force is applied to the simply supported composite beam. (3) Low-frequency vertical cyclic loading is performed to study the hysteretic behavior in the node-negative moment region for the steel-concrete composite structure system. On the other hand, many theoretical models have been established and can be roughly categorized into two types [13].

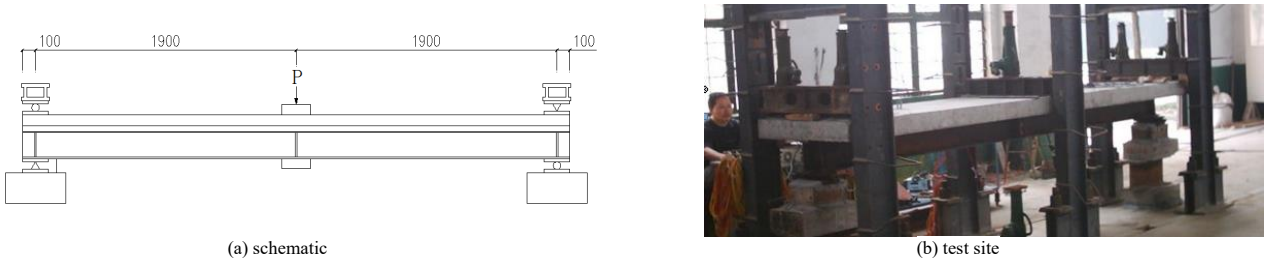


(a) schematic (b) test site

**Fig. 1** Experimental setup for vertical cyclic load

(1) Macro models: using line or frame elements and spring connectors to simulate the structural behaviors macroscopically. That is, the composite action between every structural member is implicitly reflected in the structural responses such as displacement and reactional force of nodes. These models usually make use of self-compiled and redeveloped programs to build the simplified descriptions of composite beams and commonly incorporate calibrated material constitutive models and load-slip models of connectors. For instance, Nie *et al*. [14] performed this process on composite beams under repeated and cyclic loadings. Based on the experimental research, the author established a restoring force model of steel–concrete composite beams by

considering the shear connection degree. A proposed fiber beam model was used to simulate the effects of an earthquake by Wang *et al*. [15] and Tao *et al*. [16], using MSC Marc or ABAQUS software. Ayoub and Filippou [1] proposed an inelastic beam element model for calculating steel–concrete beams partially connected under drab and cyclic loads. Zhao *et al*. [17] developed a high-efficiency macro-modelling program to analyze the nonlinear mechanical behavior of composite structural connections that consist of concrete-filled steel tubular (CFST) columns and steel-concrete composite beams [15].

(2) Micromodels: using continuum finite element (FE) modelling method, for example, solid or shell elements, to build the model contains complete geometric, boundary, and contact properties of the object structure. These models generally make use of universal FE software, such as ABAQUS and ANSYS. Research works employing this analytical technique. For instance, Nie *et al*. [18] investigated the seismic behavior of connections that were composed of steel CFST columns and steel–concrete composite beams. Then, 3D nonlinear FE models were proposed to research the mechanical character of three forms of connection via ANSYS. Bursi *et al*. [19] researched the seismic behavior of steel–concrete composite frames with a partial and full degree of shear connection and then suggested that shear connection degree should be sufficiently high to protect the shear connectors from damage. Vasdravellis *et al*. [20] evaluated the effect of partial composite action between steel girder and concrete slab of composite frames under seismic loading through ABAQUS.

At present, the research on the hysteretic performance of steel–concrete composite beams remains insufficient. Previous studies have failed to reflect stud energy dissipation capacity and its effect on structure energy dissipation distribution reasonably. In addition, the earthquake-resistant design of composite beams lacks a theoretical basis. Therefore, the present study aims to entirely research the seismic performance of steel–concrete composite beams and identify the working mechanism of studs. To this end, the vertical quasi-static finite analysis of simply supported composite beam is applied to simulate earthquake action in this study. The rationality of this test scheme on the study of seismic behaviors of composite beams has been illustrated before. Moreover, a previous experimental study [21] conducted by authors provides a solid verification of established FE models.

Based on the previous research of our team [22, 23], our current work has the following objectives. (1) A 3D solid model of steel beam–RC slab composite beams is established, and quasi-static analysis is conducted using ABAQUS software. The plastic damage constitutive model of concrete is adopted. The accuracy of the established model is fully verified against previous test results. (2) The effects of several parameters on the seismic property of composite beams are analyzed. The working performance of the stud of steel-concrete composite beams is investigated. The influences of the girder, longitudinal reinforcement, concrete slab, and stud on the components and integral energy dissipation of steel-concrete composite beams are determined. (3) To discuss the contribution of every structural component on resistance to seismic load from the point of view of energy dissipation. (4) To propose reasonable seismic structural measures for composite beams according to the FE analysis (FEA) results.

## 2. FEA

The author designed 11 I-shaped and 11 box steel beam–RC slab composite beams in the literature [12]. In the current work, a pseudo-static test of composite beams was conducted via FEA, and the validity is examined against the experimental results available in the literature [3, 12]. As mentioned above, a considerable number of analytical models were proposed by various researchers. However, most of the existing models are macro models that are essentially a design tool rather than an analytical tool because of their high simplicity. As such, the continuum element method was adopted for the steel beam and RC slab in this study to reproduce detailed experimental observation. Meanwhile, the dimension of stud in the composite beams is relatively small compared with the overall model scale so that rational simplicity can be exploited to save the computation cost. As a result, a hybrid modelling method that contains solid, shell, and liner elements were adopted in this study to perform the analytical study of pseudo-static test.

### *2.1. FE modelling*

#### *2.1.1. Material constitutive models*

The FE software ABAQUS/Standard 6.14 [24] was used in this study for detailed FE modelling. The material constitutive relationship of the concrete and steel was adopted from Ding *et al.* [21, 23].

#### *2.1.2. Mesh and element*

FE models are established via the ABAQUS program [24]. The modelling method uses four-node shell elements (S4R) to model steel beams and a two-node linear beam element (B31) to model studs (Fig. 2(a)). In addition, concrete is modelled using C3D8R (Fig. 2(b)). The reinforcement bars are modelled by a two-node linear truss element (T3D2) (Fig. 2(c)).

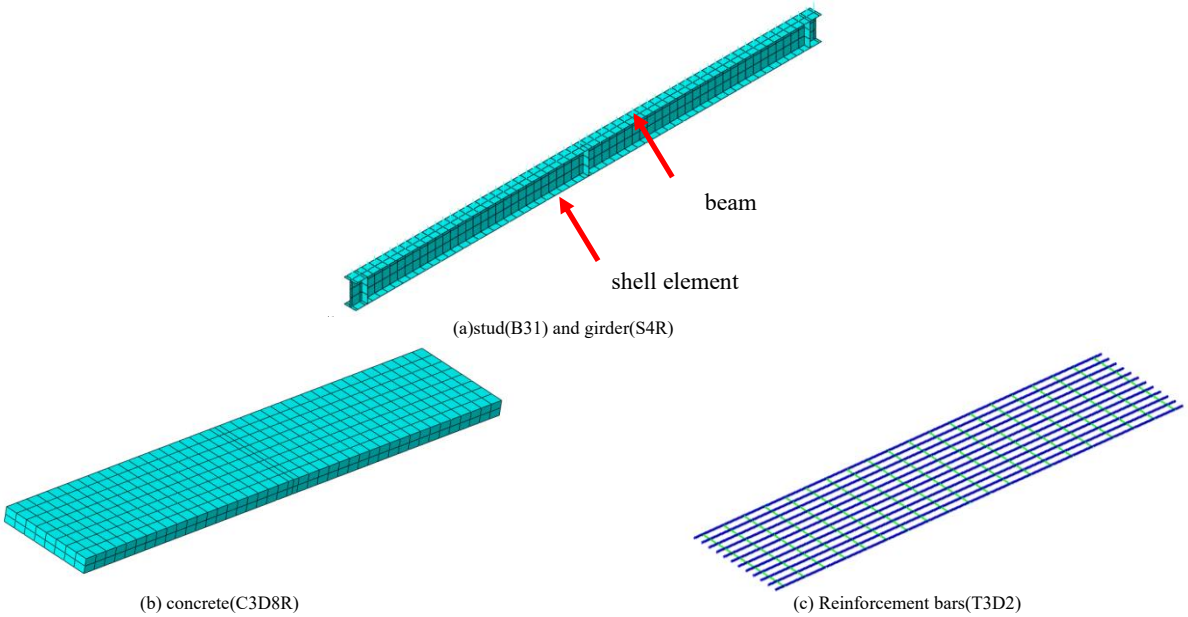


(a)stud(B31) and girder(S4R)

(b) concrete(C3D8R)

(c) Reinforcement bars(T3D2)

**Fig. 2** Simplified FE models for steel-concrete composite beams

A structured meshing technique and static general step were adopted in this study. Fig. 3 shows simplified FE models for steel–concrete composite beams. The interaction between the upper surface of the steel girder and the bottom surface of the concrete slab is simulated by the optional contact surface model in ABAQUS, which is the most rational modelling approach and is widely applied in previous studies [25,26]. The use of spring element is an efficient way to enable interactions between shear studs and the concrete slab [27]. In this study, a more realistic approach that the stud elements were embedded in the concrete solid elements was adopted to simulate the composite actions. Detailed information about the mesh convergence and contact type is available in the literature [21,28]. The boundary of the steel–concrete composite beams was simply supported, similar to that in the FE model.

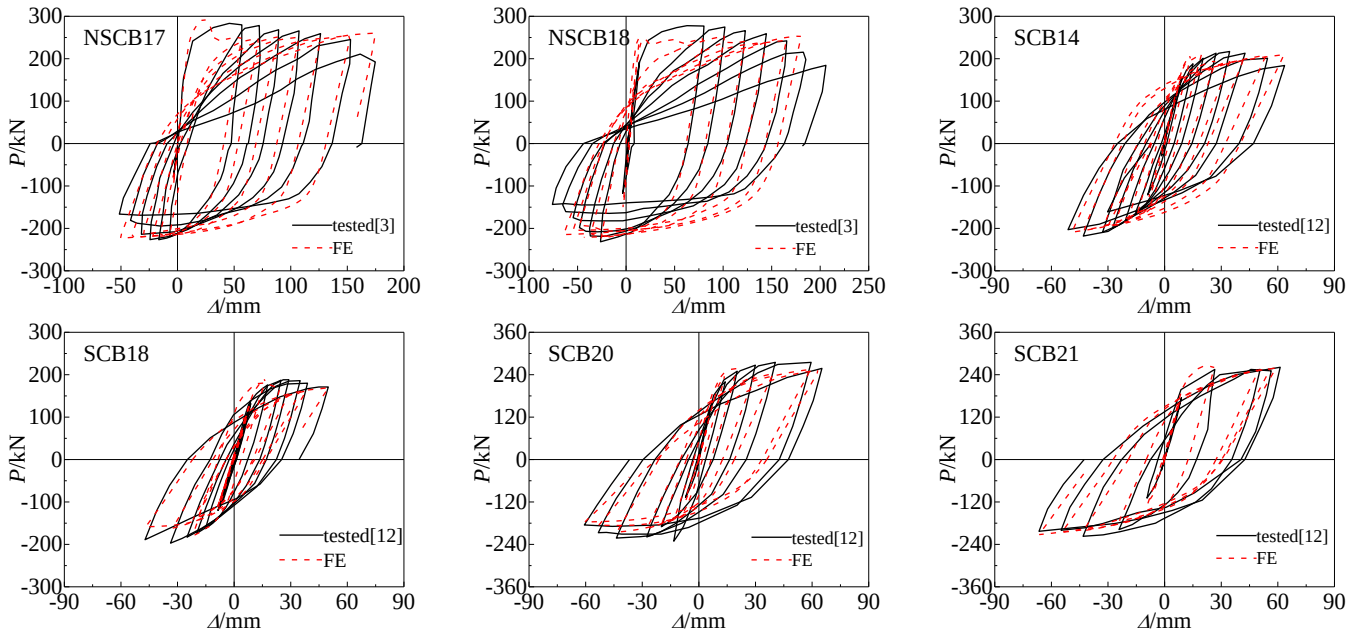


**Fig. 3** Comparison between calculated and tested load-deformation hysteresis curve of steel-concrete composite beam

*2.2. Model validation*

*2.2.1. Load–deformation curve*

FE models were established to study the hysteretic performance of specimens using ABAQUS/Standard 6.10 [24]. The typical load–deflection hysteresis curves of the specimens that were obtained through FE analysis (FEA) compared with the experimental results are shown in Fig. 2, the test data were obtained from Nie *et al*. [3] and our team[12]. The load–deflection skeleton curve of steel–concrete composite beams is shown in Fig. 4, where $\Delta$ is the displacement in mid-span, and $P$ is the vertical load. Loading displacement is considered positive or negative in the direction of loading is downward or upward, respectively.

Notably, the FE method provided an accurate experimental result. The FEA results of the ultimate bending capacity and flexural stiffness from the parametric analysis were compared with the tested ones (Fig. 5). The first method was used to calculate the FE modelling results, which are in good agreement with a maximum discrepancy of less than 10%.

*2.2.2. Load–slip curve*

The curves of slips at 1/4 span versus load are presented in Fig. 6. The figure shows that the FEA result agrees well with the experimental result.

*2.2.3. Steel girder buckling*

Fig. 7 compares the FEA and experiment results in terms of failure modes. The maximum buckling value of the steel web obtained by the FE method is 8.4 mm. The test result is 11.6 mm, thereby indicating that the FE method can simulate failure modes precisely.

Following the hysteresis curve, skeleton curve, load–slip curve, and failure mode, the FE method is reasonably performed for this study.

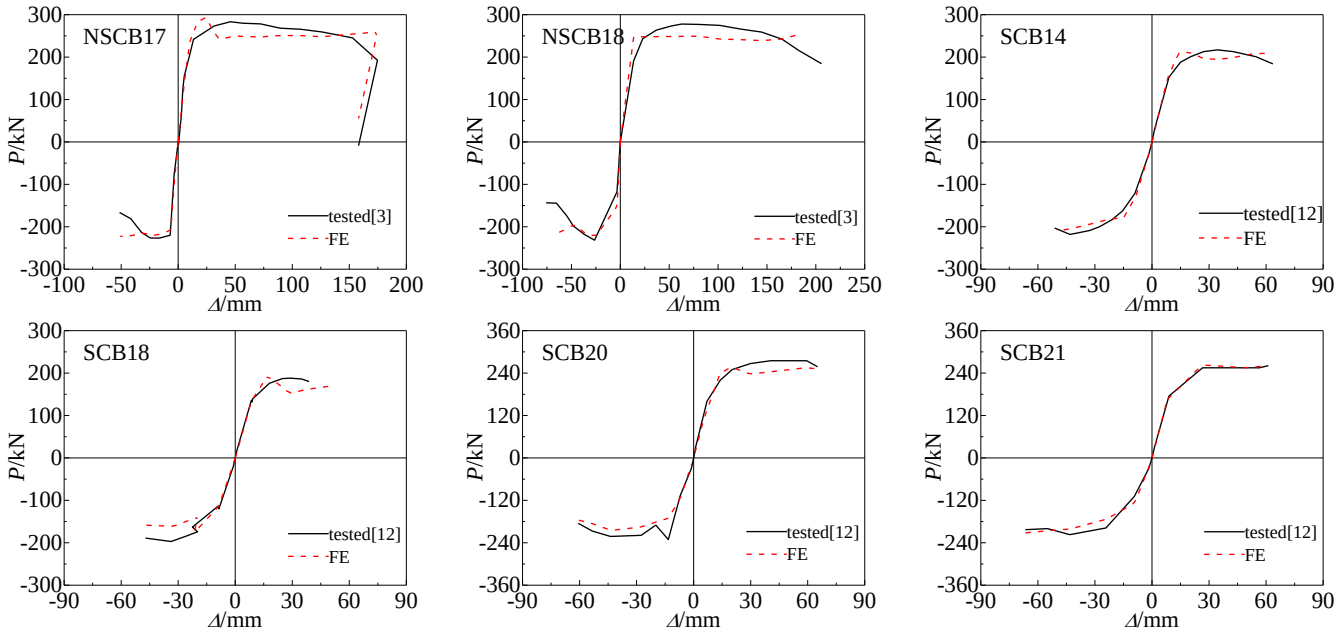


**Fig. 4** Comparison between calculated and tested load-deformation skeleton curve of steel-concrete composite beam

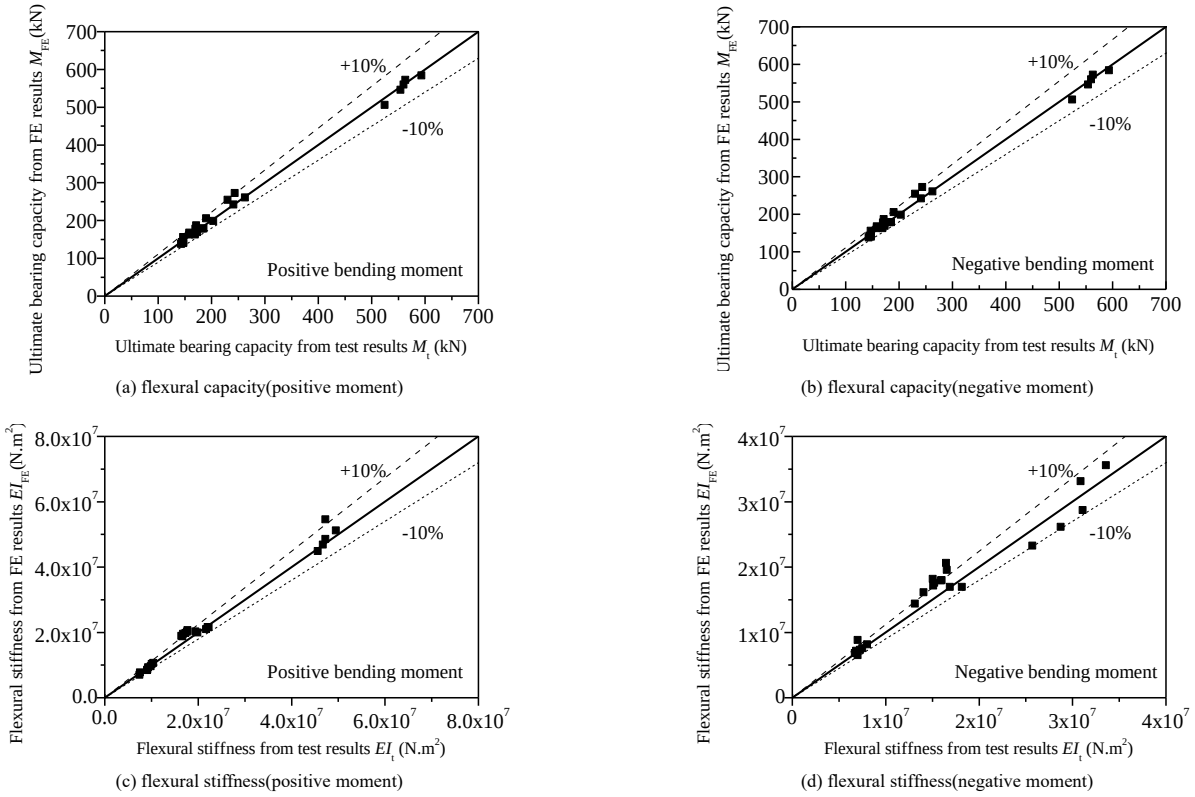


(a) flexural capacity(positive moment)

(b) flexural capacity(negative moment)

(c) flexural stiffness(positive moment)

(d) flexural stiffness(negative moment)

**Fig. 5** Comparison between calculated and tested flexural capacity and stiffness of the composite beam

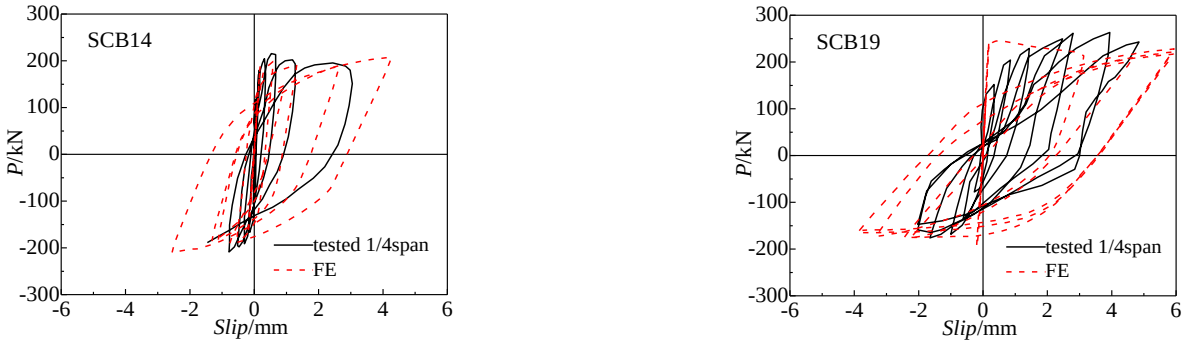


(a) SCB14

(b) SCB19

**Fig. 6** Comparison between calculated and tested load-slip of composite steel-concrete beam

(a) test result

(b) FE result

**Fig. 7** The failure modes comparison of FEA results and the experiment results

## 3. Parametric analysis

Six parameters that could affect the hysteretic behavior of composite beams, including transverse reinforcement ratio, shear connection degree, section form, force ratio, width–thickness ratio of the girder, and stud diameter, are investigated. A series of full-scale models was designed for parametric analysis using the nonlinear FE method. Table 1 demonstrates the detailed specimen parameters. Fig. 8 shows the cross-section of the girder. $l$ is the length of the specimen; $w_c$ and $w_s$ are the widths of the concrete slab and the steel girder, respectively; $h_c$ and $h_s$ are the height of the concrete and steel girder, respectively; $d$ is the diameter of the stud; $\rho_t$ and $\rho_l$ are the ratios of the transverse reinforcement and longitudinal reinforcements of the concrete slab, respectively; $f_{s,s}$ and $f_u$ are the yield and ultimate strengths of the stud, respectively; $f_{cu}$ is the cubic compressive strength of concrete; and $f_{s,b}$ is the yield strength of the girder.

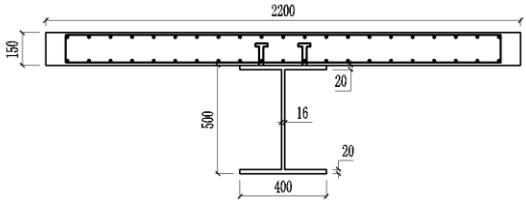


**Fig. 8** Cross-section details of the girder

**Table 1**
Geometric properties and characteristics of composite beams

| $l$/m | $w_c$/m | $h_c$/m | $w_s$/m | $h_s$/m | $d$/mm | $\rho_t$/% | $\rho_l$/% | $f_{s,s}$/MPa | $f_u$/MPa | $f_{cu}$/ Mpa | $f_{s,b}$/ MPa |
|---|---|---|---|---|---|---|---|---|---|---|---|
| 12 | 2.2 | 0.15 | 0.4 | 0.5 | 19 | 0.19 | 2.56 | 350 | 455 | 40 | 345 |

### 3.1. Influence of shear connection degree

Existing research reveals that the degree of shear connection exerts a remarkable effect on the hysteretic behavior of composite beams [11,29]. The calculation method for shear connection degree in the sagging moment or hogging moment region is defined. In this article, the shear connection degree in the positive moment was applied to distinguish from different beams.

The shear connection degree in the sagging moment region $\eta^+$ is presented as follows (China Architecture and Building Press 2017):

$$\eta^+ = n / n_f \tag{1}$$

Formula (1) parameters are defined in [12].

$$V_u = (0.2d^{0.5} - 10) f_{cu}^{\,0.8-0.15\ln(d-10)} (0.002 f_y + 0.24) \tag{2}$$

$A_{sd}$ is the cross-section area of the stud, $f_c$ is the concrete compressive strength, and $E_c$ is the concrete Young's modulus.

Figs. 9–10 and Table 2 compare the effect of shear connection degree on the hysteresis property of composite beams. The flexural stiffness could be attained as the secant stiffness at 0.4 times the ultimate load using the envelop curve. In Fig. 10, the slip was measured at the end of the beams, the lateral deformation means the displacement difference between stud top and stud bottom, and the shear force or moment is at the section of the stud bottom. The following points were observed.

(1) The plastic energy dissipation of the steel girder, reinforcement, and the entire model increases with the connection degree. When the connection degree increased from 0.5 to 1.0, the plastic energy dissipation values increased from 1209.0 kJ to 1446.3 kJ, which was an increase of 19.6%. This increment was primarily caused by an increase in the plastic energy consumption of the steel girder and bar. The single stud plastic energy dissipation value decreased from 64.2 kJ to 32.6 kJ, which was a decrease of 49.2%. The energy consumption of a single stud decreases as the stud number increases.

(2) For the positive moment region, the higher the shear connection degree is, the larger the flexural capacity and stiffness will be. Furthermore, composite beams illustrate good interaction behavior when $\eta^+$ is high, which can reduce the deflection of the composite beams under vertical loading and guarantee carrying capacity. However, this phenomenon is inevident when the connection degree is more than 1. The capacity of scb6($\eta^+$=2.0) is 26.0% and 10.0% larger than those of scb2($\eta^+$=0.5) and scb4($\eta^+$=1.0), respectively. The stiffness of scb6($\eta^+$=2.0) is 29.0% and 12.2% larger than those of scb2($\eta^+$=0.5) and scb4($\eta^+$=1.0), respectively.

For the negative moment region, the flexural capacity and stiffness difference is less than 1.1% and 1.0%, respectively, due to the shear connection degree(η-) being greater than 1 even for scb1.

(3) The slip peak value of scb2($\eta^+$=0.5) is 32.3% and 168.5% larger than those of scb4($\eta^+$=1.0) and scb6($\eta^+$=2.0), respectively. The shearing force peak value of scb2($\eta^+$=0.5) is 94.2% and 122.8% larger than those of scb4($\eta^+$=1.0) and scb6($\eta^+$=2.0), respectively. The moment peak value of scb2($\eta^+$=0.5) is 71.1% and 106.7% larger than those of scb4($\eta^+$=1.0) and scb6($\eta^+$=2.0), respectively. These results indicate that the single stud force becomes weak with an increase in shear connection degree.

(4) According to Figs. 9(b) and 9(c), a sagging degree of shear connection should range from 1.0 to 1.3. The stud spacing in the hogging moment region should not be larger than that in the sagging moment region. The specimens exhibit good seismic properties.

**Table 2**
Influence of shear degree on plastic energy dissipation values

| No. | $\eta^+$ | space/mm | $d$/mm | plastic energy dissipation (kJ) | | | | | energy dissipation proportion of stud (%) | energy dissipation of each stud (J) |
|---|---|---|---|---|---|---|---|---|---|---|
| | | | | Concrete slab | steel girder | reinforcement | stud | total | | |
| scb1 | 0.25 | 800 | 19 | 40.0 | 1056.0 | 109.0 | 4.0 | 1209.0 | 0.33 | 133.3 |
| scb2 | 0.5 | 400 | 19 | 45.0 | 1165.7 | 123.8 | 3.9 | 1338.4 | 0.29 | 64.2 |
| scb3 | 0.67 | 300 | 19 | 47.7 | 1212.2 | 125.3 | 4.3 | 1389.5 | 0.31 | 53.9 |
| scb4 | 1 | 200 | 19 | 40.5 | 1274.7 | 127.3 | 3.9 | 1446.3 | 0.27 | 32.6 |
| scb5 | 1.3 | 150 | 19 | 45.7 | 1285.5 | 136.6 | 5.6 | 1473.5 | 0.38 | 28.1 |
| scb6 | 2.0 | 100 | 19 | 43.8 | 1331.5 | 131.3 | 6.2 | 1512.8 | 0.41 | 26.0 |

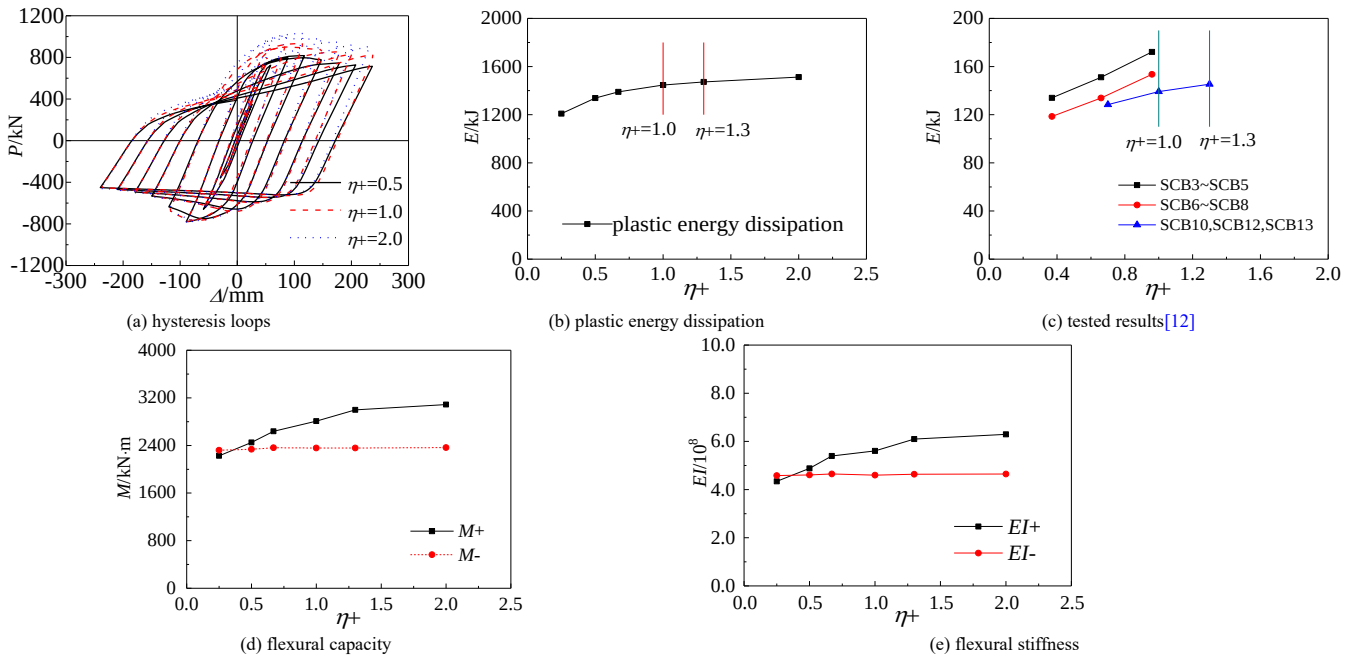


(a) hysteresis loops (b) plastic energy dissipation (c) tested results[12]

(d) flexural capacity (e) flexural stiffness

**Fig. 9** Influence of shear connection on the hysteresis performance of steel-concrete composite beams

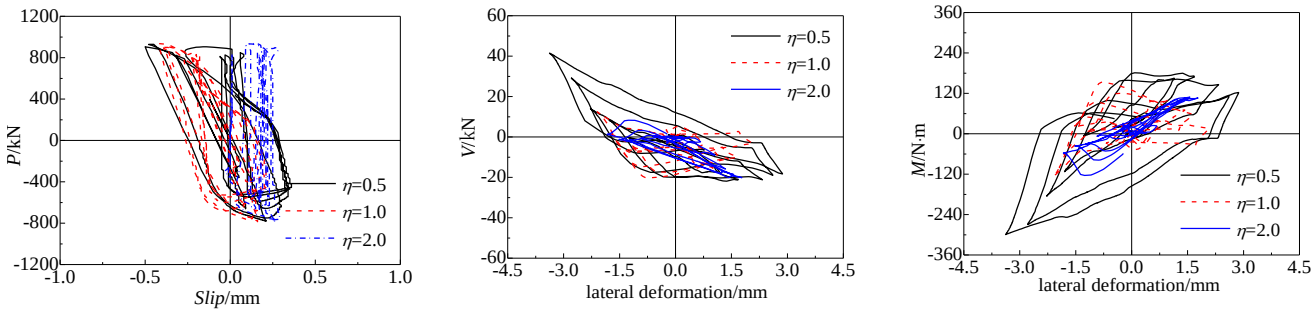


(a) loading-deformation (b) shear force of stud end-lateral deformation (c) moment of stud end-lateral deformation

**Fig. 10** Influence of shear degree on the hysteresis performance of interface slip and stud mechanical performance of steel-concrete composite beams

### *3.2. Influence of force ratio*

Force ratio considerably influences the plastic energy dissipation of steel–concrete composite beams. The force ratio can be determined by:

$$R = f_{s,l}A_{s,l} / f_{s,b}A_{s,b} \quad (3)$$

where $A_{s,l}$ and $A_{s,b}$ are the areas of the rebar and steel girder, respectively; and $f_{s,l}$ is the yield strength of the longitudinal rebar. Table 3 and Fig. 11 compare the influences of force ratio on the hysteresis performance of steel–concrete composite beams.

(1) The greater the force ratio is, the greater the reinforcement ratio will be. The greater the increase in rebar and composite beam energy dissipation is, the less the energy dissipation of the slab will be. The energy dissipation of studs is unaffected. Force ratio exerts a considerable impact on energy dissipation. That is, the energy dissipating capacity generally increases with the force ratio. When the force ratio increased from 0.07 to 0.64, the plastic energy dissipation value increased from 1282 kJ to 1615 kJ, which was an increase of 26.0%.

(2) The larger the force ratio is, the larger the negative bending capacity and flexural stiffness will be, and the positive bending capacity and flexural stiffness slightly increase. More longitudinal reinforcement that can bear force will exist because the force ratio is high. The negative bending capacity value of scb11($R$=0.68) is 24.9% and 9.9% larger than those of scb7($R$=0.07) and scb4($R$=0.36), respectively. The negative flexural stiffness value of scb11($R$=0.68) is 40.7% and 13.5% larger than those of scb7($R$=0.07) and scb4($R$=0.36), respectively.

**Table 3**
Influence of force ratio on plastic energy dissipation values

| No. | $\eta^+$ | space/mm | $d$/mm | $R$ | plastic energy dissipation (kJ) | | | | | energy dissipation proportion of stud (%) | energy dissipation of each stud (J) |
|---|---|---|---|---|---|---|---|---|---|---|---|
| | | | | | concrete slab | steel girder | reinforcement | stud | total | | |
| scb7 | 1.0 | 200 | 19 | 0.07 | 68.8 | 1129.8 | 74.6 | 4.6 | 1277.7 | 0.36 | 37.9 |
| scb8 | 1.0 | 200 | 19 | 0.14 | 56.1 | 1167.1 | 102.0 | 4.1 | 1329.3 | 0.31 | 33.8 |
| scb9 | 1.0 | 200 | 19 | 0.24 | 46.1 | 1231.9 | 110.6 | 4.0 | 1392.6 | 0.29 | 33.3 |
| Scb4 | 1.0 | 200 | 19 | 0.36 | 40.5 | 1274.7 | 127.3 | 3.9 | 1446.3 | 0.27 | 32.6 |
| scb10 | 1.0 | 200 | 19 | 0.51 | 35.8 | 1309.1 | 144.9 | 3.6 | 1493.4 | 0.24 | 29.6 |
| scb11 | 1.0 | 200 | 19 | 0.68 | 36.1 | 1343.2 | 156.8 | 4.2 | 1540.3 | 0.27 | 34.9 |

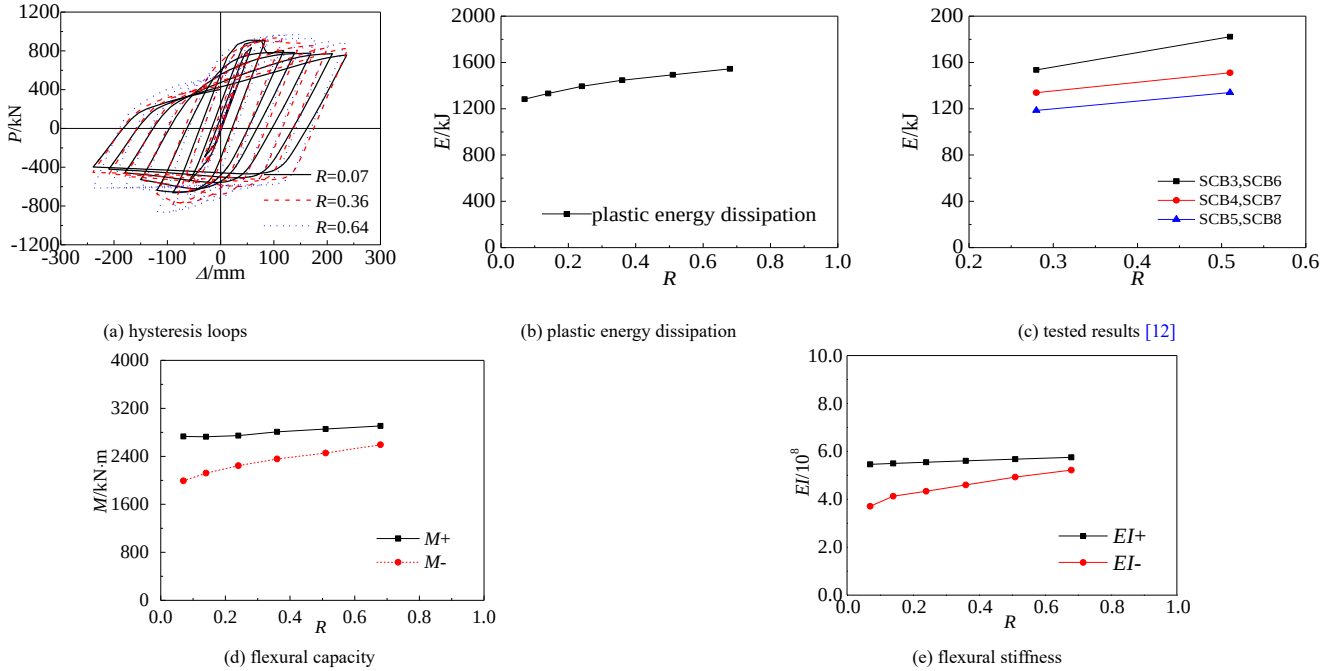


(a) hysteresis loops (b) plastic energy dissipation (c) tested results [12]

(d) flexural capacity (e) flexural stiffness

**Fig. 11** Influence of force ratio on the hysteresis performance of steel-concrete composite beams

### 3.3. Influence of the width–thickness ratio of girders

Tables 4–5 and Figs. 12–13 compare the influences of the width–thickness ratio of a girder on the hysteresis property of specimens. $R_w$ denotes the width–thickness ratio of the web. $R_f$ indicates the width–thickness ratio of the flange. The following observations were noted.

(1) The width–thickness ratio exerts a considerable impact on plastic energy dissipation, which decreases with an increase in the width–thickness ratio. The plastic energy dissipation of scb15($R_w$=19.2) is 17.8% and 48.4% larger than those of scb4($R_w$=28.8) and scb12($R_w$=57.5), respectively. The plastic energy dissipation of scb17($R_f$=6.4) is 44.8% and 114.0% larger than those of scb4($R_f$=9.6) and scb16($R_f$=19.2), respectively. The energy dissipation of studs is only slightly affected by the width–thickness ratio.

(2) Bending capacity is decreased with an increase in the width–thickness ratio. The flexural capacity of scb15($R_w$=19.2) is 13.8% and 34.7% larger than those of scb4($R_w$=28.8) and scb12($R_w$=57.5), respectively. The flexural capacity of scb17($R_f$=6.4) is 27.9% and 90.6% larger than those of scb4 ($R_f$=9.6) and scb16($R_f$=19.2), respectively.

Flexural stiffness is decreased with an increase in the width–thickness ratio. The flexural stiffness of scb15($R_w$=19.2) is 7.1% and 17.0% larger than those of scb4($R_w$=28.8) and scb12($R_w$=57.5), respectively. The flexural stiffness of scb17($R_f$=6.4) is 24.8% and 67.9% larger than those of scb4 ($R_f$=9.6) and scb16($R_f$=19.2), respectively.

**Table 4**
Influence of width-thickness ratio of the web on plastic energy dissipation values

| No. | $\eta^+$ | space/mm | $d$/mm | $R_w$ | plastic energy dissipation (kJ) | | | | | energy dissipation proportion of stud (%) | energy dissipation of each stud (J) |
|---|---|---|---|---|---|---|---|---|---|---|---|
| | | | | | concrete slab | steel girder | reinforcement | stud | total | | |
| scb12 | 1.0 | 240 | 19 | 57.5 | 29.7 | 1015.3 | 100.1 | 3.3 | 1148.4 | 0.29 | 27.6 |
| scb13 | 1.0 | 220 | 19 | 38.3 | 38.9 | 1224.5 | 118.4 | 5.8 | 1387.5 | 0.42 | 48.2 |
| scb4 | 1.0 | 200 | 19 | 28.8 | 40.5 | 1274.7 | 127.3 | 3.9 | 1446.3 | 0.27 | 32.6 |
| scb14 | 1.0 | 185 | 19 | 23.0 | 49.9 | 1392.7 | 147.1 | 5.2 | 1594.9 | 0.32 | 43.0 |
| scb15 | 1.0 | 175 | 19 | 19.2 | 55.7 | 1464.9 | 178.2 | 5.6 | 1704.5 | 0.33 | 46.9 |

Explanation: $t_f$=20mm, the $t_b$ is from 8mm to 24mm, $R_w$ is from 55.7 to 19.2.

**Table 5**
Influence of width-thickness ratio of the flange on plastic energy dissipation values

| No. | $\eta^+$ | space/mm | $d$/mm | $R_f$ | plastic energy dissipation (kJ) | | | | | energy dissipation proportion of stud (%) | energy dissipation of each stud (J) |
|---|---|---|---|---|---|---|---|---|---|---|---|
| | | | | | concrete slab | steel girder | reinforcement | stud | total | | |
| scb16 | 1.0 | 300 | 19 | 19.2 | 28.9 | 862.6 | 83.8 | 4.2 | 979.6 | 0.43 | 35.4 |
| scb17 | 1.0 | 240 | 19 | 12.8 | 37.6 | 1096.3 | 111.5 | 5.6 | 1251.0 | 0.45 | 46.6 |
| scb4 | 1.0 | 200 | 19 | 9.6 | 40.5 | 1274.7 | 127.3 | 3.9 | 1446.3 | 0.27 | 32.6 |
| scb18 | 1.0 | 170 | 19 | 7.7 | 47.9 | 1556.4 | 141.7 | 4.3 | 1750.3 | 0.25 | 35.9 |
| scb19 | 1.0 | 160 | 19 | 6.4 | 55.1 | 1872.0 | 161.9 | 4.8 | 2093.9 | 0.23 | 40.0 |

Explanation: $t_b$ =16mm, the $t_f$ is from 10mm to 30mm, $R_w$ is from 19.2 to 6.4.

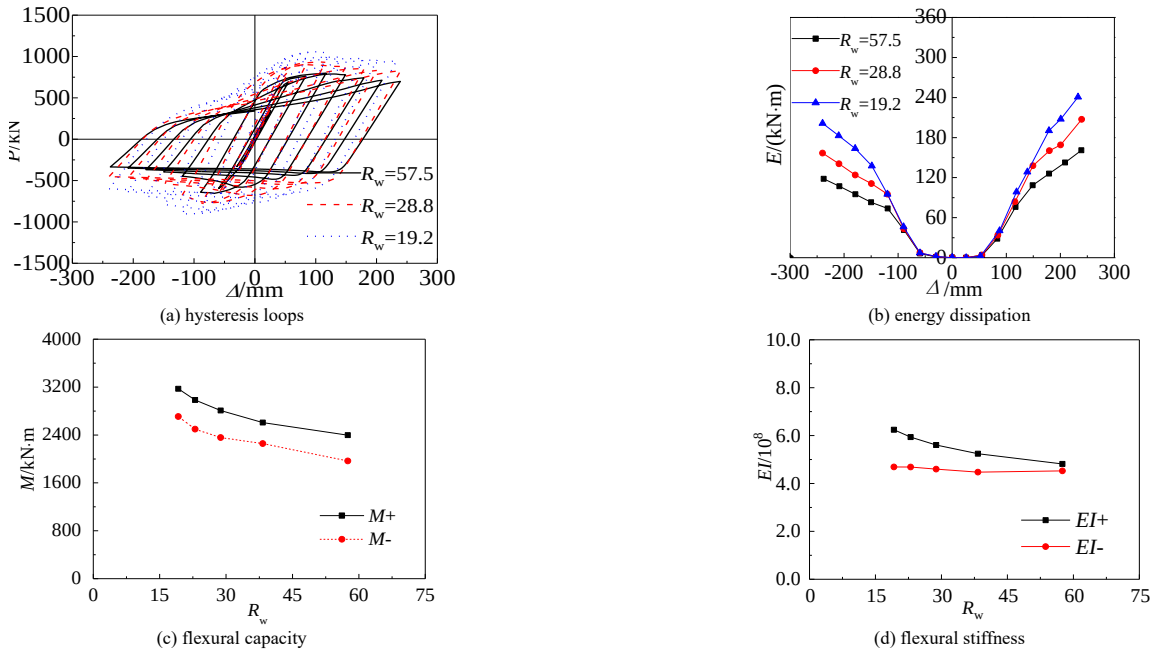


**Fig. 12** Influence of width-thickness ratio of the web on the hysteresis performance of steel-concrete composite beams

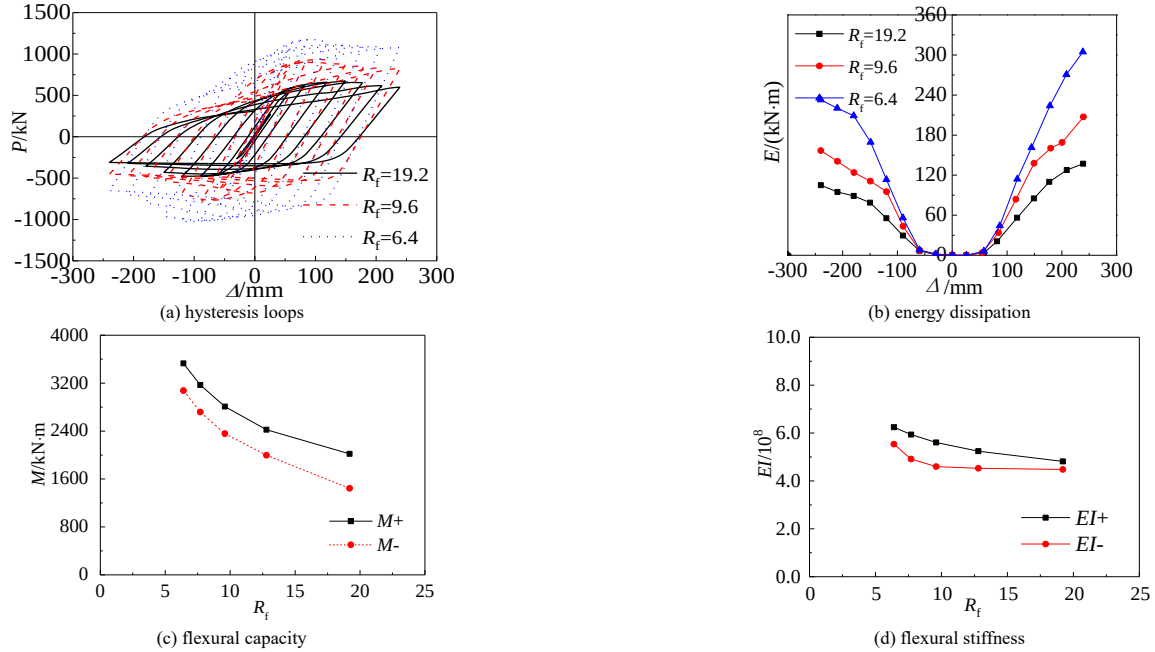


(a) hysteresis loops (b) energy dissipation (c) flexural capacity (d) flexural stiffness

**Fig. 13** Influence of width-thickness ratio of the flange on the hysteresis performance of steel-concrete composite beams

Tables 6–7 compare the thickness of the steel girder and the specification requirement. Fig. 14 illustrates the effect of the width–thickness ratio on the capacity of steel–concrete composite beams. The following observations are made.

(1) In standard [30], when an I beam works under bending, $R_w=h_s/t_w \leq 65(235/f_{s,b})1/2$, $R_f=b/t_f \leq 9(235/f_{s,b})1/2$, $b$ is the width of the web side, and $b=(w_b-t_w)/2$.

(2) The value of the width–thickness ratio is 57.5–19.2. Therefore, the specimen meets the requirements of the specification, except for $t_w$=8. The variation trend of the carrying capacity under the sagging moment of the FEA results is close to that of the standard results. However, when the thickness ratio of the web plate under the negative load changes from 38.3 to 57.5, the bearing capacity under the negative moment of the FEA results decreases faster than those of the standard results.

The value of the width–thickness ratio is 19.2–6.4. Hence, the specimen failed to meet the requirements of the specification, except for $R_f$=6.4. The variation trend of the bearing capacity under the positive moment of the FEA results is close to that of the standard results. In addition, when the thickness ratio of the web plate under the negative load changes from 12.8 to 19.2, the bearing capacity under the negative moment of the FEA results decreases faster than those of the standard results.

(3) The preceding analysis results show that the limit value of the width–thickness ratio can be relaxed, thereby limiting the values of the width–thickness ratio of the flange and the web to 15 and 45, respectively.

**Table 6**
The thickness of steel girder web compare with specification requirements

| No. | $t_w$(mm) | $t_f$ (mm) | $R_w$ | 65(235/$f_{s,b}$)1/2 | meets requirements? |
|---|---|---|---|---|---|
| 1 | 8 | 20 | 57.5 | 53.6 | No |
| 2 | 12 | 20 | 38.3 | 53.6 | Yes |
| 3 | 16 | 20 | 28.8 | 53.6 | Yes |
| 4 | 20 | 20 | 23.0 | 53.6 | Yes |
| 5 | 24 | 20 | 19.2 | 53.6 | Yes |

**Table 7**
The thickness of steel girder flange compare with specification requirements

| No. | $t_w$ (mm) | $t_f$ (mm) | $R_f$ | 9(235/$f_{s,b}$)1/2 | meets requirements? |
|---|---|---|---|---|---|
| 1 | 16 | 10 | 19.2 | 7.4 | No |
| 2 | 16 | 15 | 12.8 | 7.4 | No |
| 3 | 16 | 20 | 9.6 | 7.4 | No |
| 4 | 16 | 25 | 7.7 | 7.4 | No |
| 5 | 16 | 30 | 6.4 | 7.4 | Yes |

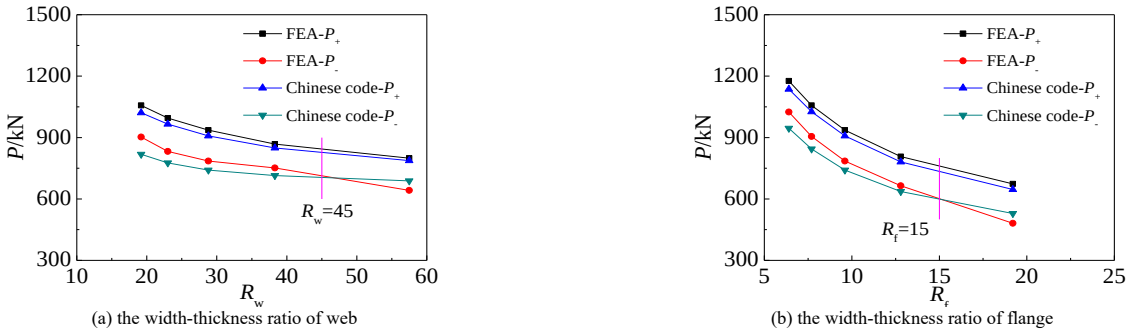


(a) the width-thickness ratio of web (b) the width-thickness ratio of flange

**Fig. 14** Influence of width-thickness ratio on the capacity of steel-concrete composite beams

### 3.4. Influence of the transverse reinforcement ratio

Table 8 and Fig. 15 compare the influences of the transverse reinforcement ratio on the hysteresis property of specimens, and the findings are presented as follows:

(1) Plastic energy dissipation is slightly increased with the transverse reinforcement ratio. The plastic energy dissipation of scb3 ($\rho_t$=1.03) is 1.1% and 0.9% larger than those of scb24($\rho_t$=0.19%) and scb21($\rho_t$=0.52%), respectively. The energy dissipation of studs was less than 1% of the total energy.

(2) Bending capacity and flexural stiffness is slightly increased with an increment in the transverse reinforcement ratio, and the transverse stirrup ensures that the concrete slab and steel girder collaborate efficiently.

The capacity in the positive and negative moment regions of scb23($\rho_t$=1.03) is 1.9% and 2.9% larger than those of scb4($\rho_t$=0.19%), respectively. The stiffness in the positive and negative moment regions of scb23($\rho_t$=1.03) is 0.1% and 0.2% larger than those of scb4($\rho_t$=0.19%), respectively.

**Table 8**
Influence of transverse reinforcement on plastic energy dissipation values

| No. | $\eta^+$ | space/mm | $d$/mm | $\rho_t$ /% | plastic energy dissipation (kJ) | | | | | energy dissipation proportion of stud (%) | energy dissipation of each stud (J) |
|---|---|---|---|---|---|---|---|---|---|---|---|
| | | | | | concrete slab | steel girder | reinforcement | stud | total | | |
| scb4 | 1.0 | 200 | 19 | 0.19 | 40.5 | 1274.7 | 127.3 | 3.9 | 1446.3 | 0.27 | 32.6 |
| scb20 | 1.0 | 200 | 19 | 0.33 | 38.2 | 1297.2 | 125.7 | 4.1 | 1465.2 | 0.28 | 34.3 |
| scb21 | 1.0 | 200 | 19 | 0.52 | 38.5 | 1291.1 | 127.6 | 4.3 | 1461.5 | 0.29 | 35.9 |
| scb22 | 1.0 | 200 | 19 | 0.75 | 35.8 | 1304.4 | 125.4 | 4.3 | 1469.9 | 0.29 | 36.1 |
| scb23 | 1.0 | 200 | 19 | 1.03 | 34.2 | 1324.2 | 122.6 | 4.3 | 1485.2 | 0.29 | 35.5 |

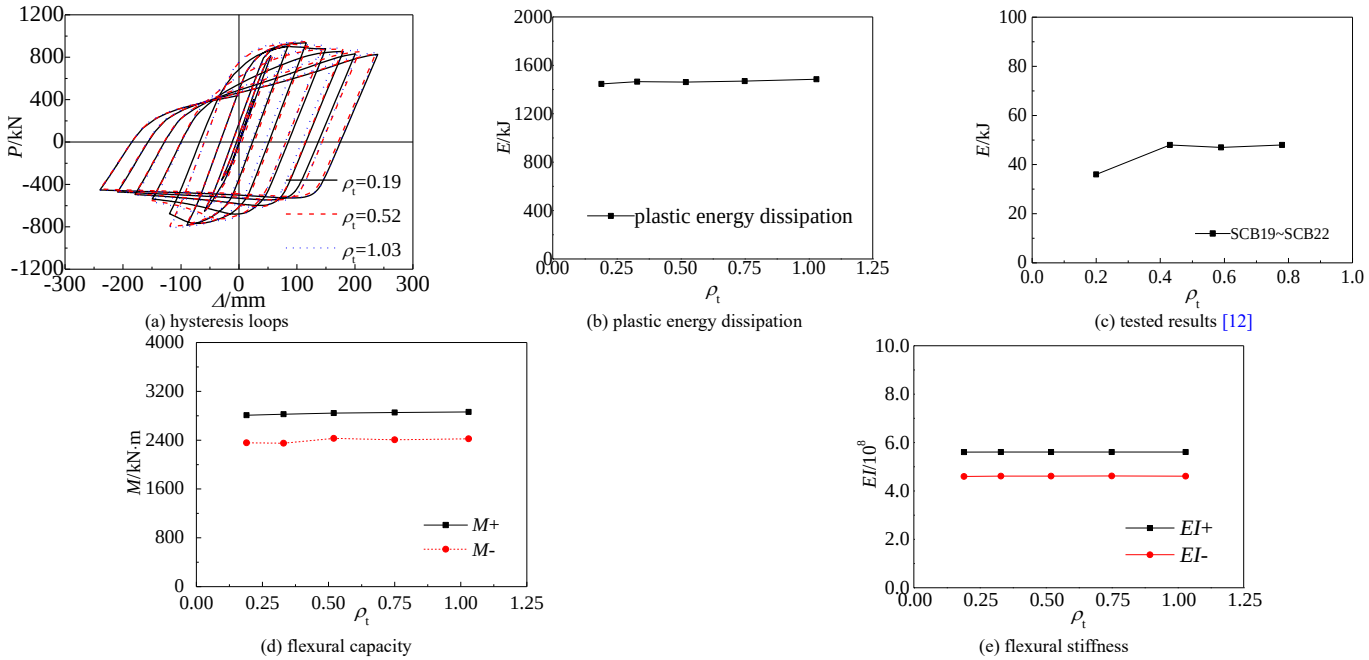


(a) hysteresis loops (b) plastic energy dissipation (c) tested results [12]

(d) flexural capacity (e) flexural stiffness

**Fig. 15** Influence of transverse reinforcement ratio on the hysteresis performance of steel-concrete composite beams

The transverse stress measuring points were set from four typical positions in the heavily loaded region from 1/4 to 1/2 spans. Fig. 16 illustrates the arrangement of the transverse stress measuring points. Fig. 17 shows the influence of the transverse reinforcement ratio on concrete slab stress (normal stress) in the mid-span region under the positive bending moment. The following observations were made.

(1) Fig. 17(a) shows the transverse stress–displacement curve, where transverse stress reaches the maximum value when center deflection displacement reaches approximately 140 mm. However, transverse stress decreases with an increase in the transverse ratio, and the slab can barely exhibit longitudinal cracks, which agrees with the test result [12].

(2) Fig. 17(b) shows the effect of the transverse reinforcement ratio on the maximum concrete transverse stress at different locations. When the transverse reinforcement ratio is 0%–0.5%, stress decreases rapidly. However, when the transverse reinforcement ratio exceeds 1.0%, stress is reduced slowly. Therefore, the transverse reinforcement ratio is suggested to range from 0.5% to 1.0%.

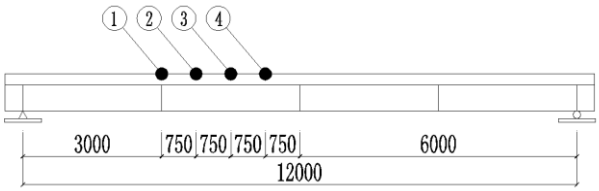


**Fig. 16** The arrangement of the transverse stress measuring points


(a) time-history curve of slab stress-displacement

(b) curve of slab stress- transverse reinforcement ratio

**Fig. 17** Influence of transverse reinforcement ratio on the stress of concrete slab

### *3.5. Influence of section form*

Table 9 and Fig. 18 compare the influences of section form on the hysteresis property of specimens, and the findings are presented as follows:

(1) The I beam has a slightly larger plastic energy dissipation capacity than the box beam. At an equivalent limit deflection, the dissipation capacity of the I beam is 3.6% larger than that of the box beam. The energy dissipation of studs is less than 1% of the total energy.

(2) Compared with the box beam, the I beam has a minor fuller hysteretic curve. Moreover, the I beam has a slightly higher bending bearing capacity than the box-shaped ones. The bearing capacity in the sagging and hogging moments of the scb4 (I beam) specimen is 1.8% and 6.5% larger than that of the scb24 (box beam) specimen. The flexural stiffness difference between the I beam and the box beam is quite modest.

The single web of the I-shaped steel girder is twice as thick as that of the box-shaped girder. Therefore, when the two types of composite beams bear a negative limit load, the maximum transverse deformation of the I-shaped and box-shaped beams is 6.53 and 0.52 mm, respectively. This web of box-beam is half as thick as the web of the I beam because the box girder have two webs. Relatively speaking, the web of the bot-girder was weak, so the maximum transverse deformation is larger.

**Table 9**
Influence of section form on plastic energy dissipation values

| No. | $\eta^+$ | space/mm | *d*/mm | section form | plastic energy dissipation (kJ) | | | | | energy dissipation proportion of stud (%) | energy dissipation of each stud (J) |
|---|---|---|---|---|---|---|---|---|---|---|---|
| | | | | | concrete slab | steel girder | reinforcement | stud | total | | |
| scb4 | 1.0 | 200 | 19 | I beam | 40.5 | 1274.7 | 127.3 | 3.9 | 1446.3 | 0.3 | 32.6 |
| scb24 | 1.0 | 200 | 19 | Box beam | 36.5 | 1245.4 | 108.8 | 5.0 | 1395.7 | 0.4 | 41.8 |

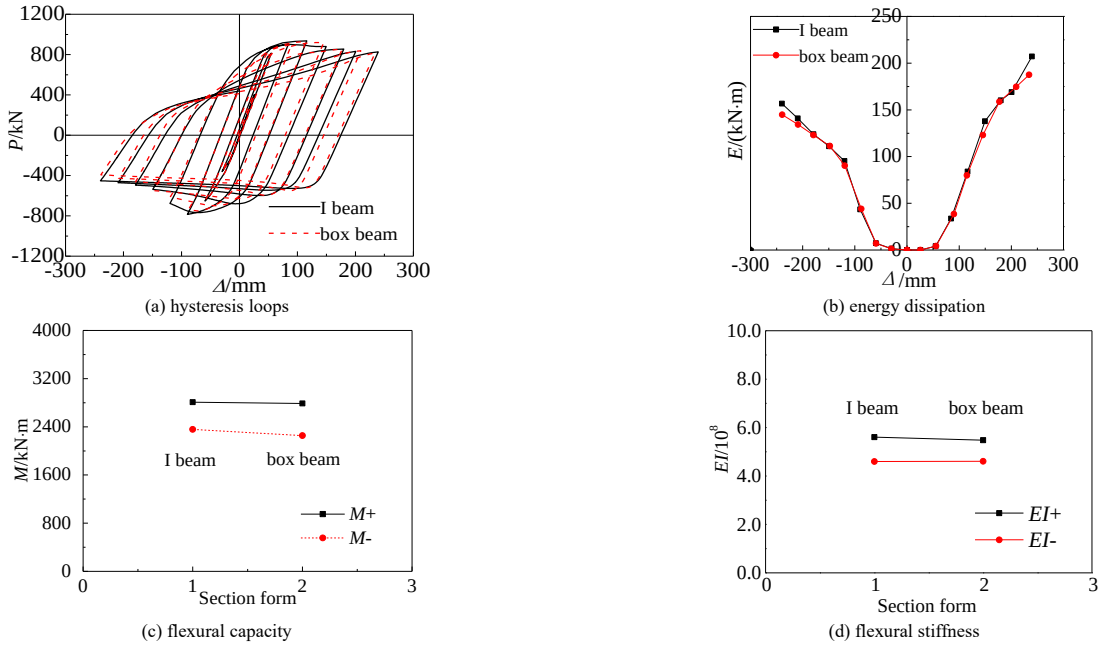


(a) hysteresis loops

(b) energy dissipation

(c) flexural capacity

(d) flexural stiffness

**Fig. 18** Influence of section form on the hysteresis performance of steel-concrete composite beams

### *3.6. Influence of stud diameter*

In structural or bridge engineering, excessive studs increase the obstruction in pouring concrete [31]. Table 10 and Fig. 19 compare the influences of stud diameter on the hysteresis property of the specimen. Researching seismic behavior under different stud diameters but the same shear connection degree is necessary for construction convenience.

(1) Stud diameter exerts an insignificant impact on plastic energy dissipation, with the largest difference between several samples being 2.6%. The plastic energy dissipation of each stud increases with stud diameter. The energy dissipation value of scb28(*d*=33 mm) is 274.5% and 141.3% larger than those of scb25(*d*=13 mm) and scb4(*d*=19 mm).

(2) Stud diameter influences the hysteresis curve of specimens minimally. The comparison of specimens illustrates that stud diameter has minimal effect on bearing capacity at the sagging or hogging moment region with the largest difference of at less than 0.6% and 1.0%, respectively. Moreover, the flexural stiffness difference at the positive and negative moment regions is less than 3.2% and 1.4%, respectively.

**Table 10**
Influence of stud diameter on plastic energy dissipation values

| No. | $\eta^+$ | space/mm | *d*/mm | plastic energy dissipation (kJ) | | | | | energy dissipation proportion of stud (%) | energy dissipation of each stud (J) |
|---|---|---|---|---|---|---|---|---|---|---|
| | | | | concrete slab | steel girder | reinforcement | stud | total | | |
| scb25 | 1.0 | 100 | 13 | 45.8 | 1259.5 | 132.8 | 5.0 | 1443.2 | 0.35 | 21.0 |
| scb26 | 1.0 | 150 | 16 | 47.6 | 1276.2 | 136.8 | 5.3 | 1465.9 | 0.36 | 32.9 |
| scb4 | 1.0 | 200 | 19 | 40.5 | 1274.7 | 127.3 | 3.9 | 1446.3 | 0.27 | 32.6 |
| scb27 | 1.0 | 300 | 26 | 44.4 | 1264.2 | 116.1 | 4.6 | 1429.3 | 0.32 | 57.6 |
| scb28 | 1.0 | 400 | 33 | 43.6 | 1264.7 | 126.3 | 4.7 | 1439.3 | 0.33 | 78.7 |

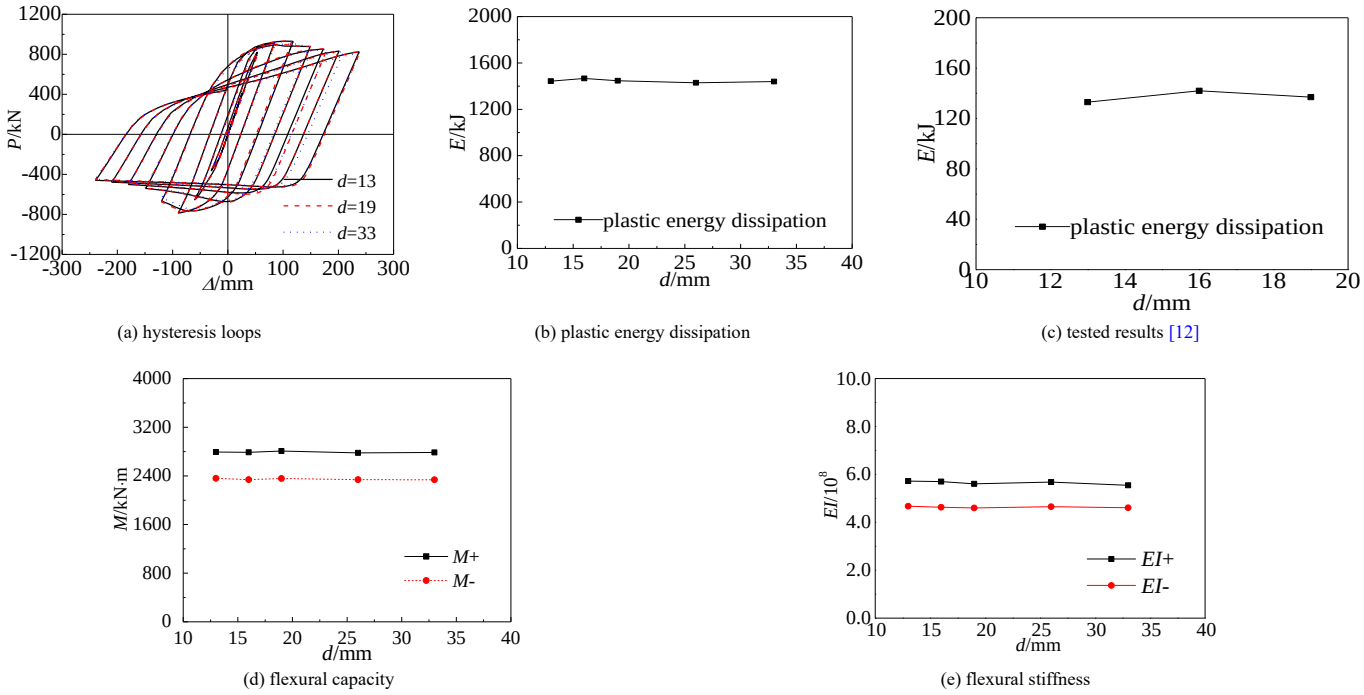


(a) hysteresis loops (b) plastic energy dissipation (c) tested results [12]

(d) flexural capacity (e) flexural stiffness

**Fig. 19** Influence of stud diameter on the hysteresis performance of steel-concrete composite beams

## 4. Conclusions

The hysteresis behavior of steel–concrete composite beams were investigated by a validated 3D FE model using ABAQUS software. Based on the analysis, the following conclusions were drawn.

(1) A reasonable constitutive model of concrete and steel and an elaborate modelling method can be used to simulate the quasi-static behavior of steel-concrete composite beams accurately. In terms of load–displacement curve, load slip, and local buckling of steel beams, the calculated results are in good agreement with the measured values.

(2) The FEA results show that the steel girder is the main energy dissipation component of the composite beam, and the energy dissipation of the steel girder is higher than 80% of the total energy. The next is longitudinal reinforcement, followed by a concrete slab. The minimum proportion is the studs, and the energy dissipation of studs is less than 1% of the total energy. However, an increase in shear connection is beneficial to enhance the energy dissipation of steel beams and rebars.

(3) Shear connection, force ratio, and width–thickness ratio are the principal factors that influence the flexural capacity, flexural stiffness, and seismic performance of composite beams, respectively. That is, the higher the shear connection and force ratio are, the less the width–thickness ratio, the larger the capacity and stiffness, and the plumper the hysteretic curve will be. Transverse ratio, section form, and stud diameter slightly affect the seismic property of composite beams.

## Acknowledgements

This research is financially supported by the National Natural Science Foundation of China under Grant Nos. 52008159, 51978664, and 52008400; Hunan Education Department Foundation Funded Project under Grant No. 21A0504; and China Postdoctoral Science Foundation under Grant No. 2018M632990.

## References

[1] Ayoub A, Filippou FC. Mixed Formulation of Nonlinear Steel-Concrete Composite Beam Element. Journal of Structural Engineering. 2000;126:371-81.
[2] Bugeja MN, Bracci JM, Moore WP. Seismic behavior of composite RCS frame systems. Journal of Structural Engineering. 2000;126:429-36.
[3] Nie JG, Yu ZL, Ye QH. Seismic behaviour of composite steel-concrete beams. Journal of Tsinghua University (Science and Technology); 38(10):35-37. (in Chinese).
[4] Coughlan DJOG. The shear stiffness of stud shear connections in composite beams. Journal of Constructional Steel Research. 1986.
[5] Lam D, El-Lobody E. Behavior of Headed Stud Shear Connectors in Composite Beam. Journal of Structural Engineering. 2005;131:96-107.
[6] Ataei A, Zeynalian M, Yazdi Y. Cyclic behaviour of bolted shear connectors in steel-concrete composite beams. Engineering Structures. 2019;198:109455.1-.15.
[7] Xing Y, Han Q, Xu J, et al. Experimental and numerical study on static behavior of elastic concrete-steel composite beams. Journal of Constructional Steel Research. 2016;123:79-92.
[8] Chen J, Zhang H, Yu QQ. Static and fatigue behavior of steel-concrete composite beams with corroded studs. Journal of Constructional Steel Research. 2019;156:18-27.
[9] Jiang LZ, Yu ZW, Cao H, et al . Effect of shear connection degree on seismic resistant performance of steel-concrete composite beams. Journal of Building Structures, 38(3):52-54. (in Chinese)
[10] Nie J, Qin K, Cai CS. Seismic behavior of connections composed of CFSSTCs and steel–concrete composite beams—experimental study. Journal of Constructional Steel Research. 2007;64.
[11] Xue WC, Li K, Li J. Study on steel-concrete composite beams under low-reversed cyclic loading. Earthquake Engineering and Engineering Vibration, 22(6):65-70. (in Chinese)
[12] Ding FX, Liu J, Li XM, et al. Experimental investigation on hysteretic behavior of simply supported steel-concrete composite beam. Journal of Constructional Steel Research. 2018;144:153-65.
[13] Spacone E, El-Tawil S. Nonlinear Analysis of Steel-Concrete Composite Structures: State of the Art. Journal of Structural Engineering. 2004;130:159-68.
[14] Nie JG, Yu ZL, Yuan YS, et al. Research on restoring force model of composite steel-concrete beam. Journal of Tsinghua University (Science and Technology), 39(6),121-123.(in Chinese)
[15] Nie JG, Cai CS. Numerical modeling on concrete structures and steel–concrete composite frame structures. Composites Part B: Engineering. 2013.
[16] Tao MX, Nie JG. Fiber Beam-Column Model Considering Slab Spatial Composite Effect for Nonlinear Analysis of Composite Frame Systems. Journal of Structural Engineering. 2014;140:04013039.
[17] Zhao H, Kunnath SK, Yuan Y. Simplified nonlinear response simulation of composite steel–

concrete beams and CFST columns. Engineering Structures. 2010;32:2825-31.
[18] Nie J, Kai Q, Cai CS. Seismic behavior of connections composed of CFSSTCs and steel–concrete composite beams — finite element analysis. Journal of Constructional Steel Research. 2008;64:680-8.
[19] Bursi OS, Sun FF. Non-linear analysis of steel–concrete composite frames with full and partial shear connection subjected to seismic loads. Journal of Constructional Steel Research. 2005;61:67-92.
[20] Vasdravellis G, Valente M, Castiglioni CA. Behavior of exterior partial-strength composite beam-to-column connections: Experimental study and numerical simulations. Journal of Constructional Steel Research. 2009;65:23-35.
[21] Ding FX, Yin GA, Wang LP, et al. Seismic performance of a non-through-core concrete between concrete-filled steel tubular columns and reinforced concrete beams. Thin-Walled Structures. 2017;110:14-26.
[22] Liu J, Ding FX, Liu XM, et al. Study on flexural capacity of simply supported steel-concrete composite beam. Steel and Composite Structures. 2016;21:829-47.
[23] Ding FX, Ying XY, Zhou LC, et al. Unified calculation method and its application in determining the uniaxial mechanical properties of concrete. Frontiers of Architecture & Civil Engineering in China. 2011;5:381.
[24] Simulia. (2014), Abaqus/standard user's manual, version 6.14 edition, Providence, RI: Dassault Systemes.
[25] Yao X-m, Zhou XH, Guan Y, Shi Y, He Z-q. 'Bending behavior of cold-formed steel–concrete composite floors.' Advanced Steel Construction. 2019;15(4).
[26] Bahaz A, Amara S, Jaspart J-P, Demonceau J-Fo. 'Numerical analysis and evaluation of effective slab width of composite continuous beams with semi-rigid joint.' Advanced Steel Construction. 2021;17(4):9.
[27] Zou Y, Zhou XH, Di J, Qin FJ. 'Partial interaction shear flow forces in simply supported composite steel-concrete beams.' Advanced Steel Construction. 2018;14(4):17.
[28] Yao X-m, Zhou XH, Guan Y, Shi Y, He Z-q. 'Bending behavior of cold-formed steel–concrete composite floors.' Advanced Steel Construction. 2019;15(4).
[29] Pardeshi RT, Patil YD. Review of various shear connectors in composite structures. Advanced Steel Construction. 2021;17(4):9.
[30] GB 50017-2017 (2017), Standard for design of steel structure; Architecture and Building Press, Beijing, China
[31] Ding FX, Ni M, Gong YZ, et al. Experimental study on slip behavior and calculation of shear bearing capacity for shear stud connectors. Journal of Building Structures, 35(9):98-106. (in Chinese)

**Advanced Steel Construction** – Vol. 18 No. 3 (2022) 670–678
**DOI:**10.18057/IJASC.2022.18.3.4


# LOW-TEMPERATURE COMPRESSION BEHAVIOUR OF CIRCULAR STUB STAINLESS-STEEL TUBULAR COLUMNS

Jia-Bao Yan [1, 2], Biao Zhang [2], Jun-Ying Feng [2], Yan-Sheng Du [1, 2, *], Yun-Biao Luo [1, 2] and Yun-Dong Shi [1, 2]

[1] *Key Laboratory of Coast Civil Structure Safety of Ministry of Education, Tianjin University, Tianjin 300350, China*
[2] *School of Civil Engineering, Tianjin University, Tianjin 300350, China*
** (Corresponding author: E-mail: duys@tju.edu.cn)*

**ABSTRACT**

This paper firstly studies mechanical properties of stainless steel (SS) S30408 at the low temperature (*T*) range of -80~20℃. Further compression tests are carried out on 20 SS stub tubular columns (SSSTCs) at low temperatures of -80, -60, -30, and 20℃ to investigate their low-temperature compression behaviour. Including the testing low temperatures, the wall thickness of SS tube (*t*) is the other investigated parameters. Test results show that decreasing the *T* from 20 to -80℃ improves the yield and ultimate strength of stainless steel by 29% and 80%, respectively, but reduces its ductility by about 25%. Under low-temperature compression, elephant foot local buckling occurs to most of SSSTCs and inelastic inward and outward local buckling occurred to specimens with 6 mm-thick SS tube. Test results also show that the decreasing *T* value increases the strength and stiffness of SSSTCs, but compromises their ductility; the wall thickness of SSSTCs significantly improves their strength, stiffness, and ductility. This paper also develops 3D finite element model (FEM) to estimate the low-temperature compression behaviour of SSSTCs, which considers nonlinearities of material and geometry, geometric imperfections, and influences of low temperatures. The validations show it predicts reasonably well the low-temperature compression behaviours of SSSTCs.

**ARTICLE HISTORY**

Received: 26 June 2021
Revised: 16 December 2021
Accepted: 21 December 2021

**KEYWORDS**

Stainless steel;
Low temperture;
Compression test;
Arctic engineering;
Finite element;
Compression behaviour



## 1. Introduction

Stainless steel (SS) possesses extensive advantages of high ductility, high environmental corrosion resistance, attracting architectural appearance, low maintenance costing, good processability and weldability, and recycling potentiality. Due to these extensive advantages, stainless steel gains increasing engineering applications especially in applications of infrastructures exposed to environmental pollution and chloride attack, e.g., roofs of buildings, offshore/onshore bridges, and harbour facilities. After its first application in Brearley (UK) and Maurer and Strauss in Germany [1], more representative engineering applications include roofs of Empire State Building and Chrysler Building in USA, Expo MRT station in Singapore, Tokyo Stadium in Japan, Millennium footbridge in UK, foot and road bridge near Siena, Shenzhen Bay bridge. Three representative types of SS are austenitic, duplex and ferritic SS [3]. Austenitic S30408 SS, a type of commonly used austenitic stainless steel, has been used in architectures, bridges, oil and chemical industry buildings, LNG containers, and pressure vessels [4-7] More recently, it has been proposed for the coastal bridges in cold regions (see Fig. 1).

The low temperature (*T*) in cold regions varies, e.g., the lowest recorded *T* in Northern China is about -50℃, the recorded lowest *T* in the Arctic and Antarctic varies from -68.0 to -89.2℃ [8]. Thus, these low temperatures tend to affect the structural behaviours of Austenitic S30408 SS used in cold-region constructions. Extensive previous studies on SS have been performed on their ambient/high-temperature structural performances. Rasmussen [9], Ashraf et al. [10], and Gardener and Netehrcot [11] contributed to mechanical properties (MPs) of SS at ambient temperatures. Quach et al. [12] and Gardner and Yun [13] proposed stress-strain constitutive models for SS. Extensive experimental and analytical works on MPs of SS at high temperatures have also extensively reported by Sakumot et al. [14], Chen and Young [15], Gardner et al. [16], Wang et al. [17], Liang et al. [18], and Fan et al. [19-20]. Rasmussen [21] studied the structural behaviours of SS tubular structures. Young and Hartono [22] investigated compression behaviours of SS tubes at room temperatures. Lui et al. [23] experimentally studied ultimate strength behaviours of SS beam-columns. Huang and Young [24] and Arrayago et al. [25] also contributed to the topic of SS beam-columns. Bu and Gardner [26] studied the structural behaviours of laser-welded SS beam-columns. Greiner and Kettler [27] studied the bending-compression interaction behaviour of SS members. Zhao et al. [28] contributed to the bending-compression interaction behaviour of slender SS members. Cai and Young [29] studied the structural behaviour of cold-formed stainless steel bolted connections at post-fire condition. Salih et al. [30] numerically studied the net section failure behaviours of SS bolted connections. Elflah [31] studied the behaviour of SS beam-column joints. Though these extensive studies made solid pavements on the applications of SS structures, they mainly concentrated on the material/member behaviours of SS at ambient/high temperatures. The information on SS materials or members is still very limited. Studies on the SS structural members at low temperatures become necessary to promote their applications.

This paper studied the compression behaviour of stub SS tubular columns (SSSTCs) at low temperatures. Twenty SSSTCs with varying wall thickness (*t*) were tested at four *T* levels of -80, -60, -30, and 30℃. Test results provided useful information on the compression behaviours of SSSTCs at low temperatures. The effects of *T* and *t* were detailed analysed and discussed. Moreover, this paper developed finite element models (FEMs) to estimate the low-temperature compression behaviour of SSSTCs, and these FEMs were validated by the reported 20 tests. At the end of this paper, conclusions were given based on these experimental and numerical investigations.

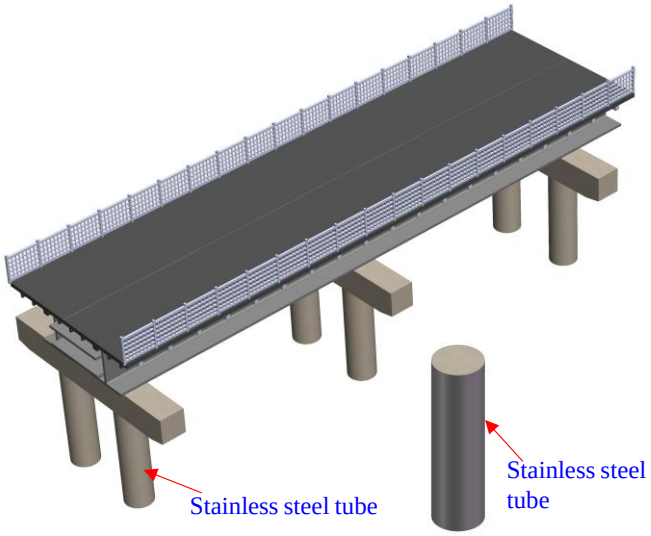


**Fig. 1** Applications of stainless steel tubular columns in a composite bridge

## 2. Axial compression tests on stub stainless steel tubular columns (SSSTCs)

### *2.1. Testing program*

Stainless steel S30408 was adopted to fabricate the SSSTCs. Table 1 lists the chemical compositions of S30408 and compared with those of mild steel Q345 with the close strength. It can be found that the SS S304 contains much

higher Chromium (Cr) (18.24%) and Nickel (Ni) (8.02%) than mild steel Q345, which are the main reason of high corrosion resistance of S304. To study the axial low-temperature compression behaviour of SSSTCs, 20 SSSTCs using S304 SS were prepared with three types of wall thickness (t), i.e., *t*=3.0, 4.5,

**Table 1**
Chemical composition of mild steel Q345 and stainless steel S30408

| Chemical composition | C (%) | Si (%) | Mn (%) | S (%) | P (%) | Cr (%) | Ni (%) |
|---|---|---|---|---|---|---|---|
| Q345 | 0.14 | 0.55 | 1.40 | - | - | 0.30 | 0.30 |
| S30408-3mm | 0.043 | 0.50 | 1.51 | 0.002 | 0.035 | 18.24 | 8.01 |
| S30408-4mm | 0.043 | 0.48 | 1.45 | 0.002 | 0.035 | 18.27 | 8.02 |
| S30408-6mm | 0.041 | 0.44 | 1.27 | 0.001 | 0.016 | 18.47 | 8.15 |
| | N (%) | Nb (%) | Mo (%) | Cu (%) | $Al_s$ (%) | Ti (%) | V (%) |
| Q345 | 0.008 | 0.021 | - | 0.30 | 0.035 | 0.008 | 0.03 |
| S30408-3mm | - | - | - | - | - | - | - |
| S30408-4mm | - | - | - | - | - | - | - |
| S30408-6mm | 0.027 | - | - | - | - | - | - |

and 6.0 mm. Therefore, these 20 SSSTCs were categorized into three groups with their different *t* values. For each group of SSSTCs with different *t* value, four testing low temperatures were set, i.e., *T*=30, -30, -60, and -80°C. And one/two SSSTCs were prepared for each *T* level. Fig. 2 plots the geometry of SSSTCs. Each SSSTC is 400 mm high with an equal external diameter of 133 mm. Table 1 provides more information on the details of tested SSSTCs.

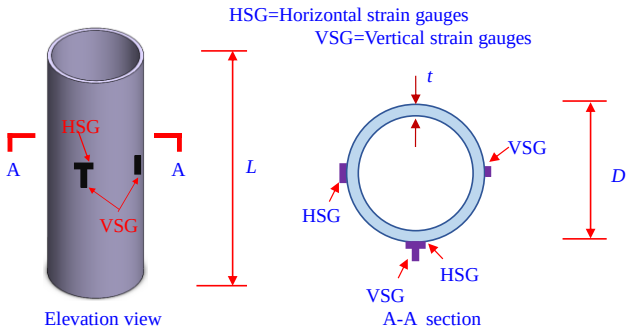


**Fig. 2** Diemension of the SSSTCs

Mechanical properties of SS S30408 were obtained from tension tests on coupons cut from those SSSTCs according to GB/T 13239-2006 [32] (See Fig. 3). Tensile stress-strain curves of SS S30408 coupons at different *T* levels are illustrated in Fig. 3(a)-(c). These figures reveal interesting findings as the following:

(1) The mechanical properties of SS are significantly influenced by the reducing *T*. Reducing *T* of the environment improves the yield and ultimate strength, but reduces the ductility of SS. As the *T* decreases from 20 to -30, -60,

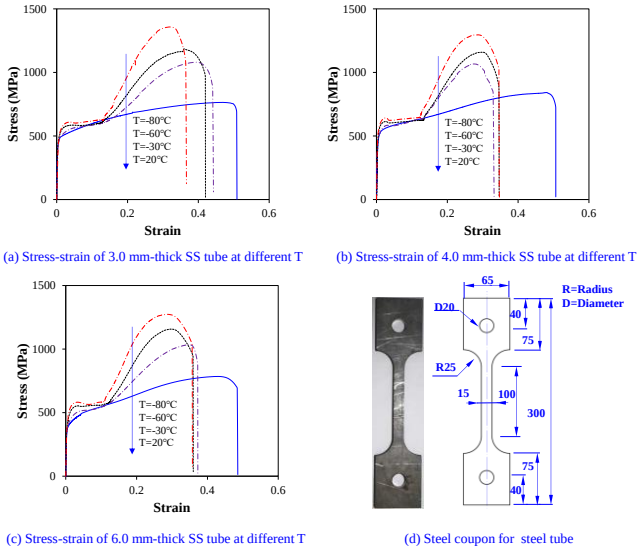


**Fig. 3** Low-tempreature tenisle stress-strain curves of SS at different low temperatures

and -80°C, the yield (or ultimate) strength of 3 mm-thick SS coupon is increased by 3% (42%), 6% (58%), and 14% (77%), respectively; the yield (or ultimate) strength of 4.5 mm-thick SS coupon is increased by 6% (27%), 11% (38%), and 24% (54%), respectively; and these increments for 6.0-thick SS coupon equal to 2% (42%), 9% (45%), and 16% (62%), respectively. However, with the decrease of *T* from 20 to -30, -60, and -80°C, the fracture strain of 3 (or 4.5, 6.0) mm-thick SS was reduced by 13% (35%, 19%), 17% (35%, 26%), and 28% (32%, 26%), respectively.

(2) The low-temperature stress-strain curves of SS behave differently from those ambient curves especially at the strain hardening stage. The ambient-temperature stress-strain curves exhibit a flat increasing rate at the strain hardening stage, but the stress-strain curves of SS at low temperatures exhibit much larger increasing slope at the strain hardening branch than that at ambient temperature.

Table 1 provides detailed information on mechanical properties of S30408 at low temperatures.

### *2.2. Setup and instrumentation*

The low-temperature compression tests on SSSTCs were performed by a 300-ton testing machine in Structural Lab of Tianjin University. Fig. 4 shows the setup of compression tests on SSSTCs. Each SSSTC was directly installed to the bottom supporting rigid plate, and surrounded by a cooling chamber made of insulation materials, which was fabricated for simulation on the cold-region environment. LNG was introduced inside the cooling chamber to cool down the SSSTC. PT100 type of thermal couples were also installed on the external surface of SSSTCs at different positions to instrument the low temperatures of SSSTCs as shown in Fig. 4. Furthermore, these monitored temperatures of SSSTCs were used as the referencing temperature readings to control the flow of the injected LNG into the cooling chamber by a magnetic valve (see Fig. 4).

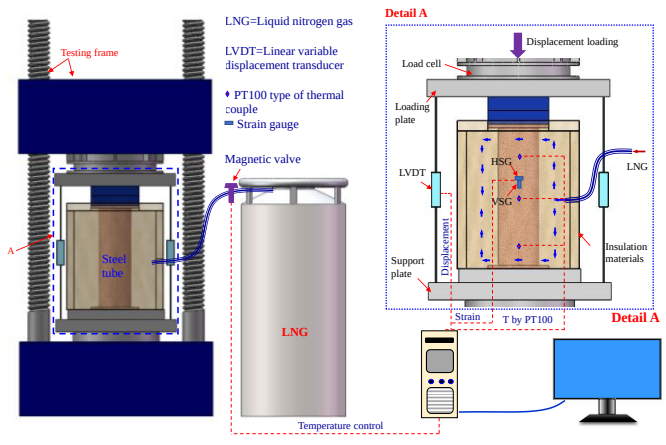


**Fig. 4** Setup and instrumentations of low-temperature compression tests on SSSTCs

Displacement loading transferred from the actuator directly acted on the top of SSSTCs, and the reaction forces of the SSSTCs were measured automatically by the testing machine. Shortenings of the SSSTC ($\Delta$) were measured by four

LVDTs installed between the loading and supporting plate (see Fig. 4). The vertical SSSTCs, and the reaction forces of the SSSTCs were measured automatically by the testing machine. Shortenings of the SSSTC ($\Delta$) were measured by four LVDTs installed between the loading and supporting plate (see Fig. 4). The vertical and circumferential strains at the mid-height of SSSTCs were instrumented by linear strain gauges (see Fig. 4), and these measured positions of the SS tube at the locations are shown in Fig. 2.

The geometric imperfections [33] were also measured at different locations of the SS tube prior to the low-temperature compression tests. Fig. 5 plots the measured geometric imperfections at quarter circumferential positions along the height of representative SSSTCs Ct6T-60-1 and Ct6T-80. The maximum measured magnitudes of imperfections for SSSTCs are given in Table 2.

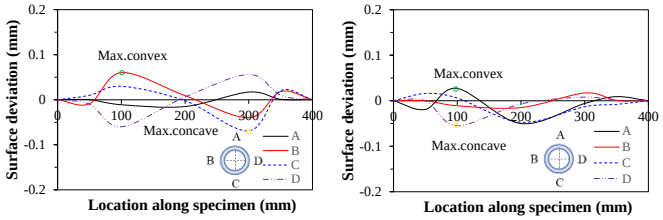


**Fig. 5** Measured local geometric imperfections along the height of SSSTCs

**Table 2**
Details of SSSTCs under low-temperature compression tests

| No. | Item | $D$ (mm) | $t$ (mm) | $v_0$ (mm) | $A_s$ (mm$^2$) | $T$ (°C) | $E_{sT}$ (GPa) | $f_{yT}$ (MPa) | $f_{uT}$ (MPa) | $\varepsilon_{yT}$ (%) | $\varepsilon_{uT}$ (%) | $\varepsilon_{FT}$ (%) |
|---|---|---|---|---|---|---|---|---|---|---|---|---|
| 1 | Ct3T20-1 | 133.1 | 2.98 | 0.120 | 1218 | 20 | 170 | 430 | 763 | 0.39 | 46.91 | 50.9 |
| 2 | Ct3T20-2 | 133.0 | 3.01 | 0.130 | 1229 | 20 | 170 | 430 | 763 | 0.39 | 46.91 | 50.9 |
| 3 | Ct3T30 | 133.1 | 3.03 | 0.094 | 1238 | -30 | 189 | 442 | 1080 | 0.48 | 39.34 | 44.3 |
| 4 | Ct3T60-1 | 132.8 | 2.98 | 0.121 | 1215 | -60 | 187 | 456 | 1209 | 0.44 | 35.95 | 42.0 |
| 5 | Ct3T60-2 | 133.1 | 2.99 | 0.111 | 1222 | -60 | 187 | 456 | 1209 | 0.44 | 35.95 | 42.0 |
| 6 | Ct3T80 | 133.3 | 3.01 | 0.120 | 1231 | -80 | 211 | 492 | 1354 | 0;46 | 32.03 | 36.6 |
| 7 | Ct4.5T20-1 | 133.2 | 4.51 | 0.134 | 1822 | -20 | 189 | 434 | 842 | 0.40 | 47.95 | 50.8 |
| 8 | Ct4.5T20-2 | 133.3 | 4.49 | 0.108 | 1816 | -20 | 189 | 434 | 842 | 0.40 | 47.95 | 50.8 |
| 9 | Ct4.5T30-1 | 133.1 | 4.49 | 0.116 | 1813 | -30 | 224 | 460 | 1066 | 0.40 | 27.30 | 33.2 |
| 10 | Ct4.5T30-2 | 133.0 | 4.60 | 0.100 | 1855 | -30 | 224 | 460 | 1066 | 0.40 | 27.30 | 33.2 |
| 11 | Ct4.5T60-1 | 133.1 | 4.51 | 0.100 | 1821 | -60 | 199 | 481 | 1158 | 0.45 | 29.44 | 34.7 |
| 12 | Ct4.5T60-2 | 133.4 | 4.50 | 0.120 | 1821 | -60 | 199 | 481 | 1158 | 0.45 | 29.44 | 34.7 |
| 13 | Ct4.5T80-1 | 133.1 | 4.48 | 0.092 | 1809 | -80 | 247 | 536 | 1295 | 0.39 | 28.08 | 34.7 |
| 14 | Ct4.5T80-2 | 132.9 | 4.49 | 0.112 | 1810 | -80 | 247 | 536 | 1295 | 0.39 | 28.08 | 34.7 |
| 15 | Ct6T20-1 | 133.1 | 5.99 | 0.067 | 2391 | 20 | 173 | 359 | 784 | 0.37 | 42.41 | 48.6 |
| 16 | Ct6T20-2 | 133.2 | 6.00 | 0.100 | 2396 | 20 | 173 | 359 | 784 | 0.37 | 42.41 | 48.6 |
| 17 | Ct6T30 | 133.3 | 6.02 | 0.120 | 2406 | -30 | 210 | 367 | 1116 | 0.42 | 32.86 | 39.5 |
| 18 | Ct6T60-1 | 133.0 | 6.01 | 0.060 | 2396 | -60 | 234 | 393 | 1139 | 0.34 | 29.85 | 36.0 |
| 19 | Ct6T60-2 | 133.1 | 6.00 | 0.042 | 2395 | -60 | 234 | 393 | 1139 | 0.34 | 29.85 | 36.0 |
| 20 | Ct6T80 | 132.8 | 6.01 | 0.027 | 2393 | -80 | 235 | 418 | 1273 | 0.40 | 28.70 | 35.8 |

$D$ is diameter of circular tube; $t$ denotes thickness of stainless steel tube; $v_0$ is the initial imperfection amplitude of stainless steel tube by measured; $T$ is low temperature; $A_s$ denotes cross-sectional area of stainless steel tube; $f_{yT}$, $f_{uT}$, and $E_{sT}$ denotes yield strength, ultimate strength, and elastic modulus of stainless steel tube, respectively; $\varepsilon_{yT}$, $\varepsilon_{uT}$, and $\varepsilon_{FT}$ denotes yield strain, ultimate strain, and fraction strain of stainless steel tube at temperature $T$.

## 3. Test result and discussions

### *3.1. Failure modes*

Fig. 6 depicts failure modes of SSSTCs after the compression tests. It shows that most of the SSSTCs exhibit ring-shaped bulge at one or two ends of SSSTCs, namely elephant foot local buckling. This prevalent type of failure mode commonly took place in tubular columns under compression [34-36], which have low imperfections. For several specimens with $t$=6 mm tested at -30~-80°C, inelastic inward and outward local buckling occurred as shown in Fig. 6.

### *3.2. Low-temperature compression load-shortening (P-Δ) curves and load-strain (P-strain) curves of SSSTCs*

Figs. 7 and 8 plot the $P$-$\Delta$ curves and P-strain curves of SSSTCs subjected to compression at low temperatures, respectively. These curves reflect that all the $P$-$\Delta$ curves behave closely even with some differences in the strength hardening branches, which can be categorized into three types as summarized in Fig. 9. The $P$-$\Delta$ curves of SSSTCs subjected to compression at low temperatures consist of four working stages, namely elastic, inelastic, plastic hardening, and recession stage. The elastic stage initiates from the start of testing and ends at about 50% ultimate load capacity ($P_u$), which corresponds to the elastic limit of SS stress-strain curves (see Fig. 3). In the following inelastic stage, both $P$-$\Delta$ and $P$-strain curves exhibit a parabolic manner, which can be also supported by the parabolic stress-strain curves of SS (see Fig. 3). Finally, vertical strains of SSSTCs achieve the yielding value (see Fig. 8). After that, the $P$-$\Delta$ curves enter into their third stage, i.e., plastic stage due to the strain hardening of SS as shown in Fig. 3. The length of the third-stage branch of $P$-$\Delta$ curves was determined by the wall thickness of SSSTCs, which determines the occurrence of local buckling in SS tube. At the third-stage end, the SSSTCs achieve their ultimate capacity ($P_u$), and local buckling of SSSTCs took place. Finally, the $P$-$\Delta$ curves enter their recession stages. Fig. 8 further confirmed that the measured strains at $P_u$ for all the SSSTCs are beyond yielding point, which implies occurrence of plastic local buckling. In addition, the overturning $P$-strain curves in Fig. 8 also confirmed the local buckling of SSSTCs.

Fig. 10 plots the representative $P/P_u$ versus hoop-to-vertical strain ($\varepsilon_h/\varepsilon_v$) curves of SSSTCs at low temperatures. It shows that as the $P/P_u$ ratio is below 0.7-0.9, the $\varepsilon_h/\varepsilon_v$ ratio exhibits values near 0.3 (within a range between 0.2 and 0.4), which implies a linear behaviour of the SSSTCs. $A_s$ the $P/P_u$ ratio is beyond 0.9, the $\varepsilon_h/\varepsilon_v$ ratio increases faster that corresponds the nonlinear behaviour of SSSTCs.

### *3.3. Ultimate load capacity ($P_u$) and its corresponding shortening ($\Delta_u$), initial stiffness($K_0$), and ductility ratio (DI)*

Determinations of $P_u$, $\Delta_u$, $K_0$, and $DI$ ratio follow the same methods used in Ref. [37]. The $K_0$ and $P_u$ are determined from the stage I and III branches of $P$-$\Delta$ curves as shown in Fig. 9, which specifies the $K_0$= $P_{45\%}/\Delta_{45\%}$ ($P_{45\%}$=45%$P_u$, and $\Delta_{45\%}$ is the shortening at $P_{45\%}$). The $\Delta_u$ and $DI$ ratio of SSSTCs are used as the index to reflect the ductility of SSSTCs under compression whilst the $DI$ ratio can be determined by following equation;

$$DI = \frac{\Delta_{85\%}}{\Delta_u} \quad (2)$$

where, $\Delta_{85\%}$ is the shortening at 85%$P_u$ of stage IV branches of $P$-$\Delta$ curves in Fig. 9; $\Delta_u$ is the shortening at $P_u$.

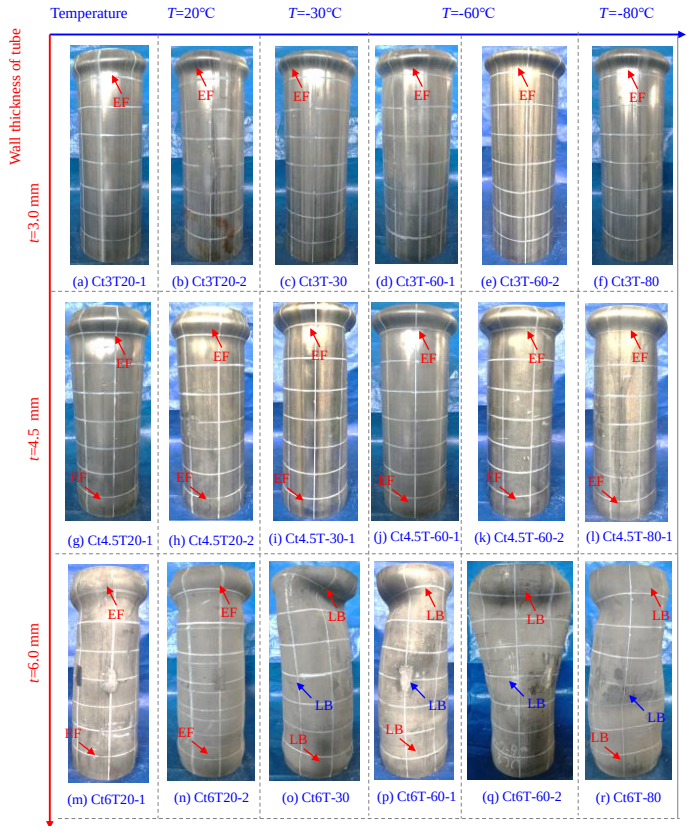


**Fig. 6** Failure modes of SSSTCs under low-temperature compression (EF=elephant foot; LB=Local buckling)

Finally, these determined $P_u$, $\Delta_u$, $K_0$, and $DI$ ratio are tabulated in Table 3.

### *3.4. Discussions*

#### *3.4.1 Effect of the low temperature (T)*

Fig. 11 illustrates the effect of $T$ on low-temperatures compression $P$-$\Delta$ behaviour of SSSTCs. Fig. 12 gives the detailed effects of T on $P_u$, $K_0$, $\Delta_u$, and $DI$ ratio of SSSTCs. They show that the decreasing $T$ significantly affected the low-temperature compression behaviour of SSSTCs in terms of improved ultimate load capacity and initial stiffness, and reduced ductility. As reflected in Fig. 12, with the decreases of T from 20 to -30, -60, and -80°C, the average increments in Pu of SSSTCs with wall thickness of 3 mm are 14%, 16%, and 19%, respectively; the average increments in $P_u$ of SSSTCs with wall thickness of 4.5 mm are 2%, 11%, and 13%, respectively; average increments in $P_u$ of SSSTCs with wall thickness of 6.0 mm are 10%, 15%, and 23%, respectively; the $K_0$ of SSSTCs with 3 (4.5, or 6.0) mm-thick SS tube was averagely increased by 4% (6%, 6%), 5% (15%, 11%), and 8% (25%, 20%), respectively. These findings show that the decreasing $T$ increases both $P_u$ and $K_0$ of SSSTCs due to the enhancements of both modulus and strength of SS materials by decreasing low temperatures (see Fig. 3). Moreover, the test results also pointed out that with the same decreasing magnitude of T, the SSSTCs with 4.5 and 6.0 mm thick SS tube exhibit much larger improvements on $K_0$ than that with 3 mm thick SS tube, but the increments of $P_u$ are very close disregarding the thickness of SS tube. This is due to that the decreasing $T$ improves the $E_s$ and strength of SS tube, which explains these improvements on both $P_u$ and $K_0$. However, the early premature local buckling terminates the fully utilization of these improved ultimate strengths of SS material due to low temperatures, which explains close improvements on $P_u$ of SSSTCs.

However, Fig. 12(c) points out that the decreasing temperature generally decreases the $\Delta_u$ of SSSTCs. It shows that with the decreasing $T$ from 20 to -30, -60, and -80°C, the $\Delta_u$ of SSSTCs with 3 (4.5, or 6.0) mm-thick SS tube was averagely reduced by 17% (19%, 12%), 15% (23%, 17%), and 16% (21%, -9%), respectively. This is because that the decreasing $T$ improves the strength of SS tube, which reduced its buckling strain compared with that at ambient temperature. Meanwhile, the influences of $T$ on $DI$ ratios of SSSTCs with 3 (4.5, or 6.0) mm-thick SS tube exhibit positive/negative improvements, which might be due to the imperfections and eccentricity of SSSTCs.

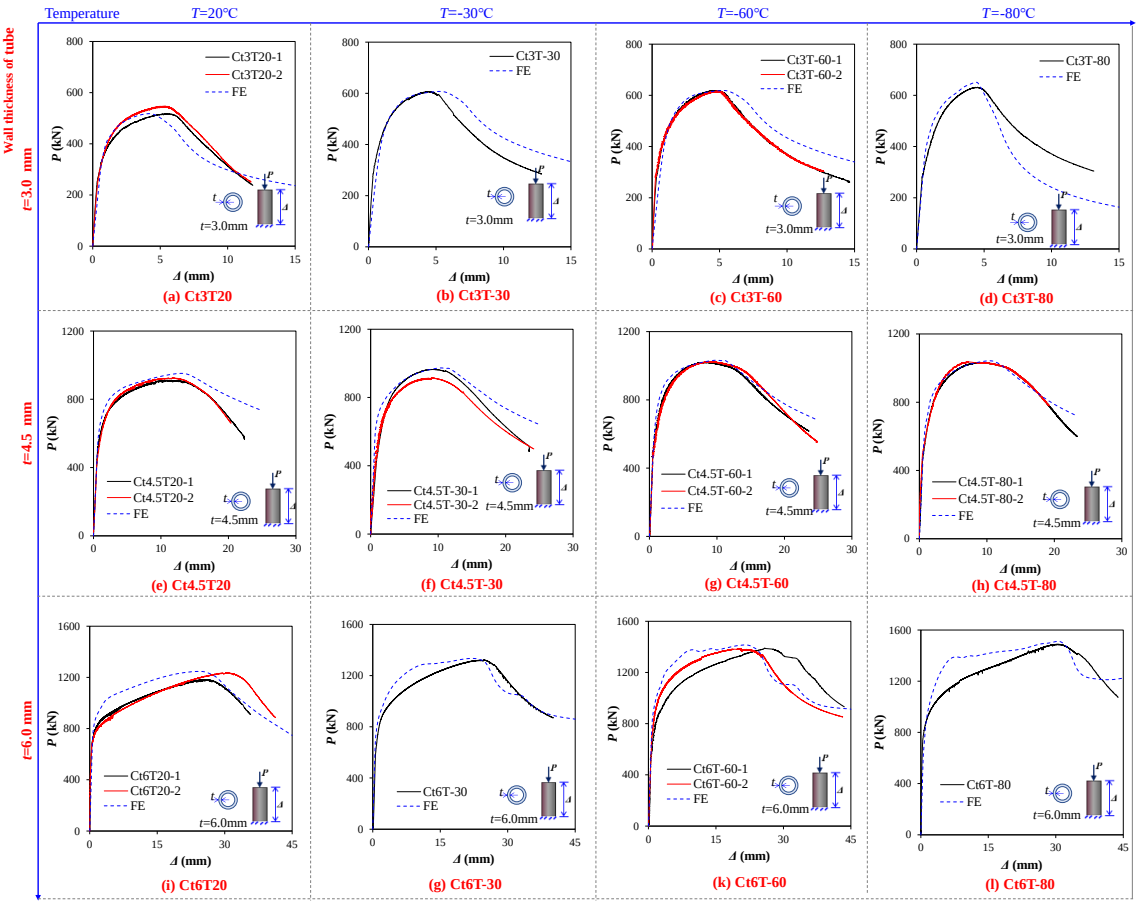


**Fig. 7** Load-shortening curves of SSSTCs under low-temperature compression

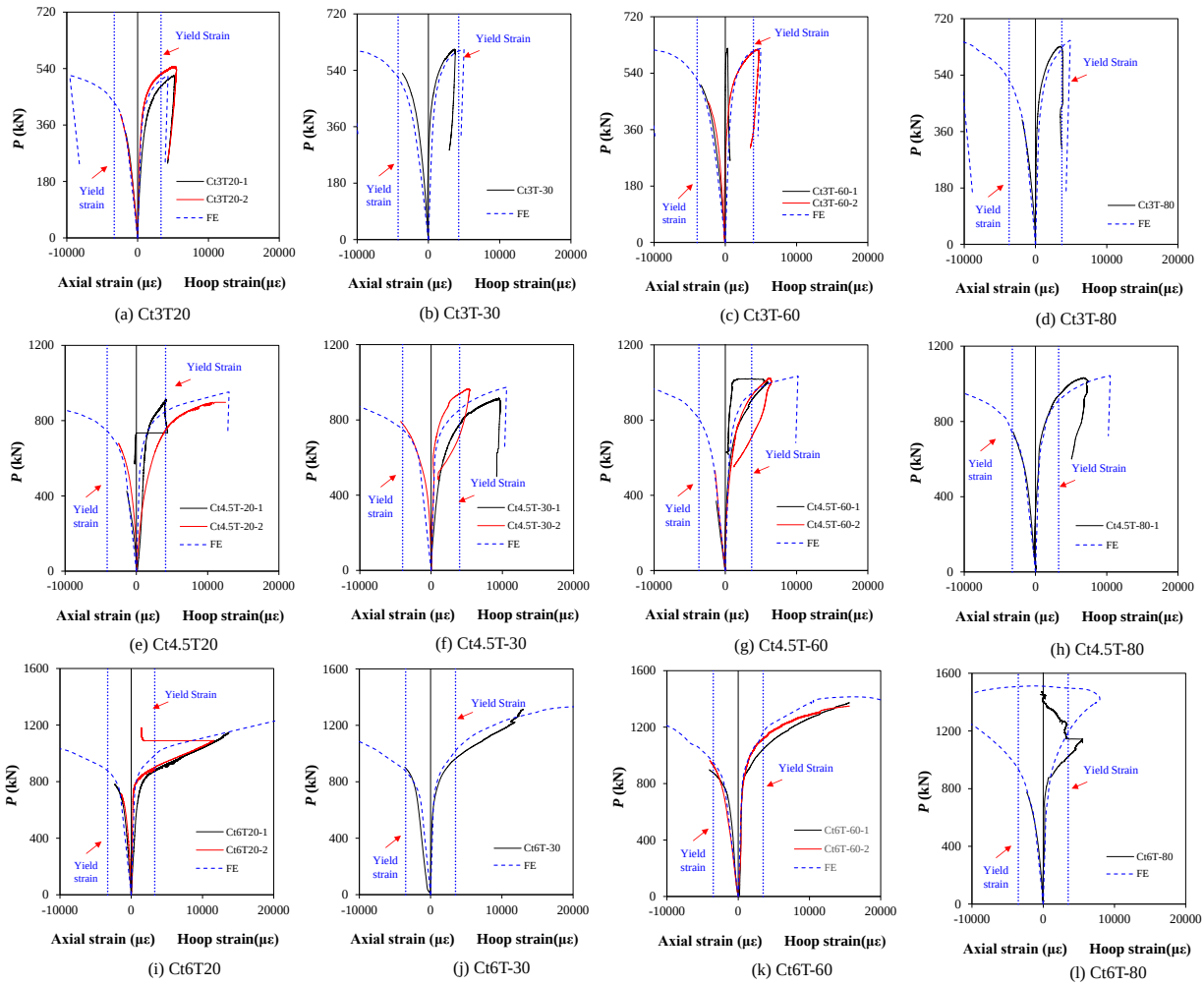


**Fig. 8** Load-strain curves of SSSTCs under low-temperature compression (Negative strain denotes compression strain and positive strain denotes tension)

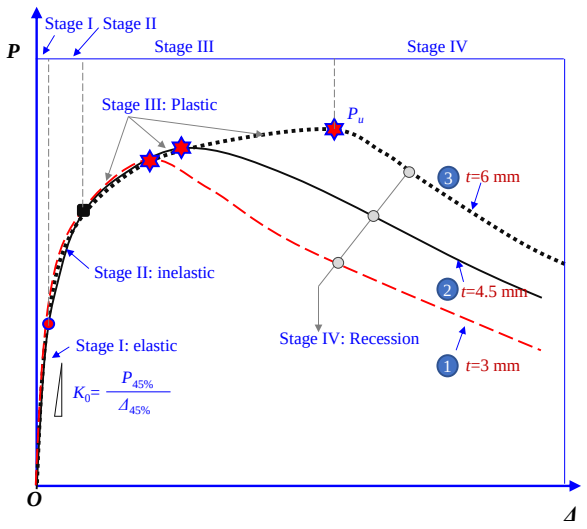


**Fig. 9** Generalized *P-Δ* curves of SSSTCs subjected to low-temperature compression

### *3.4.2 Effect of the thickness of SS tube (t)*

Fig. 13 depicts the effect of $t$ on compression *P-Δ* behaviour of SSSTCs. Fig. 14 shows the detailed effects of $t$ on $P_u$, $K_0$, $\Delta_u$, and *DI* ratio of SSSTCs. They illustrate that the increasing $t$ of SS tube generally improves both strength and ductility of SSSTCs. As $t$ increases from 3.0 to 4.5 and 6 mm, the $P_u$ values of SSSTCs tested at 20°C (or -30, -60, -80°C) were increased by 73% (65%, 55%, 64%) and 127% (125%, 118%, and 136%), respectively; the $K_0$ values of SSSTCs tested at 20°C (or -30, -60, -80°C) were increased by 70% (81%, 74%, 70%) and 140% (147%, 144%, and 129%), respectively; the $\Delta_u$ values of SSSTCs tested at 20°C (or -30, -60, -80°C) were increased by 110% (91%, 106%, 97%) and 418% (402%, 453%, and 574%), respectively. However, the influences of the increasing $t$ on the *DI* ratio exhibit no obvious improvements as reflected in Fig. 14(d). These increased $P_u$ and $K_0$ values are due to the enlarged area of cross section and the reduced $D/t$ ratio of SS tube. Meanwhile, the increased $\Delta_u$ is mainly due to the reduced $D/t$ ratio from 41 to 30 and 22 as the $t$ increases from 3.0 to 4.5 and 6 mm, respectively.

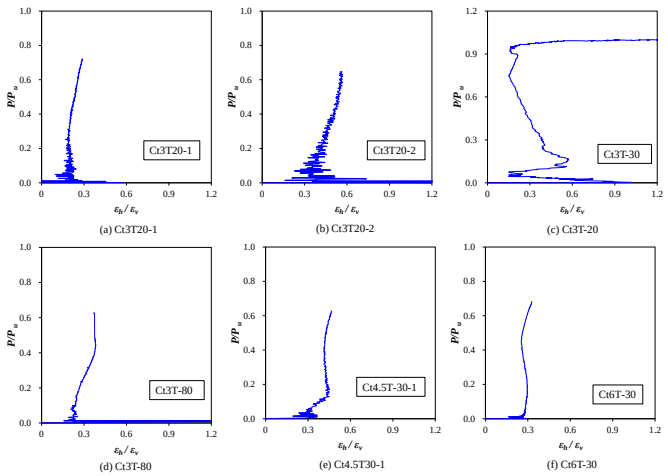


**Fig. 10** Generalized $P/P_u$ versus hoop-to-vertical strain curves of SSSTCs at low temperatures

**Table 3**
Experimental and numerical results of SSSTCs

| No. | Item | $P_u$ (kN) | $P_{u,FE}$ (kN) | $P_u/P_{u,FE}$ | $\Delta_u$ (mm) | $\Delta_{u,FE}$ (mm) | $\Delta_u/\Delta_{u,FE}$ | $K_0$ (kN/mm) | $K_{0,FE}$ (kN/mm) | $K_0/K_{0,FE}$ | *DI* |
|---|---|---|---|---|---|---|---|---|---|---|---|
| 1 | Ct3T20-1 | 517 | 517 | 1.00 | 5.48 | 4.25 | 1.29 | 492 | 514 | 0.96 | 1.36 |
| 2 | Ct3T20-2 | 547 | 517 | 1.06 | 5.33 | 4.25 | 1.25 | 480 | 514 | 0.93 | 1.38 |
| 3 | Ct3T30 | 607 | 607 | 1.00 | 4.48 | 5.28 | 0.85 | 506 | 493 | 1.03 | 1.40 |
| 4 | Ct3T60-1 | 616 | 619 | 1.00 | 4.50 | 5.28 | 0.85 | 514 | 503 | 1.02 | 1.48 |
| 5 | Ct3T60-2 | 619 | 619 | 1.00 | 4.71 | 5.28 | 0.89 | 534 | 503 | 1.06 | 1.42 |
| 6 | Ct3T80 | 631 | 650 | 0.97 | 4.54 | 4.50 | 1.01 | 610 | 610 | 1.00 | 1.27 |
| 7 | Ct4.5T20-1 | 911 | 952 | 0.96 | 10.96 | 12.97 | 0.85 | 836 | 878 | 0.95 | 1.67 |
| 8 | Ct4.5T20-2 | 925 | 952 | 0.97 | 11.78 | 12.97 | 0.91 | 819 | 878 | 0.93 | 1.52 |
| 9 | Ct4.5T30-1 | 916 | 973 | 0.94 | 9.43 | 10.60 | 0.89 | 881 | 883 | 1.00 | 1.63 |
| 10 | Ct4.5T30-2 | 964 | 973 | 0.99 | 9.05 | 10.60 | 0.85 | 878 | 883 | 0.99 | 1.64 |
| 11 | Ct4.5T60-1 | 1020 | 1032 | 0.99 | 8.51 | 10.17 | 0.84 | 978 | 882 | 1.11 | 1.84 |
| 12 | Ct4.5T60-2 | 1023 | 1032 | 0.99 | 9.07 | 10.17 | 0.89 | 922 | 882 | 1.05 | 1.85 |
| 13 | Ct4.5T80-1 | 1032 | 1042 | 0.99 | 8.96 | 10.17 | 0.88 | 1000 | 890 | 1.12 | 1.90 |
| 14 | C4.5T80-2 | 1036 | 1042 | 0.99 | 8.96 | 10.17 | 0.88 | 1069 | 890 | 1.20 | 1.90 |
| 15 | Ct6T20-1 | 1183 | 1246 | 0.95 | 25.84 | 24.20 | 1.07 | 1175 | 1174 | 1.00 | 1.29 |
| 16 | Ct6T20-2 | 1236 | 1246 | 0.99 | 30.19 | 24.20 | 1.25 | 1160 | 1174 | 0.99 | 1.24 |
| 17 | Ct6T30 | 1324 | 1334 | 0.99 | 24.76 | 21.60 | 1.15 | 1235 | 1235 | 1.00 | 1.24 |
| 18 | Ct6T60-1 | 1388 | 1415 | 0.98 | 25.75 | 21.70 | 1.19 | 1300 | 1038 | 1.25 | 1.42 |
| 19 | Ct6T60-2 | 1384 | 1415 | 0.98 | 20.51 | 21.70 | 0.95 | 1288 | 1038 | 1.24 | 1.38 |
| 20 | Ct6T80 | 1489 | 1512 | 0.99 | 30.60 | 30.72 | 1.00 | 1398 | 1174 | 1.19 | 1.27 |
| Mean | | | | 0.99 | | | 0.99 | | | 1.05 | |
| Cov | | | | 0.02 | | | 0.16 | | | 0.10 | |

$P_u$ denotes experimental ultimate compressive resistance of the column; $P_{u,FE}$ denotes ultimate compressive resistance of stainless steel column finite element model; $K_0$ denotes experimental initial stiffness of steel tube; $K_{0,FE}$ denotes initial stiffness of stainless steel stub tubular column finite element model; $\Delta_u$ denotes shortening of the stainless steel tube at $P_u$; $\Delta_{u,FE}$ denotes shortening of the stainless steel tube at $P_{u,FE}$ of stainless steel stub tubular column finite element model; *DI* is the ductility ratio for the stainless steel tube.

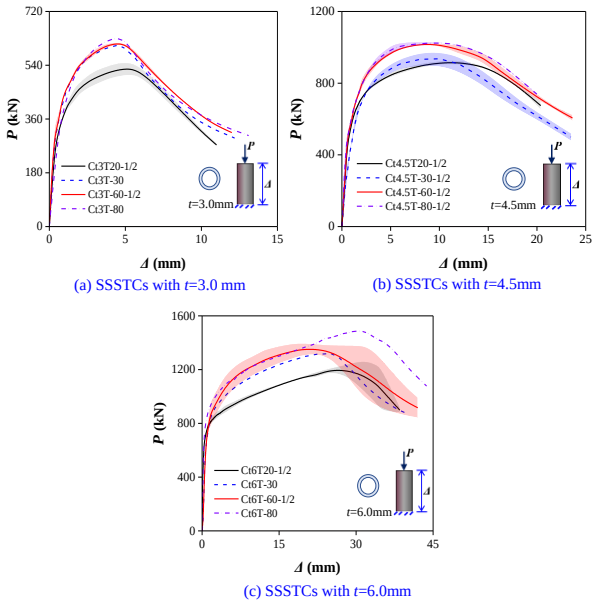


**Fig. 11** Effect of *T* on *P*-$\Delta$ curves of SSSTCs

and 418% (402%, 453%, and 574%), respectively. However, the influ-

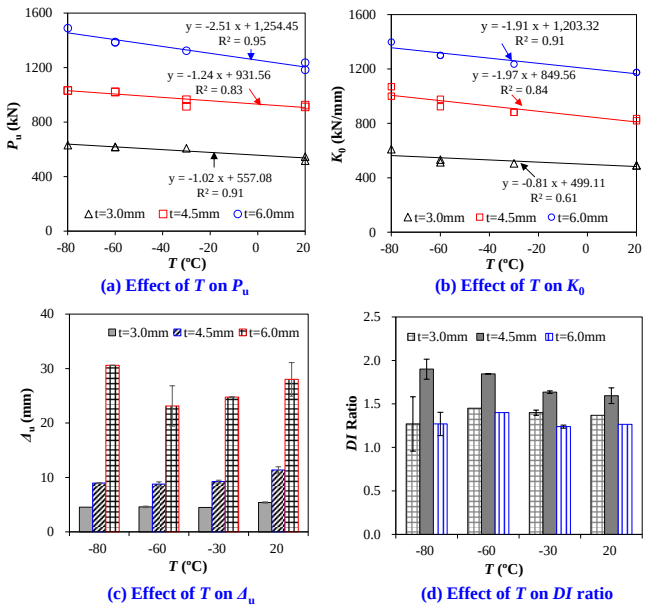


**Fig. 12** Effect of *T* on $P_u$, $K_0$, and *DI* ratio of SSSTCs

### *3.4.3. Effect of the thickness of SS tube (t)*

Fig. 13 depicts the effect of t on compression *P*-$\Delta$ behaviour of SSSTCs. Fig. 14 shows the detailed effects of t on $P_u$, $K_0$, $\Delta_u$, and *DI* ratio of SSSTCs.They illustrate that the increasing *t* of SS tube generally improves both strength and ductility of SSSTCs. As *t* increases from 3.0 to 4.5 and 6 mm, the $P_u$ values of SSSTCs tested at 20°C (or -30, -60, -80°C) were increased by 73% (65%, 55%, 64%) and 127% (125%, 118%, and 136%), respectively; the $K_0$ values of SSSTCs tested at 20°C (or -30, -60, -80°C) were increased by 70% (81%, 74%, 70%) and 140% (147%, 144%, and 129%), respectively; the $\Delta_u$ (91%, 106%, 97%)

-ence of the increasing *t* on the *DI* ratio exhibit no obvious improvements as reflected in Fig. 14(d). These increased $P_u$ and $K_0$ values are due to the enlarged area of cross section and the reduced *D*/*t* ratio of SS tube. Meanwhile, the increased $\Delta_u$ is mainly due to the reduced *D*/*t* ratio from 41 to 30 and 22 as the *t* increases from 3.0 to 4.5 and 6 mm, respectively. (91%, 106%, 97%) and 418% (402%, 453%, and 574%), respectively. However, the influences of the increasing *t* on the *DI* ratio exhibit no obvious improvements as reflected in Fig. 14(d). These increased $P_u$ and $K_0$ values are due to the enlarged area of cross

section and the reduced *D/t* ratio of SS tube. Meanwhile, the increased $\Delta_u$ is mainly due to the reduced *D/t* ratio from 41 to 30 and 22 as the *t* increases from 3.0 to 4.5 and 6 mm, respectively.

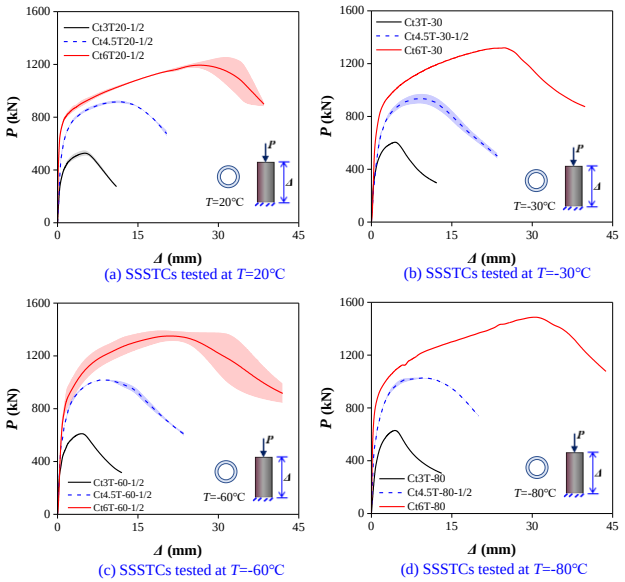


(a) SSSTCs tested at *T*=20°C (b) SSSTCs tested at *T*=-30°C

(c) SSSTCs tested at *T*=-60°C (d) SSSTCs tested at *T*=-80°C

**Fig. 13** Effect of *t* on *P-Δ* curves of SSSTCs

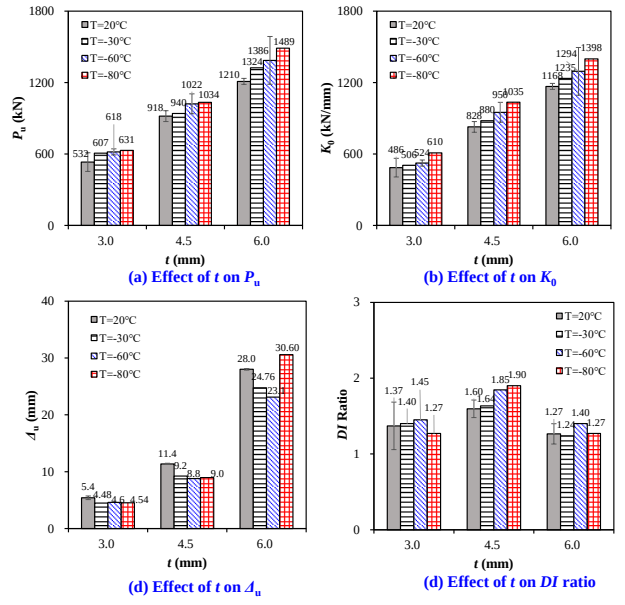


**Fig. 14** Effect of *t* on $P_u$, $K_0$, and *DI* ratio of SSSTCs

## 4. Finite element analysis on low-temperature axial compression behaviour of SSSTCs

### *4.1. General*

The developments of finite element model (FEM) on compression behaviour of SSSTCs at low temperatures adopted the general finite element software.SSSTCs at low temperatures adopted the general finite element software. ABAQUS 6.14 [38]. ABAQUS/CAE and ABAQUS/Standard implicit solver were adopted for the modelling and solution, respectively.

### *4.2. Modelling of SS materials*

The typical elastic-plastic model was adopted for the simulation of SS material. This model with kinematic hardening defined the isotropic yielding surface following the von-Mises rule. In ABAQUS, the elastic and plastic behaviours were required to be defined for the isotropic model. In the elastic behaviour, the elastic modulus and Poisson's ratio of SS at low temperatures were required to be input, which can be obtained from test values as reported in Fig. 3. For the plastic behaviour, the true stress versus inelastic strain at low temperatures were required as the input information. The true stress versus inelastic strain of SS are obtained from those engineering stress-strain curves (see Fig. 3) using the following formulae;

$$\varepsilon_{\text{true}} = \ln(1+\varepsilon_{\text{nom}}) \tag{2}$$

$$\sigma_{\text{ture}}^{\text{pl}} = \ln(1+\sigma_{\text{nom}}) - \frac{\sigma_{\text{true}}}{E_{\text{sT}}} \tag{3}$$

where, $\sigma_{\text{ture}}$ and $\varepsilon^{pl}_{\text{ture}}$ denote the true stress and inelastic true strain, respectively; $\sigma_{\text{nom}}$ denotes engineering stress; $\varepsilon_{\text{nom}}$ denotes engineering strain; $E_{\text{sT}}$ is the modulus at *T*.

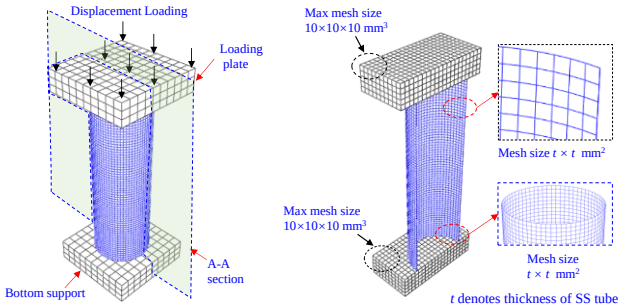


(a) 3D FEM (b) Cross section A-A

**Fig. 15** Finite element model for SSSTCs at low temperatures

### *4.3. Detials of FEM*

Fig. 15 shows the built FEM for SSSTCs at low temperatures, which consists of a bottom support plate, a top loading plate, and a SS tube. 3D eight-node continuum element with reduced integration points (C3D8R) was selected for the modelling of top and bottom plate. Four-node doubly-curved shell element (S4R) with reduced integration point and enhanced hourglass control was selected for SS tube [39], which accounts the finite membrane strains and allows transverse shear deformation [38]. A general mesh size of 10×10×10 mm$^3$ was used for the modelling of both top and bottom plates. Since different mesh sizes of the S4R for the SS tube affect the FE simulation, their influences have also been investigated. Uniform mesh sizes in the vertical and circumferential directions were used in the FEM. Three kinds of mesh size namely type A~C equalling to 0.5*t*×0.5*t*, *t*×*t*, and 2*t*×2*t* mm$^2$, respectively, were used in the FEM as shown in Fig. 16(a)-(c). Fig. 16(d)-(e) illustrates the influences of different mesh sizes on the FEM simulation results. It shows that as the mesh size decreases the FEM simulated *P-Δ* curves tend to converge to the experimental curves, which implies that the FEM with type A and B mesh sizes of S4R elements offer more accurate simulation results than that with type C mesh size. However, the differences of *P-Δ* curves between FEM with type A and B mesh size are quite limited. Thus, considering the balance of FEM simulation accuracy and efficiency, type B mesh size is finally chosen for the FE modelling.

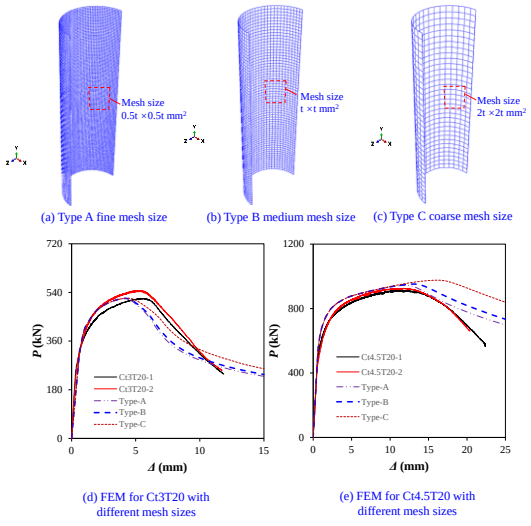


(a) Type A fine mesh size (b) Type B medium mesh size (c) Type C coarse mesh size

(d) FEM for Ct3T20 with different mesh sizes (e) FEM for Ct4.5T20 with different mesh sizes

**Fig. 16** Influences of different mesh size on the FEM simulation results

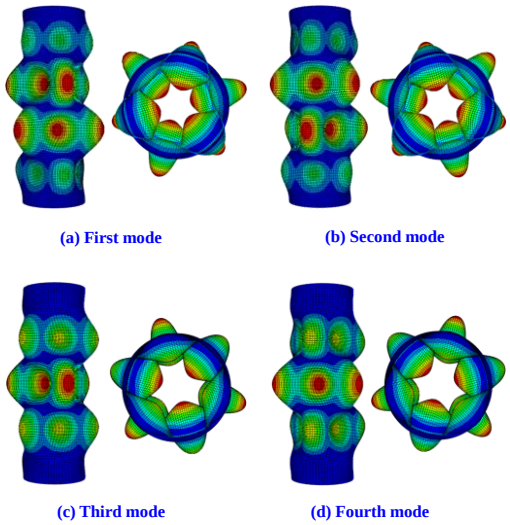


**Fig. 17** First four local buckling mode of SSSTCs

### 4.4. Boundary conditions and geometric imperfections

For each SSSTC, contact algorithm was used to simulate the interactions between two end plates and the SSSTC. "Hard contact", an algorithm defining transfer of pressure between two contacting surfaces and no pressure transferred once those two contacting surfaces are separated, was used to define the interactions perpendicular to the interacting surface between the bottom/loadingend plate and SSSTCs. "Penalty friction" algorithm, adopting a friction coefficient of 0.3, was used for the simulation of interactions along the interacting surfaces between the bottom/loading end plate and SSSTCs. The bottom end plate was restrained from moving whilst the displacement loading was applied on the top plate. A loading eccentricity of $L/2000$ [40] was also used in the FEM to considering its influence on the simulation ($L$ is the height of SSSTC).

Initial geometric imperfection of SSSTCs is mainly produced in the fabrication process of the SS tube, which could affect the developments of local buckling, plastic-initiation load, ultimate load, and post-peak response of SSSTCs at low temperatures. Thus, it requires to consider the geometric imperfections in the FEM. To realize the geometric imperfection of SSSTCs, the local-buckling mode analysis was firstly performed as shown in Fig. 17. Finally, the first buckling mode was chosen, and the magnitude is chosen as the measured magnitude for each specimen as listed in Table 2.

### 4.5. Validations

The FEM simulated $P$-$\Delta$ and load-strain curves of 20 SSSTCs are compared with those experimental curves in Fig. 7 and 8, respectively. They illustrate that the developed FEM predicted reasonably well load versus shortening/strain behaviours of SSSTCs suffering low-temperature compression. Table 3 lists FE predictions of $K_0$, $P_u$, and $\Delta_u$ as well as those corresponding test values, and Fig. 19 provides scatters of the prediction-to-test ratios of $K_0$, $P_u$, and $\Delta_u$. From these comparisons, it reveals that the developed FEM offers average test-to-FE prediction ratios (or Cov) of 0.99 (0.02), 0.99 (0.16), and 1.05 (0.10) for $P_u$, $\Delta_u$ and $K_0$, respectively. These discrepancies of FE simulations are probably due to (1) insufficient estimation on the geometric imperfections, (2) inaccurate estimations on the eccentricity of SSSTCs, (3) scatters in the strengths of SS materials, and (4) un-uniform distribution of low temperatures of SSSTCs during the testing.

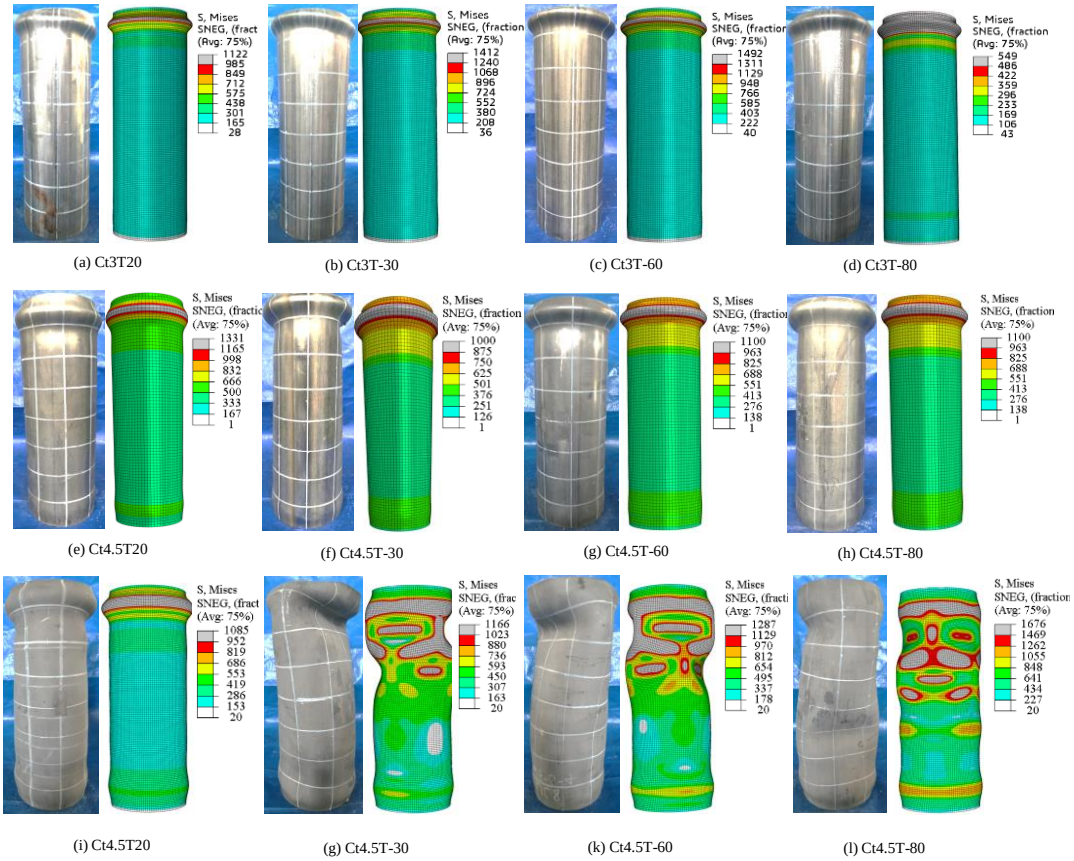


**Fig. 18** Comparisons of failure modes between tests and FEM simulations

### 4.6. Conclusions

This paper firstly studied low-temperature compression behaviors of SSSTCs. Twenty SSSTCs with varying wall thickness were tested at different $T$ levels. Including the tests, FEMs were also developed to simulate the low-temperature compression behaviors of SSSTCs. These experimental and numerical studies draw the following conclusions;

(1) Low temperatures improved the yield and ultimate strength, but reduced the ductility of SS 30408. As the T decreases from 20 to -30, -60, and -80℃, the average increments of yield (or ultimate) strength for SS in different thickness equal to 12% (27%), 25% (49%), and 29% (80%), respectively; meanwhile, the fracture strain of 3 (or 4.5, 6.0) mm-thick SS was reduced by 3% (16%, 6%), 2% (23%, 12%), and 11% (23%, 40%), respectively.

(2) Elephant foot local buckling occurred to most of the SSSTCs under low-

temperature compression. For specimens with $t$=6 mm thick SS tubes tested at -30~-80℃, inelastic inward and outward local buckling occurred.

(3) The low-temperature compression $P$-$\Delta$ curves of SSSTCs consist of four working stages, namely elastic, inelastic, plastic hardening, and recession stage. The length of the third-stage branch of $P$-$\Delta$ curves was determined by the $D/t$ ratio of SS tube that determines the occurrence of local buckling in SS tube.

(4) The decreasing T increased the strength and stiffness of SSSTCs, but reduced their ductility. As the $T$ decreases from 20 to -30, -60, and -80℃, the average increments in Pu of SSSTCs are 9%, 11%, and 18%, respectively; the average increments in $K_0$ of SSSTCs are 6%, 11%, and 15%, respectively; however, the $\Delta_u$ of SSSTCs was averagely reduced by 16%, 18%, and 9%, respectively.

(5) As $t$ increases from 3.0 to 4.5 and 6 mm, the Pu values of SSSTCs tested at 20℃ (or -30, -60, -80℃) were increased by 73% (65%, 55%, 64%) and 127% (125%, 118%, and 136%), respectively; the $K_0$ values of SSSTCs tested at 20℃ (or -30, -60, -80℃) were increased by 70% (81%, 74%, 70%) and 140% (147%, 144%, and 129%), respectively; the $\Delta_u$ values of SSSTCs tested at 20℃ (or -30, -60, -80℃) were increased by 110% (91%, 106%, 97%) and 418% (402%, 453%, and 574%), respectively.

(6) The developed FEM reasonably predicted well compression behaviours of SSSTCs at low temperatures. The developed FEM offered average test-to-FE prediction ratios of 0.99, 0.99, and 1.05 for $P_u$, $\Delta_u$ and $K_0$, respectively.

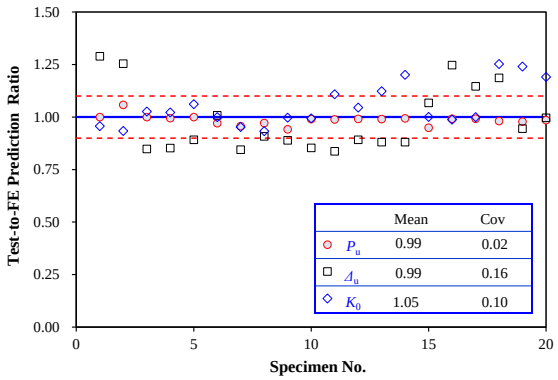


**Fig. 19** Scatters of test-to-FE prediction ratios for $P_u$, $\Delta_u$, and $K_0$

## Nomenclature

$A_s$ Cross-section area of SSSTC
$DI$ Ductility ratio of SSSTC
$D$ Diameter of SSSTC
$E_{sT}$ Elastic modules of SSSTC tube at $T$
$K_0$ Initial stiffness of SSSTC
$K_{0,FE}$ Numerical initial stiffness
$L$ Height of SSSTC
$P_u$ Experimental ultimate compressive resistance
$P_{u,FE}$ Numerical ultimate compressive resistance
$P_{45\%}$ 45%$P_u$
$T$ Low temperature
$f_{yT}$ Yield strength at $T$
$f_{uT}$ Ultimate strength at $T$
$t$ Thickness of SSSTC
$v_0$ Initial imperfection amplitude of SSSTC
$\Delta_u$ Shortening of SSSTC at $P_u$
$\Delta_{u,FE}$ Shortening of SSSTC at $P_{u,FE}$
$\Delta_{45\%}$ Shortening of SSSTC at $P_{45\%}$
$\Delta_{85\%}$ Shortening at 85%$P_u$ after peak load
$\sigma_{ture}$ Ture stress
$\sigma_{nom}$ Engineering stress
$\varepsilon^{pl}_{ture}$ Inelastic true strain
$\varepsilon_{nom}$ Engineering strain
$\varepsilon_{yT}$ Yield strain at $T$
$\varepsilon_{uT}$ Ultimate strain at $T$
$\varepsilon_{FT}$ Fraction strain at $T$

## Acknowledgment

The authors would like to acknowledge the financial supports by Municipal Education Commission of Tianjin Project（No.2019KJ122）, the Central University Fund Project (3122019106), and the Scientific Research Fund of Institute of Engineering Mechanics, China Earthquake Administration (Grant No. 2019EEEVL0504). The authors gratefully express their gratitude for the financial supports.

## References

[1] Gardner L., “The use of stainless steel in structures”, Prog. Struct. Eng. Mater., 7 (2), 45-55, 2005.
[2] Burgan B., “Guidance on the use of stainless steel in construction, Structural applications of stainless steel in building and architecture”, Brussels, 2000.
[3] Buchanana Craig, Zhao Ou, Real Esther, Gardner L., “Cold-formed stainless steel CHS beam-columns-Testing, simulation and design”, Struct. Eng., 213, 110270, 2020.
[4] Gardner L., “Aesthetics, economics and design of stainless steel structures”, Adv. Steel Constr., 4(2), 113-122, 2008.
[5] Anwar U.H., Hani M.T., Nureddin M.A., “Failure of weld joints between carbon steel pipe and 304 stainless steel elbows”, Eng. Fail. Anal., 12, 181-191, 2015.
[6] Fissoloa A., Stelmaszykb J.M., Gourdin C., Bouin P., Pérez G., “Thermal fatigue loading for a type 304-L stainless steel used for pressure water reactor: investigations on the effect of a nearly perfect biaxial loading, and on the cumulative fatigue life”, Procedia Eng., 2, 15951604, 2010.
[7] Guan K., Wang Z.M., Gao M., Li X.Y., Zeng X.Y., “Effects of processing parameters on tensile properties of selective laser melted 304 stainless steel”, Mater. Des., 50, 581-586, 2013.
[8] Xie J., Cui N., Yan J.B., Yu J.H., “Experimental study on prestress losses of post-tensioned concrete members at ultra-low temperatures”. Struct. Concrete., 20, 1828-1841, 2019.
[9] Rasmussen K.J.R., “Full range stress–strain curves for stainless steel alloys”, J. Constr. Steel Res., 59, 47-61, 2003.
[10] Ashraf M., Gardner L., Nethercot D.A., “Strength enhancement of the corner regions of stainless steel cross-sections”, J. Constr. Steel Res., 61 (1), 37-52, 2005.
[11] Gardner L., Nethercot D.A., “Experiments on stainless steel hollow sections-Part 1: Material and cross-sectional behaviour”, J. Constr. Steel Res., 60 (9), 1291-1318, 2004.
[12] Quach W. M., Teng J. G., Chung K. F., “Three-Stage Full-Range Stress-Strain Model for Stainless Steels”, J. Struct. Eng., 134 (9), 1518-1527, 2008.
[13] Gardner L., Yun X., “Description of stress-strain curves for cold-formed steels”, Constr. Build. Mater., 189, 527-538, 2018.
[14] Sakumoto Y., Nakazato T., Matsuzaki A., “High-temperature properties of stainless steel for building structures”, J. Struct. Eng., 122 (4), 399-406, 1996.
[15] Chen J., Young B., “Stress–strain curves for stainless steel at elevated temperatures”, Eng. Struct., 28 (2), 229-239, 2006.
[16] Gardner L., Insausti A., Ng K.T., Ashraf M., “Elevated temperature material properties of stainless steel alloys”, J. Constr. Steel Res., 66 (5), 634-647, 2019.
[17] Wang X., Zhang J., DU Y., “High temperature mechanical properties of 00Cr17Ni14Mo2 stainless steel”, J. Build. Mater., 18 (5), 767-772, 2015.
[18] Liang Y., Manninen T., Zhao O., Walport F., Gardner L., “Elevated temperature material properties of a new high-chromium austenitic stainless steel”, J. Constr. Steel Res., 152, 261-273, 2019.
[19] Fan S.G., Jia L.L., Lyu X., Sun W.J., Chen M.H., Zheng J.C., “Experimental investigation of austenitic stainless steel material at elevated temperatures”, Constr. Build. Mater., 155, 267-285, 2017.
[20] Fan S.G., Ding R.M., Zheng J.C., Xie F.Z., Wu Q.X., “Refined Model for the Stress-Strain Curve of Austenitic Stainless-Steel Materials at Elevated Temperatures”, J. Mater. Civ. Eng., 32 (4), 04020032, 2020.
[21] Rasmussen KJR, “Recent research on stainless steel tubular structures”, J. Constr. Steel Res., 54 (1), 75-88, 2000.
[22] Young B., Hartono W., “Compression tests of stainless steel tubular members”, J. Struct. Eng.,128, 754-761, 2002.
[23] Lui W.M., Ashraf M., Young B., “Tests of cold-formed duplex stainless steel SHS beam-columns”, Eng. Struct., 74, 111-121, 2014.
[24] Huang Y., Young B., “Experimental investigation of cold-formed lean duplex stainless steel beam-columns”, Thin-Walled Struct., 76, 105-117, 2014.
[25] Arrayago I., Real E., Mirambell E., “Experimental study on ferritic stainless steel RHS and SHS beam-columns”, Thin-Walled Struct., 100, 93-104, 2016.
[26] Bu Y., Gardner L., “Laser-welded stainless steel I-section beam-columns: Testing, simulation and design”, Eng. Struct., 179, 23-36, 2019.
[27] Greiner R., Kettler M., “Interaction of bending and axial compression of stainless steel members”, J. Constr. Steel Res., 64 (11), 1217-1224, 2008.
[28] Zhao O., Gardner L., Young B., “Buckling of ferritic stainless steel members under combined axial compression and bending”, J. Constr. Steel Res., 117, 35–48, 2016.
[29] Cai Y., Young B., “Structural behaviour of cold-formed stainless steel bolted connections at post-fire condition”, J. Constr. Steel Res., 152, 213-321, 2019.
[30] Salih E.L., Gardner L., Nethercot D.A., “Numerical investigation of net section failure in stainless steel bolted connections”, J. Constr. Steel Res., 66 (12), 1455-1466, 2010.
[31] Elflah M., Theofanous M., Dirar S., Yuan H., “Behaviour of stainless steel beam-to-column joints — Part 1: experimental investigation”, J. Constr. Steel Res., 152, 183-193, 2019.
[32] GB/T 13239-2006, Metallic Materials – Tensile Testing at Low Temperature, China Standards Press, Beijing, 2006.
[33] Zhang R., Gardner L., Buchanan C., Matilainen VP., Piili H., Salminen A., “Testing and analysis of additively manufactured stainless steel CHS in compression”, Thin-Walled Struct., 159, 107270, 2021.
[34] Buchanan C., Matilainen V.P., Salminen A., Gardner L., “Structural performance of additive manufactured metallic material and cross-sections”, J. Constr. Steel Res., 136, 35-48, 2017.
[35] Yan J.B., Dong X., Zhu J., “Behaviours of stub steel tubular columns subjected to axial compression at low temperatures”, Constr. Build. Mater., 228, 116788, 2019.
[36] Guler S., Lale E., Aydogan M., “Behaviour of SFRC filled steel tube columns under axial load”, Adv. Steel Constr., 9(1), 14-25, 2013.
[37] Yan J.B., Luo Y.L., Su L., Lin X., Luo Y.B., Zhang L.X., “Low-temperature compression behaviour of square CFST columns using Q960 ultra-high strength steel”, Constr. Build. Mater., 183, 106727, 2021.
[38] Hibbitt H.D., Karlson B.I., Sorensen, EP (2009) ABAQUS/standard user’s manual, Version 6.14, 2014.
[39] Fan S.G., Li S., He B. B., Jia, L. L., Ding R. M., “Fire resistance performance analysis of high-strength steel Q550 columns under axial compression”, Adv. Steel Constr., 15(2), 185-191, 2019.
[40] Gardner L., Nethercot D.A., “Numerical modeling of stainless steel structural components-A consistent approach”, J. Struct. Eng., 130 (10), 1586-1601, 2004.

**Advanced Steel Construction** – Vol. 18 No. 3 (2022) 679–686
**DOI:**10.18057/IJASC.2022.18.3.5


# CHARACTERISATION OF THE BEHAVIOUR OF BEAM-TO-COLUMN STEEL JOINTS UP TO FAILURE

Tudor Golea *, Jean-Pierre Jaspart and Jean-François Demonceau

*Urban and Environmental Engineering, University of Liège, Liège, Belgium*
** (Corresponding author: E-mail: tudor.golea@uliege.be)*

**ABSTRACT**

The design of steel joints is currently dealt with in Eurocode 3 through the well-known "component method". In particular, Part 1-8 of this standard provides guidance on how to apply the method to a wide range of joint configurations allowing to assess the latter's initial rotational stiffness and resistance. Nonetheless, whenever a global structural plastic analysis is contemplated, provisions of Eurocode 3 are insufficient since no clear guidance on how to determine the ultimate resistance and the ultimate rotation capacity of joints is provided. In this paper, the full-range behaviour of beam-to-column steel joints is investigated using experimental, analytical, and numerical methods. A new analytical approach based on the component method is proposed and validated against five physical experiments. Through additional analytical expressions for the characterisation of basic components of steel joints, the proposed approach extends the applicability of the component method such that strain-hardening and ductility of components are accounted for. The results show a good agreement between the analytical prediction and the experimental results and also highlight specific limitations of the classical component method. Three-dimensional finite element (FE) models are also employed to simulate the behaviour of the tested beam-to-column joints. The results prove the accuracy of numerical models to simulate the non-linear response of steel joints emphasizing, however, the importance of proper modelling assumptions.

**ARTICLE HISTORY**

Received: 7 June 2021
Revised: 24 January 2022
Accepted: 31 January 2022

**KEYWORDS**

Steel joints;
Experimental tests;
Component method;
Finite element analysis;
Steel structures



## 1. Introduction

In steel framed structures, beam-to-column joints were conventionally assumed to behave either as ideally pinned or fully rigid. This simplifying assumption was driven by the difficulty to characterise the behaviour of such joints and was widely accepted as a rule of good practice meant to ease the structural analysis and the design processes. Although its practical conveniences are undeniable, this simplification disregards the fact that most of the joints can be classified as semi-rigid, exhibiting in reality a finite stiffness. To overcome this limitation, considerable research efforts have been invested. The use of complex non-linear FE analyses may be seen as a solution for such purposes but, most of the times, it implies a tremendous computational effort which is not compatible with the daily practice in design offices. Accordingly, most of the research efforts have been dedicated to the derivation of practical tools and procedures to predict the behaviour of semi-rigid joints. In particular, a simple approach based on mechanical analytical models has been proposed, known nowadays as the "component method" [1]–[3].

Validated throughout extensive experimental campaigns, the component method proved to be a robust tool allowing to predict the strength and the initial stiffness of steel joints. In this regard, it has been implemented in Eurocode 3 [4] as a practical solution to be used by designers in global structural analyses of semi-rigid frames where the rotational behaviour of joints becomes an additional variable. Part 1-8 of this standard deals with the application of the component method, providing a comprehensive set of design rules that enables the designer to derive the moment-rotation curve $M_j$ - $\phi$ for a variety of joint configurations. In general terms, the joint is considered as a set of individual basic components which, based on their mechanical properties, may have significant or negligible contributions to the overall behaviour of the joint. The contribution of each basic component is accounted for through an assembly procedure that assists the practitioner in the evaluation of the initial rotational stiffness $S_{j,ini}$ and the bending plastic design resistance $M_{j,Rd}$ of the joint. These two parameters are used further to generate a simplified $M_j$ - $\phi$ curve which is rather an idealisation of the actual one since there is no ultimate bending resistance $M_{Ru}$ or strain-hardening (post-plastic) stiffness $S_{j,st}$ taken into account. Therefore, this simplification comes at the expense of the ability to predict the actual response of the joints up to their failure while this ability of prediction is of great interest when considering the robustness of structure which is part of the normative requirements imposed by modern codes and standards [5]–[7].

Hereinafter, a general approach proposed by Jaspart et al. [8] is used to estimate the full $M_j$ - $\phi$ curve of beam-to-column steel joints. This approach can be seen as an extension to the component method integrated in the current version of Eurocode 3. The analytical expressions provided in the European normative document are used to characterise the behaviour of the joints up to their plastic bending capacity. For the post-plastic behaviour, analytical expressions proposed after studies on numerous test results [1] are employed in the evaluation of the strain-hardening stiffness of the basic joint components. Procedures for the evaluation of the post-plastic stiffness $S_{j,st}$, the ultimate bending resistance $M_{Ru}$ and the ultimate rotation capacity $\phi_u$ are introduced. Based on these key parameters, the $M_j$ - $\phi$ curve is estimated up to the failure of the joints, thus making possible to predict their full non-linear behaviour.

The experimental campaign conducted at the University of Liège within the research project RobustImpact [9] serves as a reference database for this paper. Five physical specimens of double-sided beam-to-column joints were tested under quasi-static loading conditions. The test specimens consisted of two I-section beams connected to an H- or I-section column. The fastening between these members was ensured through end-plates and high-strength bolts for three of the specimens, whilst for the other two, the beams were welded directly to the column. Throughout the tests, failure occurred in distinct basic components.

## 2. Experimental programme

### *2.1. Test setup*

The experimental programme, including the test setup, was thoroughly presented by Demonceau et al. [10]. A schematic view of the experimental setup is illustrated in Fig. 1; a detailed presentation of the specific instrumentation used to acquire the experimental data is to be found in [11]. The double-sided beam-to-column joints were subjected to a monotonic load applied at the top of the column. A hydraulic jack was used to apply the load up to the failure of the joints. Several loading-unloading cycles were performed in order to identify the actual stiffness of the specimens. The displacements and deformations were tracked using displacement transducers and extensometers placed along the beams and at the level of the load application point. To simulate the support conditions corresponding to a simply supported element, a specific system that accommodates horizontal displacements and rotations was designed.

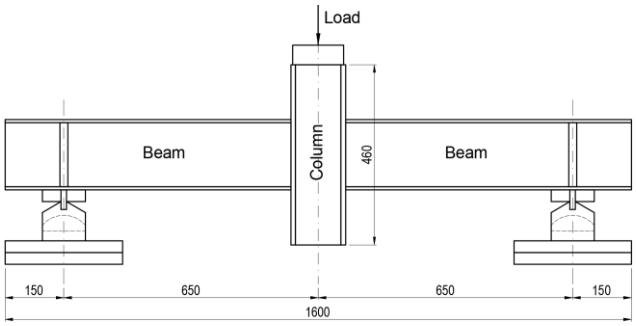


**Fig. 1** Elevation view of the test setup

### 2.2. Test specimens

The global dimensions of the specimens were imposed by the limitations of the available laboratory setup. The length of the beams was chosen such that the specimen does not exceed a length of 1.6 m as depicted in Fig. 1. The specimens consisted of two IPE 180 sections that served as beams and a HEB 140 or an IPE 180 section representing the column. Three out of five specimens were designed and manufactured having bolted end-plate connections, whilst the other two were manufactured as joints with welded connections. All sections and end-plates were of steel grade S355. A total of eight M16 bolts of grade 10.9 were used for each joint with bolted end-plate connections. To ensure an adequate diffusion of transverse compression and tension forces transferred from the beams to the column, the length of the column was set at the value of 460 mm.

A summary of the main characteristics of the experimental specimens is reported in Table 1. A detailed view of their general layout is provided in Fig. 2. The first specimen named RJ (Real Joint) was designed as a reference joint configuration. From this actual joint configuration, four others were derived by modifying the geometrical properties or by providing additional stiffening elements with the objective of investigating the behaviour of several basic components from the Real Joint in isolation; accordingly, these adjustments were performed in such a way that the failure of only one basic component of the joint would occur. The specimens are identified through a specific label that corresponds to the failing basic component of the considered specimen: EPB for End-Plate in Bending, CFB for Column Flange in Bending, BFC for Beam Flange in Compression and CWC for Column Web in Compression.

**Table 1**
Characteristics of specimens

| Specimen | Connection type | Column section | Beams section | End-plate |
|---|---|---|---|---|
| RJ | Bolted end-plate | HEB 140 | IPE 180 | 120x210x15 |
| EPB | | HEB 140 | IPE 180 | 120x210x8 |
| CFB | | HEB 140 | IPE 180 | 120x220x18 |
| BFC | Welded | HEB 140 | IPE 180 | - |
| CWC | | IPE 180 | IPE 180 | - |

### 2.3. Material tests

Quasi-static uniaxial tension tests were performed on coupons extracted from the end-plates and from the flanges/web of the IPE and HEB sections. A detailed report on the coupon tests and the stress-strain curves ($\sigma_{eng}$ - $\varepsilon_{eng}$) of the steel material may be found in [11]. The main actual mechanical properties of the materials acquired from the tests are summarised in Table 2.

**Table 2**
Mechanical properties of materials

| Element | Coupon | $f_y$ [MPa] | $\varepsilon_y$ [%] | $f_u$ [MPa] End | $\varepsilon_u$ [%] |
|---|---|---|---|---|---|
| IPE 180 | Flange | 413.3 | 1.97 | 537.7 | 21 |
| | Web | 435.5 | 2.07 | 545.2 | 25 |
| HEB 140 | Flange | 385.3 | 1.83 | 539.6 | 20.6 |
| | Web | 433.7 | 2.06 | 544 | 22 |
| End-plates | 8 mm | 409.3 | 1.95 | 594.8 | 18 |
| | 15 mm | 416.6 | 1.98 | 588.7 | 23 |
| | 18 mm | 384.5 | 1.83 | 556.2 | 22 |

The mechanical properties of the bolts material were not evaluated experimentally. However, tests on coupons from similar bolts of grade 10.9 were performed within the same research project. The values reported for the yield strength $f_{yb}$=1020 MPa and the ultimate strength $f_{ub}$=1080 MPa are taken as reference parameters for the computations carried out in the present paper.

## 3. Component method

### 3.1. Principles of the method

The component method emerged as a solution to the demand of practitioners seeking the influence of the behaviour of structural joints on the response of building frames. The method uses a hybrid analytical-mechanical approach to derive the $M_j$ - $\phi$ curve of steel or steel-concrete composite joints.

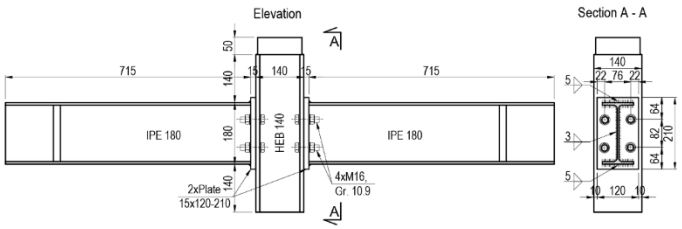


(a) RJ specimen

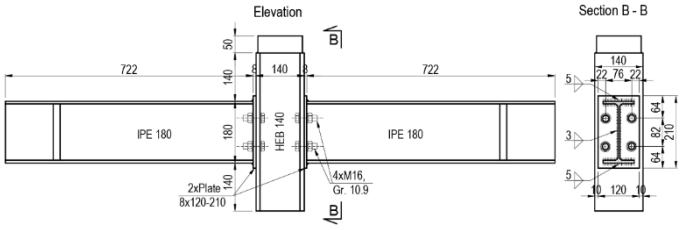


(b) EPB specimen

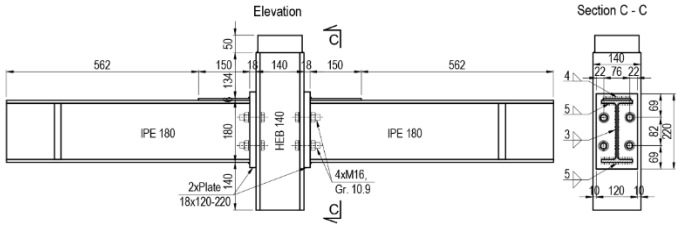


(c) CFB specimen

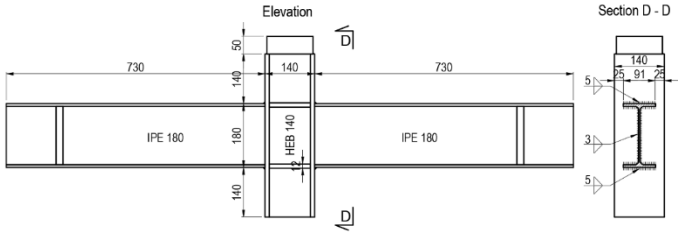


(d) BFC specimen

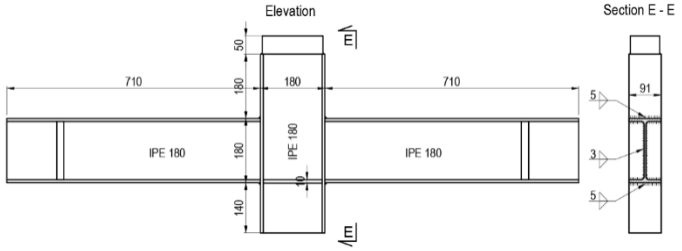


(d) CWC specimen

**Fig. 2** Detailed views of the specimens

This is achieved by considering the joint as a set of individual basic components. Each of these components represents a part of the joint and is modelled as an extensional spring with mechanical properties (strength and stiffness) depending on the loading type. The full model of a joint comprises all these springs combined with infinitely rigid pin-ended elements. Some of the components may have contributions for both resistance and stiffness of the joint; these are identified as elastic-plastic components, whereas the ones contributing only to the resistance are labelled as rigid-plastic components. For the sake of exemplification, Fig. 3 illustrates the mechanical model of the RJ specimen investigated in this paper.

The components contributing to the overall response of the joints are associated with three distinctive zones - compression, tension, and shear zones. In this study, the investigated joints are symmetrically loaded, hence there is no

shear action in the column web panel; so, the shear zone is disregarded in this particular case. Consequently, the relevant components are identified for the two zones as follows:

- compression zone: column web in compression (cwc) and beam flange in compression (bfc);
- tension zone: column web in tension (cwt), column flange in bending (cfb), bolts in tension (bt), end-plate in bending (epb) and beam web in tension (bwt).

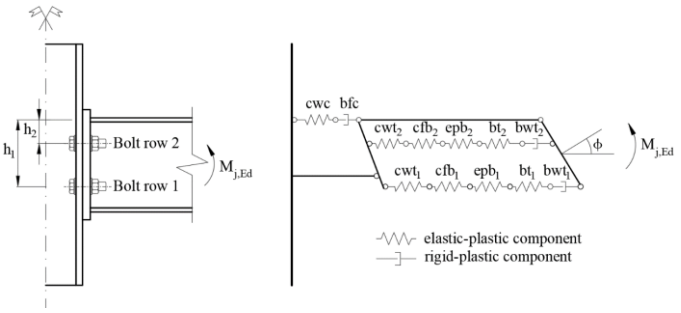


**Fig. 3** Mechanical model of the RJ specimen

Relying on the mechanical properties of these basic components, the initial stiffness $S_{j,ini}$ and the plastic moment resistance $M_{Rpl}$ of the joint are estimated through an assembly procedure. To accomplish this, a comprehensive three-step procedure is envisaged [2]:

1. identification of the active components in the investigated joint;
2. evaluation of mechanical properties in terms of stiffness and/or strength for each active component;
3. assembly of all the components and evaluation of the stiffness and/or resistance characteristics of the whole joint.

Eurocode 3 Part 1-8 provides rules and analytical expressions to characterise a variety of components in terms of stiffness and strength. The information available on the characterisation of components and on assembly procedures allows to cover a wide range of joint configurations and, for common design practice, it is generally sufficient to satisfy the needs of practitioners.

### *3.2. Application of the component method*

#### *3.2.1. Characterisation of active components*

The level of refinement of the component method is highly dependent on the accuracy of the components characterisation. In this regard, the stiffness, the strength, and the deformation capacity of components may be derived using various techniques with different levels of accuracy and complexity such as experimental testing, numerical simulations, and analytical methods.

Herein, the analytical expressions provided in Eurocode 3 Part 1-8 are used to derive the mechanical properties of the basic components. Prior to their actual characterisation, the active components of the joints are identified as suggested by the first step of the component method. Table 3 lists the basic components activated in the five joints investigated within this paper. The contribution of each active component to the overall resistance or stiffness of the joint is marked correspondingly.

All the active components being identified, their characterisation in terms of resistance, stiffness, and deformation capacity is contemplated. This implies the definition of force-deformation *F-Δ* curves for the extensional springs simulating the behaviour of the actual components. The classic approach proposed in Eurocode 3 enables the user to define an elastic-perfectly plastic *F-Δ* curve for each active component as depicted in Fig 4 (a). Therefore, the components are considered to deform elastically up to their plastic resistance and, if no brittle failures nor instability phenomena occur, they may deform plastically to the extent of their deformation capacity.

The assumption of considering an elastic-perfectly plastic model leads to a conservative prediction of the overall behaviour of the joints. Potential strain-hardening effects and membrane effects are simply disregarded, defining thus the post-plastic behaviour as a yield plateau without a well-specified limit. To overcome this limitation and to enhance the accuracy of the analytical prediction, emphasis has shifted towards the characterisation of the post-plastic response of basic joint components. Based on studies of numerous test results, Jaspart et al. [8] proposed analytical expressions for the evaluation of the strain-hardening stiffness of various basic components. Consequently, the full non-linear response of components may be defined through simplified bi-linear *F-Δ* curves describing the elastic and the post-plastic behaviour as shown in Fig. 4 (b) Therefore, the ductility of components, roughly and only partially addressed in the present version of Eurocode 3, becomes a quantifiable characteristic.

**Table 3**
Basic active components in the investigated joints

| Component | RJ, EPB and CFB | | BFC and CWC | |
|---|---|---|---|---|
| | Resistance | Stiffness | Resistance | Stiffness |
| Column web in compression | ✓ | ✓ | ✓ | ✓ |
| Column web in tension | ✓ | ✓ | | |
| Column flange in bending | ✓ | ✓ | | |
| End-plate in bending | ✓ | ✓ | | |
| Beam flange in compression | ✓ | * | ✓ | * |
| Beam web in tension | ✓ | * | | |
| Bolts in tension | ** | ✓ | | |

* The contribution of the component is accounted for in the deformation of the beam;
** The contribution of the component is accounted for in the equivalent T-stub model.

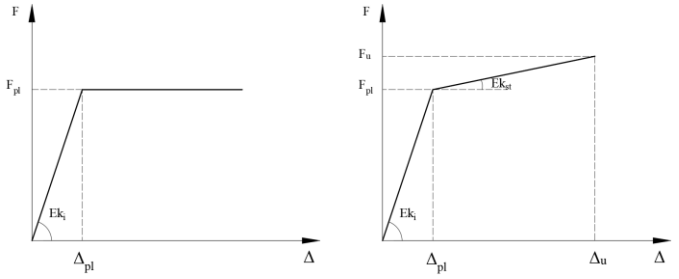


(a) *F-Δ* curve according to Eurocode 3 (b) *F-Δ* curve proposed by Jaspart et al [8]

**Fig. 4** Characterisation of components through force-deformation curves

Analytical expressions proposed in Eurocode 3 Part 1-8 are used to estimate the plastic resistance $F_{Rpl}$ and the initial stiffness coefficients $k_i$ of basic components. A brief survey of these is provided in Table 4 covering all the components of interest within the scope of this paper.

**Table 4**
Basic active components in the investigated joints

| Component | Plastic resistance | Stiffness coefficient |
|---|---|---|
| Column web in compression | $F_{c,wc,Rd} = \frac{\omega k_{wc} b_{eff,c,wc} t_{wc} f_{y,wc}}{\gamma_{M0}}$ but $F_{c,wc,Rd} \le \frac{\omega k_{wc} \rho b_{eff,c,wc} t_{wc} f_{y,wc}}{\gamma_{M1}}$ | $k_2 = \frac{0.7 b_{eff,c,wc} t_{wc}}{d_c}$ |
| Column web in tension | $F_{t,wc,Rd} = \frac{\omega b_{eff,t,wc} t_{wc} f_{y,wc}}{\gamma_{M0}}$ | $k_3 = \frac{0.7 b_{eff,t,wc} t_{wc}}{d_c}$ |
| Column flange in bending | * Equivalent T-stub model | $k_4 = \frac{0.9 l_{eff} t_{fc}^3}{m^3}$ |
| End-plate in bending | * Equivalent T-stub model | $k_5 = \frac{0.9 l_{eff} t_p^3}{m^3}$ |
| Beam flange in compression | $F_{c,fb,Rd} = \frac{M_{c,Rd}}{h - t_{fb}}$ | $k_7 = \infty$ |
| Beam web in tension | $F_{t,wb,Rd} = \frac{b_{eff,t,wb} t_{wb} f_{y,wb}}{\gamma_{M0}}$ | $k_8 = \infty$ |
| Bolts in tension | $F_{t,Rd} = \frac{0.9 f_{ub} A_s}{\gamma_{Mb}}$ | $k_{10} = \frac{1.6 A_s}{L_b}$ |

* The reader is asked to refer to the T-stub model addressed in EN 1993-1-8

The post-plastic behaviour of the active components is evaluated as proposed in [8]. The ultimate resistance is simply estimated by substituting the yield strength of steel $f_y$ by the ultimate strength $f_u$ in the formulae listed in Table 4. The strain-hardening stiffness coefficients $k_{st}$ are estimated on the basis of $k_i$ as follows in Eq. (1). This expression is valid only for such components as the column web in compression (cwc), column web in tension (cwt), column flange in bending (cfb), and the end-plate in bending (epb), i.e. for components which can exhibit a ductile behaviour.

$$k_{st} = \frac{E_{st}}{E} k_i \tag{1}$$

In Eq. (1), $k_i$ is the initial stiffness coefficient of the component, $E$ is the modulus of elasticity of steel and $E_{st}$ is the strain-hardening modulus in the steel $\sigma$-$\varepsilon$ curve. As proposed in [1], the ratio $E_{st}/E$ is taken as 1/50 for all components contributing to the strain-hardening stiffness.

*3.2.2. Moment resistance*

Eurocode 3 suggests an assembly procedure for the estimation of the design moment resistance of joints. In general lines, the assembly procedure allows to derive the mechanical properties of the whole joint from those of the active basic components. This implies the fulfilment of the static theorem by determining the distribution of internal forces so that the equilibrium with the external forces acting on the joint is satisfied. Additionally, this internal distribution of forces has to account for the behaviour of the components under specific loading, ensuring the displacement compatibility (kinematic theorem) with respect to the stiffness, the resistance, and the ductility of components.

The plastic bending resistance of a joint $M_{Rpl}$ is associated to the plastic resistance $F_{Rpl}$ of the weakest individual joint component of each activated row. If there is no axial force to be transferred to the joint from the connected member, the plastic flexural resistance is estimated based on the following equilibrium equation:

$$M_{Rpl} = \sum_r h_r F_{tr,Rpl} \tag{2}$$

where $F_{tr,Rpl}$ is the plastic resistance of the row $r$, $h_r$ is the distance from the row $r$ to the centre of compression, and $r$ is the row number. For joints with bolted connections, $r$ stands for the number of bolt rows in tension, whereas for welded connections, only one row in tension can be identified - located at the level of the column web in tension component.

The plastic resistance of a bolt row is taken as the minimum of the resistances of components active at the level of row $r$ as follows:

$$F_{tr,Rpl} = \min(F_{cwt}, F_{cfb}, F_{epb}, F_{bwt}, F_{bt}) \tag{3}$$

The full procedure is exemplified in [12] for the RJ specimen investigated in this paper. Another worked example of a beam-to-column joint with a bolted end-plate connection can be found in [2].

A reasonable estimation of the ultimate moment resistance of the joints $M_{Ru}$ can be achieved by performing the same assembly procedure as described for $M_{Rpl}$ using the ultimate resistances of components $F_{Ru}$ instead of $F_{Rpl}$. It is worth noting that special attention has to be paid to the risk of instability in the components subjected to compression such as the column web in compression and the beam flange in compression.

*3.2.3. Initial stiffness*

The initial stiffness $S_{j,ini}$ characterises the rotational behaviour of a joint up to the limit of the elastic region. As long as the elastic resistance is not exceeded, the rotational stiffness depends solely on the initial rigidity of the joint basic components and is derived from the latter's elastic stiffnesses. The estimation of $S_{j,ini}$ is exemplified in Fig. 5 for the mechanical model of the RJ joint previously illustrated in Fig. 3.

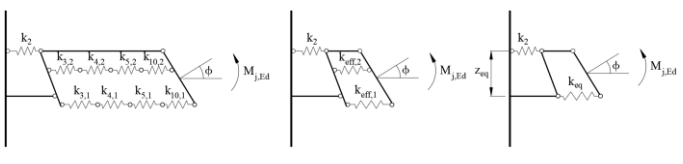


**Fig. 5** Spring model for the evaluation of $S_{j,ini}$ for end-plated joints (RJ, EPB and CFB)

For an end-plated joint with two or more bolt-rows in tension, it is assumed that the deformations of the bolt rows are proportional to the distance to the centre of compression. The elastic forces in these rows depend on the stiffness of the components working as a series of springs $k_i$ in the row in question. The deformations of each component can be added so that the series of individual springs $k_i$ is replaced by a single spring with an effective stiffness $k_{eff,r}$ as shown in Fig. 5. Furthermore, these effective springs per bolt-row can be replaced by an equivalent spring $k_{eq}$ acting at a distance $z_{eq}$ from the centre of compression.

The assumptions described here above allow for the evaluation of the initial stiffness of the joint as follows:

$$S_{j,ini} = \frac{E z^2}{\sum_i \frac{1}{k_i}} \tag{4}$$

where $k_i$ is the elastic stiffness of the i[th] contributing component, $z$ is the lever arm and $E$ is the modulus of elasticity of steel.

Eq. (4) can be applied straightforwardly to joints with welded connections (as herein for BFC and CWC specimens), whilst for end-plated joints (RJ, EPB and CFB) additional parameters described above have to be determined using Eqs. (5)-(7):

$$k_{eff,r} = \frac{1}{\sum_i \frac{1}{k_{i,r}}} \tag{5}$$

$$z_{eq} = \frac{\sum_r k_{eff,r} h_r^2}{\sum_r k_{eff,r} h_r} \tag{6}$$

$$k_{eq} = \frac{\sum_r k_{eff,r} h_r}{z_{eq}} \tag{7}$$

The stiffness model depicted in Fig. 5 is defined in line with the provisions of Eurocode 3 Part 1-8. Its application has to be in compliance with the static theorem, ensuring the equilibrium between the internal forces distributed within the joint with the external bending moment. The assumed infinite transverse stiffness of the beam allows to apply the Bernoulli assumption and to fulfil the compatibility of displacements. As long as the elastic resistance of the constitutive springs is not reached, the plasticity criterion is met as well. In the same time, referring only to the elastic range of behaviour, the deformation capacity of the springs is not prone to limitations due to ductility requirements.

*3.2.4. Strain-hardening stiffness*

The elastic moment resistance $M_{Rel}$ of the joints is conventionally considered as $2/3M_{Rpl}$. Beyond this limit, the behaviour of the joints becomes non-linear. To characterise this non-linear response, the stiffness of the joints may be derived from $S_{j,ini}$ by affecting the latter with a stiffness ratio $\mu$. For end-plated and welded connections, provided that the bending moment $M_j$ varies between $M_{Rel}$ and $M_{Rpl}$, this assumption allows to approximate the rotational stiffness to $S_{j,ini}/7$, as illustrated in Fig. 6 (a).

The approach proposed in Eurocode 3 enables the user to estimate with a reasonable accuracy the initial stiffness $S_{j,ini}$ (up to $M_{Rel}$) and the secant stiffness which characterises the rotational behaviour of the joint up to $M_{Rpl}$. Beyond its plastic moment resistance, the joint is assumed to exhibit no rotational stiffness, leading thus to a conservative idealisation of its post-plastic response. This general-purpose idealisation is acceptable for common design practises, whilst for specific cases where a precise prediction of the post-plastic behaviour is sought, it is insufficient.

Based on the analytical expressions reported here above, the strain-hardening stiffness $S_{j,st}$ may be derived based on the strain-hardening stiffness coefficients $k_{st}$ of the individual basic components. In [8], the authors propose an assembly procedure for the assessment of $S_{j,st}$. This allows for the characterisation of the post-plastic behaviour of the joints beyond the plastic moment resistance $M_{Rpl}$ up to the ultimate one $M_{Ru}$ as depicted in Fig. 6 (b).

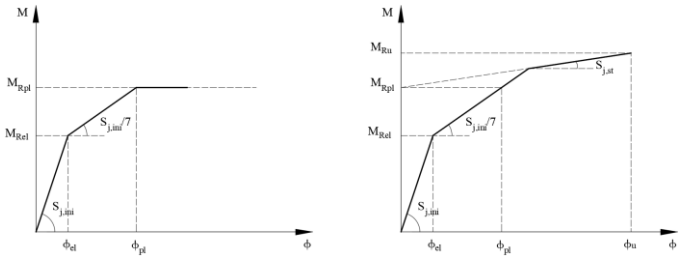


(a) According to Eurocode 3 (b) According to Jaspart et al [8]

**Fig. 6** Rotational stiffness of joints

The assembly procedure relies on the relative importance of the plastic moment resistance $M_{Rpl,comp,i}$ of each individual basic component when compared to the plastic resistance $M_{Rpl}$ of the joint. For all active components, $M_{Rpl,comp,i}$ is calculated by considering the i$^{th}$ component as being the only one active within the joint. Once evaluated for each isolated component, $M_{Rpl,comp,i}$ is compared to the plastic moment resistance of the whole joint $M_{Rpl}$. Components with $M_{Rpl,comp,i}$ considerably higher than $M_{Rpl}$ are assumed to contribute in an elastic way to $S_{j,st}$. Contrarily, the components with $M_{Rpl,comp,i}$ closer to $M_{Rpl}$ would undergo plasticity and, implicitly, strain-hardening effects would develop in the components affecting thus the $S_{j,st}$. Therefore, the evaluation of $S_{j,st}$ implies a classification of the components according to their own plastic resistance with a view to identifying the components contributing to $S_{j,st}$ by means of their initial elastic stiffness coefficient $k_i$ and the ones contributing with their strain-hardening stiffness coefficient $k_{st}$ assumed to be equal to $k_i/50$. A boundary value of the moment capacity has been proposed by Jaspart [1] after extensive studies of experimental tests on end-plated joints as follows in Eq.8.

$$M_{Rpl,limit} = 1.65 M_{Rpl} \tag{8}$$

Accordingly, a component with $M_{Rpl,comp,i} > M_{Rpl,limit}$ is considered to remain in its elastic range of behaviour, therefore having an elastic contribution to $S_{j,st}$. Conversely, when $M_{Rpl,comp,i} \leq M_{Rpl,limit}$, the i$^{th}$ component contributes to $S_{j,st}$ with its strain-hardening stiffness. The strain hardening stiffness of the joint $S_{j,st}$ is estimated in the following way:

$$S_{j,ini} = \frac{Ez^2}{\sum \frac{1}{k^*}} \tag{9}$$

where:

$$\sum \frac{1}{k^*} = \sum_m \left( \frac{1}{k_{i,m}} \right)_{M_{Rpl,comp,i} > M_{Rpl,limit}} + \sum_k \left( \frac{1}{k_{st,k}} \right)_{M_{Rpl,comp,i} \leq M_{Rpl,limit}} \tag{10}$$

with $k$ and $m$ - indices for components.

*3.2.5. Rotation capacity*

Limited guidance on the assessment of the rotation capacity of joints $\phi_{Cd}$ is provided in the current version of Eurocode 3. Rules to assure adequate rotation capacity for joints with bolted and welded connections are given as general requirements meant to avoid brittle failures associated to the rupture of bolts or weld failure. The few guidelines related to the assessment of $\phi_{Cd}$ lead to a rather qualitative estimation of it. However, an alternative method to quantify the rotation capacity may be contemplated on the basis of the procedure described here above. Referring to Fig. 6 (b), the ultimate rotation capacity $\phi_u$, i.e. the rotation of the joint corresponding to its ultimate resistance may be readily estimated on the basis of $M_{Rpl}$, $M_{Ru}$ and $S_{j,st}$ in the following manner:

$$\phi_u = \frac{M_{Ru} - M_{Rpl}}{S_{j,st}} \tag{11}$$

Similarly, the plastic rotation $\phi_{pl}$ is given by:

$$\phi_{pl} = \frac{3M_{Rpl}}{S_{j,ini}} \tag{12}$$

## 4. Finite element simulations

Physical tests conducted on full-scale specimens represent the most reliable method of assessment of the full non-linear behaviour of steel joints. However, such practices are in general economically inefficient and challenging to perform due to the limitations of available instrumentation. Moreover, experimental testing may be irrelevant for the investigation of local effects (i.e. stress distribution, prying and contact forces etc.) due to the difficulty to be measured with sufficient accuracy in reality. To overcome these challenges, numerical simulations are frequently used in the investigation of steel joints subjected to various types of loads. Hereafter, FE Analyses are employed in the evaluation of the $M_j$ - $\phi$ curve of steel joints subjected to quasi-static loads. The objective is to assess the potential and the accuracy of FE solutions in reproducing the complex non-linear behaviour of the joints.

*4.1. FE models description and modelling assumptions*

The joint configurations addressed in this paper were modelled in a 3D numerical environment using specific FE modelling techniques. The FE models were developed using the commercial software Abaqus/CAE [13]. For static analyses, the iterative Newton-Raphson method is used to solve the non-linear equilibrium equations in Abaqus/Standard.

Referring to Fig. 1, the symmetry of the test assemblies in terms of geometry, loading, and boundary conditions is easily noticeable. By exploiting this symmetry, only 1/4$^{th}$ of the physical specimen was explicitly modelled, thus allowing for the reduction of the computational effort. This modelling assumption was used to build the FE models of the four joints (RJ, EPB, CFB and BFC) in which no instability phenomena occurred in the experimental tests. Due to the unsymmetrical behaviour of the CWC specimen associated to the instability in the column web, the full assembly was numerically modelled so that the geometrical imperfections are properly taken into account.

Three-dimensional solid C3D8R 8-node linear brick elements with reduced integration were used to model the main structural parts as shown in Fig. 7. Exceptions were made for the welds and the root radius regions of the I and H sections, for which C3D6 wedge elements were used. The welds were modelled as parts with triangular cross-section. The threads of the bolts were not explicitly modelled; hence the bolts were modelled as having a smooth shank with a diameter of 14.1 mm which would simulate the resistant area in the threaded region.

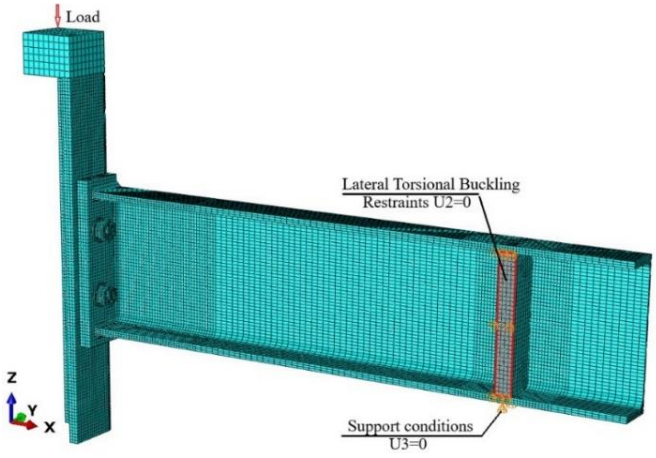


**Fig. 7** 3D view of the FE model (RJ specimen)

Fig. 8 depicts the mesh density for specific parts of the model. A dense mesh was assigned to the regions where local effects are likely to occur. Therefore, the end-plate, the bolts, and the region in the immediate proximity of the connection were discretised using small-size elements. Generally, a minimum number of 3 elements over the thickness was assigned for all plates of the model. Mesh seeds of 4 mm were applied to the parts in the regions with high density mesh, excepting the bolts for which mesh seeds of 2 mm were used.

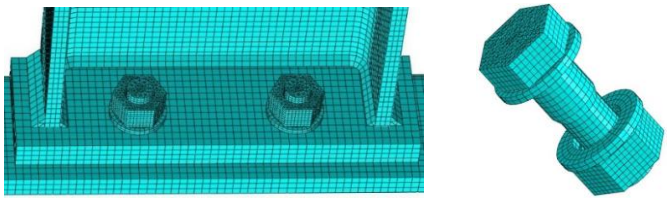

(a) End-plate region (b) Bolt part

**Fig. 8** Mesh density

The entire model was composed of approximately 60 000 elements and, because the simulations provided results that agreed with the experimental data, the mesh density was considered to be adequate. Additionally, several mesh sensitivity studies were conducted, and it has been demonstrated that an enhanced mesh refinement would minimally affect the global response.

### *4.2. Materials*

The non-linear behaviour of steel was implemented in the FE models through a non-linear stress-strain relationship with material hardening. Damage evolution or failure criteria were not explicitly implemented in the material model. The stress-strain constitutive relationships were derived from tensile coupon tests conducted on samples extracted from the plates of the specimens. For the elastic range of behaviour, a modulus of elasticity $E$=210 GPa was considered for all materials, whilst the yield stress $\sigma_y$ was assigned to each material based on the data reported in Table 2.

The engineering stress-strain ($\sigma_{eng}$ - $\varepsilon_{eng}$) curves generated throughout the tests were converted into true stress-logarithmic plastic strain ($\sigma_{true}$ - $\varepsilon_{pl}$) curves. The latter served as constitutive laws for the post-plastic behaviour of the materials allowing to consider adequately the strain-hardening of steel. To convert the $\sigma_{eng}$ - $\varepsilon_{eng}$ curves into the corresponding $\sigma_{true}$ - $\varepsilon_{pl}$ ones, reference is made to Eqs. (13)-(15).

$$\sigma_{true} = \sigma_{eng}(1+\varepsilon_{eng}) \tag{13}$$

$$\varepsilon_{true} = \ln(1+\varepsilon_{eng}) \tag{14}$$

$$\varepsilon_{pl} = \varepsilon_{true} - \frac{\sigma_{true}}{E} \tag{15}$$

### *4.3. Loading and boundary conditions*

The support conditions provided by the test setup were replicated in the FE environment by defining specific boundary conditions. The beam is simply supported at one of its end, hence the vertical displacement ($U_3$) has been restrained at the positon of the support as shown in Fig. 7. Additional supports were provided laterally to the stiffeners welded to the beam in order to prevent the loss of stability and the lateral torsional buckling of the beam. Since the initial modelling assumption was based on the symmetry of the system, appropriate symmetry conditions were applied on the two symmetry planes. A displacement control option was used in the FE simulations to mimic the monotonic load applied on the column top. The bolts were only snug tightened in reality, hence the pre-tensioning of the bolts was not considered.

To simulate the local buckling of plates occurring during the experimental test conducted on the CWC specimen, initial imperfections were implemented in the numerical model. A linear buckling analysis (LBA) was performed in order to evaluate the relevant buckling modes. The eigenvalues of these buckling modes were used further in a post-buckling analysis performed under the assumption of having initial imperfections with a magnitude of $d$/200, where $d$ is the clear depth of the column.

### *4.4. Interaction and contact*

The interaction between the constitutive parts of the FE model was simulated through imposed constraints and contact conditions. Tie constraints were used to connect the elements between which relative displacements are not allowed. Accordingly, this type of constraint was used to connect: the weld to the beam/end-plate/column, the beam to the end-plate/column, the stiffeners to the beam/column, and the loading plate to the column.

A surface-to-surface type of contact was defined for the interaction of several contact pairs such as: the bolt-heads with the end-plate, the bolt-shank with the bolt-holes in the end-plate and column flange, the nuts with the column flange, and the end-plates with the column flange. The behaviour for the normal direction was defined using a “Hard contact” property, so that the interpenetration of the surfaces in contact is not allowed. For the tangential direction, a Coulomb friction model with a penalty formulation was applied. A friction coefficient of 0.3 was assumed for all contact pairs of the model.

## 5. Results and discussion

In order to validate the methods of assessment presented in the previous sections, a comparison between the results is provided hereafter. The efficiency of analytical and numerical approaches is evaluated by confronting the results in terms of $M_j$ - $\phi$ curves for all five joint configurations. An additional validation criterion concerns the failure mode or the failing components of the joints. A comparison between the numerical values of the key parameters characterising the behaviour of the joints is reported in Table 5. The elastic moment resistance $M_{Rel}$ is chosen as a reference due to its convenience of being detectable visually on the experimental $M_j$ - $\phi$ curve. Thorough presentations and discussion of the results for each individual joint are provided in the following sections.

**Table 5**
Results comparison for the key parameters

| Parameter | Assessment method | Specimens | | | | |
|---|---|---|---|---|---|---|
| | | RJ | EPB | CFB | BFC | CWC |
| $M_{Rel}$ [kNm] | Experimental | 26.47 | 18.89 | 28.64 | 67.65 | 25.23 |
| | Analytical | 25.92 | 17.02 | 26.01 | 71.99 | 27.95 |
| | FE simulation | 27.81 | 19.02 | 28.07 | 69.57 | 37.27 |
| $M_{Ru}$ [kNm] | Experimental | 47.23 | 38.48 | 50.85 | 91.69 | 43.40 |
| | Analytical | 44.75 | 31.56 | 44.74 | 91.85 | 41.92 |
| | FE simulation | 44.72 | 36.78 | 50.37 | 95.03 | 48.81 |
| $S_{j,ini}$ [kNm/rad] | Experimental | 3267.9 | 1749.1 | 3719.5 | 35077 | 19584 |
| | Analytical | 5107.2 | 3058.6 | 5392.9 | ∞ | 16765 |
| | FE simulation | 3271.8 | 1811.4 | 3598.7 | 38650 | 26683 |
| $S_{j,st}$ [kNm/rad] | Experimental | 383.94 | 104.24 | 140.11 | 284.2 | N/A |
| | Analytical | 102.13 | 436.94 | 107.86 | 0.0000 | N/A |
| | FE simulation | 66.826 | 90.653 | 83.991 | 160.19 | N/A |
| $\phi_{el}$ [rad] | Experimental | 0.0081 | 0.0108 | 0.0077 | 0.0032 | 0.0018 |
| | Analytical | 0.0051 | 0.0056 | 0.0048 | 0.0000 | 0.0017 |
| | FE simulation | 0.0085 | 0.0105 | 0.0078 | 0.0018 | 0.0014 |
| $\phi_u$ [rad] | Experimental | 0.0739 | 0.1172 | 0.0728 | 0.0891 | 0.0058 |
| | Analytical | 0.0611 | 0.0631 | 0.0572 | N/A | 0.0075 |
| | FE simulation | 0.0744 | 0.1151 | 0.0809 | 0.1046 | 0.0038 |

### *5.1. Test 1: RJ specimen*

Fig. 9 illustrates the comparison between the $M_j$ - $\phi$ curves obtained through experimental, analytical, and numerical methods for the RJ specimen. The method proposed in this paper leads to a prediction in good agreement with the experimental results, even though the initial rotational stiffness $S_{j,ini}$ is somewhat overestimated. The representative limits for the moment resistance ($M_{Rel}$, $M_{Rpl}$ and $M_{Ru}$) and the post-elastic stiffness ($S_{j,ini}$/7 and $S_{j,st}$) are estimated with a satisfactory precision, shaping thus a tri-linear $M_j$ - $\phi$ curve with a high degree of reliability. For this specimen, the analytical prediction of the rotation capacity is similar to the actual value, hence the ductility of the joint is reasonably estimated as well. The failure mode analytically predicted corresponds to the failure of the column flange in bending (cfb) with plastic deformations in the end-plate in bending (epb) and in the column web in compression (cwc). The same failure mode has been observed in reality, the column flange exhibiting clear evidences of plasticity at the level of the first bolt row in tension. As expected, the differences between the Eurocode 3 method and the approach proposed in this paper are noticeable only for the post-plastic range. Given the fact that the joint’s plastic moment resistance is limited by the resistance of the column flange in bending (cfb), no estimation of the rotation capacity of the joint can be established with the standard method as, in Eurocode 3, this component is assumed to be infinitely ductile. Note that, for the sake of

completeness, the extent of the plateau represented with a dashed red line in Fig. 9 has been arbitrarily set, what represents an assumption for all the cases investigated hereafter.

The numerically derived $M_j$ - $\phi$ curve is as well in a good agreement with the experimental one. The initial stiffness $S_{j,ini}$ is estimated with a remarkable accuracy, whilst for the post-plastic range, the numerical prediction seems to underestimate slightly the rotational stiffness. The decrease in the post-plastic stiffness $S_{j,st}$ can be explained based on the plastic deformations developed within the joint. The equivalent plastic strain distribution shows that the column flange undergoes plastic deformations up to its failure, losing gradually its stiffness. Therefore, the failure mode can be associated to the column flange in bending component, this being in compliance with the experimental and analytical results.

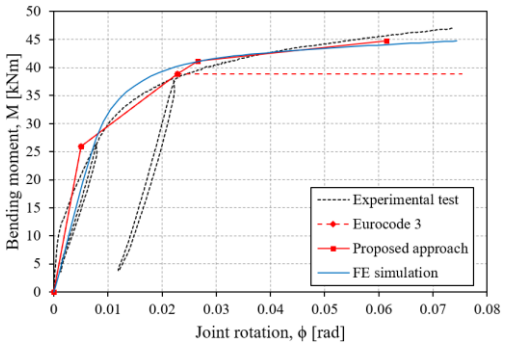


**Fig. 9** Results comparison – RJ specimen

### *5.2. Test 2: EPB specimen*

The results reported in Fig. 10 show that the proposed method provides a rather conservative prediction for the ultimate bending resistance and for the ultimate rotation capacity of the EPB joint. Otherwise, the analytical prediction follows closely the real behaviour of the joint, leading to an acceptable estimation of the elastic/plastic moment resistances and of the secant/strain-hardening stiffnesses. The significant discrepancy between the analytical prediction and the real behaviour may be attributed to the limitations of the equivalent T-stub model used to characterise the end-plate in bending component. In this case, the end-plate in bending (epb) is the failing component and governs the global behaviour of the joint. Due to its relatively small thickness of 8 mm, the end-plate can fall into the category of "thin" plates if compared to the conventional range of thicknesses for such joint parts. The T-stub model may be well-calibrated for plates with thicknesses in the usual range, yet it underestimates the extent of the plastic yield mechanism (for Failure mode 1) or of the yield lines in the component (for Failure mode 2) when applied to thinner plates as already highlighted in [14]. These aspects remain to be addressed in further investigations on the improvement of the equivalent T-stub model proposed in Eurocode 3 Part 1-8.

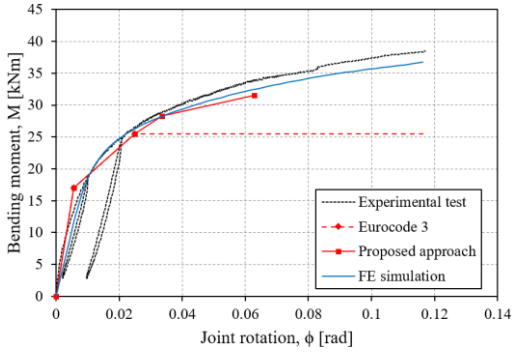


**Fig. 10** Results comparison – EPB specimen

The FE simulation provides a prediction with a good accuracy. The main characteristics of the non-linear behaviour of the joint are well estimated; only the ultimate moment resistance is marginally underrated. The failure mode corresponds to the failure of the end-plate in bending in the region of the first bolt row in tension where significant concentration of plastic deformations is localised. The failure of the same joint component was observed during the experimental test, thus validating the FE model.

### *5.3. Test 3: CFB specimen*

A conservative prediction for the $M_j$ - $\phi$ curve of the CFB specimen is obtained with the analytical approach (see Fig. 11). The ultimate moment resistance is significantly underestimated, whereas an acceptable prediction for the rotational stiffness is observed (note the parallelism between the strain-hardening branches). Since the analytically predicted failing component is the column flange in bending, what is in line with the test observations, the difference between the results may be once again linked to the limitations of the T-stub model on which the characterisation of the component relies.

A very good agreement is noticed between the results acquired from the test and the ones provided by the numerical simulation. The FE model replicates with a high accuracy the response of the physical specimen, all the validation criteria enounced previously being met.

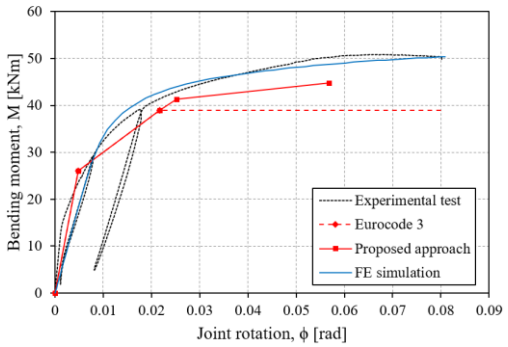


**Fig. 11** Results comparison – CFB specimen

### *5.4. Test 4: BFC specimen*

The component method provides only a partial prediction for the $M_j$ - $\phi$ curve for the BFC joint. The peculiarity of this specimen is that it was designed in such a way that the "deemed-to-fail" component would be the beam flange and web in compression (bfc). Therefore, the global response of the joint is characterised solely by the behaviour of this particular component which, as a matter of fact, is the only one active within the joint. Referring to the provisions of Eurocode 3, this component is assumed to exhibit an infinite initial stiffness. As long as the elastic range of behaviour is investigated, Fig. 12 shows that this assumption leads to satisfactory results. On the other hand, the characterisation of the post-plastic behaviour of the joint raises specific challenges. For class 1 and 2 cross-sections, the plastic resistance is expected to be reached without the occurrence of local buckling phenomena. An IPE 180 section is classified as a class 1 cross-section which can undergo plastic deformations beyond its plastic resistance. This allows to estimate the ultimate bending resistance of the BFC joint with a rather good precision. The strain-hardening stiffness and the ultimate rotation capacity have to be derived based on the characteristics of the beam as well. However, since the behaviour of members is outside the scope of this paper, an arbitrary "expectable" value for the ultimate rotation capacity of the joints is assumed here.

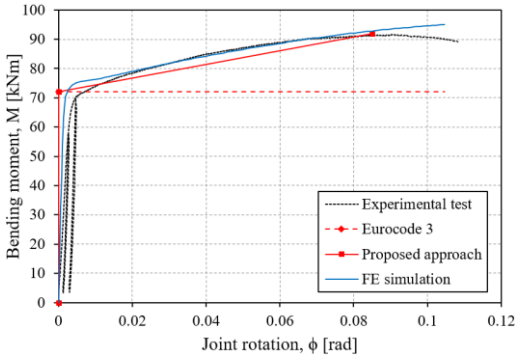


**Fig. 12** Results comparison – BFC specimen

The shortcoming of the analytical method can be overcome by conducting a FE analysis. This tool proves to be very reliable, the numerical prediction being very similar to the actual behaviour of the BFC specimen.

### 5.5. Test 5: CWC specimen

Observations of the experimental test on the CWC specimen indicate a failure mode associated to the buckling of the column web (cwc), which is a non-ductile failure mode. Once the buckling resistance of this component is reached, the failure of the whole joint occurs without any resistance reserve. Therefore, the joint's bending resistance corresponding to the buckling of the column web would represents the "plastic" and the "ultimate" moment resistance as well. This means that the Eurocode 3 approach and the method introduced in this paper would lead to identical results, hence, only the results for the standard approach are reported in Fig. 13.

Due to complexity related to instability phenomena, the rules prescribed by Eurocode 3 are intended to cover the most unfavourable scenarios so that, in common design practice, the resistance of components in compression under instability would not be overestimated. Accordingly, the design standard addresses this issue by assuming extreme or maximum-expected initial imperfections introduced in computations by means of buckling reduction factors $\rho$. Fig. 13 illustrates the very conservative $M_j - \phi$ curve of the CWC joint estimated using the buckling reduction factors set by the standard. If the influence of these initial imperfections is disregarded ($\rho$=1), the analytical prediction is enhanced and somewhat in a better agreement with the real behaviour of the CWC joint but reflects an unrealistic situation.

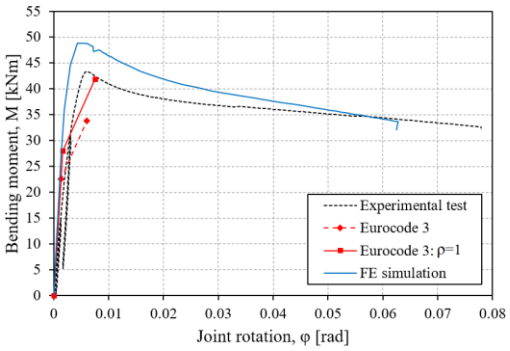


**Fig. 13** Results comparison – CWC specimen

The FE post-buckling analysis conducted on the CWC numerical model leads to results in partial agreement with the experimental data. The numerical prediction captures well the initial elastic stiffness of the joint, yet it overestimates by 12% the buckling load. This discrepancy may arise from the inadequate consideration of initial imperfections in the FE model or from the fact that, in reality, the load could be applied with a small eccentricity, thus inducing a parasitic bending moment that leads to a further reduction in the buckling capacity of the column web (cwc).

As main outcome, it can be concluded that further investigations are required for this joint component in view of improving the accuracy of the analytical formulation presently proposed in the standard for the prediction of its resistance.

## 6. Conclusions

Analytical and numerical methods have been employed to investigate the behaviour of beam-to-column steel joints under quasi-static loading. Predictions for five joint configurations were compared with experimental data, thus assessing the reliability of the two approaches. The analytical procedure proposed for the estimation of the full non-linear behaviour of joints is to be seen as an extension of the component method implemented nowadays in Eurocode 3 Part 1-8. Its application yields relevant results, allowing a more accurate and realistic prediction of the joint properties to be used in non-linear structural analysis. FE simulations of physical tests have been performed in a three-dimensional numerical environment. Generally, the simulations captured with a good accuracy the behaviour of the joints investigated in this paper. The following essential observations and conclusions may be drawn:

(1) The analytical approach based on the component method represents an interesting tool for the assessment of the non-linear response of steel joints subjected to quasi-static loads. The results reported in this paper are in a partial-to-good agreement with the experimental data despite the simplifying assumptions of the method. The rather tedious computational process can be readily dealt with by developing comprehensive computational routines in any available mathematical solver.

(2) When applied to thin plates, the equivalent T-stub model integrated in the current version of Eurocode 3 leads to conservative predictions of the ultimate moment resistance of joints. Further investigations on its sensitivity to the thickness of plates have to be carried out. Such studies are conducted currently at the University of Liège aiming at enhancing the accuracy of the equivalent T-stub model.

(3) The prediction of the resistance of the "Column Web in Compression" component as presently recommended in Eurocode 3, Part 1-8, is very conservative. As for the previous point, further investigations have to be conducted in order to improve the accuracy of the existing models. Such studies are also conducted currently at the University of Liège.

(4) The reliability of the proposed approach is highly dependent on the characterisation of basic components. To ensure an accurate prediction for the behaviour of a joint, the geometrical and mechanical properties of its active components must be rigorously assessed. Some of the analytical expressions proposed for this purpose still require additional investigations and in-depth studies of basic components' behaviour.

(5) FE simulations represent a very reliable alternative to experimental testing, even though they are still computationally expensive and require a set of skills and knowledge around FE solutions and modelling techniques.

(6) A special attention has to be paid when simulating the behaviour of joints in which instability phenomena are likely to occur. The initial imperfections and/or the possible eccentricities in the load application have to be meticulously accounted for in the FE model.

## Acknowledgements

Part of the presented work was carried out with a financial grant from the Research Fund for Coal and Steel of the European Community (Robustimpact project - Grant N° RFSR-CT-2012-00029).

## References

[1] Jaspart J.-P., "Etude de la semi-rigidité des noeuds poutre-colonne et son influence sur la résistance et la stabilité des ossatures en acier", PhD Thesis, University of Liège, Liège, Belgium, 1991.
[2] Jaspart J.-P. and Weynand K., Design of joints in steel and composite structures, ECCS Eurocode Design Manual, Wiley, Ernst & Sohn, 2016.
[3] Da Silva L. S., "Towards a consistent design approach for steel joints under generalized loading", Journal of Constructional Steel Research, vol. 64, no. 9, 1059–1075, 2008.
[4] EN 1993-1-8, Eurocode 3 - Design of steel structures - Part 1-8: Design of joints, Brussels: European Committee for Standardisation, 2005.
[5] Francavilla B. A., Latour M., Rizzano G., Jaspart J.-P. and Demonceau J.-F., "On the robustness of earthquake-resistant moment-resistant frames: influence of innovative beam-to-column joints", Open Construction and Building Technology Journal, vol. 12, 2018
[6] Kuhlmann U., Jaspart J. P., Vassart O., Weynand K. and Zandonini R., "Robust structures by joint ductility", RFCS Publishable Report, 2008.
[7] Demonceau J.-F. and Jaspart J.-P., "Experimental test simulating a column loss in a composite frame", Advanced Steel Construction, vol. 6, no. 3, 891–913, 2010.
[8] Jaspart J.-P., Corman A. and Demonceau J.-F., "Ductility assessment of structural steel and composite joints", 2019.
[9] Kuhlmann U. *et al.*, Robust impact design of stel and composite building structures (RobustImpact), European Commission, 2017.
[10] Demonceau J.-F., Vanvinckenroye H., D'Antimo M., Denoël V. and Jaspart J.-P., "Beam-to-column joints, column bases and joint components under impact loading", ce/papers, vol. 1, no. 2–3, 3890–3899, 2017.
[11] Hoffmann N. *et al.*, "RobustImapct: Deliverable D.5a. Detailed results of the experimental tests", 2016.
[12] Golea T., "Behaviour of steel joints under dynamic actions", Master Thesis, University of Liège, Liège, Belgium, 2020.
[13] Dassault Systèmes, "ABAQUS", 2016.
[14] Demonceau J.-F., "Steel and composite building frames: sway response under conventional loading and developmet of membrane effects in beams further to an exceptional action", PhD Thesis, University of Liège, Liège, Belgium, 2008.

**Advanced Steel Construction** – Vol. 18 No. 3 (2022) 687–698
**DOI:**10.18057/IJASC.2022.18.3.6



# SEGMENTED ASSEMBLY CONSTRUCTION FORMING METHOD WITHOUT BRACKETS OF SPATIAL CABLE-TRUSS STRUCTURE WITHOUT INNER RING CABLES

Jian Lu *, Su-Duo Xue, Xiong-Yan Li and Majid Dezhkam

*College of Civil and Architecture Engineering, Beijing University of Technology, 100 Ping Le Yuan, Chaoyang District, Beijing 100124, China*

** (Corresponding author: E-mail: lujian2020@126.com)*

**ABSTRACT**

Spatial cable-truss structure without inner ring cables (SCSWIRC) is a new cable-truss tension structure (CTTS), the features of which are composed of a series of planar cable-truss frames interwoven with each other. Its anti-collapse capacity is better, but its construction forming is complex. The reasons are that the strut's number and length will be enlarged with the span increase. Serious collision and winding of struts occur during construction due to SCSWIRC formed by a series of planar cable-truss frames interwoven with each other, which cause many difficulties in construction. According to the complex problem of construction forming, the segmented assembly construction forming method without brackets is proposed for SCSWIRC, and the basic idea of the proposed method is elaborated in detail. The SCSWIRC's experimental model with a 6m is designed, and numerical simulation and experimental research were carried out on the experimental model. The experimental results show that the error range of the internal forces of cables and struts is 6.99%~11.58%, and displacement errors of node 1 and node 2 are 3.27mm and 3.81mm, respectively verifies the feasibility and correctness of the proposed method. Then the static and dynamic experiment is carried out based on the final formed model. The static and dynamic experiment verifies the feasibility of the final formed model, which further shows the rationality and correctness of the segmented assembly construction forming method without brackets.

**ARTICLE HISTORY**

Received: 17 June 2021
Revised: 16 January 2022
Accepted: 31 January 2022

**KEYWORDS**

Spatial cable-truss structure without inner ring cables (SCSWIRC);
Segmented assembly without brackets;
Model design;
Construction forming;
Static and dynamic experiment



## 1. Introduction

At present, tensegrity structures are a research field that many scholars pay attention. More and more designers favor tensegrity structures because those kinds of structures have many good points, like little self-weight, beautiful appearance, strong spanning ability, and short construction period [1-3]. Meanwhile, cable-truss tension structures (CTTS) are one of the most typical structural forms of tensegrity structures. CTTS refers to the integral tension structure formed by the same kind of planar cable-truss frames according to certain layout principles. This kind of structure's common point is that the integral structure can be divided into planar cable-truss frames. Planar cable-truss frames share the same characteristics: lightweight, high stiffness, strong spanning ability, and simple construction. Now, CTTS mainly includes spoke cable-truss structures [4-5] shown in Fig. 1(a) and spatial cable-truss structures without inner ring cables shown in Fig. 1(b) [2-3,6]. The cable dome structure is a special CTTS [7,8] shown in Fig. 1(c).

Cable dome structure and spoke cable-truss structure have many practical projects domestic and overseas. There is an Olympics stadium in Seoul (1988) [9], the Florida Suncoast Dome in ST. Petersburg (1988) [10], the oval plan Levy form of cable dome for the Olympics in Georgia (1996) [11] in overseas. There is the National Fitness center in Ejin Horo Banner, Inner Mongolia (2012) [12], the Stadium of Tianjin University (2017) in domestic, and so on. For spoke cable-dome structures, there are Naka Stadium (1993), Kuala Lumpur Stadium (1998) [13], Busan Stadium (2001) [14] overseas. There are Shenzhen Bao'an Stadium (2001) [15], Yueqing Stadium (2013) [16], Zaozhuang Stadium (2017) in domestic. However, spatial cable-truss structure without inner ring cables is still in the theoretical and experimental research stage, and there are no practical projects domestic and overseas.

Through the research on SCSWIRC, it can be known that SCSWIRC is a novel CTTS, the features of which are composed of a series of planar cable-truss frames interwoven with each other [2-3,6]. It evolves from a spoke cable-truss structure with strong anti-collapse capacity because it has multiple load transfer paths [17]. Through the research on SCSWIRC, it can be known that although its anti-collapse capacity is excellent, its construction forming is more complicated. The reasons are that the strut's number and length will be enlarged with the span increase. Serious collision and winding of struts occur during construction due to SCSWIRC formed by a series of planar cable-truss frames interwoven with each other, which cause many difficulties in construction. If the strut's length is too long can be solved, the strut's collision and will be avoided during construction, which is beneficial to the structural application in projects. At present, SCSWIRC lacks the results related to construction forming. In contrast, construction forming is a significant problem faced by SCSWIRC, so it is necessary to carry out research related to its construction forming.

By studying construction forming's data, it can be known that the construction forming can be divided into two methods: construction forming method without brackets and construction forming method with brackets. The two methods have their advantages and disadvantages. The main difference is that the construction forming method without brackets avoids high-altitude operations and avoids using bed-jig, but it needs longer tooling cables; The construction forming method with brackets needs to use bed-jig to build a construction platform, which reduces the length of tooling cables but increases the project costs due to using bed-jig.

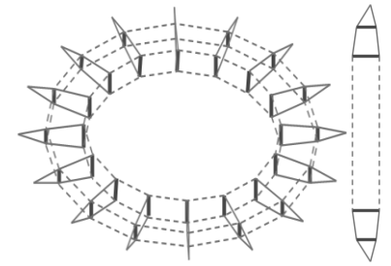

(a) Spoke cable-truss structure

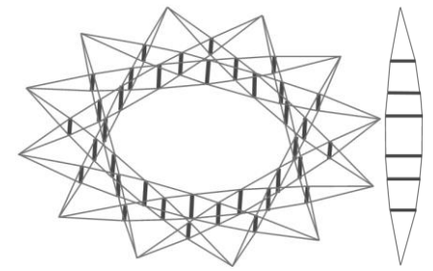

(b) Spatial cable-truss structure without inner ring cables

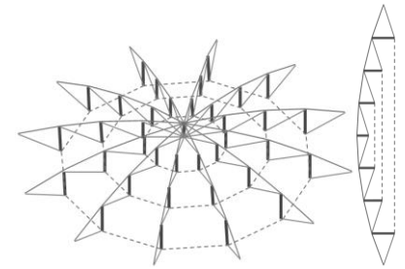

(c) Cable dome structure

**Fig. 1** Three types of cable-truss tension structures

In order to solve the complicated problem of SCSWIRC's construction forming, the segmented assembly construction forming method without brackets is proposed based on the above discussions. The paper first elaborates on the segmented assembly construction forming without brackets. Then the SCSWIRC's experimental model with a 6m is designed. Moreover, the feasibility of the proposed method is verified by using numerical simulation and experimental research. Meanwhile, the final formed model is verified using the static and dynamic trials. Finally, the conclusions are given in the paper.

## 2. Segmented assembly construction forming method without brackets' basic idea

SCSWIRC is a new type of tensegrity structure. The topological relationship and structural features are different from the previous tensegrity structures, so its construction forming cannot wholly adopt the previous construction forming methods. The segmented assembly construction forming method without brackets is proposed in the paper based on the structural characteristics of SCSWIRC. The solved flow of the new construction forming method is shown in Fig. 2a.

The basic idea of the new method: the main cable system structure in Fig. 2a can be divided into three parts: upper single-layer crossed cable net formed by upper chord cables in Fig. 2b, lower single-layer crossed cable net formed by lower chord cables in Fig. 2b, and struts connecting upper and lower single-layer crossed cable nets in Fig. 2c. Then use tooling cables to stretch the upper single-layer crossed cable net to a certain height. Moreover, assemble the segmented struts in Fig. 2c. After the last section of struts is raised to a certain height, the lower single-layer crossed cable net is assembled, and cable nets and struts are fixed with particular cable-strut joints. Finally, the assembled main cable system structure is lifted to the design configuration using tooling cables, which are connected and fixed with ring beams. The schematic diagram of the construction forming process for SCSWIRC is shown in Fig. 2d.

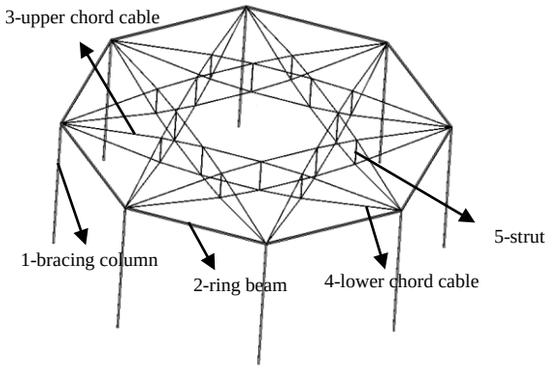


(a) Spatial cable-truss structure without inner ring cables

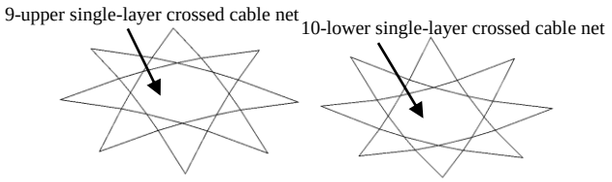


(b) Upper and lower single-layer crossed cable net

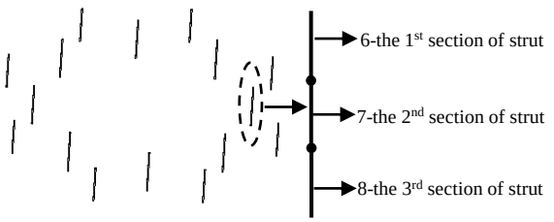


(c) Schematic diagram of segmented strut

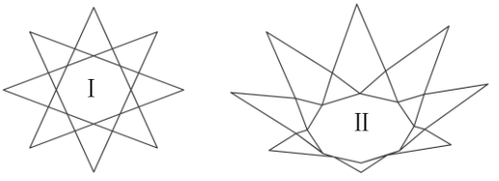


Ⅰ Segment upper single-layer crossed cable net on the ground
Ⅱ Lift upper single-layer crossed cable net to a certain height

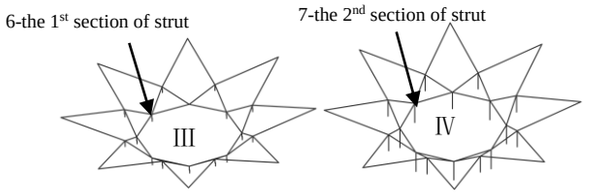


Ⅲ Segment the 1st section of strut Ⅳ Segment the 2nd section of strut

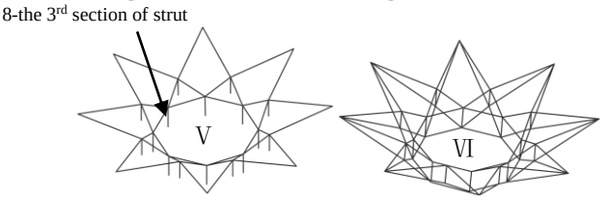


Ⅴ Segment the 3rd section of strut Ⅵ Segment lower single-layer crossed cable net on the ground

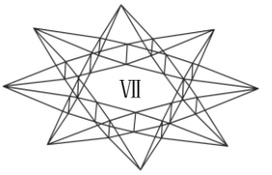


Ⅶ Stretch main cable system structure to design configuration

(d) Steps of construction forming based on proposed method

**Fig. 2** Relative diagrams of segmented assembly construction forming method without brackets

According to Fig. 2, the steps of the segmented assembly construction forming method without brackets are as follows:

**The 1st step**: Install bracing column 1 and ring beam 2 according to the construction scheme. Then check whether the position of bracing column 1 is correct or not and whether the ring beam 2 is installed to the design height or not;

**The 2nd step**: Assemble upper single-layer crossed cable net 9 formed by upper chord cables according to non-stress cable length in the center of a construction site, and fix and clamp the joints among crossed cable net.

**The 3rd step**: Install the tooling cables of upper single-layer crossed cable net and then connect tooling cables and lifting equipment;

**The 4th step**: Use synchronous lifting equipment like hydraulic jacks to slowly lift tooling cables of upper single-layer crossed cable net 9 to a certain height (provide a construction platform for workers to facilitate following construction process);

**The 5th step**: At this time, install the first section 6 of strut using the height difference between upper single-layer crossed cable net and the ground according to construction scheme and then connect it with upper single-layer crossed cable net 9;

**The 6th step**: Continue lifting the upper single-layer crossed cable net 9 to a certain height, and then segment the 2nd section of strut 7. Flanges are used to connect the 2nd section of strut 7, which is bolted or welded;

**The 7th step**: Repeat the 4th~5th steps until all segmented struts are assembled;

**The 8th step**: Assemble lower single-layer crossed cable net 10 formed by lower chord cables according to non-stress cable length in the center of the construction site, and then fix and clamp the joints among crossed cable net;

**The 9th step**: Install the tooling cables of lower single-layer crossed cable net 10 and connect it with lifting equipment together;

**The 10th step**: Connect lower single-layer crossed cable net 10 with the last section of strut 8 together. At this time, the whole structure's relaxed state is formed by an upper single-layer crossed cable net with stresses and a lower single-layer crossed cable net without stresses.

**The 11th step**: Stretch tooling cables of the segmented central cable system to the design configuration, and then connect the ends of the upper and lower single-layer crossed cable net with a ring beam. At this time, the whole process of construction forming is completed.

The method is considered from the perspectives of actual construction (the spans of practical projects are generally greater than 200m), which avoids collision and winding among struts and crossed cable nets due to a large number of struts and too long length of struts and avoids high-altitude operations and improves construction efficiency and guarantees construction quality. The proposed method provides a practical and feasible way for SCSWIRC and promotes the application of SCSWIRC in projects to a certain extent. Meanwhile, the segmented assembly construction forming method without brackets can also be applied to other tensegrity structures with rigid struts.

## 3. Model design

In order to verify the feasibility and correctness of the segmented assembly construction method without brackets, a trial model with a diameter of 6m is designed for SCSWIRC. The trial model design includes the main cable system structure, ring beam, bracing column, cable-strut joint, cable-beam joint, and strut connector.

### *3.1. Material property experiment*

Considering the unknown mechanical properties of cable and strut, four groups of cable and strut test-pieces were selected from the same batch of materials, shown in Fig. 3. The cable and strut mechanical properties are calibrated at the Strength Testing Institute of Beijing University of Technology. The mean values of trial results are used as the final trial values. The material properties of cable and strut obtained through material property experiment are shown in Table 1.

### *3.2. Design of main cable system structure*

The main cable system structure comprises the upper and lower single-layer crossed cable net and strut, which is the central force of SCSWIRC. Its main cable system structure can be seen as composed of N planar cable-truss frames, and N is equal to 10 in the paper's trial model shown in Fig. 4a. Both


**Fig. 3** Test-pieces of cable and strut

**Table 1**
Material properties of cable and strut

| Element Type | Size | Area /mm$^2$ | Elastic modulus/MPa | Broken force/kN |
|---|---|---|---|---|
| Cable | Φ6 | 21.487 | 1.21*10$^5$ | 36 |
| Strut | P20*3 | 141.300 | 2.05*10$^5$ | 52.02 |

planar cable truss frame's upper and lower chord cables conform to parabola's shape like Eq. (1). According to Ref. [18], it can be known that the ranges of the optimal rise-span ratio of upper and lower chord cables are 1/25~1/20 and 1/20~1/15, respectively. So, the rise-span ratios of upper and lower chord cables are selected as $f_u$=1/24 and $f_b$=1/16, respectively. All Eq. (1) parameters can be solved according to $f_u$, $f_b$, N, and d, so $A_1$=-0.091778, $B_1$=0.075665, $A_2$=0.137668 $B_2$=-0.113497. The program of solving nodal coordinates is compiled based on the layout relationship of cable-truss frames and Fortran Language. The solved nodal coordinates are shown in Table 2. The geometry model formed by all nodal coordinates is shown in Fig. 4b. The feasible self-stress mode of the geometry model can be solved using Ref. [19], and the results are shown in Table 3. The integral finite element model can be obtained according to the feasible self-stress mode in Table 3, the finite element model shown in Fig. 4c.

$$\begin{cases} y_1 = A_1 x_1^{\ 2} + B_1, A_1 < 0 \\ y_2 = A_2 x_2^{\ 2} + B_2, A_2 > 0 \end{cases} \tag{1}$$

### *3.3. Design of ring beam and bracing column*

The ring beam is made of H-shaped steel, and its size is H200×200×12×12. The bracing column is made of circular

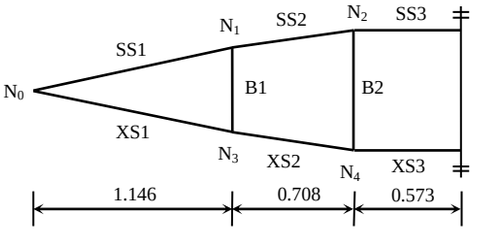


(a) Planar cable-truss frame Unit: m

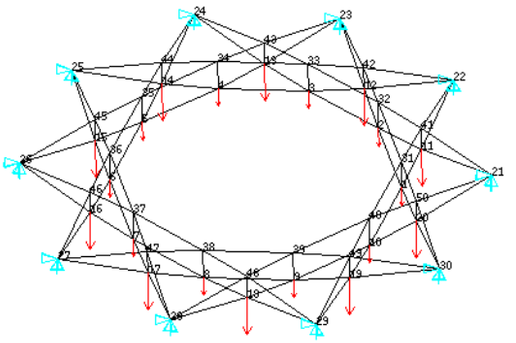

(b) Geometry model and nodal number

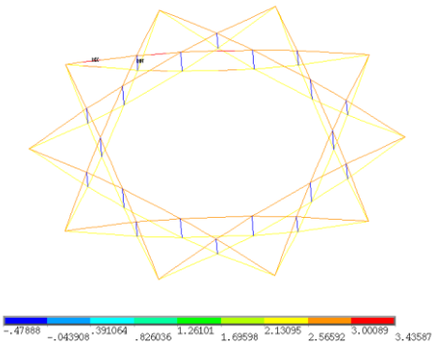


(c) Finite element model Unit: kN

**Fig. 4** Main cable system structure of geometry model

**Table 2**
Nodal coordinates of geometry model

| Nodal number | *x*/*m* | *y*/*m* | *z*/*m* | Nodal number | *x*/*m* | *y*/*m* | *z*/*m* | Nodal number | *x*/*m* | *y*/*m* | *z*/*m* | Nodal number | *x*/*m* | *y*/*m* | *z*/*m* | Nodal number | *x*/*m* | *y*/*m* | *z*/*m* |
|---|---|---|---|---|---|---|---|---|---|---|---|---|---|---|---|---|---|---|---|
| 1 | 3.000 | 0.000 | | 11 | 2.073 | 0.674 | | 21 | 1.854 | 0.000 | | 31 | 2.073 | 0.674 | | 41 | 1.854 | 0.000 | |
| 2 | 2.427 | 1.763 | | 12 | 1.281 | 1.763 | | 22 | 1.500 | 1.090 | | 32 | 1.281 | 1.763 | | 42 | 1.500 | 1.090 | |
| 3 | 0.927 | 2.853 | | 13 | 0.000 | 2.180 | | 23 | 0.573 | 1.763 | | 33 | 0.000 | 2.180 | | 43 | 0.573 | 1.763 | |
| 4 | -0.927 | 2.853 | | 14 | -1.281 | 1.763 | | 24 | -0.573 | 1.763 | | 34 | -1.281 | 1.763 | | 44 | -0.573 | 1.763 | |
| 5 | -2.427 | 1.763 | 0.000 | 15 | -2.073 | 0.674 | 0.159 | 25 | -1.50 | -1.090 | 0.208 | 35 | -2.073 | 0.674 | -0.195 | 45 | -1.500 | 1.09 | -0.255 |
| 6 | -3.000 | 0.000 | | 16 | -2.073 | -0.674 | | 26 | -1.854 | 0.000 | | 36 | -2.073 | -0.674 | | 46 | -1.854 | 0.000 | |
| 7 | -2.427 | -1.763 | | 17 | -1.281 | -1.763 | | 27 | -1.0500 | -1.090 | | 37 | -1.281 | -1.763 | | 47 | -1.500 | -1.090 | |
| 8 | -0.927 | -2.853 | | 18 | 0.000 | -2.180 | | 28 | -0.573 | -1.763 | | 38 | 0.000 | -2.180 | | 48 | -0.573 | -1.763 | |
| 9 | 0.927 | -2.853 | | 19 | 1.281 | -1.763 | | 29 | 0.573 | -1.763 | | 39 | 1.281 | -1.763 | | 49 | 0.573 | -1.763 | |
| 10 | 2.427 | -1.763 | | 20 | 2.073 | -0.674 | | 30 | 1.500 | -1.090 | | 40 | 2.073 | -0.674 | | 50 | 1.500 | -1.090 | |

**Table 3**
Feasible self-stress mode of geometry model

| Nodal number | Cable | | | | | | Strut | |
|---|---|---|---|---|---|---|---|---|
| | SS1 | SS2 | SS3 | XS1 | XS2 | XS3 | B1 | B2 |
| Cable length/m | 1.157 | 0.7104 | 1.146 | 1.163 | 0.7106 | 1.146 | 0.354 | 0.463 |
| Non-stress cable length/m | 1.153 | 0.7090 | 1.142 | 1.161 | 0.7094 | 1.144 | – | – |
| internal force/kN | 3.416 | 3.392 | 3.381 | 2.848 | 2.818 | 2.805 | -0.476 | -0.472 |

Steel tube of P89×5. The ring beam and bracing column are all Q235 steel, and the detailed diagram of the ring beam and bracing column are shown in Fig. 5.

### *3.4. Design of cable-strut joint*

The design rules of cable-strut joints: (1) Try not to cut cables as much as possible so that the whole cable can pass through cable-strut joints. That is, cables are continuous and through; (2) Joints can significantly reflect structural characteristics;

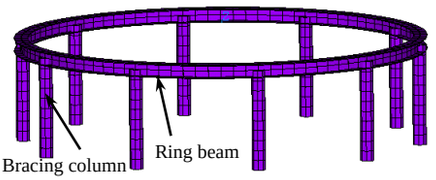


(a) Finite element model

(b) Solid model

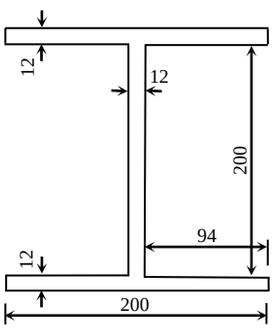


(c) Size of ring beam

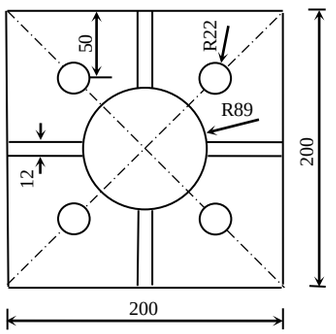


(d) Detailed diagram of column's top

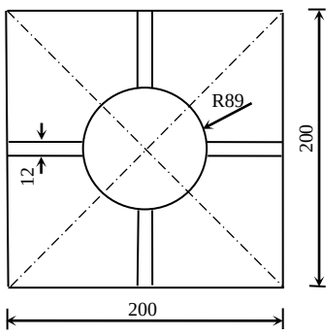


(e) Detailed diagram of column's foot

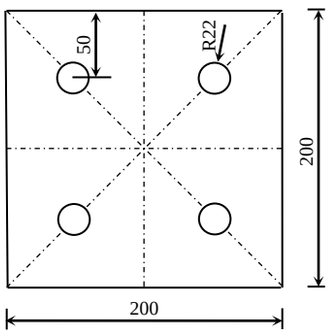


(f) Cover plate between ring beam

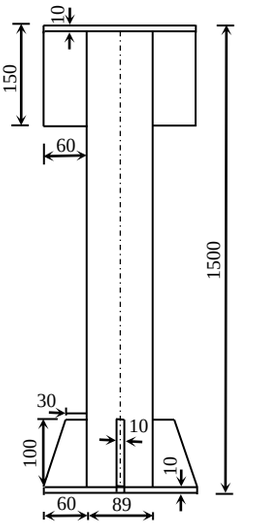


(g) Detailed diagram of bracing column

**Fig. 5** Model and detailed diagram of ring beam and bracing column

(3) Joints should be as simple as possible, and the force transmission road is clear; (4) Joints can have a small amount of rotation so that joints can be fine-tuned to make cables pass through the strut's center after assembling the main cable system structure. According to the above four design rules, the detailed diagram of the cable-strut joint is shown in Fig. 6.

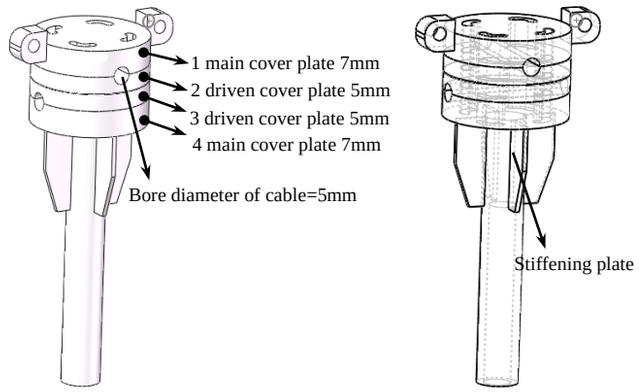


(a) Three-demission diagram of cable-strut joint


(b) Detailed diagram of cover plate

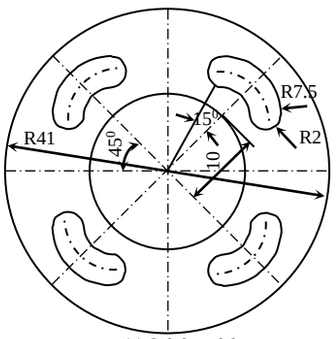


(c) Solid model

**Fig. 6** Detailed diagram of cable-strut joint

### *3.5. Design of cable-beam joint*

The design of the cable-beam joint should be based on the angle between every two cable-truss frames like nodes 21~30 in Fig. 4b. The cable-beam joint's correlation diagram is shown in Fig. 7.

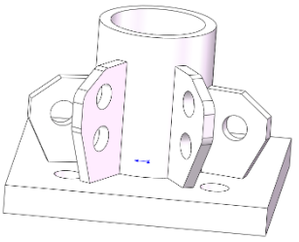

(a) Three-demission model

(b) Solid model

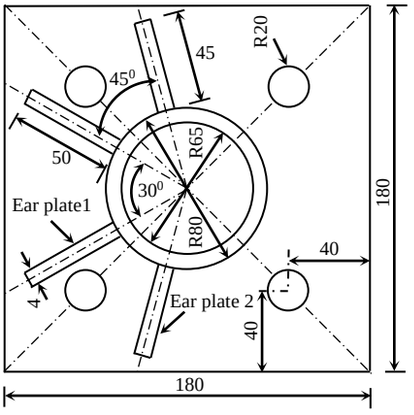


(c) Graphic diagram

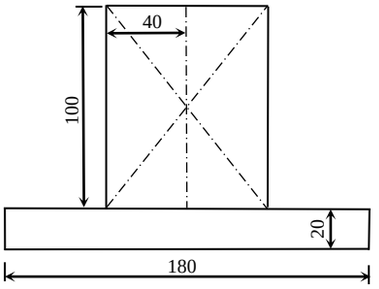


(d) Elevation diagram

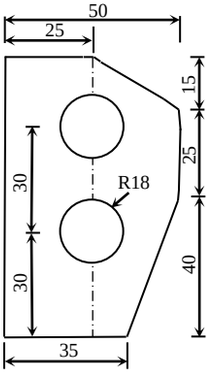


(e) Ear-plate 1

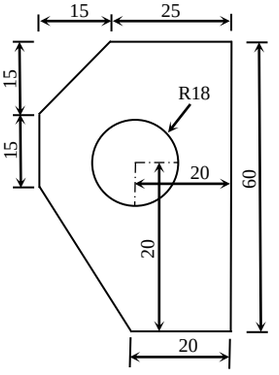


(f) Ear-plate 2

**Fig. 7** Correlation diagram of cable-beam joint

*3.6. Design of strut connector*

It needs to divide struts into several sections in advance when using segmented assembly construction forming method without brackets. Flanges are used to connect the sections of struts, shown in Fig. 8.

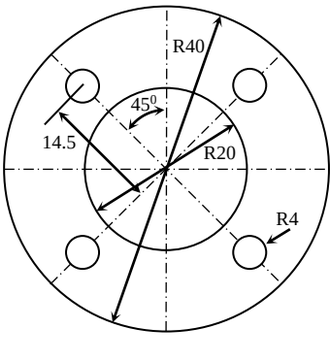


(a) Detailed diagram of flange

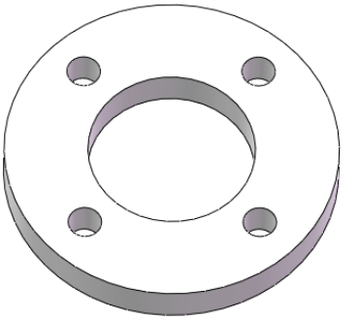

(b) Three-demission model of flange

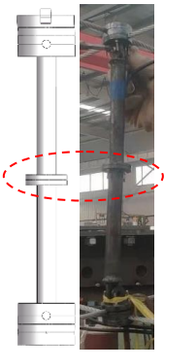

(c) solid model of strut B1

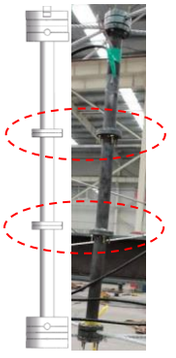

(d) solid model of strut B2

**Fig. 8** Correlation diagram of strut connector

## 4. Construction forming trial based on segmented assembly construction forming method without brackets

*4.1. The influence of ring beam and bracing column on main cable system structure*

It can be known from Ref. [3] that ring beam and bracing column have some influence on SCSWIRC, so the influence should be considered during construction forming. The integral finite element model is shown in Fig. 9.

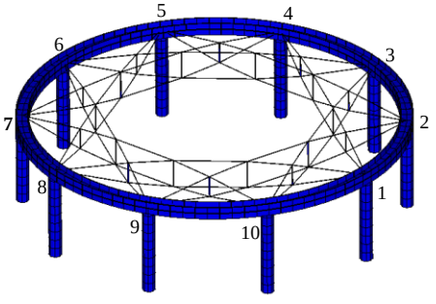


**Fig. 9** Integral finite element model

*4.2. Layout of monitoring points in trial*

Cable-strut joints are node 1~10, shown in Fig. 9. The trial model can be divided into 10 planar cable-truss frames based on the number of cable-beam joints, including cable-truss frame 1-4, cable-truss frame 2-5, cable-truss frame 3-6, cable-truss frame 4-7, cable-truss frame 5-8, cable-truss frame 6-9, cable-truss frame 7-10, cable-truss frame 8-1, cable-truss frame 9-2, cable-truss frame 10-3. The internal forces of upper and lower chord cables and struts are monitored during construction. Meanwhile, the z-components of all nodal displacements for these two cable-truss frames are monitored in crucial steps of construction forming. Monitoring points of internal forces and displacements are shown in Fig. 10. Cable-truss frames 1-4 and cable-truss frames 6-9 are in symmetrical positions in Fig. 9.

During the experiment, strain gauges were used to monitor the change of cables and struts' internal forces, attached to pre-designed threaded sleeves shown in Fig. 10. All the strain gauges are connected to the static collection instrument JM3813 through the collection line, shown in Fig. 11a. Static collection instrument JM3813 collects the signal and transmits the signal to a computer. Finally, the signal is converted into strain by computer, and the internal force values of cables and struts can be obtained by further calculation. Level gauge and steel ruler are used to monitor nodal displacement of the cable-truss frame at critical positions, shown in Fig. 11b.

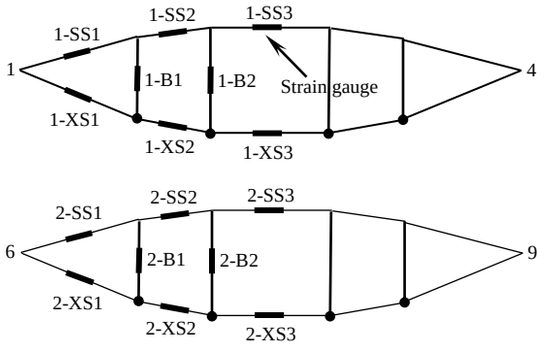


**Fig. 10** The layout of monitoring points of internal forces and displacements

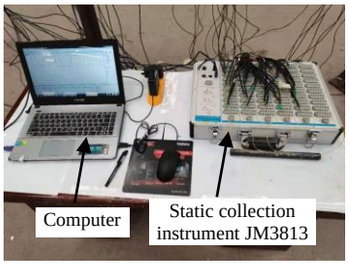


(a) Static collection instrument

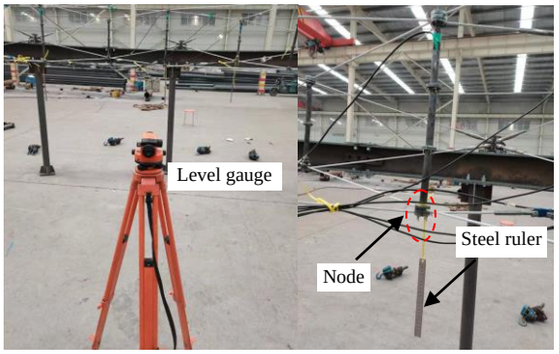


(b) Level gauge and steel ruler

**Fig. 11** Static collection instrument JM3813, level gauge and steel ruler

*4.3. Segmented assembly construction forming trial*

The segmented assembly construction forming method is a new construction forming method that can solve the complex problem of construction forming for SCSWIRC in concept. However, it is still necessary to further verify the feasibility and effectiveness of the proposed method in experiment. The paper adopts the construction forming mode with the fixed-length cable. The non-stress cable length can be obtained based on the finite element model in Fig. 4b, shown in Table 3.

The "segment" for segmented assembly construction forming method without brackets refers to dividing struts into several sections in advance. Then the segmented struts are assembled section by section in construction. In experiment, strut B1 and B2 are divided in advance. The strut B1 is divided into two sections, including B11 and B12; the strut B2 is divided into three sections, B21, B22, and B23, as shown in Fig. 12. The construction forming process is divided into six key steps according to segmented assembly construction forming method characteristics without brackets.

**The 1st step**: Install the upper single-layer crossed cable net on the ground;

**The 2nd step**: Use tooling cables and synchronous lifting equipment to lift the upper single-layer crossed cable net to a certain height, and then assemble the 1st section of the strut on the ground. The 1st section of strut and upper single-layer crossed cables are fixed and clamped with cable-strut joints;

**The 3rd step**: Continue lifting the segmented parts to a certain height, and then assemble the 2nd section of a strut. Flanges connect the 1st section of strut and 2nd section of the strut;

**The 4th step**: Continue lifting the segmented parts to a certain height, and then assemble the 2nd section of the strut. The 2nd section of the strut and the 3rd section of strut are connected by flanges;

**The 5th step**: Continue lifting the segmented parts to a certain height, and then assemble a lower single-layer crossed cable net. The segmented parts and lower single-layer crossed cable net are fixed and clamped by cable-strut joints;

**The 6th step**: Use tooling cables and synchronous lifting equipment to lift the segmented main cable system structure to design configuration.

Strut B1 is divided into two sections, so its construction steps are steps 1~3 and steps 5~6. Strut B2 is divided into three sections, so its construction steps are steps 1~6. Due to adopting construction forming mode with the fixed-length cable, the configuration and cable forces generally conform to the design values after the main cable system structure is stretched to design configuration when the manufacturing errors of ring beam, cable, and strut are not considered. When cable forces and configuration do not meet design values, the length of the threaded sleeve of the cable's ends can be adjusted appropriately to compensate for the manufacturing and assembly process errors.

The methods of solving the convergence problem of construction forming based on ANSYS finite element software include: (1) Ref. [20] proposed the extensive temperature method to improve the convergence of construction simulation. (2) Ref. [21] proposed the added cables method to improve the convergence of construction simulation. (3) Ref. [22] proposed the inverse-construction and rigid displacement methods. The convergence problem of construction simulation was solved by the inverse-construction method and applying rigid displacement on nodes that are prone to rigid displacement. (4) Ref. [23] proposed the effective damping method that can improve the convergence of construction simulation by applying significant damping to structures to make the structure be in a viscoelastic liquid environment. (5) Ref. [24] proposed the added beam method to solve the convergence problem of construction simulation. (6) Ref. [25] proposed the nodal displacement hypothesis to improve the convergence of construction simulation. The paper solves the convergence problem of construction simulation of SCSWIRC based on Ref. [20] and Ref. [22].

Meanwhile, due to the SCSWIRC's construction forming from ground to the design configuration belonging to large displacement and deformation, the internal forces of cables and struts can be monitored in the whole construction, but the changes of nodal displacement are difficult to monitor. So, the experimental values of nodal displacement of cable-truss frame 1-4 and cable-truss frame 6-9 in Fig. 10 are only given when the length of tooling cables is 5cm, 4cm, 3cm, 2cm, 1cm and 0cm. That is, the construction process is divided into six key steps. The six key steps of construction simulation and construction forming trial are shown in Fig. 13.

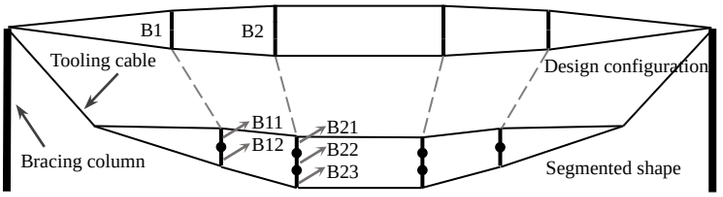


**Fig. 12** Schematic diagram of strut's segments of single cable-truss frame

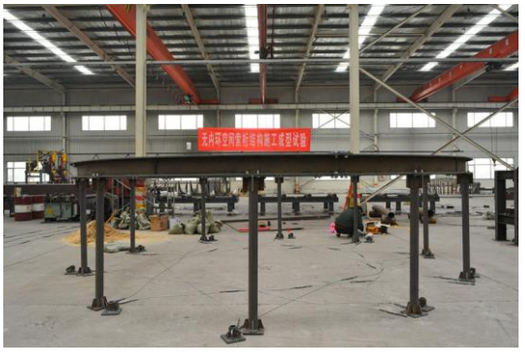


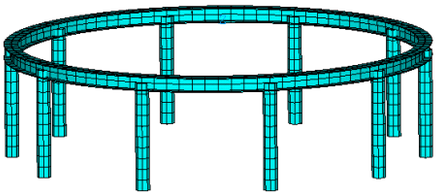

**Start**: Install ring beam and bracing column

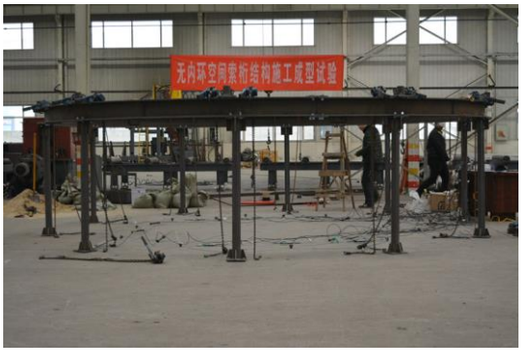


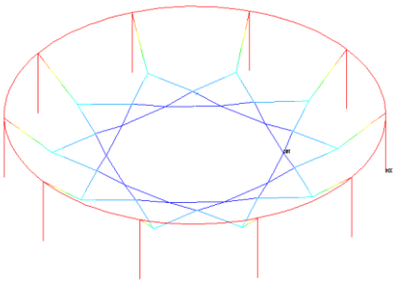

**The 1st step**: Assemble upper single-layer crossed cable net on the ground and install tooling cables


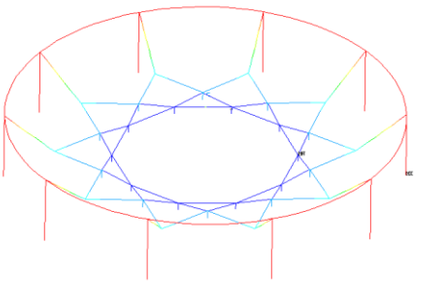

**The 2nd step**: Lift upper single-layer crossed cable net to a certain height and then assemble strut B11 and B21

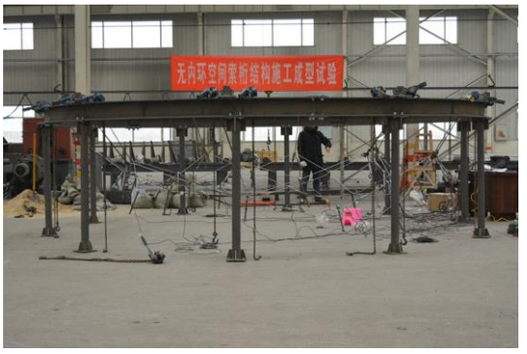


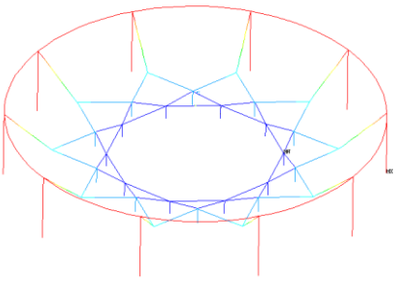

**The 3rd step**: Continue lifting the segmented parts to a certain height and then assemble B12 and B22


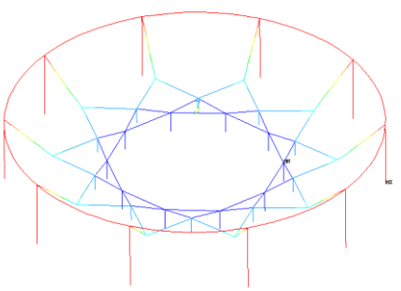

**The 4th step**: Continue lifting the segmented parts to a certain height and then assemble B23

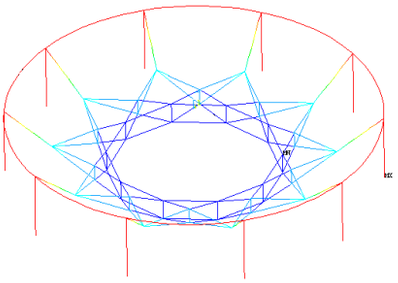

**The 5th step**: Continue lifting the segmented parts to a certain height, and then assemble a lower single-layer crossed cable net and connect it with the segmented parts

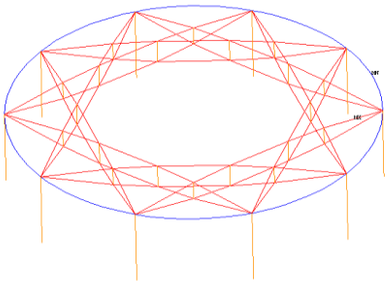

**The 6th step**: Continue lifting the segmented main cable system structure to design height and then dismantle tooling cables and connect it with ring beam together.

**Fig. 13** The experimental process of segmented assemble construction forming method without brackets

In the experiment, the internal forces of cables and struts and nodal displacements for cable-truss frame 1-4 and cable-truss frame 6-9 are monitored. Cable-truss frame 1-4 and cable-truss frame 6-9 are in the symmetric position and the experimental datum is the same, so take cable-truss frame 1-4 as an example and give the detailed data in construction. The comparison results of simulation values and experimental values are shown in Table 4 and Fig. 14.

**Table 4**
Internal forces of cables and struts in the six key steps of construction

| Nodal number | Key construction steps | | | | | | Nodal number | Key construction steps | | | | | |
|---|---|---|---|---|---|---|---|---|---|---|---|---|---|
| | 1th | 2th | 3th | 4th | 5th | 6th | | 1th | 2th | 3th | 4th | 5th | 6th |
| SS1- experimental value | – | 0.0065 | 0.00649 | 0.00645 | 0.0064 | 3.654 | XS1-experimental value | – | – | – | – | 0.0218 | 3.137 |
| SS1-simulation value | – | 0.0055 | 0.00539 | 0.00565 | 0.0073 | 3.416 | XS1-simulation value | – | – | – | – | 0.0243 | 2.848 |
| SS2- experimental value | – | 0.0041 | 0.00413 | 0.0041 | 0.0041 | 3.673 | XS2- experimental value | – | – | – | – | 0.0211 | 3.048 |
| SS2-simulation value | – | 0.0055 | 0.0037 | 0.0057 | 0.0049 | 3.392 | XS2-simulation value | – | – | – | – | 0.0245 | 2.818 |
| SS3- experimental value | – | 0.00078 | 0.00079 | 0.00079 | 0.00080 | 3.732 | XS3- experimental value | – | – | – | – | 0.0238 | 3.103 |
| SS3-simulation value | – | 0.00063 | 0.00066 | 0.00084 | 0.00092 | 3.381 | XS3-simulation value | – | – | – | – | 0.0292 | 2.805 |
| B1- experimental value | – | -0.0047 | -0.0047 | -0.0047 | -0.0047 | -0.522 | B2- experimental value | – | 0.0053 | 0.0053 | 0.0053 | -0.0054 | -0.508 |
| B1-simulation value | – | -0.0085 | -0.0078 | -0.0059 | -0.0063 | -0.476 | B2-simulation value | – | 0.0036 | 0.0074 | 0.0085 | -0.0056 | -0.472 |

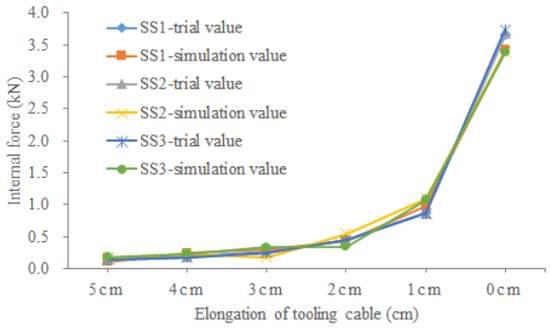


(a) Internal forces of upper chord cables

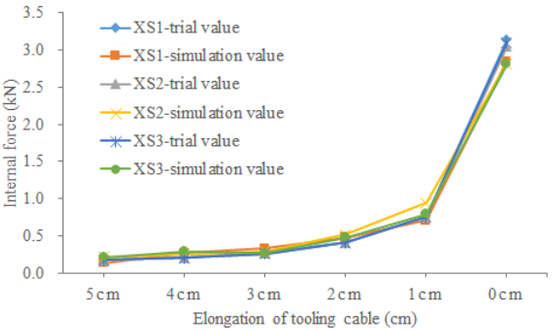


(b) Internal forces of lower chord cables

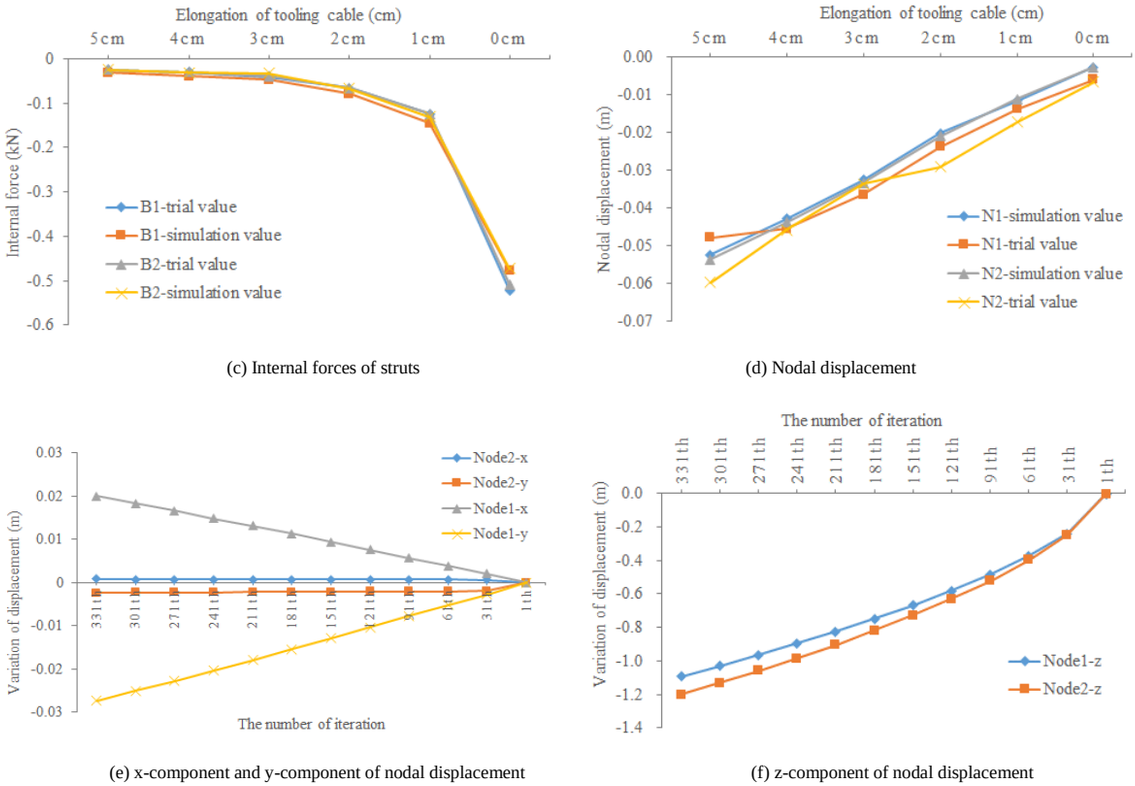


(c) Internal forces of struts

(d) Nodal displacement

(e) x-component and y-component of nodal displacement

(f) z-component of nodal displacement

**Fig. 14** Change curves of internal forces of cables and struts and nodal displacement in experiment

In ANSYS finite element software, the inverse construction method can complete the construction simulation in Fig. 13 [22]. It can be seen from the experimental process that construction forming steps are simple and the operation is convenient, and the construction forming process is relatively smooth. The SCSWIRC's construction forming belongs to an extensive deformation process. At the same time, it can be seen from the construction forming process in Fig. 13 that the upper chord cables are in a relaxed state in the 1st step, so the values of the internal forces cannot be measured. The struts are not assembled in the 1st step, so their internal forces cannot be measured. The lower chord cables start to install in the 5th step, so their internal forces can be measured in the 5th step. It can be seen from Table 4 and Fig. 14(a)~(d) that experimental values and simulation values are identical. The internal forces of upper and lower chord cables increase with the decrease of the length of tooling cables. The main cable system structure is stretched to design configuration when the length of tooling cables is shortened to zero. Then the final formed model will conform to the design shape by cable's fine-tuning threaded sleeve several times. In the final formed state, the error range of upper chord cables' internal forces is 6.99%~10.2%; the error range of lower chord cables' internal forces is 8.20%~11.58%; the error range of struts' internal forces is 9.21%~11.31%.

The displacement errors of node 1 and node 2 are 3.27mm and 3.81mm, respectively. The errors are within the acceptable range. The main reasons for errors are the drift of strain gauge, the manufacturing and construction errors, and measuring instrument errors. Fig. 14(e)~(f) shows that the changing trend of displacement components of node 1 and node 2 in the *x*, *y*, *z* directions during the whole construction forming experiment. It can be seen from Fig. 14(e)~(f) that the x and y coordinate values change very little and linearly in construction. Nevertheless, the changes in the z-component are significant and nonlinear, so the total displacement of three components x, y, and z are also nonlinear, which is consistent with the nonlinear nature of large deformation in construction forming. So, it can be seen from the analysis results that the segmented assembly construction forming method without brackets can solve the difficulty of SCSWIRC's construction forming.

### *4.4. Further discussions*

(1) There are lots of struts for SCSWIRC with a large span, and its length is long. When a segmented assembly construction forming method without brackets is used, struts will be divided into several sections. The segmented struts are connected with flanges, so many cable-strut joints and flanges will significantly increase workers' workload. While jumping layout or removed struts can simplify SCSWIRC [2]. Jumping layout means that a strut that needs to be removed is not modeled in design, and structural integrity is not damaged. Therefore, the grid-jumped layout differed from the broken cable and broken strut. The process of grid-jumped layout for SCSWIRC is shown in Fig. 15. The grid-jumped layout's positions should be symmetrical to ensure structural symmetry and integrity. The number of struts will decrease after grid-jumped layout, and the number of cable-strut joints and flanges will also decrease. So, jumping layout reduces project cost and worker's workload and saves time to a certain extent.

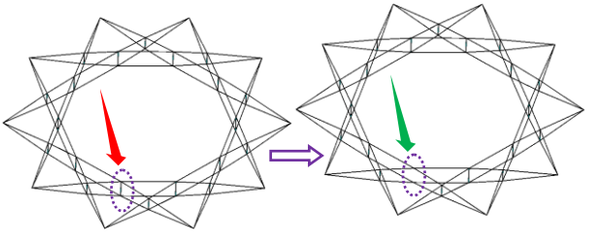

**Fig. 15** Grid-Jumped layout's process of SCSWIRC

(2) When the segmented assembly construction forming method without brackets is used, struts will be divided into several sections, and flanges connect the segmented struts. If the segmented positions of all struts are the same as shown in Fig. 16a, a segmented surface will be generated at all segmented positions. The segmented surface is a weak part, which is unfavorable to SCSWIRC. The struts need to be staggered in segmented positions (shown in Fig. 16b). The segmented positions of all struts do not form segmented surfaces at a certain height, eliminating the safety hazards brought by segmented surfaces.

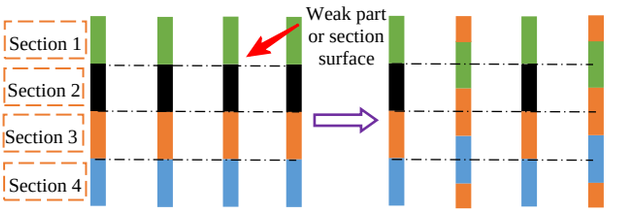


(a) Segmented positions of struts are the same (b) Segmented positions of struts are not same

**Fig. 16** Schematic diagram of segmented position of struts

## 5. Static and dynamic experiment

### 5.1. Static experiment

In order to verify the static performance of the final formed model, the static loading experiment is carried out on the final formed model. Static loading experiment includes full-span loading experiment and half-span loading experiment, shown in Fig. 17. The formed experimental model's equivalent nodal load **F** can be obtained by solving equivalent nodal load in Ref. [2]. In Fig. 4a, the equivalent load of node 1 is $F_1$=0.429kN, the equivalent load of node 2 is $F_2$=0.361kN, that is, **F**=10*[ $F_1$, $F_2$]. The static loading trial uses sandbags to load step by step. When the load is 0.8**F**, 0.9**F**, 1.0**F**, 1.1**F**, 1.2**F**, structural static response is investigated respectively.

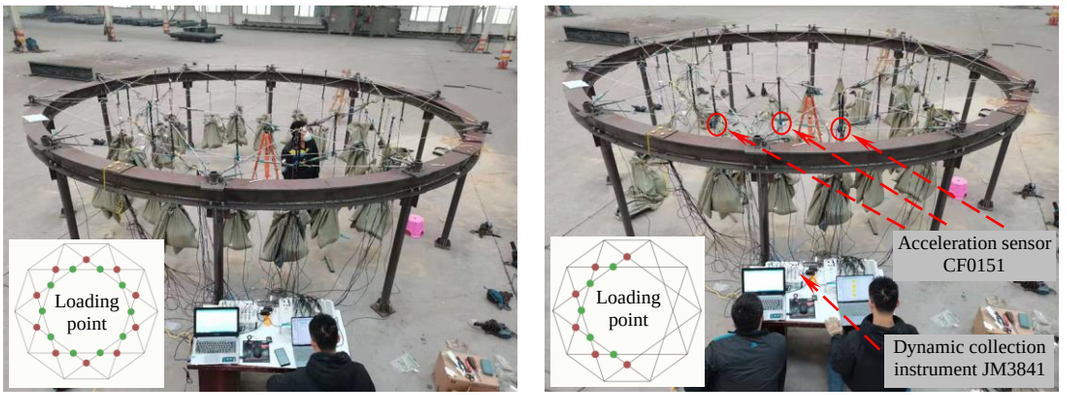


(a) Full-span laods (b) half-span loads

**Fig. 17** Layout diagram of full-span loads and half-span loads

#### 5.1.1. Under full-span loads

The responses of internal forces and displacements of the structure under full-span loads are shown in Fig. 18.

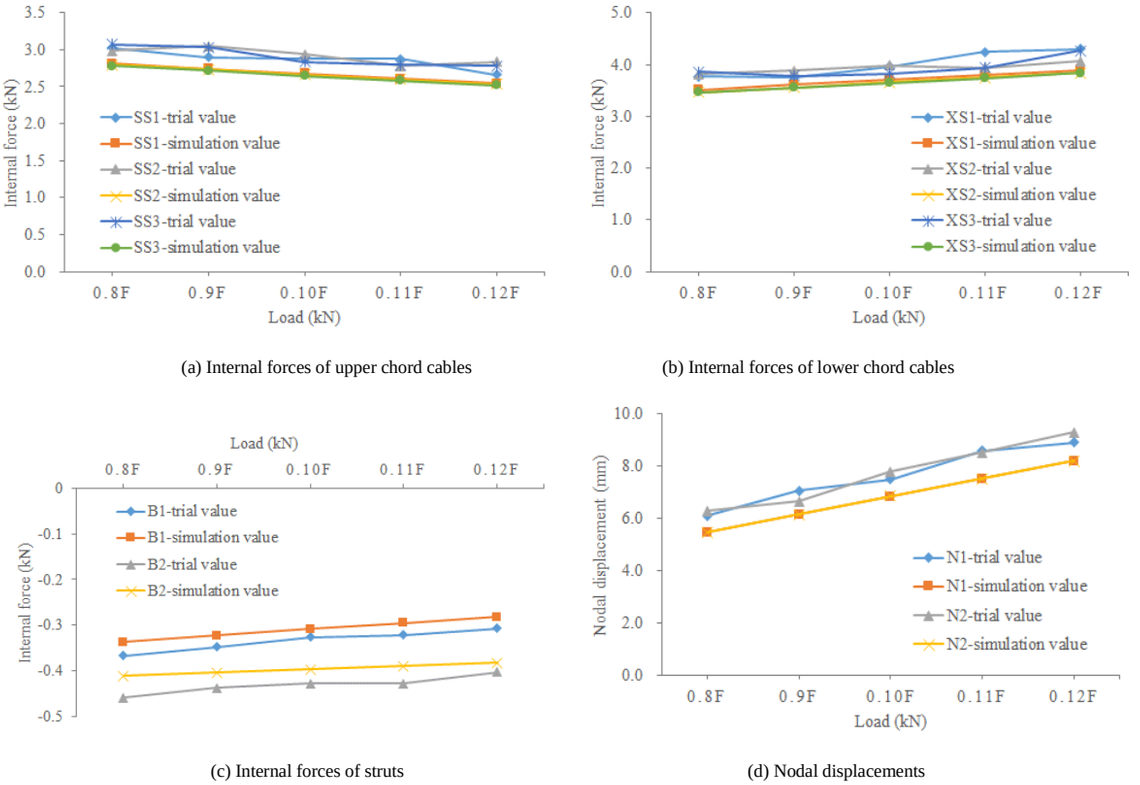


(a) Internal forces of upper chord cables (b) Internal forces of lower chord cables

(c) Internal forces of struts (d) Nodal displacements

**Fig. 18** Internal forces of cable and strut and nodal displacements under full-span loads

It can be seen from Fig. 18 that the internal forces of cables and struts and nodal displacements linearly change under full-span loads, which shows that the final formed model has an excellent static performance. With the increase of loads, the internal forces of upper chord cables are decreasing; the internal forces of lower chord cables and struts are increasing; nodal displacements are increasing. The change laws of internal forces and cables and struts and nodal displacements conform to the mechanical characteristics of those kinds of structures. Under load 0.8**F**~1.2**F**, the maximum error of internal forces of upper chord cables SS1~SS3 is 11.61%; the maximum error of internal forces of lower chord cables XS1~XS3 is 10.16%; the maximum error of internal forces of struts B1~B2 is 10.43%; the maximum errors of displacement of nodes $N_1$ and $N_2$ are 10.86% and 12.89%, respectively. Technical Specification for Cable Structure (JGJ257-2012) [26] specifies the maximum allowable displacement [σ]=*l*/200= 30mm (*l* is structural span.). The maximum displacement is 9.1mm, which meets the Code's requirements. Judging from the errors between experimental and theoretical values, the errors are within the acceptable range. The main reasons for errors: (1) There is a distinct difference between the final formed shape and design configuration; (2) The strain gauges are slightly drifting in measurements; (3) Measuring instrument will produce some errors.

#### 5.1.2. Under half-span loads

The responses of internal forces and displacement of the structure under half-span loads are shown in Fig. 19.

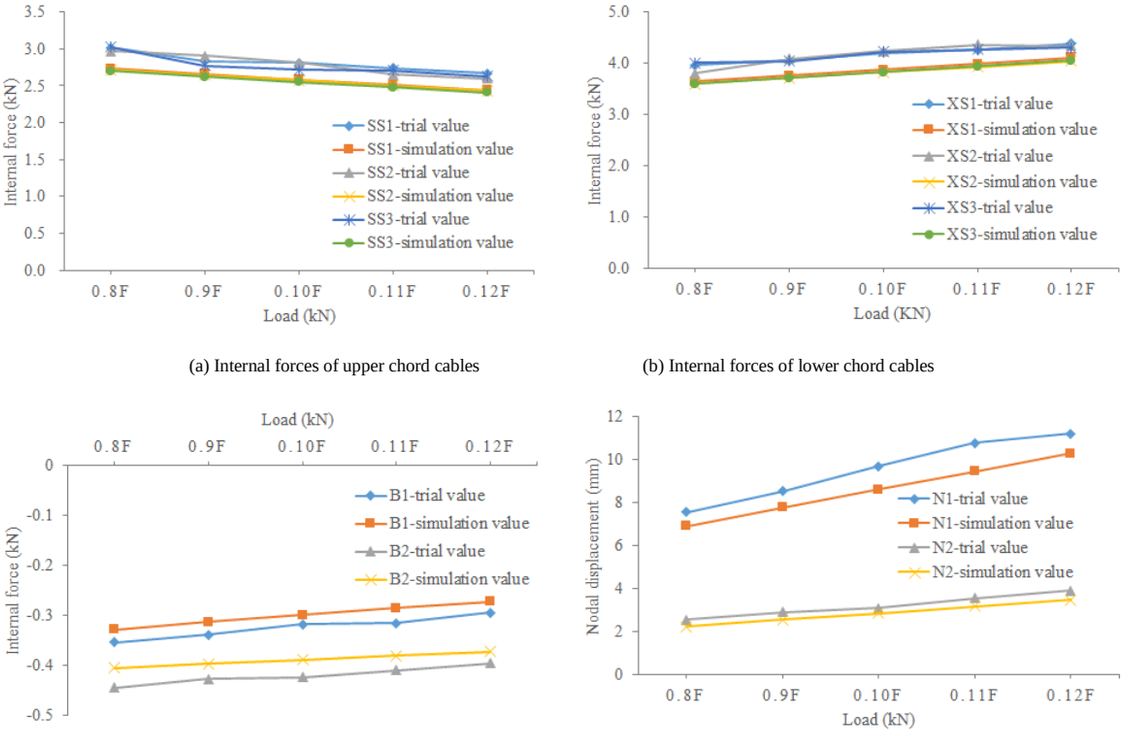


(a) Internal forces of upper chord cables

(b) Internal forces of lower chord cables

(c) Internal forces of struts

(d) Nodal displacement

**Fig. 19** Internal forces of cable and strut and nodal displacement under half-span loads

It can be seen from Fig. 19 that the change laws of internal forces of cable and strut and nodal displacement under half-span loads are the same as those under full-span loads. The error range is roughly the same, and the reasons for errors are the same, so it is no longer described again.

*5.2. Dynamic experiment*

To further verify the correctness of the final formed model, it is necessary to study the dynamic characteristics of SCSWIRC. Meanwhile, SCSWIRC is a new type of CTTS, and its natural vibration characteristics are the basis of wind resistance and earthquake resistance, and no scholars have studied it. In the paper, the final formed model is tested for the dynamic characteristic of the initial prestress state, full-span load state, and half-span load state. The change laws of natural vibration frequency under three conditions are analyzed. The dynamic experiment under loads considers the action of hierarchical load that is the same as **F** in Section 4.1.

In the dynamic experiment, as the structure is symmetrical about the ring direction, three acceleration sensors are installed at different nodes on one side of the structure. The CF0151 acceleration sensors are used, and their positions are shown in Fig. 17. The structural acceleration time curve under external excitation can be obtained through dynamic collection instrument JM3841 shown in Fig. 17. Dynamic signal test and analysis software can calculate structural natural vibration frequency based on the obtained acceleration time curve (JMTEST).

As three CF0151 acceleration sensors on the experimental model, the mean value of three experimental values is seen as the final trial values. Theoretical values can be solved by Block Lanczos Method (LANB) in Ref. [2]. The influence of prestress effect and large deformation on the structure can be considered by setting the prestress stiffening effect and large deformation command in ANSYS finite element software. Based on the above discussions, the first 6-order frequencies of theoretical and experimental values are shown in Table 5-1~5-3.

**Table 5-1**
First 6 natural frequencies in initial prestress state Unit: HZ

| Type | 1st order | 2nd order | 3rd order | 4th order | 5th order | 6th order |
|---|---|---|---|---|---|---|
| S-value | 6.809 | 6.879 | 7.322 | 7.541 | 8.670 | 8.908 |
| T-value | 6.742 | 6.742 | 7.296 | 7.302 | 8.573 | 8.574 |

Description: S-value is simulation value; T-value is trial value, the same as below.

**Table 5-2**
First 6 natural frequencies in full-span load state Unit: HZ

| Load times | Type | 1st order | 2nd order | 3rd order | 4th order | 5th order | 6th order |
|---|---|---|---|---|---|---|---|
| 0.8F | S-value | 4.636 | 4.718 | 5.364 | 5.446 | 6.143 | 6.263 |
| | T-value | 4.419 | 4.53 | 5.121 | 5.124 | 5.869 | 5.993 |
| 0.9F | S-value | 4.371 | 4.417 | 5.110 | 5.314 | 5.776 | 5.897 |
| | T-value | 4.173 | 4.213 | 4.836 | 4.954 | 5.541 | 5.665 |
| 1.0F | S-value | 4.156 | 4.221 | 4.861 | 4.932 | 5.412 | 5.533 |
| | T-value | 3.964 | 3.864 | 4.593 | 4.643 | 5.263 | 5.385 |
| 1.1F | S-value | 3.913 | 3.875 | 4.494 | 5.512 | 5.257 | 5.372 |
| | T-value | 3.784 | 3.764 | 4.384 | 4.422 | 5.023 | 5.144 |
| 1.2F | S-value | 3.825 | 3.954 | 4.481 | 4.521 | 5.040 | 5.164 |
| | T-value | 3.626 | 3.752 | 4.201 | 4.321 | 4.813 | 4.935 |

**Table 5-3**
First 6 natural frequencies in half-span load state Unit: HZ

| Load times | Type | 1st order | 2nd order | 3rd order | 4th order | 5th order | 6th order |
|---|---|---|---|---|---|---|---|
| 0.8F | S-value | 4.402 | 4.522 | 4.724 | 4.865 | 5.549 | 5.651 |
| | T-value | 4.228 | 4.320 | 4.567 | 4.521 | 5.370 | 5.421 |
| 0.9F | S-value | 4.108 | 4.230 | 4.502 | 4.621 | 5.196 | 5.234 |
| | T-value | 3.992 | 4.144 | 4.313 | 4.356 | 5.071 | 5.112 |
| 1.0F | S-value | 3.965 | 4.088 | 4.203 | 4.354 | 5.062 | 5.134 |
| | T-value | 3.792 | 3.944 | 4.096 | 4.126 | 4.817 | 4.954 |
| 1.1F | S-value | 3.819 | 3.938 | 4.084 | 4.132 | 4.817 | 4.821 |
| | T-value | 3.620 | 3.762 | 3.909 | 4.012 | 4.597 | 4.624 |
| 1.2F | S-value | 3.606 | 3.724 | 3.957 | 4.025 | 4.590 | 5.621 |
| | T-value | 3.469 | 3.543 | 3.746 | 3.654 | 4.405 | 4.251 |

It can be known from Table 5 that the theoretical values are slightly larger than the experimental values. The main reasons are that the finite element model is a simplified

model. The finite element model's quality is less than that of the experimental model, and its prestress distribution is more uniform than that of the experimental model. From the first 6 frequencies, the 1st order frequency is the same as the 2nd order frequency; the 3rd order frequency is the same as the 4th order frequency; the 5th order frequency is the same as the 6th order frequency, which shows there is a symmetrical axis for the structure. In the initial prestress state, the first 6 order frequencies' theoretical values are in the range of 6.809~8.908HZ, and its experimental values are 6.742~8.574HZ, which shows that structural frequency distribution is dense. Its frequencies gradually increase with the increase of orders. Whether under full-span load state or half-span load, the natural frequency distribution and change laws are the same as those in the initial prestress state. Meanwhile, structural frequencies gradually decrease with the increase of loads, which conforms to the change laws of dynamic characteristics. It can be seen from a characteristic dynamic experiment that experimental values are in agreement with theoretical values indicating that the final formed experiment model is rational and reasonable.

## 6. Conclusions

In order to solve the difficulty of SCSWIRC's construction forming, a segmented assembly construction forming method without brackets is proposed. Based on the experimental model of SCSWIRC with a diameter of 6m, the segmented assembly construction forming method without brackets is studied by numerical simulation and experimental research.

The results show that experimental values and simulation values are identical. The error range of internal forces of cables and struts is in the range 6.99%~11.58%, and errors of displacement of node 1 and node 2 are 3.27mm and 3.81mm, respectively. The errors are in the acceptable range, which verifies the feasibility of the segmented assembly construction forming method without brackets. Then the static and dynamic experiments are carried out based on the final formed model. Under full-span loads and half-span loads, the error of internal forces of cables and struts is 10% or so; the maximum displacement errors of nodes 1 and 2 are 10.86% and 12.89%, respectively. The errors are in the acceptable range. It can be seen from the dynamic experiment that the experimental values and theoretical values are identical under three conditions. The natural frequency distribution is dense, and natural frequencies increase with the increase of orders. Structural frequencies gradually decrease with the increase of loads, which conforms to the change laws of dynamic characteristics. So, the static and dynamic experiment verifies the correctness and rationality of the final formed model.

The simulation and experimental results verify the feasibility and correctness of the segmented assembly construction forming method without brackets. The proposed new method can solve the difficulty of construction forming.

## Acknowledgements

The authors would like to acknowledge the financial support of the National Natural Science Foundation of China (51778017), the National Natural Science Foundation of China (51878014).

## References

[1] Liang Xiaotian. Optimization and control research of cable-strut tensile strutctures. Hangzhou: School of Architecture and Engineering, Zhejiang Univesity, 2017.
[2] Xue Suduo，Lu Jian，Li Xiongyan，et al. The influence of grid-jumping arrangement on the static and dynamic performance of annular crossed cable-truss structure. Journal of Jilin University (Engineering and Technology Edition), 2020, 50(5), 1687-1697.
[3] Lu Jian, Xue Suduso, Lu Jian, Li Xiongyan, et al. Key Construction Technology of Annular Crossed Cable-truss Structure. Journal of Tianjin University (Science and Technology), 2021, 54(1), 101-110.
[4] Guo Yanlin, Wang Kun, Tian Guangyu, et al. Research and design of structural form of spoke structure. Journal of Building Structures, 2013, 34(5): 1-10.
[5] Deng Hua, Jiang Q., Kwan A. (2005). Shape finding of incomplete cable-strut assembies containing slack and prestressed elements. Computer Structures, 83,1767-79.
[6] Lu Jian, Xue Suduo, Li Xiongyan, Liu Renjie. Study on membrane roof schemes of annular crossed cable-truss structure. International Journal of Space Structures, 2019, 34(3-4):85-96.
[7] Levy M.P., The Georgia Dome and beyond: Achieving light weight-long span structures, Spatial, lattice and tension structures, proceedings IASS-ASCE international symposium, New York, 1994, pp. 560-562.
[8] Ge J.Q., Zhang A.L., Liu X.G., Zhang G.J., Ye X.B., Wang S., and Liu X.C., "Analysis oftension form-finding and whole loading process simulation of cable dome structure", Journal of Building Structures, 33(4), 1-11, 2012.
[9] Geiger DH. Stefaniuk A, Chen D. The design and construction of two cable domes for the Korean Olympics. Shells, membrane and space frames, proceedings IASS symposium, Osaka, Japan, Vol. 2. p. 265−72.
[10] Geiger D H, Campbell D, Chen D, et al. Design details of an elliptical cable dome and a large span cable dome under construction in the United States//Proceedings,1st Oleg Kerenslry Memorial Conference, London England,1988:14-17.
[11] Levy MP. The Georgia Dome and beyond: Achieving lightweight-longspan structures. Spatial, lattice and tension structures, proceedings IASS-ASCE international symposium, New York. P. 560−2.
[12] Zhang Guojun, Ge Jiaqi, Wang Shu, et al. Design and research on cable dome structural system of the national Fitness Center in Ejin Horo Banner, Inner Mongolia. Journal of building structures, 2012;33(04):12−22.
[13] Sehlaich J, Bergermann R, Goppert K. National Sports ComPlex-Kuala LumPur, Malaysia, Lightweight Roof Structures for the Outdoor Stadium and the Swimming ComPlex[Z], 1997.
[14] Jeon BS, Lee JH. Cable membrane roof structure with oval opening of stadium for 2002 FIFA world Cup in Busan. In: Proceedings of sixth Asian-Pacific conference on shell and spatial structures, vol. 2, Soul, South Korea; 2000. P.1037−42.
[15] Tian Guangyu. Reasearch on Key Technology of Design Theory and Construction Control in Spoke Tension Structures. Tsinghua University, 2012.
[16] Deng Hua, Zhang Minrui, Liu Hongchuang, et al. Numerical analysis of the pretension deviations of novel Crescent-shaped tensile canopy structural system, Engineering Structure,2016;119:24−33.
[17] Liu Renjie, Li Xiongyan, Xue Suduo, Marijke Mollaert, Ye Jihong**.** Numerical and experimental research on annular crossed cable-truss structure under cable rupture. Earthquake Engineering and Engineering Vibration, 2017, 16(3): 557-569.
[18] Shen Shizhao., Xu Chongbao, Zhao Chen. "Suspension structure design", Beijing, China Architecture & Building Press, 17-19, 2006.
[19] Xue Suduo, Lu Jian, Li Xiongyan, Liu Renjie. Improved force iteration method based on rational shape design solving self-stress modes of cable-truss tensile structure, Advanced Steel Construction. 2020,16(2), 170-180.
[20] Zhao Ping, Sun shanxing, Zhou Wensheng. Construtction process inverse simulation analysis of cable dome based on ansys. Industrial Construction, 2013, 43(04), 127-130.
[21] Zhang Ailin, Hu Yang, Liu Xuechun. Numerical simulation analysis and research on the whole construction process of ribbed ring cable structure[A]. Tianjin University, Shanghai University of Jiaotong. Proceeding of the 10th National Symposium on Modern Structural Engineering [C]. Tianjin University, Shanghai University of Jiaotong: Academic Committee of the National Symposium on Modern Structural Engineering, 2010: 6.
[22] Yuan Xingfei, Dong Shilin. Inverse analysis of construction process for cable dome. Journal of building structures, 2001, 22(02), 75-80.
[23] Liu Renjie. Annular Crossed Cable-truss Structures: Numerical and experimental verification. Beijing University of Technology, 2017.
[24] Guo Yanlin., Tian Guagnyu. "Cable structure system, design theory and construction control", Beijing, Science Press, 2014.
[25] Shen Zuyan, Zhang Lixin. Simulation of erection procedures of cable domes based on nonlinear FEM. Journal of Computation Mechanics, 2002, 19(04), 466-471.
[26] Technical Specification for Cable Structure, JGJ257-2012. Beijing: China Architecture & Building Press, 2008.

**Advanced Steel Construction** – Vol. 18 No.3 (2022) 699–706
**DOI:**10.18057/IJASC.2022.18.3.7


# BUCKLING BEHAVIOUR OF THE STEEL PLATE IN STEEL – CONCRETE – STEEL SANDWICH COMPOSITE TOWER FOR WIND TURBINE

Yu-Hang Wang [1], Shu-Qi Wang [2], Xu-Hong Zhou [1], Ji-Ke Tan [3,*], Jiu-Lin Bai [1] and Ke Ke [1]

[1] *School of Civil Engineering, Chongqing University, Chongqing, China*
[2] *Northwest Electric Power Design Institute Co., Ltd. of China Power Engineering Consulting Group, Xian, China*
[3] *Department of Civil Engineering, Tsinghua University, Beijing, China*
** (Corresponding author: E-mail: tjk23@sina.com)*

**ABSTRACT**

To solve the problem of collapses caused by local buckling of steel plates under compression in traditional steel towers, a novel steel-concrete-steel (SCS) sandwich composite tower for a wind turbine is proposed in this paper. To study the buckling behaviour of steel plates in SCS sandwich composite towers, six specimens were designed and tested under axial compression. The specimens were designed considering the key parameters of curvature radius, thickness of the steel plate, and the spacing-to-thickness ratio (the ratio of stud spacing to the thickness of steel plate). The failure modes, normalised average stress-strain curves and load-strain curves of the specimens were assessed, and the effects of the curvature radius and the spacing-to-thickness ratio of the steel plate were analysed. The experimental results showed that the buckling strength of the steel plate increased with a decrease in the ratio of the curvature radius to the thickness of the steel plate. The finite element (FE) model of the elastic buckling stress of the steel plate of the SCS sandwich composite tower was employed and validated against the test results. In parametric study, the effects of governing parameters including the curvature radius of the steel plate, thickness of the steel plate and spacing of the studs, on the effective length factors of the inner and outer steel plates were analysed. Subsequently, the design rules of the effective length factor of the inner and outer steel plates, and the design methods of spacing of studs to prevent local instability of the inner and outer steel plates before yielding were proposed.

**ARTICLE HISTORY**

Received: 23 June 2021
Revised: 17 January 2022
Accepted: 31 January 2022

**KEYWORDS**

Axial compression;
Buckling behaviour;
Curvature radius;
Effective length factor;
Finite element;
Composite tower



## 1. Introduction

Wind energy is a type of clean renewable energy, and wind power generation is the most widely used and fastest-growing new energy generation technology. As the main load-bearing structure of the wind turbine, the tower not only supports the weight of the nacelle and rotor, but also bears the wind and dynamic loads. Therefore, the tower plays an important role in the stable operation of the entire wind turbine. Currently, steel towers are the most common form of wind turbine support structures because of their simple structure, high construction efficiency, and good safety. The steel tower is a large-size thin-walled steel tube structure that is very sensitive to initial imperfections. Under compression, the minor imperfections in the steel tower structure may cause local buckling or even collapse, as shown in Fig. 1 [1]. Once the tower collapses, it causes significant economic losses.

**Fig. 1** Steel tower collapse accident caused by instability failure

It is well known that steel plates in concrete-filled steel tube (CFST) structures have better stability than traditional steel tubular structures [2-3]. Therefore, to solve the problem of collapse caused by local buckling of steel plates under compression in traditional steel towers, a novel steel-concrete-steel (SCS) sandwich composite tower for a wind turbine is proposed in this paper, as shown in Fig. 2. The inner and outer steel plates of the SCS sandwich composite tower are connected to the concrete through studs, which have a constraining effect on the concrete, and the concrete plays an out-of-plane support role on the steel plate, which can give full play to the material advantages of both concrete and steel. Therefore, the buckling capacity of the steel plate in the SCS sandwich composite tower is higher than that of the steel plate in the steel tower. In the design of the tower structure, as shown in Fig. 3, six types of loads should be considered: the gravity load of the wind wheel and engine room ($G_1$), eccentric bending moment ($M_{YT}$), aerodynamic thrust ($F_{XH}$), and torque ($M_{XH}$) caused by the wind wheel and engine room, gravity load of the tower ($G_2$) and transverse wind load of the tower ($q(z)$). Under the combined action of the aforementioned six types of loads, the inner and outer steel plates at the bottom section of the composite tower with greater compressive stress may suffer local instability failure, which will affect the safety of the tower structure. Therefore, the compression stability of the steel plate at the bottom of the tower is of great significance for structural safety. In this study, to make full use of the mechanical properties of the steel plate material and ensure that the steel plate does not buckle before yielding, the local stability behaviour of the steel plate in the SCS sandwich composite tower under axial compression was investigated. This study aims to provide a theoretical basis for the application of SCS sandwich composite structures for wind turbine.

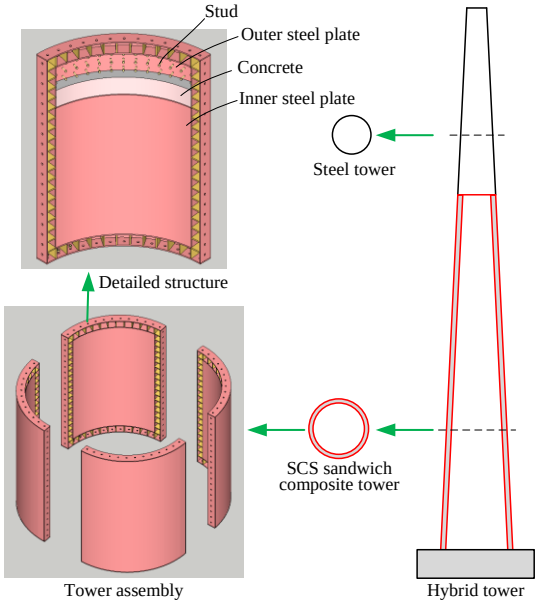


**Fig. 2** Schematic diagram of SCS sandwich composite tower

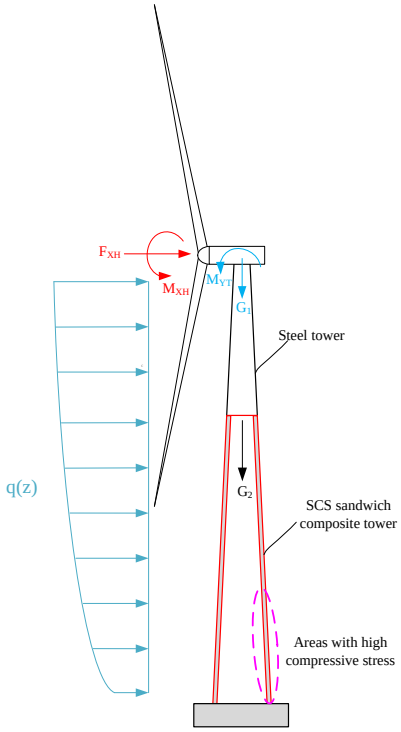


**Fig. 3** Load diagram of a new type of hybrid tower

There have been many studies on the buckling performance of steel plates of SCS sandwich composite structures [4-6]. Choi et al. [7-9] conducted an axial compression test of steel plate-concrete wall structures, and the experimental results showed that local buckling of the steel plate occurred between adjacent studs. When the spacing-to-thickness ratio was relatively large, increasing the yield strength of the steel plate has little effect on the compression strength of the steel plate. In addition, the buckling coefficient and the effective length factor of the steel plate were studied based on the plate theory and column theory, respectively, and a simplified formula for calculating the critical elastic buckling stress of the steel plate was proposed. Yan et al. [10] proposed a new type of SCS sandwich composite wall and completed eight axial compression tests. Based on the test results, a theoretical model of the wall compressive strength under different connection modes was established. The effective length factor was determined to be 0.825 by summarizing the 62 test results. Yang et al. [11] carried out 10 axial compression tests on double-skin composite wall specimens considering the influence of stud arrangement and spacing-to-thickness ratio. Based on the test results, they proposed a formula for limiting the spacing-to-thickness ratio to prevent local instability of the steel plates. Uy et al. [12-13] studied the buckling behaviour of steel plates of steel-concrete composite members by using the finite strip model, and proposed a design method for determining the buckling coefficient and effective length factor of steel plates, as well as a design method for selecting the width-thickness ratio of the steel plate. Cai et al. [14] theoretically investigated the elastic local buckling of steel plates in rectangular CFST columns with restraint bars under axial compressive loads. Furthermore, they derived the formula for calculating the critical stress of elastic buckling of steel plate is derived by using the energy method. They also determined the limit values for the spacing of restraint bars, the width-height ratio, and the width-thickness ratio to ensure that local bucking failure of steel plate does not occur before the steel plate yielding. Hu et al. [15] conducted axial compression tests on 12 square CFST columns with restraint bars, and the loads were only applied on the steel plates. The influences of the width-to-thickness ratio of the steel plate and the ratio of the vertical spacing of the tie bars to the width of the steel plate on the stability performance of the steel plate were studied. Based on the FE parameter analysis results, a calculation method for steel plate buckling coefficient was proposed.

Previous studies on SCS sandwich composite structures mainly focused on the buckling behaviour of steel plates under axial loads, while there are few studies on the stability of steel plates when the axial load is only applied to the steel plate in the SCS sandwich composite structure. In addition, no relevant reports are available on the buckling behaviour of SCS composite sandwich tower structure under axial compression. Therefore, to study the stability performance of the steel plate under axial compression of the SCS sandwich composite tower structure proposed in this paper, six specimens were designed with curvature radius and spacing-to-thickness ratio as the key parameters. In the tests, the axial load was only applied to the steel plate, while the concrete only acted as the out-of-plane support for the steel plate without bearing any load. The buckling behaviour of the steel plate of the composite tower was investigated, and the design rules of the effective length factor and the design methods of spacing of studs to prevent local instability of the inner and outer steel plates before yielding were elucidated. The outcome of this study provides a theoretical basis and design guidance for the application of the SCS sandwich composite structure for wind turbines.

## 2. Experimental study

### 2.1. Specimens

Owing to the limitation of the size and loading capacity of the test device, only a partial structure of the composite tower was selected for the design of the test specimens. In this study, six specimens were designed with a height of 1000 mm and a core concrete thickness of 100 mm. The inner and outer steel plates of the SCS sandwich composite structure specimens were connected to the concrete through studs. The diameter and length of all the studs are 13 mm and 60 mm, respectively. A 12 mm thick endplate was welded at the upper and lower ends of the specimens, and the section centroid of the steel plate coincided with the endplate centroid. Detailed parameter information for the specimens is shown in Fig. 4 and Table 1. The grade of concrete of all specimens was C30, and the grade of the steel material was Q235. The average measured 28-day compressive strength of the concrete cube was 37.3 MPa. Tensile coupon tests of steel plates were carried out, and the measured steel plates material properties are listed in Table 2.

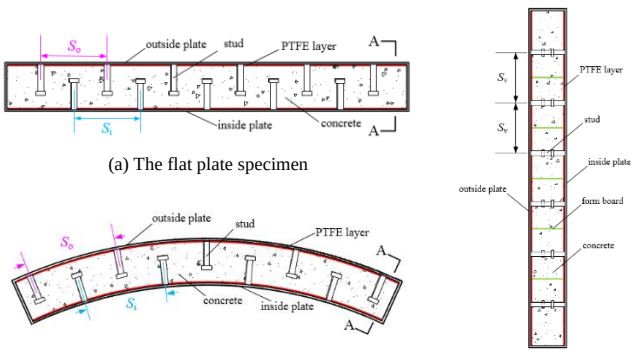


(a) The flat plate specimen

(b) The curved plate specimen

(c) A-A section

**Fig. 4** Dimensions and detailed information of specimens

**Table 1**
Detailed parameters of specimens

| Specimens | Concrete | Studs | $R_i$ (mm) | $R_o$ (mm) | $t$ (mm) | $S_i$ (mm) | $S_o$ (mm) | $S_v$ (mm) | $S_v/t$ (-) | $\rho$ (mm) |
|---|---|---|---|---|---|---|---|---|---|---|
| SPB1 | - | - | 1000 | 1100 | 2.45 | - | - | - | - | 7 |
| SPB2 | Yes | Yes | 1000 | 1100 | 2.30 | 244 | 269 | 250 | 109 | 30 |
| SPB3 | Yes | Yes | 1000 | 1100 | 4.70 | 147 | 161 | 150 | 32 | 10 |
| SPB4 | Yes | Yes | 1000 | 1100 | 2.30 | 147 | 161 | 150 | 65 | 27 |
| SPP1 | Yes | Yes | ∞ | ∞ | 2.28 | 150 | 150 | 150 | 66 | 25 |
| SPP2 | Yes | - | ∞ | ∞ | 2.31 | - | - | - | - | 0 |

where, $R_i$ is the curvature radius of the inner steel plate, $R_o$ is the curvature radius of the outer steel plate, $t$ is the thickness of the steel plate, $S_i$ is the spacing of studs on the inner steel plate along the arch direction, $S_o$ is the spacing of studs on the outer steel plate along the arch direction, $S_v$ is the spacing of studs on the inner and outer steel plates along the height direction, $S_v/t$ is the spacing-to-thickness ratio of the steel plate, and $\rho$ is the distance between the load point and centroid of the section.

**Table 2**
Mechanical properties of steel materials

| Thickness (mm) | Yield strength (MPa) | Ultimate strength (MPa) | Modulus of elasticity (GPa) |
|---|---|---|---|
| 2.5 | 332 | 455 | 189 |
| 5.0 | 298 | 458 | 199 |

As illustrated in Fig. 4, to prevent the axial load from acting on the concrete, a polytetrafluoroethylene layer with a very small elastic modulus was placed between the steel plate and the concrete, and a series of 10 mm thick form boards were placed between the adjacent studs to cut off the vertical force path of the concrete. To accurately control the height of each layer of concrete and facilitate placing of the boards, a series of 50 mm × 50 mm holes were reserved at the design height of the side plate of the specimen. After the concrete was poured, the hole was welded shut with a small steel plate. The specimen preparation process is illustrated in Fig. 5.

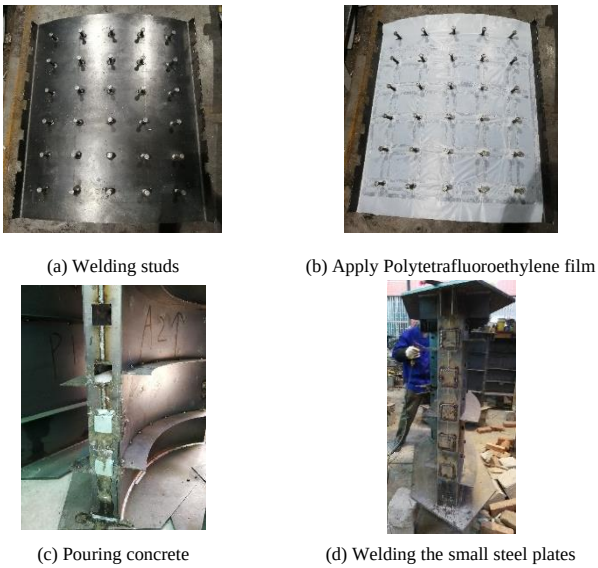

(a) Welding studs (b) Apply Polytetrafluoroethylene film

(c) Pouring concrete (d) Welding the small steel plates

**Fig. 5** Fabrication process of specimens

### 2.2. Testing programme

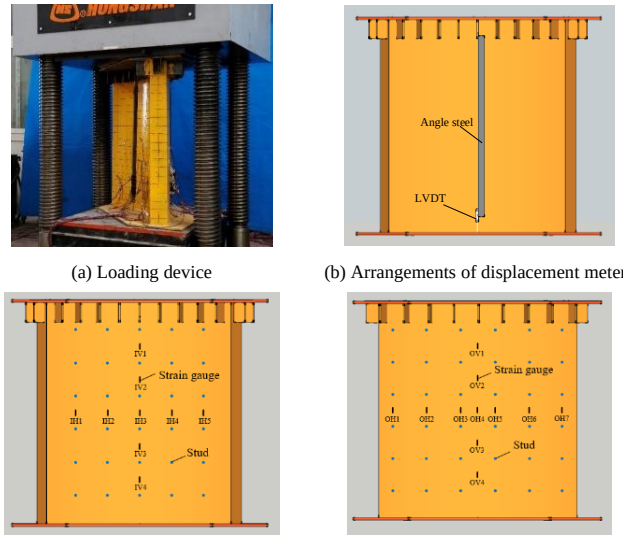


(a) Loading device (b) Arrangements of displacement meters

(c) Strain gauges arrangement of inner steel plate (d) Strain gauges arrangements of outer steel plate

**Fig. 6** Test setup and instrumentation plan

Compression tests were conducted using servo-controlled electrohydraulic testing machine. The test device and measurement scheme are shown in Fig. 6. The axial force applied to the specimens was measured by the force sensor of the device, and the axial deformation of the specimens was measured using linear variable differential transformers (LVDTs) arranged symmetrically at the centre of the inner and outer steel plates (see Fig. 6b). To capture the strain change of the steel plate during the entire loading process and analyse the stress of the inner and outer steel plates, vertical strain gauges were arranged in the middle of the specimens along the horizontal and vertical directions, as shown in Figs. 6c and 6d. Before testing, the specimens were preloaded to 10% of the nominal bearing capacity (equal to $f_y A_s$) to check whether the specimens were uniformly stressed and whether the displacement measurement worked properly. The test was conducted using displacement control, and when the specimens were severely damaged or the load dropped to below its 85% of the peak strength of the specimens, the tests were terminated.

## 3. Experiments and analysis

### 3.1. Structural behaviours and failure modes

The failure modes of all specimens are shown in Fig. 7. As presented in Fig. 7a, in the early stage of loading, the specimen SPB1 was approximately in the elastic stage. During the loading process, when the load reached approximate $0.65N_m$ ($N_m$, the corresponding peak load of the specimens), the upper left part of the outer steel plate exhibited local buckling. When continuing to load to $0.72N_m$, local buckling appeared in the middle and lower parts of the inner steel plate. When the load continued to increase, the lower left part of the inner steel plate buckled. When the load reached the peak load $N_m$, the specimen made a loud noise and the load began to drop very quickly. When the load continued to increase, local buckling appeared near the mid-height of the outer steel plate, the lower right side of the inner steel plate and the left side of the inner and outer steel plates buckled.

For specimen SPB2, when the load reached approximately $0.92N_m$, the inner steel plate first began to buckle; then the steel plate buckled below the first row of studs on the upper left of the outer steel plate. When the load reached the peak load $N_m$ (i.e. 771.4 kN), the curve at the upper left of the outer steel plate was pulled through, and three intervals of studs on the upper left of the inner steel plate buckled. When the load continued to increase, the upper right of inner steel plate began to buckle, and the steel plate on the top of the left plate and right plate buckled. The final failure mode of specimen SPB2 is shown in Fig. 7b.

As shown in Figs. 7c and 7d, the specimens SPB3 and SPB4 had similar failure modes, and the buckling positions of the inner and outer steel plates of specimens SPB3 and SPB4 were almost at the same height as the specimen. When loaded to $0.9N_m$, the first row of studs on the upper right of the outer steel plate buckled, and the first row of the studs of the inner steel plate also began to buckle. When the load reached $N_m$, the curve at the upper right of outer steel plate was pulled through, and the curve in the second row of the inner steel plate was pulled through between the horizontal studs. When the load continued to increase, the curve on the inner and outer steel plates was pulled through the left and right side plates.

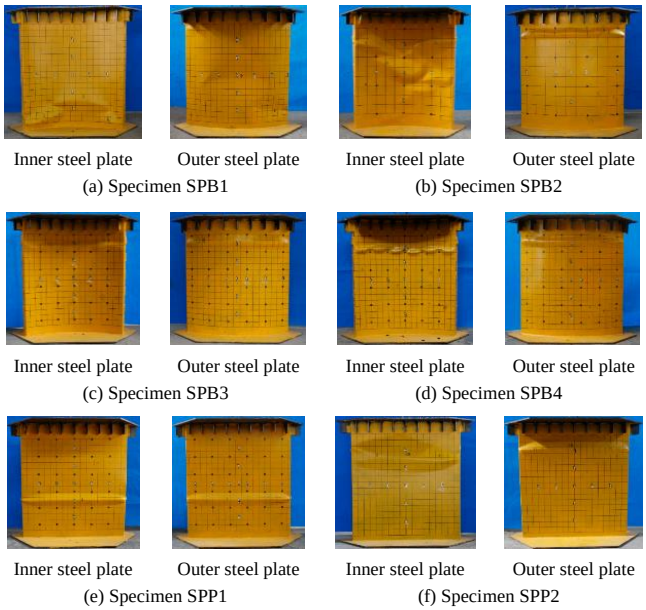

Inner steel plate Outer steel plate Inner steel plate Outer steel plate
(a) Specimen SPB1 (b) Specimen SPB2

Inner steel plate Outer steel plate Inner steel plate Outer steel plate
(c) Specimen SPB3 (d) Specimen SPB4

Inner steel plate Outer steel plate Inner steel plate Outer steel plate
(e) Specimen SPP1 (f) Specimen SPP2

**Fig. 7** Failure modes of the specimens obtained from test

Specimens SPP1 and SPP2 were flat steel plate specimens. For specimen

SPP1, when loaded to approximately 0.95$N_m$, local buckling occurred on the lower middle of outer steel plate. When the load reached the peak load of 550.3 kN (i.e. $N_m$), the lower middle of the inner steel plate buckled. The local buckling position of the specimen SPP1 occurred between two rows of studs, and the vertical displacements of each stud were consistent, and there was no damage to the concrete between the studs. The final failure mode of specimen SPP1 is illustrated in Fig. 7e. For specimen SPP2, when loaded to approximately 0.88$N_m$, the upper left part of the outer steel plate buckled. When the load continued to increase, the upper left part of the inner steel plate buckled. When loaded to the peak load $N_m$, the upper right part of the inner and outer steel plates buckled. For specimen SPP2, because the concrete only provided out-of-plane support for the steel plates, there was no damage to the concrete. The final failure mode of SPP2 is illustrated in Fig. 7f.

### *3.2. Normalised average stress-strain curves*

Fig. 8 shows the normalised average stress-strain curves of SCS sandwich composite tower specimens with different spacing-to-thickness ratios. The spacing-to-thickness ratios of specimens SPB2, SPB4 and SPB3 were 109, 65, and 32, respectively, and the corresponding spacing of the studs was 250, 200, and 150 mm, respectively. As reported in Fig. 8, the peak strength tends to increase with a decrease in the spacing-to-thickness ratio, especially for the specimen with the smaller spacing-to-thickness ratio. Fig. 9 shows the effect of the steel plate curvature radius on the peak strength of the specimens. As presented in Fig. 9, a steel plate with a small curvature radius has a larger peak strength. This is because when the curvature radius of the steel plate decreases, the out-of-plane stiffness of the steel plate increases, the stability of the steel plate is improved, and the peak strength increases accordingly.

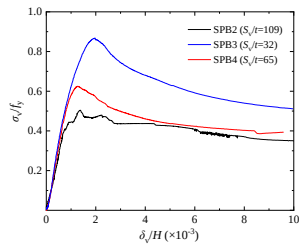


**Fig. 8** Effect of $S_v/t$ on the peak strength

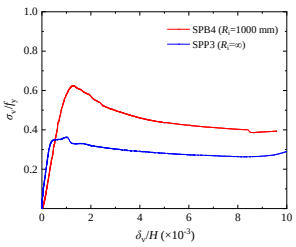


**Fig. 9** Effect of steel plate curvature radius on the peak strength

### *3.3. Load-strain curves*

Using SPB2 as an example, the load-strain curve of the specimen was analysed. Fig. 10 presents the load-strain curve of the measuring point at the instability failure position of specimen SPB2, where "positive value" represents the tensile strain and "negative value" represents the compressive strain. As shown in Fig. 10, when the applied load is less than approximately 680 kN (equal to 0.88$N_m$), the relationship between load and strain is basically linear. The experiments showed that there was an obvious local buckling that occurred in the steel plate when the load reached 0.88$N_m$, resulting in the corresponding strain data of the inner and outer steel plates having an obvious mutation. According to the research results reported in literature [11], the load corresponding to the strain mutation point can be considered as the local buckling load of the steel plate. If the load-strain curve does not change, the load value corresponding to the first buckling of the steel plate is considered as the local buckling load of the steel plate. Similarly, local buckling loads of the inner and outer steel plates can be reached. The peak load ($N_u$), and the local buckling load of the inner steel plate ($N_{li}$), and outer steel plate ($N_{lo}$) of the specimens are listed in Table 3.

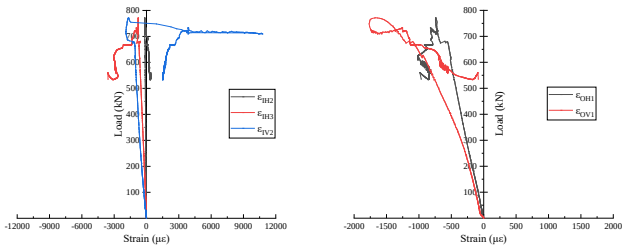


(a) The inner steel plate (b) The outer steel plate

**Fig. 10** Load-strain curves of specimen SPB2

**Table 3**
The peak load and local buckling load of specimens

| Specimens | $R_i$ (mm) | $S_v/t$ (-) | $N_u$ (kN) | $N_{li}$ (kN) | $N_{lo}$ (kN) |
|---|---|---|---|---|---|
| SPB1 | 1000 | - | 621.8 | 426.8 | 400.4 |
| SPB2 | 1000 | 109 | 771.4 | 679.6 | 766.4 |
| SPB3 | 1000 | 32 | 2432.8 | 2265.6 | 2398.3 |
| SPB4 | 1000 | 65 | 955.2 | 800.6 | 857.0 |
| SPP1 | ∞ | 66 | 550.3 | 503.8 | 528.5 |
| SPP2 | ∞ | - | 544.9 | 527.7 | 481.8 |

## 4. Finite element analysis

### *4.1. Development of models*

The ABAQUS package was employed for the FE element analysis. An ideal elastic-plastic constitutive model was adopted for the steel material. It can be seen from the experimental results that the load was applied only to the steel plate during the test, and the concrete only served as an out-of-plane support for the steel plate; therefore, an elastic constitutive model was adopted for the concrete. The elastic modulus of concrete was 32500 MPa, and the Poisson's ratio was 0.2. A gap was reserved between the concrete to consider the effect of 10mm thickness form boards with a negligible elastic modulus.

In the FE model, as shown in Fig. 11, S4R and C3D8R were selected to simulate the steel plate and concrete, respectively. To balance the calculation accuracy and efficiency of the FE model, a characteristic mesh element size of 20 mm for the steel plate and concrete was considered. In accordance with the test results, a linear elastic spring element was employed in the FE model to simplify the simulation of the studs. The stiffness of the studs along the length direction was 455.5 kN/mm, and the shear stiffness of the studs was not considered. The "surface-surface contact" was used to define the interface between steel plate and concrete, and the "hard contact" was used to simulate the normal behaviour interaction between the steel plate and concrete; the frictionless interaction was applied in the tangential direction. The top end of the specimen was completely fixed. The reference point RP-1 was introduced and coupled with the bottom surface of the steel plate to consider the effect of the endplate. Meanwhile, the lateral displacement of the reference point was limited (U1=U2=0), and the load was applied to the reference point RP-1.

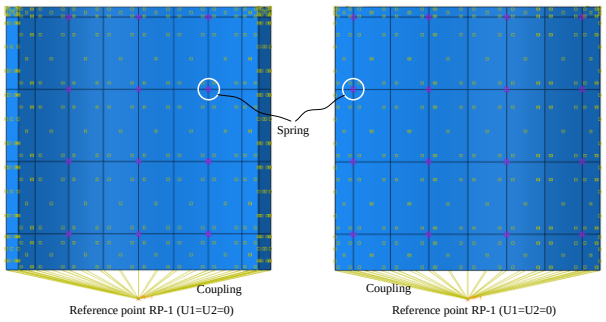


**Fig. 11** Finite element modelling

In the FE model, the initial geometric imperfection and the initial eccentricity of the load of the specimens were introduced. Generally, there are two methods for considering the initial imperfections of the specimens. One is based on the eigenvalue buckling analysis results. In this method, the first buckling modes were selected as the initial imperfections of the specimens, and 1/1000 of the height of the specimen was set as the magnitude of the initial imperfections. The other method introduced the measured initial defect data of the specimen. In this study, the measured data of the initial out-of-plane deformation (see Fig. 12) of the steel plate were introduced into the model to consider the initial geometric imperfection.

The initial load eccentricity was applied by adjusting the position of the reference point RP-1, and the magnitude and direction of the eccentricity were determined by the following methods. Note that, in practical design and analysis, the initial imperfections caused by initial load eccentricity can not be considered.

Assuming that the axial load is $N$, and the eccentricity of the load toward the outer plate is ρ, as shown in Fig. 13, the centroid of the sections between the centre points A and B of the steel plate are $y_1$ and $y_2$, respectively. Then, the vertical stress of the steel plate at positions A and B in the elastic stage can be

expressed as:

$$\sigma_{\mathrm{A}} = \frac{N}{A} + \frac{N\rho y_1}{I}$$
$$\sigma_{\mathrm{B}} = \frac{N}{A} - \frac{N\rho y_2}{I} \quad (1)$$

where, $A$ is the sectional area of the steel plate, and $I$ is the moment of inertia of the section. According to Hooke's law, the vertical strain of the steel plate at A and B in the elastic stage can be obtained using Eq. (2), where $E_s$ is the elastic modulus of the steel.

$$\varepsilon_{\mathrm{A}} = \frac{\sigma_{\mathrm{A}}}{E_{\mathrm{S}}}$$
$$\varepsilon_{\mathrm{B}} = \frac{\sigma_{\mathrm{B}}}{E_{\mathrm{S}}} \quad (2)$$

Then, the initial load eccentricity of the specimen can be obtained as follows:

$$\rho = \frac{2I}{A} \frac{1}{\frac{\varepsilon_{\mathrm{A}}+\varepsilon_{\mathrm{B}}}{\varepsilon_{\mathrm{A}}-\varepsilon_{\mathrm{B}}}(y_1+y_2)-(y_1-y_2)} \quad (3)$$

The initial eccentricity of the load was determined by calculating the strain data at the same height as the centreline of the inner and outer steel plates. The initial eccentricity, $\rho$, of the load was obtained by averaging the initial eccentricity at each height. The initial eccentricities of the load of the specimens are listed in Table 2.

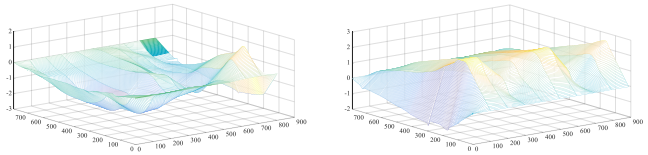

(a) Inner steel plate (b) Outer steel plate

**Fig. 12** Measured geometric imperfections of specimen SPB1

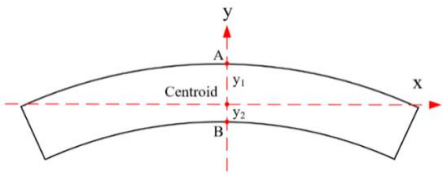


**Fig. 13** Calculation and analysis diagram of load initial eccentricity

### *4.2. Model validation*

#### *4.2.1. Failure modes*

Fig. 14 shows the failure modes of the specimens obtained from the FE modelling. Although the initial geometric imperfection and eccentricity of the load were introduced in the FE model, the FE model did not consider the influence of residual stress and the initially introduced geometric imperfection and eccentricity of the load were not identical to those of the specimens. Therefore, the above factors lead to slight differences between the numerical and experimental results. In general, the failure modes obtained from the FE results are in good agreement with the test results.

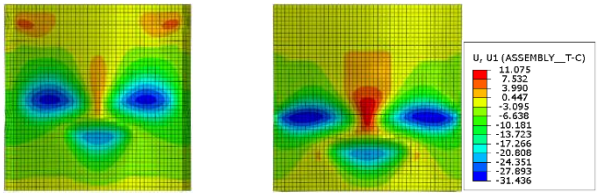


Inner steel plate Outer steel plate

(a) Specimen SPB1

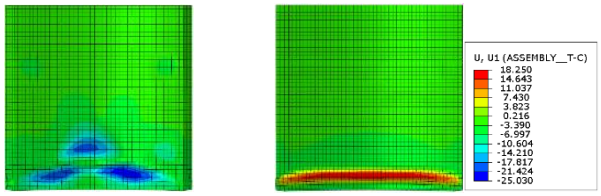


Inner steel plate Outer steel plate

(b) Specimen SPB2

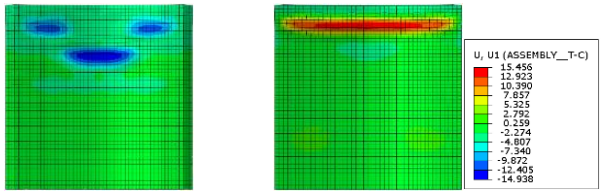


Inner steel plate Outer steel plate

(c) Specimen SPB3

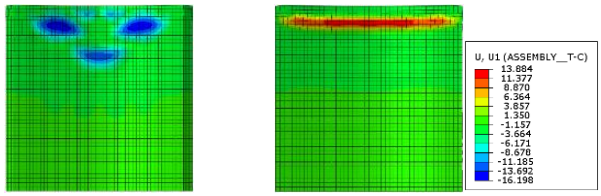


Inner steel plate Outer steel plate

(d) Specimen SPB4

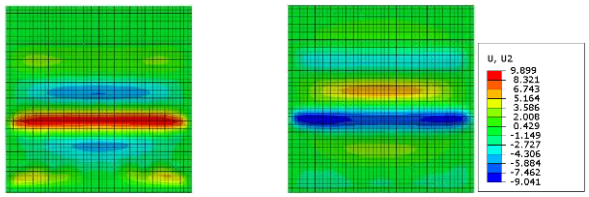


Inner steel plate Outer steel plate

(e) Specimen SPP1

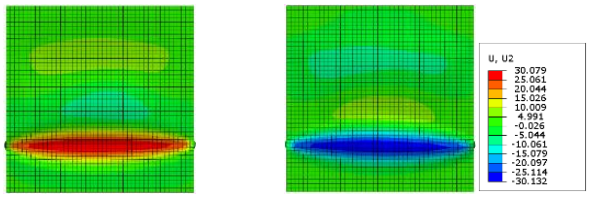


Inner steel plate Outer steel plate

(f) Specimen SPP2

**Fig. 14** Failure modes of specimens obtained from FE modelling

#### *4.2.2. Load-displacement curves*

Fig. 15 shows a comparison of the load-displacement curves between the test and FE results and Table 4 shows the comparison of the bearing capacity between the test and FE results. Owing to the manufacturing defects and measurement deviations of the specimens, there might be a slight difference between the FE results and the test results. However, the FE model accurately simulate the bearing capacity and elastic stiffness of the specimens. Therefore, it can be observed that the FE model is in good agreement with the experimental results.

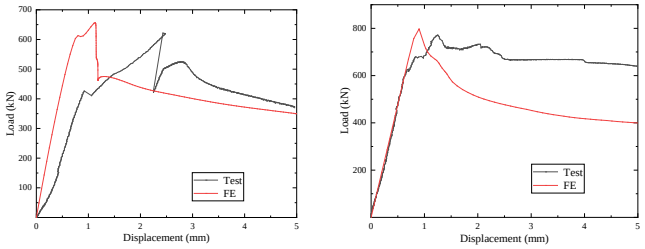


(a) Specimen SPB1 (b) Specimen SPB2

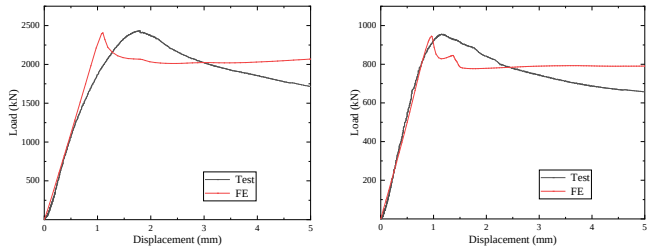


(c) Specimen SPB3 (d) Specimen SPB4

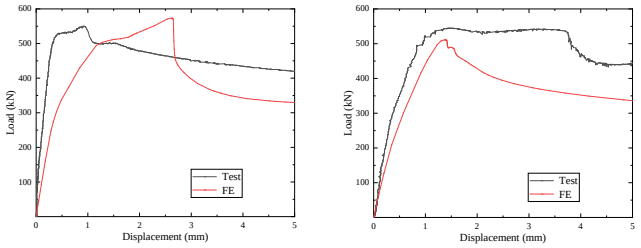


(e) Specimen SPP1 (f) Specimen SPP2

**Fig. 15** Comparison of load-displacement curves between test and FE results

**Table 4**
Comparison of bearing capacity between test and FE results

| | Specimens | SPB1 | SPB2 | SPB3 | SPB4 | SPP1 | SPP2 |
|---|---|---|---|---|---|---|---|
| Bearing capacity | Test (kN) | 621.8 | 771.4 | 2432.8 | 955.2 | 550.2 | 544.9 |
| | FE (kN) | 655.9 | 797.7 | 2407.3 | 945.2 | 573.1 | 510.9 |
| | FE/Test | 1.05 | 1.03 | 0.99 | 0.99 | 1.04 | 0.94 |

## 5. Parametric study

According to the failure mode of the specimens of the SCS sandwich composite tower, the local buckling of the steel plate only occurred in all specimens between two rows of studs. Therefore, in this study, the stud was regarded as the supporting point of the steel plate, and the steel plate within the spacing of the studs was considered as the axial compression member, as shown in Fig. 16. The critical elastic buckling load ($P_{cr}$) of the steel plate was calculated using the following Eq. (4).

$$P_{cr} = \frac{\pi^2 E_s I}{(kl)^2} \tag{4}$$

where, $E_s$ is the elastic modulus of the steel plate; $I$ is the moment of inertia of the section; $k$ is the effective length factor of the steel plate.

As shown in Fig. 16, the thickness of the steel plate is $t$, the vertical spacing of the studs is $S_v$, and the horizontal spacing is $S_h$. Then, the critical elastic buckling load of the steel plate can be obtained from Eq. (5):

$$P_{cr} = \frac{\pi^2 E_s (t^3 S_h/12)}{(kS_v)^2} \tag{5}$$

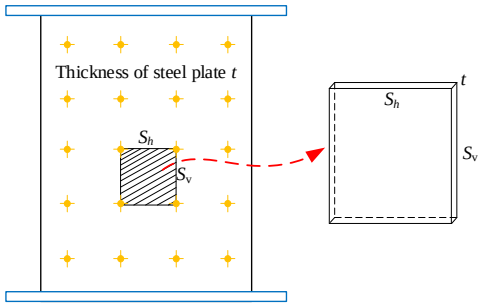


**Fig. 16** Elastic buckling stress model of steel plate

The corresponding critical stress of elastic buckling is:

$$\sigma_{cr} = \frac{P_{cr}}{A} = \frac{\pi^2 E_s (t^3 S_h/12)}{(kS_v)^2 (tS_h)} = \frac{\pi^2 E_s}{12k^2 \left(\frac{S_v}{t}\right)^2} \tag{6}$$

According to Eq. (6), the effective length factor $k$ is an important factor affecting the critical stress of the elastic buckling of the steel plate; therefore, it is necessary to study the effective length coefficient. In this study, the key parameters affecting the effective length factor of steel plates in SCS sandwich composite towers are the curvature radius of the steel plate, the thickness of the steel plate and the spacing of the studs. Therefore, in the parametric study, the effect of the above key parameters on the effective length factor of the SCS sandwich composite tower is analysed, which is expected to provide a basis for the proposal of a design method for the effective length factor.

### 5.1. Finite element model of tower structure

To accurately simulate the critical elastic buckling stress of a steel plate in an actual tower structure, an FE model was established to analyse the critical elastic buckling stress of the steel plate in the SCS sandwich composite tower. Owing to the support provided by the core concrete to the inner and outer steel plates, the buckling and deformation directions of the inner and outer steel plates are different, which leads to different local stabilities of the inner and outer steel plates. Therefore, in a parametric study, the inner and outer steel plates should be studied separately.

In the parametric study, the parameters of the FE model of the tower structure (see Fig. 17) are the same as those of the above-mentioned specimen FE model, but it should be noted that: (1) the eigenvalue buckling analysis is used to obtain the critical elastic buckling load of the steel plate, and the effective length factor of the steel plate can be obtained by calculating the critical elastic buckling stress using Eq. (6); (2) the vertical and horizontal spacing of the studs in all the FE models is equal; (3) The heights of all specimens were set as 6-10 times the spacing of the studs to eliminate the influence of boundary conditions on the FE analysis results.

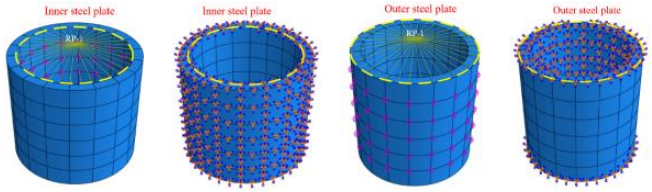


(a) Inner steel plate (b) Outer steel plate

**Fig. 17** FE model of SCS sandwich composite tower

### 5.2. Effect of the stud spacing

In the parametric study, the spacing of the studs of the inner and outer steel plates was considered as $S_v$ = 100, 115, 133 and 150 mm. Fig. 18 shows the effect of the stud spacing on the effective length factor of the inner and outer steel plates. It can be seen that the effective length factor of the inner and outer steel plates decreasing trend is basically the same. With an increase in the stud spacing, the effective length factor decreases, and the outer steel plate has a larger effective length factor than that of the inner steel plate.

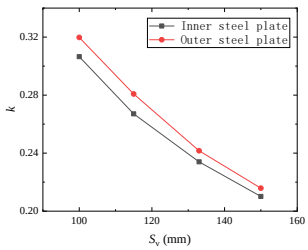


**Fig. 18** Effect of the stud spacing on the effective length factor

### 5.3. Effect of the steel plate thickness

In the parametric study, steel plate thicknesses ($t$) of 2, 3, 4, and 5 mm were considered. The effect of the steel plate thickness on the effective length factor is shown in Fig. 19. As shown in Fig. 19, for a steel plate of the same thickness, the effective length factor of the outer steel plate is greater than that of the inner steel plate. The increase in the thickness of the steel plate has a positive effect on the effective length factor, especially for the outer steel plate. The effect of the spacing-to-thickness ratio $S_v/t$ on the effective length factor is shown in Fig. 20. As illustrated in Fig. 20, with an increase in the spacing-to-thickness ratio,

the effective length factor decreases and the influence of the spacing-to-thickness ratio on the effective length factor of the inner and outer steel plates is similar. The effective length factor of the outer steel plate was greater than that of the inner steel plate with the same spacing-to-thickness ratio.

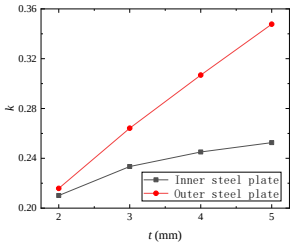


**Fig. 19** Effect of steel plate thickness on the effective length factor

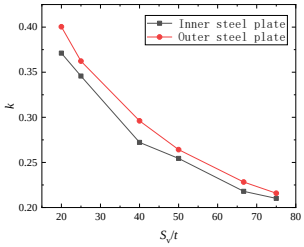


**Fig. 20** Effect of $S_v/t$ on the effective length factor

### *5.4. Effect of the steel plate curvature radius*

In the parametric study, the steel plate curvature radius ranged between 400 and 1000 mm at 200 mm intervals. Fig. 21 shows the effect of the steel plate curvature radius on the effective length factor. With an increase in the curvature radius of the steel plate, the effective length factors increase. The effective length factors of the outer steel plate are generally larger than those of the inner steel plate, and the increase in the effective length factors of the outer steel plate is greater. This is because when the curvature radius of the steel plate increases, the local stability of steel plate becomes worse, and the steel plate is more prone to local instability failure. The effect of $S_v/R$ on the effective length factor is shown in Fig. 22. As shown in Fig. 22, the effective length factor of the steel plate is smaller when the $S_v/R$ becomes larger, and the effective length factor of the outer steel plate is larger than that of the inner steel plate and the trends of the two curves are similar.

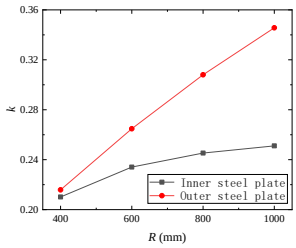


**Fig. 21** Effect of steel plate curvature radius on the effective length factor

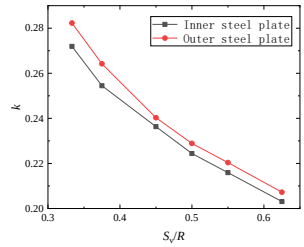


**Fig. 22** Effect of $S_v/R$ on the effective length factor

## 6. Development of design rules

In this study, the critical stress of elastic buckling of a steel plate was analysed based on the column stability theory. The integral FE model of the actual tower structure was developed based on the validated FE model and actual tower structure form. The influence of the curvature radius of the steel plate, thickness of the steel plate and vertical spacing of the stud on the effective length factor of the inner and outer steel plates were studied. From the results of the parametric analysis, it can be seen that the governing parameters of the effective length factors of the inner and outer steel plates are the spacing-to-thickness ratio $S_v/t$ and the spacing-to-curvature radius of the steel plate $S_v/R$, and the effective length factors of the inner and outer steel plates are smaller when the spacing-to-thickness ratios $S_v/t$ and $S_v/R$ have larger values. Note that $S_v/t$ and $S_v/R$ are dimensionless coefficients, which can effectively eliminate the influence of the size effect on the analysis results. When the curvature radius of the steel plate tends to infinity (i.e. the flat steel plate), the effective length factor of the flat steel plate proposed by Yan et al. [10] is 0.825. Because the steel plate of the SCS sandwich composite tower is curved, l the local stability of the steel plate with curvature is different from that of the flat steel plate, and the effective length factor $k$ is no longer a constant value for the steel plate with curvature.

In the form of Eq. (6), based on the newly generated 240 FE analysis results, the design method of the effective length factor k for the inner and outer steel plates of the SCS sandwich composite tower is achieved through linear regression, as follows:

Inner steel plate:

$$k = \frac{1}{0.5170\left(\frac{S_v}{R}\right)^{0.45}\left(\frac{S_v}{t}\right)^{0.55}+1.212} \tag{7}$$

Outer steel plate:

$$k = \frac{1}{0.2316\left(\frac{S_v}{R}\right)^{1.1}\left(\frac{S_v}{t}\right)^{0.9}+1.212} \tag{8}$$

Fig. 23 shows a comparison of the effective length factor calculated using Eq. (7) and the FE analysis results, and good agreement was observed between the predicted and the numerical results. As shown in Fig. 23, the mean values of predicted results to the numerical results of the inner and outer steel plates were 1.01 and 1.00 respectively, and the coefficients of variation (COV) of the inner and outer steel plates were 0.0026 and 0.0082 respectively. This indicates that the proposed design method can provide accurate and consistent predictions.

Substituting Eqs. (7) and (8) into Eq. (6), the design method for calculating the critical elastic buckling stress of the inner and outer steel plates can be obtained as follows:

Inner steel plate:

$$\sigma_{\text{cri}} = \frac{\pi^2 E_s\left(0.5170\left(\frac{S_v}{R}\right)^{0.45}\left(\frac{S_v}{t}\right)^{0.55}+1.212\right)^2}{12\left(\frac{S_v}{t}\right)^2} \tag{9}$$

Outer steel plate:

$$\sigma_{\text{cro}} = \frac{\pi^2 E_s\left(0.2316\left(\frac{S_v}{R}\right)^{1.1}\left(\frac{S_v}{t}\right)^{0.9}+1.212\right)^2}{12\left(\frac{S_v}{t}\right)^2} \tag{10}$$

If the critical elastic buckling stress is no less than the yield strength of the steel plate, that is, no buckling occurs before the steel plate yields, then the limit design method of the spacing of the studs of the inner steel plate can be obtained as follows:

Inner steel plate:

$$S_{\text{vi}} \le \frac{1.212}{\sqrt{\frac{12f_y}{\pi^2 E_s t^2}-\frac{0.5170}{R^{0.45}t^{0.55}}}} \tag{11}$$

Outer steel plate:

$$S_{\text{vo}} \le \frac{1.212}{\sqrt{\frac{12f_y}{\pi^2 E_s t^2}-\frac{0.2316}{R^{1.1}t^{0.9}}}} \tag{12}$$

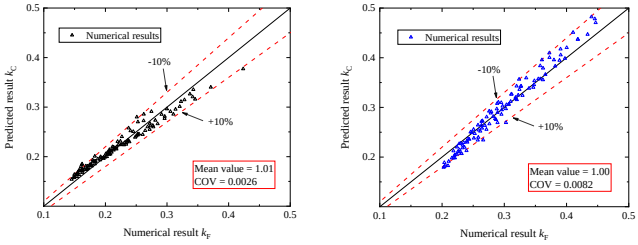


(a) Inner steel plate (b) Outer steel plate

**Fig. 23** Comparison between formula calculation value $k_C$ and FE value $k_F$

## 7. Conclusions

Six specimens of SCS sandwich composite towers were tested under axial compression, and FE models were employed and validated against the test results. The test results showed the following: (1) in all the specimens the local failure mode occurred between the studs; (2) the peak strength of the steel plate increased with a decrease in the curvature radius of the steel plate and a decrease in the spacing-to-thickness ratio; (3) the peak strength of the steel plate increased with a decrease in the spacing-to-thickness ratio (the decrease of the spacing of the studs and the increase of the thickness of the steel plate), and the influence of the thickness of the steel plate on the peak strength was more significant. An FE model of the tower structure was developed to analyse the critical elastic buckling stress of the steel plate in the SCS sandwich composite

tower. The influence of three parameters (curvature radius of the steel plate, thickness of the steel plate, and the spacing of the studs) on the effective length factors of the inner and outer steel plates was studied. Based on the parameter analysis results, the design rules of the effective length factor of the inner and outer steel plates, and design methods for the spacing of studs to prevent local instability of the inner and outer steel plates before yielding were proposed. The outcome of this study provides a theoretical basis and design guidance for the application of SCS sandwich composite structures in the field of wind power generation.

## Acknowledgments

The research is supported by China Postdoctoral Science Foundation (Grant No. 2022M711863) and Fok Ying Tung Education Foundation (Grant No. 171066).

## References

[1] Pan F.S., Wang F.W., Ke S.T. and Tang G., Buckling analysis and stability design of wind turbine tower with geometic imperfections, Acta Energiae Solaris Sinica, 10, 2659-2664, 2017.

[2] Wang S.Y., Chen A.Y. and Wan H.Y., Seismic behaviour of concrete-filled steel tube frames with external composite wall panels, Advanced Steel Construction, 17(1), 10-19, 2021.

[3] Wang Z., Yan J.B. and Liu X.M., Numerical and theoretical studies on double steel plate composite walls under compression at low temperatures, Advanced Steel Construction, 17(4), 376-384, 2021.

[4] Qi Y., Gu Q., Sun G.H., Zhao B.C. and Wang H.F., Tensile force and bending moment demands on headed stud for the design of composite steel plate shear wall, Advanced Steel Construction, 15(4), 338-348, 2019.

[5] Yan J.B., Wang Z. and Wang X., Behaviour of steel-concrete-steel sandwich plates under different ice-contact pressure, Advanced Steel Construction, 15(1), 116-122, 2019.

[6] Liu S.M., Ding H.S., Taerwe L. and De Corte W., Modifications to the global and interactive shear buckling analysis methods of trapezoidal corrugated steel webs for bridges, Advanced Steel Construction, 15(4), 349-363, 2019.

[7] Choi B.J., Kim W.K., Kim W.B. and Kang C.K., Compressive performance with variation of yield strength and width-thickness ratio for steel plate-concrete wall structures, Steel and Composite Structures, 14(5), 473-491, 2013.

[8] Choi B.J., Kang C.K., and Park H.Y., Strength and behavior of steel plate–concrete wall structures using ordinary and eco-oriented cement concrete under axial compression, Thin-Walled Structures, 84, 313-324, 2014.

[9] Kang C.K., Choi B.J., and Jeoung B.S., Compressive Behavior of Steel Plate-Concrete Structures using Eco-Oriented Cement Concrete. Journal of Korean Society of Steel Construction, 24(5), 583, 2012.

[10] Yan J.B., Wang Z., Luo Y.B. and Wang T., Compressive behaviours of novel SCS sandwich composite walls with normal weight concrete. Thin-Walled Structures, 141, 119-132, 2019.

[11] Yang Y., Liu J. and Fan J., Buckling behavior of double-skin composite walls: an experimental and modeling study, Journal of Constructional Steel Research, 121, 126-135, 2016.

[12] Uy B. and Bradford M.A., Local buckling of thin steel plates in composite construction: experimental and theoretical study, Structure and Buildings,110(4), 426-440,1995.

[13] Uy B. and Bradford M.A., Elastic local buckling of steel plates in composite steel-concrete members, Engineering Structures, 18(3), 193-200, 1996.

[14] Cai J. and Long Y.L., Local Buckling Of Steel Plates In Rectangular CFT Columns With Binding Bars. Journal of Constructional Steel Research, 65(4), 965-972, 2009.

[15] Hu H.S., Fang P.P., Liu Y., Guo Z.X. and Shahrooz B.M., Local buckling of steel plates in composite members with tie bars under axial compression, Engineering Structures, 205, 110097, 2020.

**Advanced Steel Construction** – Vol. 18 No. 3 (2022) 707–714
**DOI:**10.18057/IJASC.2022.18.3.8



# MECHANICAL BEHAVIOUR OF CORRODED STRUCTURAL STEEL SUBJECTED TO MONOTONIC TENSION

Qi Si [1], Yang Ding [1, 2], Liang Zong [1, 2, *] and Hua-Tian Zhao [3]

[1] *School of Civil Engineering, Tianjin Univ., Tianjin 300072, China.*
[2] *Key Laboratory of Coast Civil Structure Safety, Ministry of Education, Tianjin Univ., Tianjin 300072, China*
[3] *Key Laboratory of Civil Engineering Safety and Durability of China Education Ministry, Tsinghua University, Beijing 100084, China*
** (Corresponding author: E-mail: zongliang@tju.edu.cn)*

**ABSTRACT**

This study aims to investigate the mechanical properties of corroded structural steel under monotonic tensile loading. First, structural steel coupons with various corrosion degrees were produced by electrolytic accelerated corrosion using a particular etchant solution proposed by the authors. Second, the corroded morphologies of the specimens were observed through a morphology scanner; then, the mechanical properties were examined by monotonic tensile loading tests. An analytical model on the relationship between mass loss and surface morphology with the mechanical properties of corroded structural steel was established. Finally, a numerical simulation method was proposed on the mechanical behaviour of corroded structural steel based on random rough surface theory. The finite element was consistent with experimental tests, which indicates the feasibility and accuracy of the proposed simulation method.

**ARTICLEHISTORY**

Received: 11 August 2021
Revised: 22 January 2022
Accepted: 31 January 2022

**KEYWORDS**

Accelerated corrosion;
Structural steel;
Mechanical properties;
Corrosion morphology;
Simulation method



## 1. Introduction

Steel structures, which are designed to be permanently exposed to corrosive environments such as industry and the marine atmosphere, always have difficulties avoiding corrosion. Corrosion changes the surface appearance of the steel and deteriorates its mechanical properties, which affects the safety and durability of the steel structure. The mechanical behaviour of corroded structural steel has been studied by many scholars through different accelerated corrosion methods such as salt spray tests, cyclic immersion corrosion, and electrolytic corrosion [1-6]. Xu [7] investigated the mechanical behaviour of rusted steel plates using the neutral salt spray method, as shown in Fig. 1(a). Chen [8] studied the degradation of the mechanical properties of corroded cables by a copper accelerated acetic acid salt spray test (Fig. 1(b)). Ma [9] investigated the effect of pitting corrosion by using galvanic accelerated corrosion on the seismic performance of NV-D36 steel, as shown in Fig. 1(c).

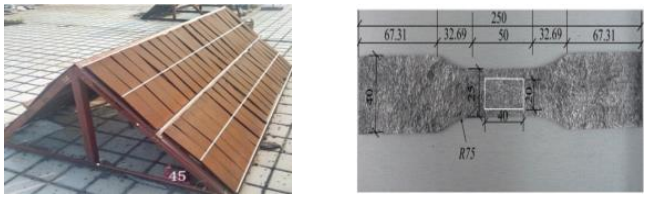


(a) Neutral salt spray corrosion

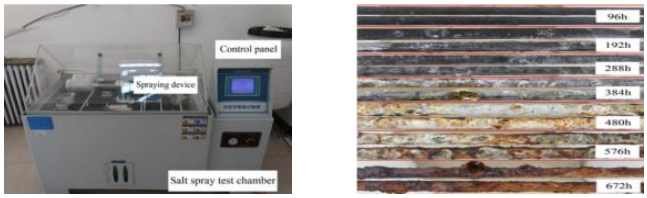


(b) Acid salt spray test

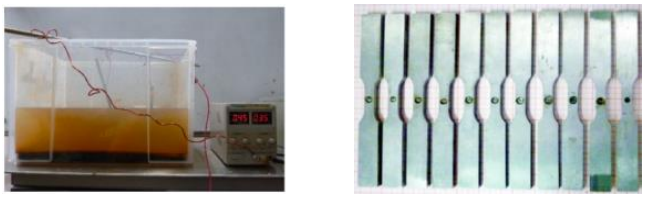

(c) Electrolytic corrosion

**Fig. 1** Experimental Research on Corroded Steel

In addition to electrolytic accelerated corrosion, it may take 60-120 days to achieve a 10% mass loss of steel using other accelerated corrosion methods. A long time is required to obtain corroded steel specimens, which is not conducive to the study of corroded steel. Existing studies have shown that the stress concentration due to the uneven corrosion morphology of corroded steel surfaces is a major factor in the degradation of the mechanical properties of steel materials [10]. Compared with salt spray corrosion and cyclic immersion corrosion, the electrolytic accelerated corrosion method can greatly reduce the corrosion time, but the corroded surface of the specimen is relatively uniform, which cannot reflect the true corrosion morphology [11] and limits the application of electrolytic accelerated corrosion methods.

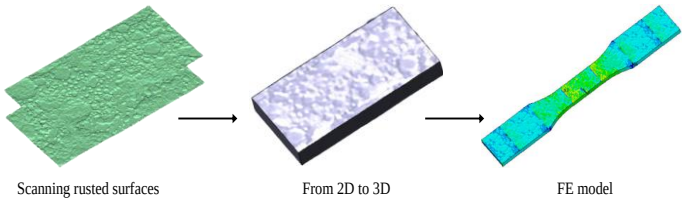


(a) Reverse modelling method

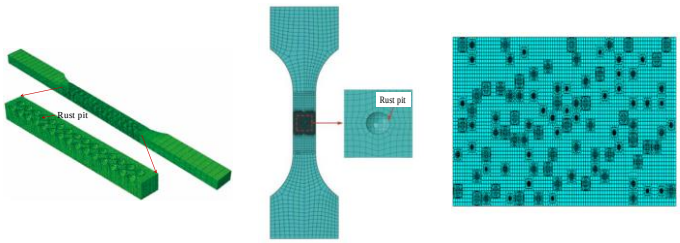


(b) Regular pits (c) Single pit (d) Random pits

**Fig. 2** FE model of corroded steel

Concerning the numerical modelling of corroded steel, the existing simulation methods can be divided into two main categories [12-14]: the reverse modelling method based on the actual measurement and the method of simplifying the three-dimensional shape of pits into regular shapes. Xu [16] obtained corroded surface data by scanning a corroded steel surface with a 3D noncontact topographic scanner, importing the data into Goemagic Studio software to generate the corroded surface, building a model corresponding to the scanned area, and utilizing the finite element software ANSYS for calculation and analysis, as shown in Fig. 2(a). Xiao [17] studied the mechanical properties of corroded Q460D steel specimens based on 3D

scanning. Wang [18] simulated and analysed the ductile degradation of steel plates after corrosion damage, assuming a uniform distribution of pits, as shown in Fig. 2(b). Song [19] studied the effect of corrosion on the low-cycle fatigue performance of steel by simulating specimens with a single pit in the finite element software (Fig. 2(c)). Wang [20] performed a nonlinear analysis of 200 models by constructing a numerical model of a steel plate with random pitting damage to investigate the degradation pattern of the ultimate strength of the steel plate under random pitting damage, as shown in Fig. 2(d). Sharifi [21] studied the ultimate capacity of steel beams with pitting corrosion by artificial neural networks and analysed the safety of corroded steel box girder bridges [22]. The reverse modelling method can reflect the actual morphology of the corroded steel surface, but it heavily depends on the data obtained through scanning and is only suitable for simulating the object or area being scanned. The method of simplifying the three-dimensional shape of pits often simplifies a single pit into a regular circular or elliptical shape, and the FE model established by this method has difficulty considering the overall corrosion morphology of the corroded structure.

In this paper, an electrolytic accelerated corrosion test of steel using a suitable solution that can reflect real atmospheric corrosion was performed to obtain specimens with different corrosion degrees. Then, a 3D noncontact scanner was used to scan the surface morphology of corroded specimens to obtain the relationship between the corrosion morphology and the mass loss. A deterioration model of the mechanical properties of corroded steel was established by monotonic tensile tests. Finally, a new simulation method for corroded steel based on random rough surfaces was proposed, which was verified by comparing it with the test results.

## 2. Accelerated corrosion test

### *2.1. Test Details*

Q355B is the most common and widely used steel material in steel construction in China. In this paper, Q355B structural steel was selected as the specimen material. The chemical composition of the Q355B structural steel is shown in Table 1. Tensile specimens were designed according to GB/T 228.1-2010 [23], and the geometric profile of the coupons is shown in Fig. 3.

**Table 1**
Q355B steel chemical composition (*wt.*%)

| Material | C | Si | Mn | P | S | Alt | Fe |
|---|---|---|---|---|---|---|---|
| Q355B | 0.19 | 0.107 | 0.42 | 0.009 | 0.002 | 0.023 | Balance |

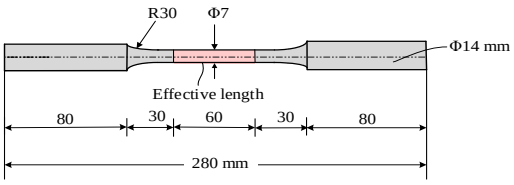


**Fig. 3** Dimensional diagram of the specimen

Before the accelerated corrosion test, the specimens should be well prepared. The surface of the specimens was polished by 800#-1200# water-resistant sandpaper and subsequently cleaned with acetone. Electric wires were connected at the clamping end of the specimen and sealed with waterproof tape. In the electrolytic accelerated corrosion test, the negative electrode was made of graphite material. The two electrodes were placed 50 mm apart and symmetrically in the test container. The test container was made of acrylic, and the direct current (DC) was delivered by the SS-3010 DC power supply, as shown in Fig. 4(a). During the test, the room was kept well ventilated, and the average temperature was approximately 28 °C. The specimens and graphite were placed in the test container, as shown in Fig. 4(b).

Four groups of specimens, labelled A-D, were designed for electrolytic accelerated corrosion testing, and the durations of electrolytic accelerated corrosion were 2.5, 5.0, 7.5, and 10.0 hours, respectively. The electrolytic corrosion solution was a mixture of 0.2% NaCl and 5% $CH_3COONa$, which could make the steel after electrolytic accelerated corrosion form a corrosion morphology corresponding to actual atmospheric corrosion [24]. The current density of the accelerated corrosion was controlled at 400 A/m$^2$.

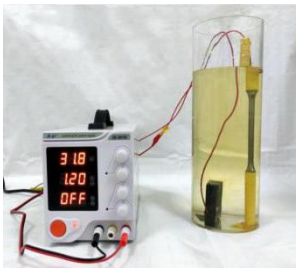


(a) Power supply and container

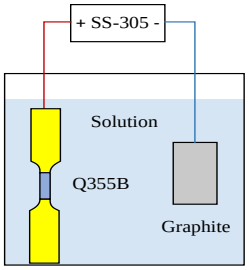


(b) Schematic diagram of the current

**Fig. 4** Electrolytic accelerated corrosion test

### *2.2. Results of accelerated corrosion*

After electrolytic accelerated corrosion, the mass loss was used to express the degree of corrosion of the specimens. The mass loss of the specimens was recorded as $w$ and calculated with Eq. (1). For all corroded specimens, the derusting process was performed before the loading test with 500 ml HCl ($\rho$=1.19 g/ml), 3.5 g $C_6H_{12}N_4$, and 500 ml distilled water following GB/T 16545-2015 [25]. A precise electronic balance with an accuracy of 0.001 g was employed to measure and record the initial weight of the specimens and the weight of the specimens after the electrolytic accelerated corrosion test.

$$w = \frac{\Delta m}{m_1} \times 100\% \tag{1}$$

where $m_1$ is the initial mass, $m_2$ is the mass of the specimen after rust removal, and $\Delta m$ is the changing mass of the specimen, $\Delta m = m_1 - m_2$.

The mass loss of the four specimen groups is listed in Table 2. The results show that the corrosion degree ($w$) of electrolytic corrosion is linearly related to the duration of the test. The uncorroded specimen is recorded as N, and the macroscopic corrosion morphologies of specimens A1, B1, C1, and D1 are shown in Fig. 5. When the mass loss reaches 6.88%, small corrosion pits appear on the surface of the specimen, and there is no obvious change in geometric size of the specimen. When the mass loss increases, the range of corrosion gradually expands, and circular pits begin to combine to form long strips and large round pits. When the mass loss reaches 23.97%, corrosion pits continue to develop and expand, and the entire corrosion state is developed.


**Fig. 5** Macro corrosion morphology of the specimens

**Table 2**
Mass loss of electrolytic accelerated corrosion

| Duration (h) | Groups | Specimen | $\Delta m$ (g) | $w$ (%) | Average $\Delta m$ (g) | Average $w$ (%) |
|---|---|---|---|---|---|---|
| 2.5 | A | A1 | 3.065 | 6.87 | 3.068 | 6.88 |
| | | A2 | 3.072 | 6.89 | | |
| | | A3 | 3.067 | 6.88 | | |
| 5.0 | B | B1 | 6.235 | 13.98 | 6.168 | 13.83 |
| | | B2 | 6.158 | 13.81 | | |
| | | B3 | 6.11 | 13.70 | | |
| 7.5 | C | C1 | 9.168 | 20.56 | 9.177 | 20.58 |
| | | C2 | 9.193 | 20.62 | | |
| | | C3 | 9.17 | 20.56 | | |
| 10.0 | D | D1 | 10.802 | 24.22 | 10.687 | 23.97 |
| | | D2 | 10.65 | 23.88 | | |
| | | D3 | 10.608 | 23.79 | | |

## 3. Corrosion morphology

### 3.1. Corrosion morphology scanning

A three-dimensional noncontact surface profiler ST-400 was adopted to scan the surface morphology of each specimen after removing the rust, as shown in Fig. 6(a). Round specimens were adopted, and any position in the gauge length had equal probability of being affected by corrosion, so each test piece was scanned twice along the axis of the specimen to characterize the roughness of the corroded specimen. The scanning lines are shown in Fig. 6(b). For simplicity, only the scanning results of specimens A1, B1, C1, and D1 are shown in Fig. 7.

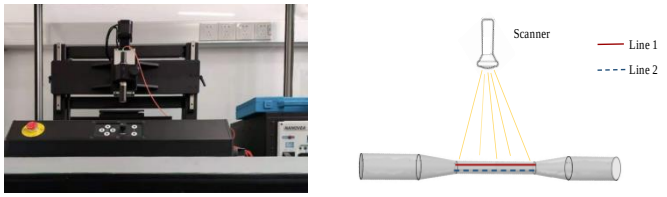


(a) 3D scanner (b) Scanned area

**Fig. 6** Morphological scanning of specimens

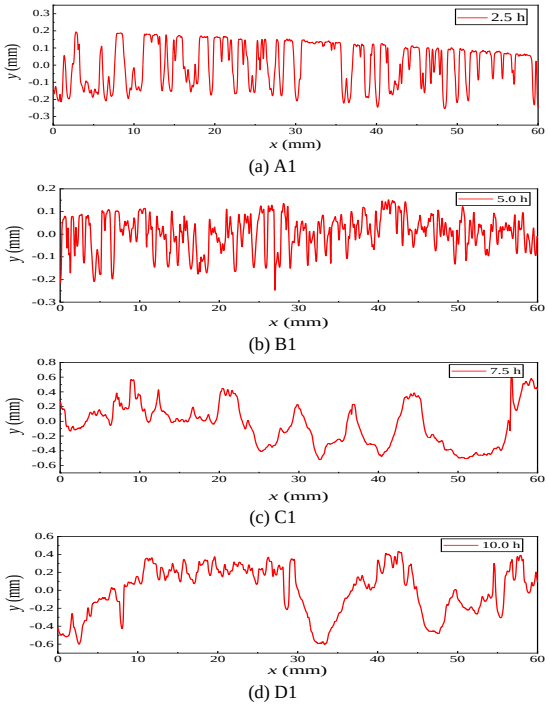


(a) A1
(b) B1
(c) C1
(d) D1

**Fig. 7** Scanning results of some specimens

### 3.2. Roughness variation patterns

The surface of the corroded steel was characterized by the arithmetic average height ($R_a$), root mean square height ($R_q$), and maximum height ($R_z$) in the roughness theory [26]. The specific calculation formulas for each parameter are shown in Eqs. (2)-(4).

$$R_a = \frac{1}{l}\int_0^l |Z(x)|\,dx \tag{2}$$

$$R_q = \sqrt{\frac{1}{l}\int_0^l Z^2(x)dx} \tag{3}$$

$$R_z = R_p + R_v \tag{4}$$

where $Z(x)$ is the scanning surface of the specimen; $R_p$ is the maximum peak height; $R_v$ is the maximum valley depth; $l$ is the side length of the sampling area. Based on the scanning results, $R_a$, $R_q$, and $R_z$ were calculated and recorded in Table 3.

**Table 3**
Values of $R_a$, $R_q$, and $R_z$ of the specimens

| Specimens | $R_a$ (mm) | $R_q$ (mm) | $R_z$ (mm) |
|---|---|---|---|
| A1 | 0.075 | 0.09 | 0.371 |
| | 0.060 | 0.074 | 0.399 |
| A2 | 0.078 | 0.09 | 0.447 |
| | 0.075 | 0.085 | 0.371 |
| A3 | 0.074 | 0.089 | 0.421 |
| | 0.071 | 0.081 | 0.385 |
| B1 | 0.105 | 0.122 | 0.49 |
| | 0.084 | 0.106 | 0.606 |
| B2 | 0.097 | 0.117 | 0.582 |
| | 0.085 | 0.098 | 0.631 |
| B3 | 0.098 | 0.119 | 0.553 |
| | 0.083 | 0.103 | 0.622 |
| C1 | 0.145 | 0.193 | 1.173 |
| | 0.144 | 0.186 | 0.965 |
| C2 | 0.154 | 0.187 | 0.859 |
| | 0.161 | 0.208 | 1.232 |
| C3 | 0.157 | 0.191 | 0.925 |
| | 0.163 | 0.211 | 1.383 |
| D1 | 0.229 | 0.269 | 1.04 |
| | 0.187 | 0.249 | 1.859 |
| D2 | 0.192 | 0.253 | 1.706 |
| | 0.174 | 0.201 | 1.245 |
| D3 | 0.181 | 0.225 | 1.556 |
| | 0.232 | 0.27 | 1.704 |

The average mass loss and surface parameters of each group are shown in Table 4. The results of the average mass loss and surface parameters were fitted, as shown in Fig. 8.

**Table 4**
Average mass loss and average surface parameters

| Groups | $w$ (%) | $R_a$ (mm) | $R_q$ (mm) | $R_z$ (mm) |
|---|---|---|---|---|
| A | 6.88 | 0.072 | 0.085 | 0.399 |
| B | 13.83 | 0.092 | 0.111 | 0.581 |
| C | 20.58 | 0.154 | 0.196 | 1.090 |
| D | 23.97 | 0.199 | 0.245 | 1.518 |

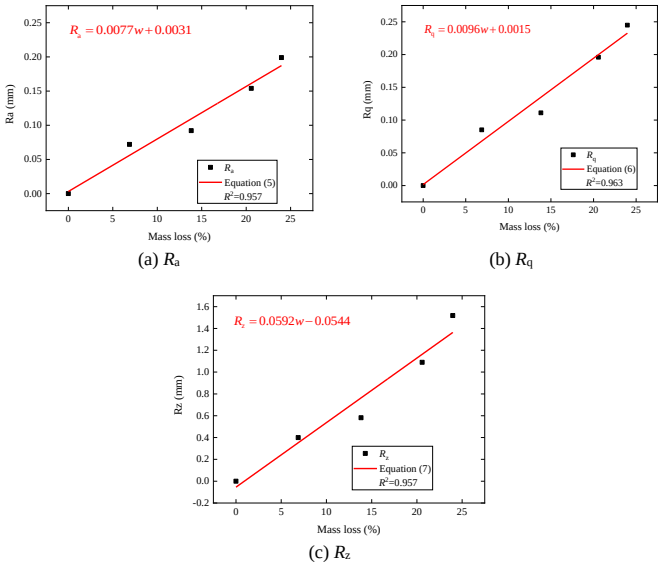


(a) $R_a$ (b) $R_q$

(c) $R_z$

**Fig. 8** Relationship between surface parameters and mass loss

Fig. 8 shows that the arithmetic average height ($R_a$), root mean square height ($R_q$), and maximum height ($R_z$) of the one-dimensional roughness parameters of the corroded steel surface are linearly related to the mass loss and satisfied in Eqs. (5)-(7).

$$R_a = 0.0077w + 0.0031 \quad (5)$$

$$R_q = 0.0096w + 0.0015 \quad (6)$$

$$R_z = 0.0592w - 0.0544 \quad (7)$$

## 4. Mechanical behaviour tests under monotonic tensile loading

### *4.1. Mechanical behaviour tests*

A monotonic tensile loading test was performed on all corroded steel specimens, as shown in Fig. 9. The tensile test was controlled by the strain. The strain loading rate was 0.00025/s according to GB/T228.1-2010, which was 0.75 mm/min.

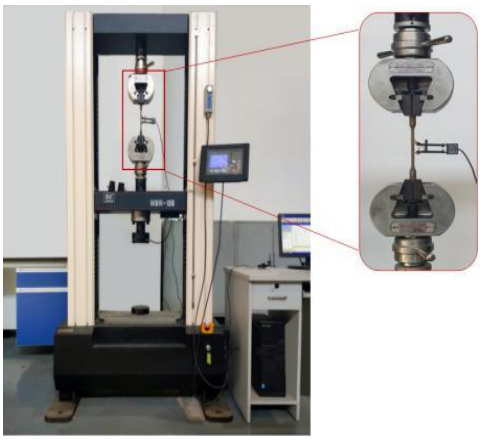

**Fig. 9** Tensile test

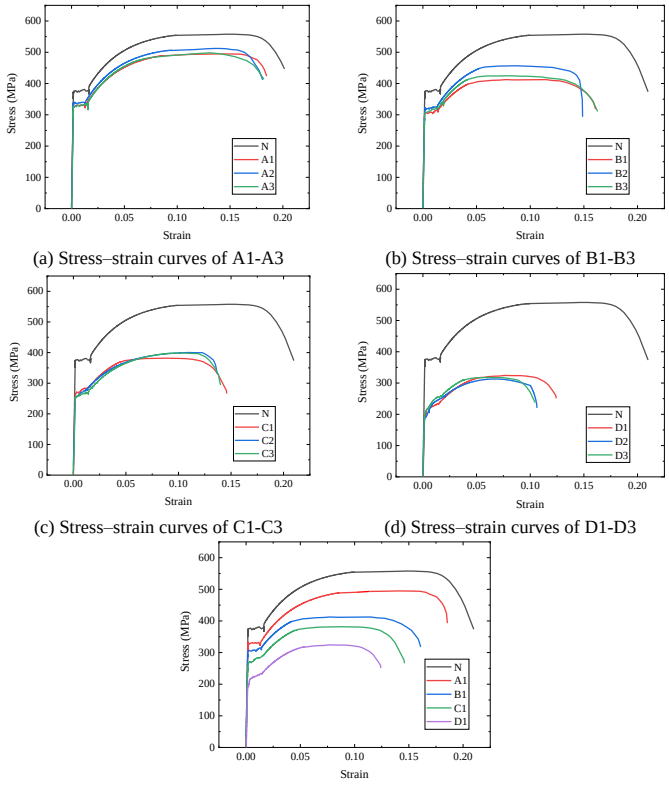


(a) Stress–strain curves of A1-A3

(b) Stress–strain curves of B1-B3

(c) Stress–strain curves of C1-C3

(d) Stress–strain curves of D1-D3

(e) Stress–strain curves of A1-D1

**Fig. 10** Stress–strain curves of corroded steel

In this study, nominal stresses were adopted, and the ratio of the magnitude of the actual load to the initial cross-sectional area of the specimen was adopted to obtain the stress value. The stress–strain curves of specimens with different corrosion degrees were obtained by tensile tests, as shown in Fig. 10. The mechanical behaviour parameters of the individual specimens obtained from the tests were sorted out, and the results are shown in Table 5, where $F_y$ is the yield capacity of the specimen, $F_u$ is the ultimate capacity, $f_y$ is the yield stress, $f_u$ is the tensile stress, $\varepsilon_u$ is the fracture strain, and $E$ is the elastic modulus.

The influence of different corrosion degrees on the mechanical properties of Q355B steel was compared and analysed. From Table. 5, the mechanical properties of corroded specimens declined to varying degrees compared to those of uncorroded specimens, with a maximum reduction of 38.6% in yield strength, 44.0% in ultimate strength, and 52.4% in fracture strain when the degree of corrosion reaches 23.97%, which indicates that corrosion significantly affects the mechanical properties of Q355B structural steel. Interestingly, the nominal stress–strain curves of Groups A and B presented a similar behaviour to the uncorroded specimens, which contained an evident yield plateau. However, with the increase in corrosion damage, the yield plateau continued fading away, and no yield plateau was found in the stress–strain curves of the specimens in Groups C and D.

**Table 5**
Mechanical properties of corroded steel

| Specimens | $F_y$ (*kN*) | $F_u$ (*kN*) | $f_y$ (MPa) | $f_u$ (MPa) | $\varepsilon_u$ | $E$ ($10^5$MPa) |
|---|---|---|---|---|---|---|
| N | 14.67 | 21.46 | 381.2 | 557.7 | 0.21 | 2.12 |
| A1 | 12.79 | 19.04 | 332.3 | 494.7 | 0.19 | 1.94 |
| A2 | 13.10 | 19.71 | 340.3 | 512.2 | 0.18 | 2.03 |
| A3 | 12.94 | 19.17 | 336.2 | 498.1 | 0.19 | 1.97 |
| B1 | 12.07 | 15.87 | 313.6 | 412.3 | 0.16 | 2.00 |
| B2 | 12.51 | 17.43 | 325.0 | 452.8 | 0.15 | 1.85 |
| B3 | 12.37 | 16.33 | 321.3 | 424.2 | 0.16 | 1.88 |
| C1 | 10.92 | 14.64 | 283.8 | 380.5 | 0.15 | 1.76 |
| C2 | 10.82 | 15.38 | 281.2 | 399.7 | 0.14 | 1.75 |
| C3 | 11.07 | 15.26 | 287.6 | 396.4 | 0.14 | 1.77 |
| D1 | 9.00 | 12.47 | 233.9 | 323.9 | 0.13 | 1.44 |
| D2 | 9.29 | 12.03 | 241.5 | 312.5 | 0.11 | 1.49 |
| D3 | 9.92 | 12.08 | 257.8 | 313.8 | 0.10 | 1.50 |

### *4.2. Fracture analysis*

The strain at break of the uncorroded specimens is nearly 20%, the section shrinkage is high, and the ductility is good. The tensile process of the corroded steel specimen is approximately identical to that of the uncorroded specimen, which follows a tensile-necking-fracture process. Due to the reduced cross-sectional area of the corroded specimen, necking and fracture occur at the pitting, and the fracture shows a fibrous shape. The specimen has no obvious sound at fracture, and the strain is large, so the corroded specimen was still determined to be a ductile fracture.

According to the metal inspection method of microstructure, metallographic specimens were cut out of the fractured specimens with a line cutting machine and polished. The specimens were subjected to microscopic observation of the metallographic organization using a Leica metallographic microscope, which magnified the specimens 1000 times, and the metallographic organization of the fractured specimens is shown in Fig. 11.

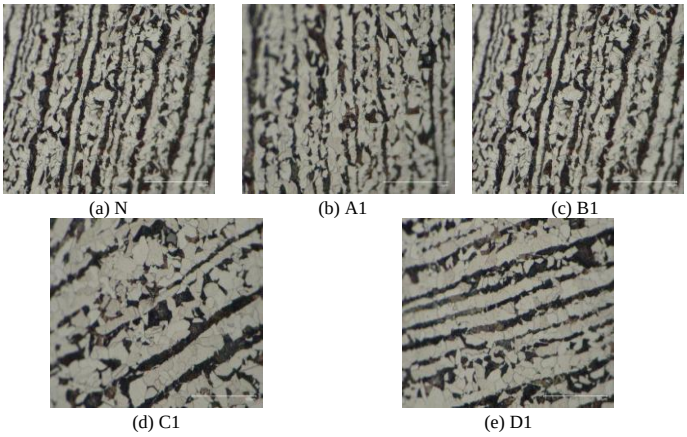

(a) N (b) A1 (c) B1

(d) C1 (e) D1

**Fig. 11** Metallographic organization diagram

From Fig. 11, both uncorroded and corroded specimens are composed of white pre-eutectic ferrite and grey–black pearlite. The tissue distribution of uncorroded and corroded specimens reflects that ferrite and pearlite have identical distribution characteristics: ferrite and pearlite are distributed in strips, and the interface between pearlite and ferrite is obvious, which indicates that corrosion does not affect the tissue structure of steel, and the decrease in mechanical properties of corroded steel is mainly due to the stress concentration caused by the uneven corrosion. The existence of corrosion pits makes the specimens discontinuous. Under the action of axial tensile force, the stress concentrations occurred near corrosion pits, which caused unequal tensile stresses and increased the local strain rate in the corrosion pits. The presence of corrosion pits can easily cause the steel to be in a more brittle state, which causes the formation and progressive development of microcracks around the pits and ultimately deteriorates the mechanical properties of the steel.

### *4.3. Degradation law of mechanical properties*

The mechanical behaviour of the corroded Q355B structural steel was analysed. The average values for each group of specimens are shown in Table 6.

**Table 6**
Average mechanical properties of corroded steel

| Groups | $f_y$ (MPa) | $f_u$ (MPa) | $\varepsilon_u$ | $E$ ($10^5$MPa) |
|---|---|---|---|---|
| N | 381.2 | 557.7 | 0.21 | 2.12 |
| A | 336.3 | 501.7 | 0.19 | 1.98 |
| B | 320.0 | 429.8 | 0.16 | 1.91 |
| C | 284.2 | 392.2 | 0.14 | 1.76 |
| D | 244.4 | 316.7 | 0.11 | 1.48 |

The yield strength of corroded steel is recorded as $f_y'$, the ultimate strength is $f_u'$, the strain at fracture is $\varepsilon_u'$, and the modulus of elasticity is $E'$. The ratio of the mechanical properties of corroded Q355B structural steel to the initial uncorroded state is shown in Table 7 and Fig. 12.

**Table 7**
Ratio of the mechanical properties of corroded steel to its initial state

| Groups | $f_y'/f_y$ | $f_u'/f_u$ | $\varepsilon_u'/\varepsilon_u$ | $E'/E$ |
|---|---|---|---|---|
| A | 0.88 | 0.90 | 0.89 | 0.93 |
| B | 0.84 | 0.77 | 0.75 | 0.90 |
| C | 0.75 | 0.70 | 0.68 | 0.83 |
| D | 0.64 | 0.57 | 0.54 | 0.70 |

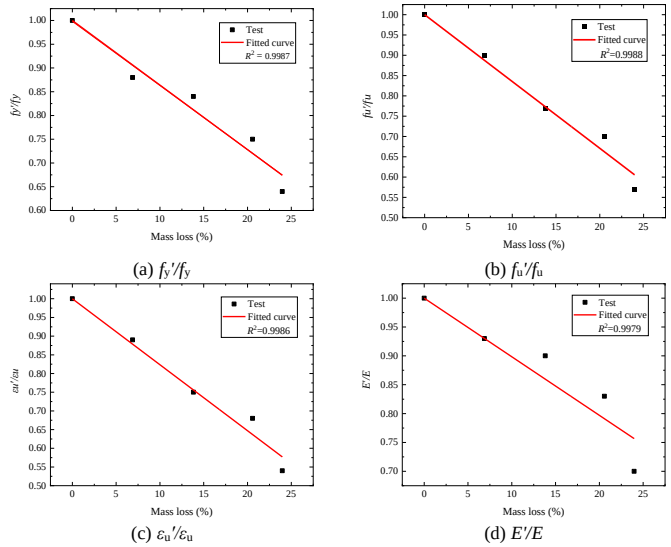


**Fig. 12** Changes in the mechanical properties of corroded steel

Fig. 12 shows that the yield strength, ultimate strength, fracture strain, and elastic modulus of the steel decrease when the mass loss increases, and the following equations are fulfilled:

$$f_y'/f_y = 1 - 0.01359w \tag{8}$$

$$f_u'/f_u = 1 - 0.01646w \tag{9}$$

$$\varepsilon_u'/\varepsilon_u = 1 - 0.01765w \tag{10}$$

$$E'/E = 1 - 0.01015w \tag{11}$$

## 5. Modelling methods based on surface morphology

### *5.1. Modelling process based on surface morphology*

The existing numerical modelling methods for corroded steel have two problems: it is completely based on measured data, and the corrosion pit is simplified to a circular or oval shape, which ignores the overall morphology of the corroded surface.

In this study, the surface of corroded steel is considered a two-dimensional random rough surface, as shown in Fig. 13, where the shaded areas represent the corrosion part, and the blue region is the steel matrix. The area between the highest and lowest points on the corroded surface is recorded as $S_1$, the distance from the lowest point on the corroded surface to the centerline is recorded as $b$, and the area covered is recorded as $S_2$. The radius of the specimen in its uncorroded state is recorded as $r$, and the diameter is recorded as $d$.

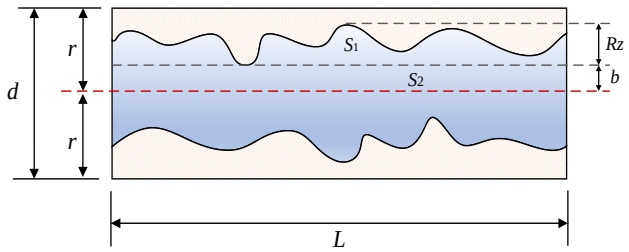


**Fig. 13** Two-dimensional model of corroded steel

The Monte Carlo method was used to generate a one-dimensional randomly rough surface corresponding to the mass loss. In this paper, the length ($L$) of the generated one-dimensional curve is equal to the effective length in Fig. 1, which is 60 mm. The interval of adjacent data points is 0.01 mm, i.e., each model contains 6000 data points. Next, the distance from the lowest point of the corroded surface to the centreline was calculated. Finally, the obtained one-dimensional rough surface was combined with other surfaces to produce a corroded steel model, as shown in Fig. 14.

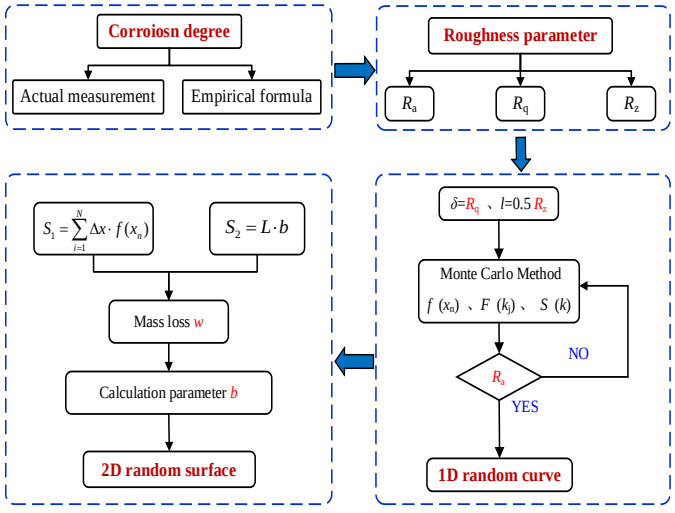


**Fig. 14** Flowcharts of modelling methods

For a one-dimensional randomly rough surface, a one-dimensional rough surface sample [27] with length $L$ and data point $N$ is generated by Eq. (12).

$$f(x_n)=\frac{1}{L}\sum_{j=-N/2+1}^{N/2}F(k_j)e^{ik_jx_n} \tag{12}$$

where $x_n=n$. $\Delta x$ is the $n$th sample point on the rough surface, and $F(k_j)$ and $f(x_n)$ are called Fourier transform pairs and defined as:

$$F(k_j)=\left[2\pi LS(k_j)\right]^{1/2}\cdot\begin{cases}[N(0,1)+iN(0,1)]/\sqrt{2} & j\neq 0,N/2\\ N(0,1) & j=0,N/2\end{cases} \tag{13}$$

$S(k_j)$ is the power spectral density of the rough surface; $N(0,1)$ is the random number of a normal distribution with mean 0 and variance 1; $\delta$ is the height of the root mean square; $l$ is the correlation length.

The power spectrum [28] corresponding to the one-dimensional Gaussian rough surface is:

$$S(k)=\frac{\delta^2 l}{2\sqrt{\pi}}\exp\left(\frac{-k^2l^2}{4}\right) \tag{14}$$

When generating a one-dimensional randomly rough surface with the Monte Carlo method, the root mean square height ($\delta$) and associated length ($l$) were involved, $R_q$ was calculated using Eq. (6), and $R_z$ was calculated using Eq. (7) with $\delta=R_q$ and $l=0.5R_z$.

According to Fig. 13, in the simplified model of steel after corrosion, $S_1$ and $S_2$ are calculated as follows:

$$S_1=\sum_{i=1}^{N}\Delta x\cdot f(x_n) \tag{15}$$

$$S_2=L\cdot b \tag{16}$$

Based on Eq. (15) and Eq. (16), the mass loss ($w$) can be expressed as:

$$w=1-\frac{S_1+S_2}{r\cdot L}\times 100\% \tag{17}$$

The formula of $b$ is:

$$b=\frac{r\cdot L\cdot(1-w)-\sum_{i=1}^{N}\Delta x\cdot f(x_n)}{L} \tag{18}$$

The calculation was performed in MATLAB software using the loop command to generate the one-dimensional random curve, and the value of $R_a$ calculated by Eq. (5) was used as a criterion for determination. When the mean square height of the generated curve satisfies the condition, the generated curve was output, and the loop stopped. The one-dimensional roughness curve corresponding to the specimens in the accelerated corrosion test obtained by the above method is shown in Fig. 15.

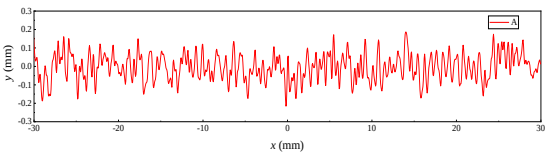


(a) Curves corresponding to group A

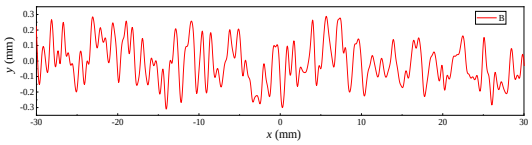


(b) Curves corresponding to group B

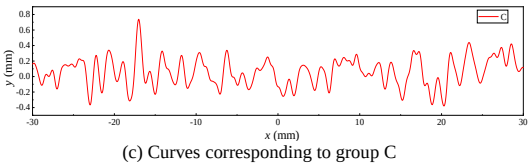


(c) Curves corresponding to group C

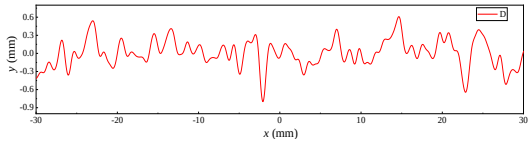


(d) Curves corresponding to group D

**Fig. 15** One-dimensional random rough curves

### 5.2. Calculation and analysis of the FE model

After obtaining the random curve of the corroded surface corresponding to the mass loss, distance $b$ from the lowest point in the corroded surface to the centerline was calculated using the above algorithm. The FE model corresponding to the specimen obtained from the accelerated corrosion test is shown in Fig. 16. The FE models corresponding to the electrolytic corrosion tests were denoted as FE-A, FE-B, FE-C, and FE-D. The model corresponding to the uncorroded specimen was recorded as FE-N.

In the FE model, the boundary conditions were fixed on the left side, and a reference point was established on the right side. This point was coupled with the right side surface, and displacement was loaded at this point. Taking the FE-A model as an example, its specific boundary conditions are shown in Fig. 17.

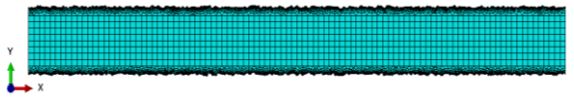

(a) FE-A

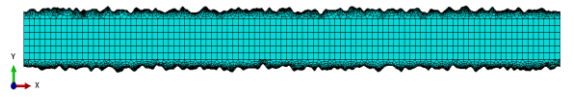

(b) FE-B

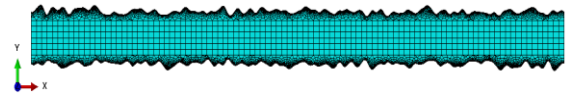

(c) FE-C

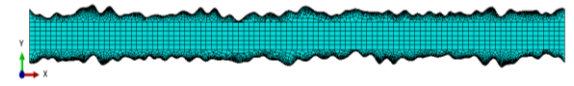

(d) FE-D

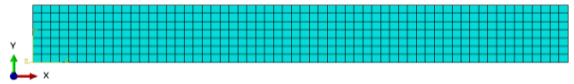

(e) FE-N

**Fig. 16** Two-dimensional FE model of corroded steel

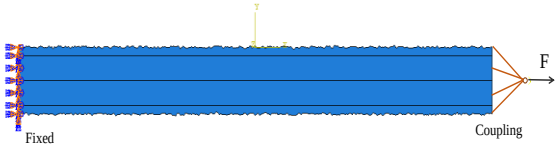


**Fig. 17** Schematic boundary conditions

The material constitutive adopted in each FE model was the stress – strain relationship of steel without corrosion, and the static general analysis step was used to solve the model. The strain corresponding to the stress was reduced to 85% of the ultimate stress as the fracture strain. The stress – strain curve of each model is shown in Fig. 18.

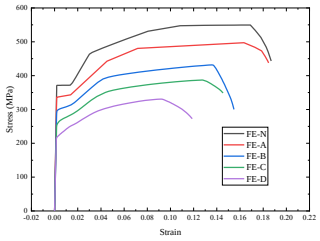


**Fig. 18** Stress–Strain Curve of FE Models

### *5.3. Comparison and validation of results*

The stress–strain curves obtained by the finite element models were compared with the tensile test, as shown in Fig. 19. Fig. 20 shows the comparison of various mechanical parameters calculated by finite element with Eqs. (8)-(11).

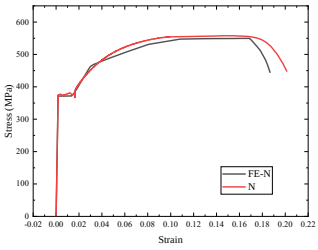


(a) Stress–strain curves of group N

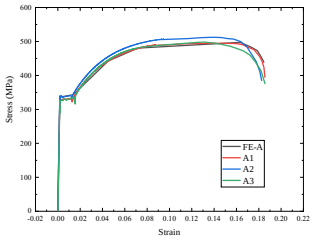


(b) Stress–strain curves of A1-A3

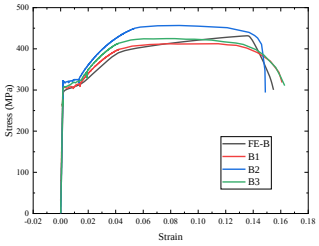


(c) Stress–strain curves of B1-B3

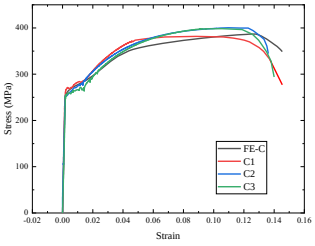


(d) Stress–strain curves of C1-C3

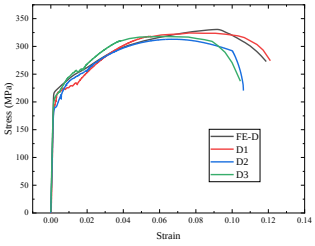


(e) Stress–strain curves of D1-D3

**Fig. 19** Comparison diagram of the stress–strain curve

The comparative diagram shows that the FE model has consistent results with the experimental test, which indicates that the mechanical behaviour of the steel calculated by the FE model is consistent with the tensile test and confirms the feasibility and accuracy of the proposed method based on surface morphology.

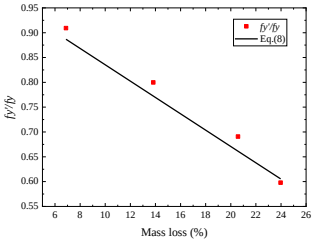


(a) Yield stress

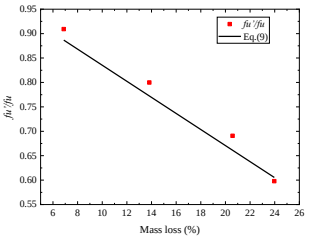


(b) Ultimate strength

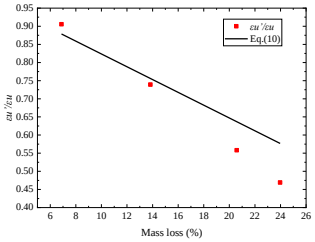


(c) Fracture strain

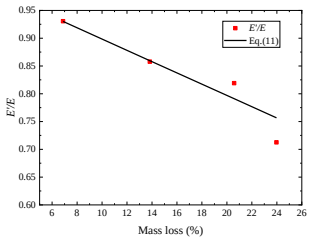


(d) Elastic modulus

**Fig. 20** Comparison diagram of the FE model and tests

## 6. Conclusion

Based on structural steel Q355B, the surface morphology, mechanical behaviour, and simulation method of corroded structural steel were studied. A model to calculate the surface morphological parameters of steel with mass loss was developed. The degradation law of the mechanical behaviour of corroded steel was obtained. A novel simulation method of corroded steel based on random rough surface theory was proposed. The main conclusions are as follows:

(1) As corrosion develops, an uneven corrosion morphology gradually appears on the steel surface. The arithmetic average height ($R_a$), root mean square height ($R_q$), and maximum height ($R_z$) of the corroded steel surface are linearly related to the mass loss, which increases when the mass loss increases.

(2) The uneven corrosion morphology may cause concentrated localized stress, which results in a nonuniform distribution of stresses under axial tension. When the corrosion degree increases, the yielding platform of the steel gradually disappears, and the yield strength, ultimate strength, fracture strain, and elastic modulus of the steel decrease.

(3) By simplifying the corroded steel into a two-dimensional random rough surface and combining the surface morphology parameters of the corroded surface, the method based on the random rough surface theory can be used to establish the FE model corresponding to various corrosion degrees. The validity of the simulation method was verified by comparing the simulated results with experimental tests.

## Acknowledgement

The reported research work was sponsored by the National Key Research and Development Program of China (2018YFC1504304).

## References

[1] Xiao L, Peng J, Zhang J, et al. Comparative assessment of mechanical properties of HPS between electrochemical corrosion and spray corrosion[J]. Construction and Building Materials. 2020, 237: 117735.
[2] Wu H, Lei H, Chen Y F, et al. Comparison on corrosion behaviour and mechanical properties of structural steel exposed between urban industrial atmosphere and laboratory simulated environment[J]. Construction and Building Materials. 2019, 211: 228-243.
[3] Xu S, Zhang Z, Li R, et al. Effect of cleaned corrosion surface topography on mechanical properties of cold-formed thin-walled steel[J]. Construction and Building Materials. 2019, 222: 1-14.
[4] Zhang C, Zhu H, Zhu L. Effect of interaction between corrosion and high temperature on mechanical properties of Q355 structural steel[J]. Construction and Building Materials. 2020: 121605.
[5] Rajput A, Paik J K. Effects of naturally-progressed corrosion on the chemical and mechanical properties of structural steels[J]. Structures. 2020.
[6] Jia C, Shao Y, Guo L, et al. Incipient corrosion behavior and mechanical properties of low-alloy steel in simulated industrial atmosphere[J]. Construction and Building Materials. 2018, 187: 1242-1252.
[7] Xu S, Wang H, Li A, et al. Effects of corrosion on surface characterization and mechanical properties of butt-welded joints[J]. Journal of Constructional Steel Research. 2016, 126: 50-62.
[8] Chen, Z., Chen, H., Liu, H., and Yang, S. Corrosion behavior of different cables of large-span building structures in different environments. Journal of Materials in Civil Engineering. 2020, 32: 04020345.
[9] Ma H, Yang Y, He Z, et al. Experimental study on mechanical properties of steel under extreme cyclic loading considering pitting damage[J]. Ocean Engineering. 2019, 186: 106091.
[10] Xu, S., Wang, H., Li, A., Wang, Y., and Su, L. Effects of corrosion on surface characterization and mechanical properties of butt-welded joints. Journal of constructional steel research. 2016, 126: 50-62.
[11] Yuan, Y., Zhang, X., and Ji, Y. A comparative study on structural behavior of deteriorated reinforced concrete beam under two different environments. China civil engineering journal. 2006, 39: 42-46.
[12] Zheng Y, Wang Y. Damage evolution simulation and life prediction of high-strength steel wire under the coupling of corrosion and fatigue[J]. Corrosion Science. 2020, 164: 108368.
[13] Wang H, Zhang Z, Qian H, et al. Effect of local corrosion on the axial compression behavior of circular steel tubes[J]. Engineering Structures. 2020, 224: 111205.
[14] Jasra Y, Singhal S, Upman R, et al. Finite element simulation of stress corrosion cracking in austenitic stainless steel using modified Lemaitre damage model[J]. Materials Today: Proceedings. 2020, 26: 2314-2322.
[15] Zhao Z, Zhang H, Xian L, et al. Tensile strength of Q345 steel with random pitting corrosion based on numerical analysis[J]. Thin-Walled Structures. 2020, 148: 106579.
[16] Xu Shanhua, Wang Hao, Su Lei, et al. Ductility degradation of corroded steel plates with pitting damage[J]. 2016, 46(6): 1257-1263. (In Chinese)
[17] Xiao L F, Peng J X, Zhang J R, et al. Mechanical properties of corroded high performance

steel specimens based on 3d scanning[J]. Advanced Steel Construction. 2019, 15(2): 129-136.
[18] Wang Y, Shi T, Zhang H, et al. Hysteretic behavior and cyclic constitutive model of corroded structural steel under general atmospheric environment[J]. Construction and Building Materials. 2020: 121474.
[19] Song F , Xie X .Effect analysis of corrosion on low cycle fatigue behavior of structural steel. Journal of Zhejiang University (Engineering Science) . 2018, 52(12): 2285-2294. (In Chinese)
[20] Wang R, Ajit Shenoi R, Sobey A. Ultimate strength assessment of plated steel structures with random pitting corrosion damage[J]. Journal of Constructional Steel Research. 2018, 143: 331-342.
[21] Sharifi Y, Tohidi S. Ultimate capacity assessment of web plate beams with pitting corrosion subjected to patch loading by artificial neural networks[J]. Advanced Steel Construction. 2014, 10(3): 325-350.
[22] Sharifi Y, Paik J, et al. Safety analysis of steel box girder bridges with pitting corrosion[J]. Advanced Steel Construction. 2016,12(4): 359-379.
[23] GB/T 228.1, Tensile Test of Metallic Materials Part 1: Room Temperature Test Method, Standards Press of China, Beijing, 2010. (In Chinese)
[24] Si Q, Ding Y, Zong L. Electrolytic Accelerated Corrosion Morphology for Structural Steel based on an improved solution. Corrosion Reviews. 2021, 39(4):373-386.
[25] GB/T 16545, Corrosion of metals and alloys - Removal of corrosion products on corrosion specimens, Standards Press of China, Beijing, 2012. (In Chinese)
[26] ISO 25178-2: Geometrical product specifications (GPS) - Surface texture: Areal Part 2: Terms, definitions and surface texture parameters. 2012.
[27] Guo L . Basic theory and method of compound electromagnetic scattering between random rough surface and target[M]. Science Press, 2014. (In Chinese)
[28] Chen H, Hu Y, Wang H, et al. Computer Simulation of Rough Surfaces[J]. Lubrication Engineering. 2006(10): 52-55, 59. (In Chinese)

**Advanced Steel Construction** – Vol. 18 No. 3 (2022) 715–727
**DOI:**10.18057/IJASC.2022.18.3.9


# EXPERIMENTAL STUDY OF HYSTERETIC BEHAVIOR OF RESILIENT PREFABRICATED STEEL FRAMES WITH AND WITHOUT INTERMEDIATE COLUMNS

Meng-Yao Cheng [1], Yan-Xia Zhang [1, 2, *], Zhen-Xing Li [1] and Wen Wen [1]

[1] *School of Civil and Transportation Engineering, Beijing University of Civil Engineering and Architecture, Beijing, China*

[2] *Beijing Energy Conservation & Sustainable Urban and Rural Development Provincial and Ministry Co-construction Collaboration Innovation Center, Beijing University of Civil Engineering and Architecture, Beijing, China*

** (Corresponding author: E-mail: zhangyanxia@bucea.edu.cn)*

**ABSTRACT**

The research innovatively proposed a seismic resilient structural system including a prefabricated self-centering steel frame (PSC) and an intermediate column with a friction damper (CD). The CD, installed in the mid-span beam of the PSC, was expected to provide additional stiffness and damping, The seismic performance of the newly-developed resilient structural system thus can be greatly improved. This paper stated the experimental study on the hysteretic behaviors of the newly-developed system. Comparative pseudo-dynamic tests were conducted for the validation where two systems, a PSC with CD and a PSC without CD, were tested respectively. The testing results indicated that a PSC with CD has better seismic performance for long-span structures under catastrophic earthquakes' attack. The CD overall provided additional stiffness for requirements of earthquake fortification criteria. The friction damper, part of CD greatly improves the damping effect together with the energy-dissipation bolts. The small residual rotations of beam-column connections on the PSC subsystem provides a satisfactory self-centering mechanism. Moreover, the steel strands of the resilient structural system can maintain the elasticity even after the highest-intensity earthquake. In turn, the satisfactory seismic performance of the proposed PSC with CD structural system validated. This research developed a series of design formula for the T-plate and L-plate friction damper in the CD to guarantee the designed seismic performance of the proposed seismic resilient structural system. The theoretical hysteresis curve of the system was proposed for the future design specification.

**ARTICLE HISTORY**

Received: 14 August 2020
Revised: 10 July 2021
Accepted: 8 June 2022

**KEYWORDS**

Seismic performance;
Pseudo-dynamic test;
Resilient prefabricated steel frame;
Friction damper;
Comparative analysis



## 1. Introduction

Self-centering steel resilient frames (SC-SRFs) are trends of future seismic resilient structural systems which are known for the self-centering mechanism and the energy-dissipation property. The SC-SRFs can greatly reduce the structural damages through the embedded damping devices, which in turn guarantee the structural reliability for larger-span structures under greater earthquakes. The self-centering mechanism on the other hand improve the structural resilience, which minimizing the cost of structural rehabilitation.

Worldwide scholars proposed various types of SC-SRFs and explored their seismic performance theoretically and experimentally in recent years. The original SC-SRFs were proposed by Ricles et al. [1] which were composed of steel frames, bolted connections, steel strands and steel angles. The bolted connections of the SC-SRFs demonstrated the similar rigidity as welded connections [2-5]. The strands and anchorages provide proper self-centering mechanism. The steel angles offer energy-dissipation properties to ensure the elastic performance of major structural members, e.g. beams and columns. Numerical simulations were conducted to conclude damage identification criteria. The researchers proposed various methods to improve the damping of the system by replacing the steel angles with energy-dissipation rods [6], frictional devices [7-10], and brass-plate -dissipation devices [11].

The steel frames require satisfactory lateral stiffness for the overall structural system. Thus, an intermediate column with dampers (CD) were designed to install in-between a steel frame. Experimental research [12-14] were conducted to study its mechanical properties and seismic effects. The setting of CD can effectively reduce the displacement response of the frame.

The steel strands require in situ pretension during installation on the self-centering frame which was unsafe and costly. The research group [15-19] proposed an prefabricated self-centering steel frame (PSC) where the steel strands were prestressed before erection. An innovative seismic resilient structural system, a CD connected to PSC were proposed [20] to satisfy the seismic performance and earthquake fortification criteria. The newly-developed system was also economic and safe for structural erections.

## 2. Design and analysis of PSC-CD resilient structural system

### *2.1. Design of PSC-CD*

The PSC (Fig. 1) comprises three components: the fixed column, the flexible beam, and the self-centering connections with post-tensioned steel strands and friction bolts [18]. The PSC requires additional lateral stiffness for larger-span structures. The CD, therefore, is proposed where an intermediate column with a friction damper is connected to the mid-span of the beam in the PSC (Fig. 2). The friction damper is placed in-between the upper and lower columns where a T-shape steel plate connecting to the upper column, and two L-shape steel plates connecting to the lower column (Fig. 3(a)). The T-shape plate has two rows of elongated holes, and the L-shape plates has 2 by 2 holes aligned with the elongated holes. Two brass plates are squeezed by the T-shape and L-shape plates. The frictional high-strength bolts are installed to connect the plates and dissipate energy through sliding along the elongated slotted holes (Fig. 3(b)).

The friction damper functions when the external load exceeds the maximum static frictions and the connections transmit the internal force steadily. The fluent transmission of the connections requires the stiffness of the CD satisfying following criteria: 1) the CD provides additional stiffness to the PSC; 2) the connections sustain external loads together with the PSC; 3) the friction damper provides effective stiffness in comparison with overall stiffness of the PSC. Overall, the CD maintain elastic states and the loads are transmitted to the friction damper.

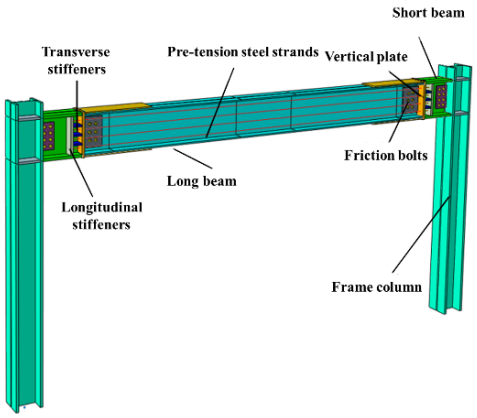


**Fig. 1** Details of PSC

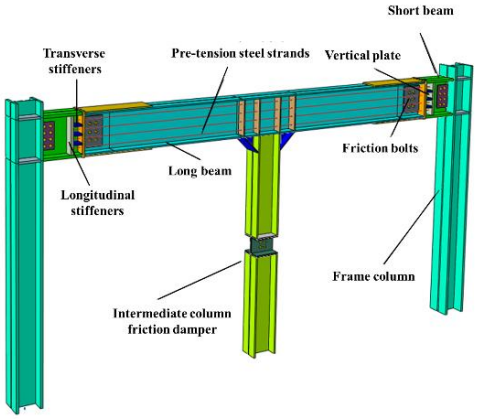


**Fig. 2** Details of PSC-CD

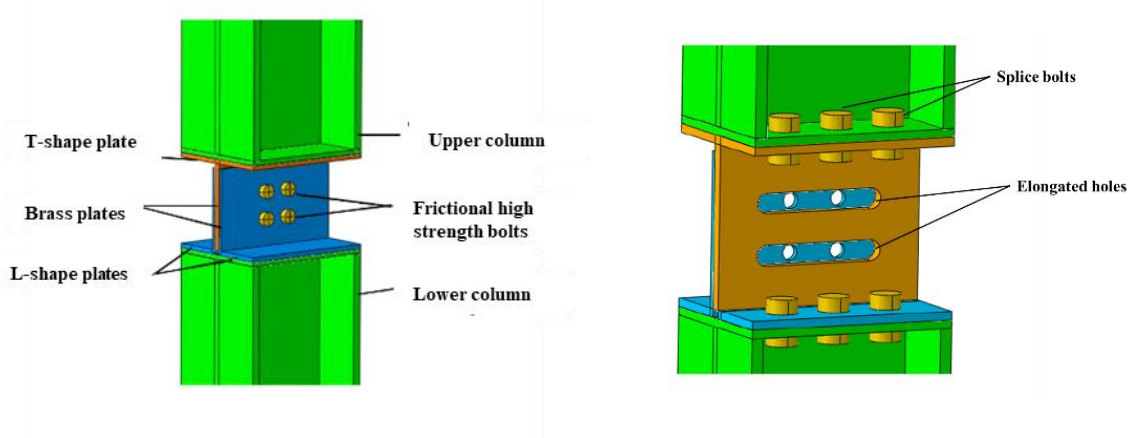


(a) details of CD

(b) details of friction dampers

**Fig. 3** Design of CD

### *2.2. Theoretical analysis of PSC-CD*

Gaps exist in-between the T-shape plate and the lower connecting component, and the L-shape plates and the upper connecting components as shown in Fig. 4. The upper column and the lower column are designed to be straight and vertically. The friction damper has no initial deviation in rorations and translations. Under the assumptions, the minimum distance of the gaps are calculated as following:

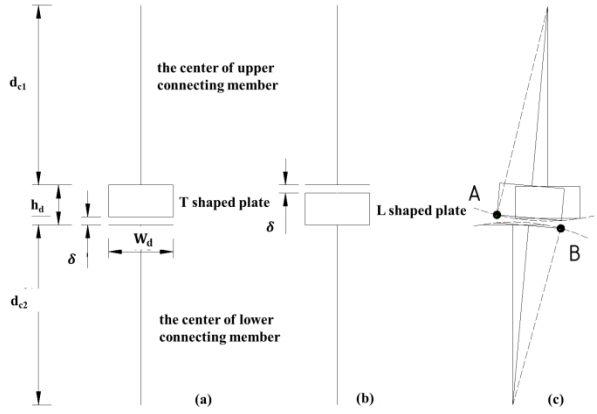


**Fig. 4** Structural details of friction dampers

$$\delta \geq d_{c1} + h_d - \sqrt{(2d_{c1} + h_d - \sqrt{(\frac{W_d}{2})^2 + d_{c1}^2})^2 - (\frac{W_d}{2})^2} \quad (1)$$

$$\delta \leq h_d \quad (2)$$

$$d_{c1} = d_{c2} \quad (3)$$

where
$d_{c1}$ is the height of the upper column;
$d_{c2}$ is the height of the lower column;
$W_d$ is the width of the CD;
$h_d$ is the height of the friction damper;
$\delta$ is the distance of the gaps.

The T-shape plate and L-shape plates are required to maintain elasticity and sustain the friction without deformation. The T- and L-shape plates should meet the following criteria:

$$\frac{3F_{max}}{2t_T \times W_d} < f_V \quad (3)$$

$$\frac{3F_{max}}{4t_L \times W_d} < f_V \quad (4)$$

where
$t_T$ is the thickness of T-plate;
$t_L$ is the thickness of L-plate;
$f_V$ is the shear strength of the steel;
$F_{max}$ is the friction;
$W_d$ is the modulus of section.

### *2.3. Theoretical hysteresis curve of PSC-CD*

The performance of PSC-CD under cyclic loads are carefully analyzed theoretically. The CD provides additional stiffness through frictions with small

shift. As the lateral displacement of PSC-CD increases, the frictions of the friction damper increases till the maximum value achieved. The CD can still provides additional stiffness as the self-centering connections start to work, i.e. the gap between the fixed connection and flexible beam appears. Based on this qualitative analysis, the hysteresis curve of the PSC-CD is proposed with the zigzag shape as shown in Fig. 5.

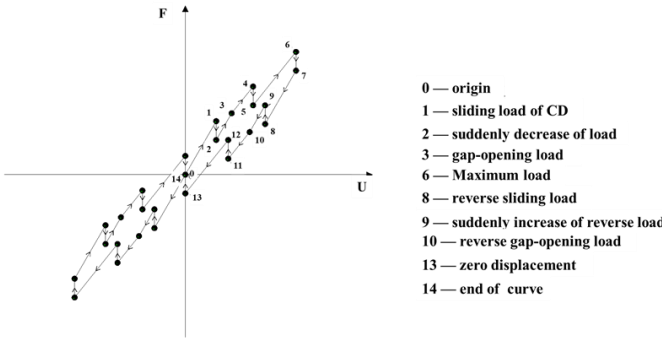


**Fig. 5** Theoretical force displacement curve of PSC-CD

The origin indicates that the frame is located in its original state. Point 1 indicates that the load transmitted to the CD reaches the maximum friction and the friction damper starts to slide. The upper and lower columns of the CD suddenly changed from a vertical state to an inclined state. The additional stiffness provided by the CD thus disappeared observed from point 1 to 2 where a drop occurred. The stiffness at segment 2-3 resembles to that at segment 0-1. Point 3 indicates that the self-centering connection starts to work where the stiffness of the frame decreases. The stiffness at segment 3-4 is mainly provided by the frame. Point 6 indicates the loading capacity of the PSC-CD, and a drop appears from segment 6 to segment 7 represents the maximum friction achieved and the CD slides. Point 8 represents that the loads taken by CD reach the sliding friction in reverse and the additional stiffness suddenly disappears. The external load suddenly increases and the increase value is equal to the sliding load. The stiffness of segment 7 to 8 is consistent with that of segment 0 to 1. Point 10 indicates that the gap openings of the connections begin to close, the segment 10-11 show the stiffness of the entire structure decreases similar to that at segment 3-4. Point 13 indicates that the gap of connection is completely closed, and the damper reaches the sliding load. The curve suddenly returns to points 14, the origin.

## 3. Experimental design

### *3.1. Experimental prototype*

A 3x5 four-story prefabricated resilient steel structure (Fig. 6) is designed with requirement of 50-year service life and 2nd-rank safety level according to the structural properties of the resilient frame and the specification of seimic design [21]. The prefabricated resilient steel structure is located in Beijing, China. The seismic fortification intensity is at level 8, the designed acceleration is 0.2 g, and the site category is level III. The dead load of the floor is 7.0 kN/m$^2$ and the live loads of floors and roofs are both 2.0 kN/m$^2$. The snow load is 0.45 kN/m$^2$. The first-story height is 3.9 m and that of other floors is 3.6m. General beam-column connections are hinged. The frames circled by magenta boxes are the designed resilient prefabricated steel frames. The dimension of the frame column and beam are □400×400×34 mm and H588×300×12×20 mm, respectively. The cross sections of upper and lower columns of the CD are H400×500×20×24 mm. Four M20 high-strength frictional bolts are used in the friction damper. The post-tensioned (PT) high-strength steel strands is 1×19 with the nominal diameter, 21.6mm and the nominal area, 285mm$^2$. The ultimate strength of the strands is 1860 Mpa.

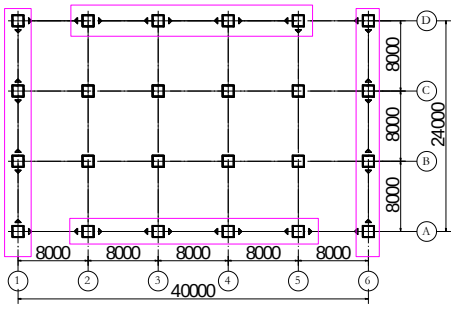


**Fig. 6** The plane diagram of prototype structure

A resilient prefabricated steel frame is selected as a prototype. The study is composed of two parts, i.e. experimental testing and numerical simulations. The first floor is selected for experimental study. The upper floors are studied numerically (Fig. 7). This paper only focus on the experimental study.

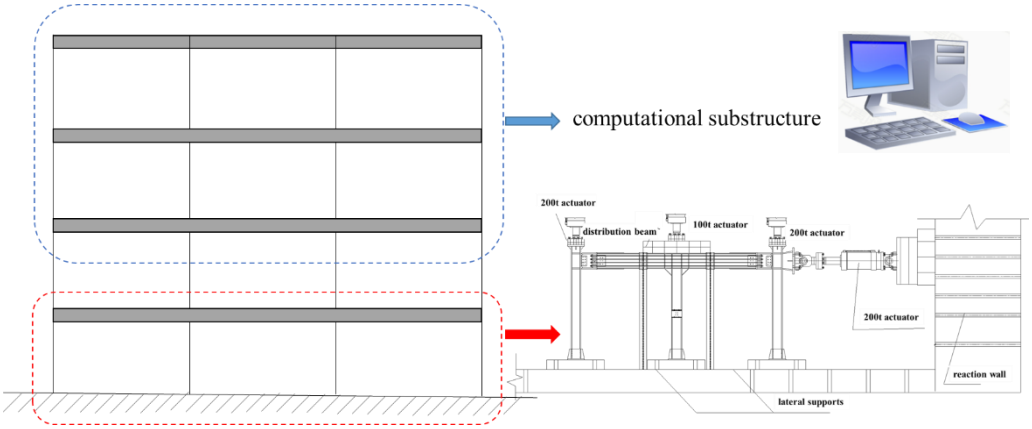


**Fig. 7** Substructures of pseudo-dynamic test

### *3.2. Experimental structures*

The model structure is scaled 0.75 times to the dimension of the prototype and the axial compression ratio is same to the prototype [22]. The detailed dimensions of PSC and PSC-CD are shown in Fig. 8. The story height is 3.15 m and the span is 6 m. The sizes of two testing specimens are as follows: the dimension of column is H300×300×20×30 mm and the thicknesses of column stiffening ribs are 30 mm. The length of long beam(H450×250×14×16 mm) and short beam (H482×250×14×30 mm) are 4740 mm and 450 mm, respectively. The thicknesses of the transverse and the longitudinal stiffening ribs are 30 mm and 20 mm. The cover plates, 800×220×16 mm, are set up on the two ends of the long-beam flanges. The dimension of the vertical plate is 500×250×30 mm, and the frictional plates are welded on the outer surface of the column flange whose dimension is 300×175×14 mm. The thickness of brass plate is 3 mm. Six energy dissipating bolts which connect the short-beam and long-beam adopt M24 high-strength bolts [23] and the eight high-strength bolts which connect the column and short-beam are M20 bolts. Eight 1 × 19 steel strands are selected in each frame beam with the value of the initial PT force for single steel strand of 0.25$T_u$. The size of the connection components for intermediate column is H300×250×16×18 mm and the 4 friction-type high strength bolts of the frictional damper are M16 bolts.

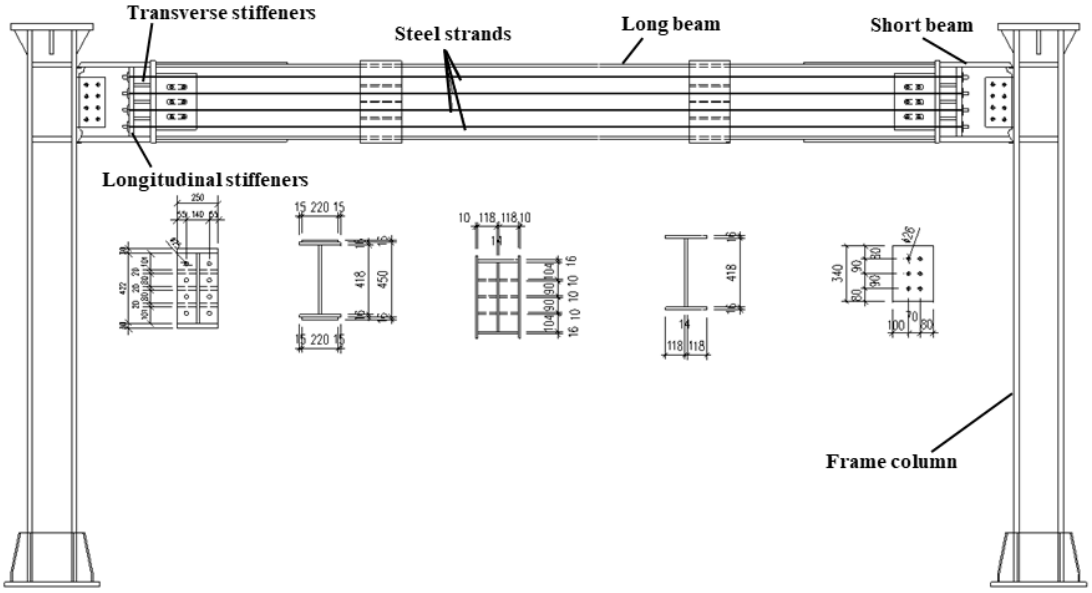


(a) Detailed diagram of PSC

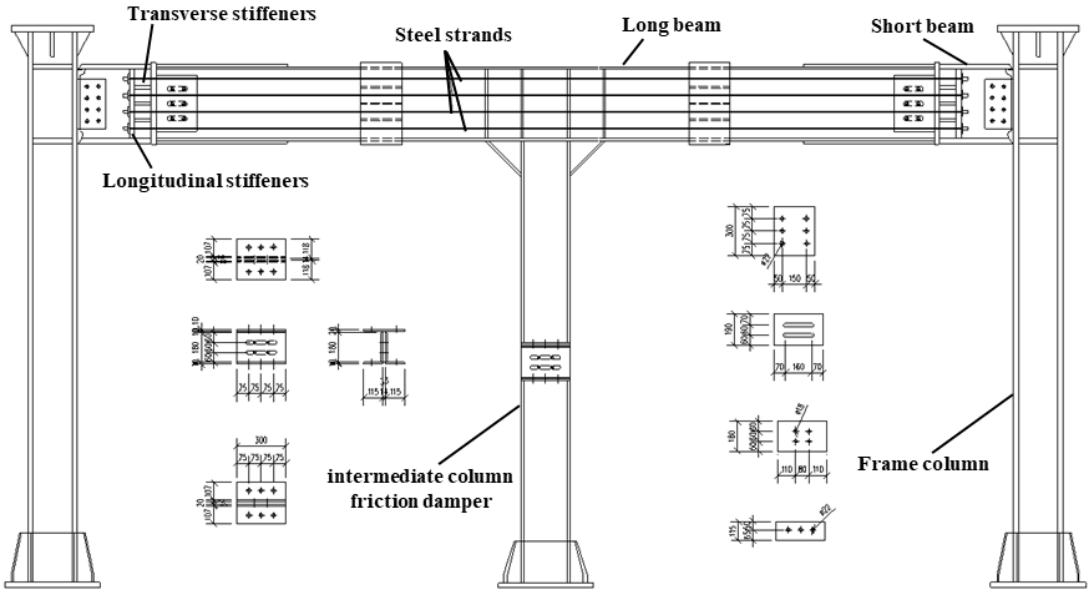


(b) Detailed diagram of PSC-CD

**Fig. 8** Detailed diagram of specimens

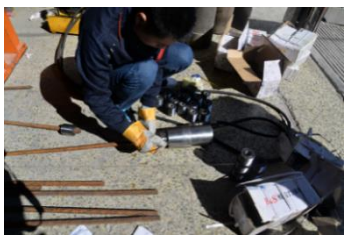

(a) Fix the wedges in the end of strands

(b) Install the sensors in the end of strands

(c) Preloaded in the stressing end

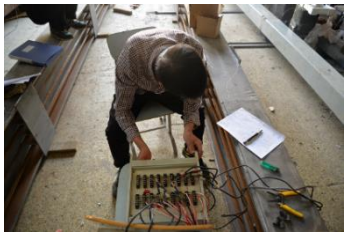

(d) Monitor the variation of cable force

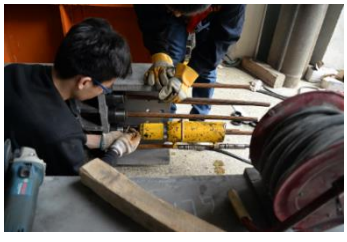

(e) Adjust the cable force

(f) Cut the redundant lengthof steel strands

**Fig. 9** The whole process of tensioning steel strands

(a) Installation of beam and column of the model structure

(b) Installation of CD of the PSC-CD model structure

**Fig. 10** Installation procedures of PSC-CD

The short and long beams of the resilient prefabricated steel frame are connected by 8 PT high strength steel strands. The steel strands are post-tensioned on ground level instead of that in the air. This technique is safe and economic which is conducted as follows (Fig. 9): 1) the long beam and short beam are connected through the frictional plates and bolts; 2) steel strands are fixed through the holes with pressure sensors are mounted on the anchors at both ends; 3) steel strands are initially tensioned to the 70% of the designed values at one end with the other end fixed; 4) the steel strands achieved its targeted force in the second tensioning. The whole post-tension technique thus achieved.

The model structure is built up. The columns are bolted to the ground through the hold-down. A shear plate is welded to the hanging end of the column. The beam, i.e. long beam connected with the short beam, is installed to the columns through bolting and welding. The web of the beam is tightly connected to the shear plate on the column. Two flanges of the I-section beam are angle welded to the column. Thus the PSC model structure is set up (Fig. 10(a)).

Regarding to the PSC-CD model structure, the upper column is mounted on the long beam firstly. The lower column of the CD is installed through hold-down similar to other columns. The friction damper bridges the lower column to the upper column via the T-shape an L-shape plates' combinations. The high-strength frictional bolts are eventually tightened and the entire PSC-CD model structure is completed (Fig. 10(b)).

### *3.3. Material properties*

The model structures, i.e. PSC and PSC-CD are made of Q345B steel [24]. Three types of material testing are conducted: steel-tensile tests, steel-strands tests and plate-friction tests.

The tensile tests prepare 6 types of coupons categorized by the thickness. Each types of coupons have 3 testing samples. The coupon tests are tested by the universal material testing machine. The material properties of Q345B steel used in the experiment are shown in the Table. 1.

Three steel strands are stretched in the steel-strands tests. The steel strands are cut from the long steel strands and place in the universal material testing machine for testing. The material properties of steel strands are shown in Table. 2.

The brass plates in the frictional damper is designed to dissipate energy through frictions between brass and steel. The plate-friction tests are set up for the frictional damper embedded in the CD. The specimen is made of two brass plates and a steel plate in-between (Fig. 11(a)). The frictional coefficient between the steel- and the brass- plates range from 0.34 to 0.38. The hysteresis curve of the test is shown in Fig. 11(b).

**Table 1**
Material test of Q345B

| Material | Thickness (mm) | $E$ ($\times10^5$N/mm$^2$) | Yield strength (N/mm$^2$) | Ultimate strength (N/mm$^2$) | Elongation percentage (%) |
|---|---|---|---|---|---|
| Q345B | 12 | 2.08 | 435 | 570 | 27 |
| | 14 | 2.05 | 384 | 561 | 24.15 |
| | 16 | 2.1 | 392 | 555 | 24.05 |
| | 18 | 2.09 | 381 | 555 | 24.5 |
| | 20 | 2.1 | 384 | 550 | 26.95 |
| | 30 | 2.07 | 350 | 505 | 28.05 |

**Table 2**
Material test of steel strands

| Steel strands | Specimen | $E$($\times10^5$N/mm$^2$) | Yield strength/(N/mm$^2$) | Tensile strength (N/mm$^2$) |
|---|---|---|---|---|
| 1×19 | Specimen1 | 2.03 | 1728.3 | 1894.5 |
| | Specimen2 | 2.05 | 1727.1 | 1895.8 |
| | Specimen3 | 2.00 | 1732.8 | 1875.4 |
| | Average | 2.03 | 1729 | 1889 |

(a) Friction test of brass plates

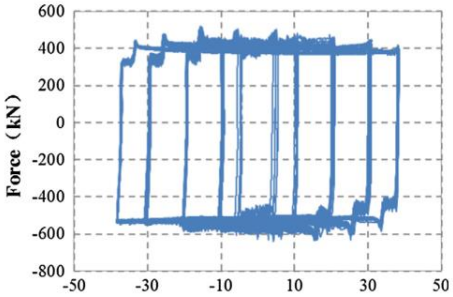


(b) Force-displacement hysteresis loops

**Fig. 11** The friction experiment of Q345B steel and brass plates

### *3.4. Testing set-up*

The 200-ton horizontal actuator mounted on the reaction wall provides lateral loads to the specimen under the displacement command by the computer. Two 200-ton hydraulic jacks are placed on the top of two columns, providing 756 kN axial compression. A distribution beam is place in the mid-span of

beams of the model structures. The 100-ton hydraulic jack simulates the live load together with a distribution beam and loads at the frame beam with 96 kN. Two lateral supports at the 1/3- and 2/3-span prevent the out-of-plane buckling of the frame beam (Fig. 12).

The pseudo-dynamic testing are conducted for both PSC and PSC-CD through the multi-story structural remote-control hybrid pseudo-dynamic testing platform (NestSLab_MSBSM1.0.0). The commanded displacement is integrated from accelerations of a selected seismic signal considering both the experimental substructure and the numerical substructure. Floor weights and theoretical hysteretic curves are input for the numerical substructures. The damping ratios of each floor are set as 0.05 for the testing in the platform. The stiffness before and after the opening of self-centering beam-column connections, i.e. $K_1$ and $K_2$, are obtained from the numerical simulations of the model structures, same to those displacement $d_1$ and $d_2$ of the entire model structures (Table. 3&4). The selected seismic waves are El-Centro and Wenchuan (Fig. 13 and Fig. 14). The peak accelerations of selected waves are scaled as 0.07g, 0.2g, 0.4g, 0.51g, 0.62g, 0.8g, 1.0g corresponding to different earthquake intensities: frequent-, fortification-, rare-, medium-rare, 9-degree rare-, and extreme-rare intensities according to the specification [21]. The time steps of the original waves are 0.01s and those of the input waves are scale to 0.0086s for the 0.75-time model structures. The response spectrum of the waves are shown in Fig. 15.

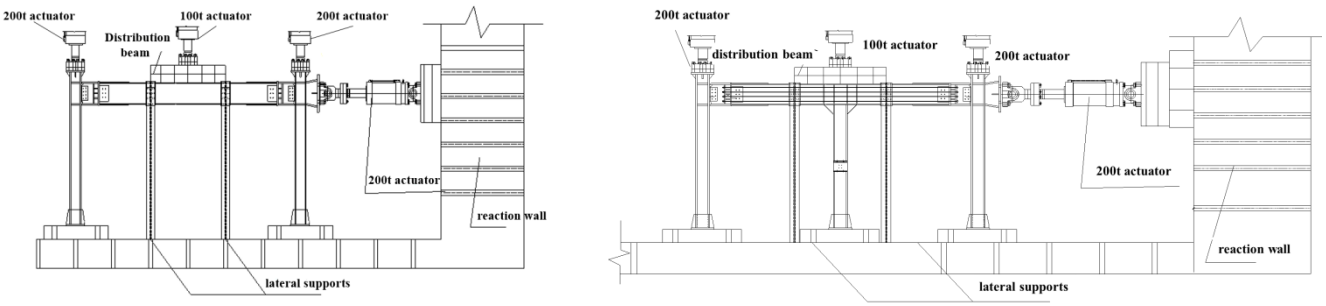


(a) PSC (b) PSC-CD

**Fig. 12** Diagrammatic sketch of loading

**Table 3**
Input parameters of the test

| Story | $M$ (t) | $K_1$ (kN/m) | $K_2$ (kN/m) | $d_1$ (mm) | $d_2$ (mm) |
|---|---|---|---|---|---|
| 4 | 162 | 14176 | 3677 | 24.0 | 20.0 |
| 3 | 162 | 14178 | 3676 | 24.9 | 20.3 |
| 2 | 162 | 13376 | 3692 | 21.6 | 20.3 |
| 1 | 162 | 28449 | 10988 | 29.0 | 23.6 |

**Table 4**
Input parameters of pseudo-dynamic test for resilient prefabricated steel frame with intermediate column friction damper

| Story | $M$ (t) | $K_1$ (kN/m) | $K_2$ (kN/m) | $d_1$ (mm) | $d_2$ (mm) |
|---|---|---|---|---|---|
| 4 | 170 | 31600 | 4990 | 16.2 | 29.2 |
| 3 | 170 | 34327 | 6087 | 16.2 | 29.2 |
| 2 | 170 | 32295 | 8839 | 16.2 | 29.2 |
| 1 | 170 | 38313 | 10512 | 12.5 | 25.0 |

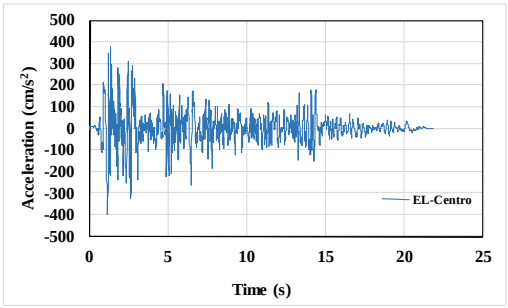


**Fig. 13** Time history curve of EL-Centro

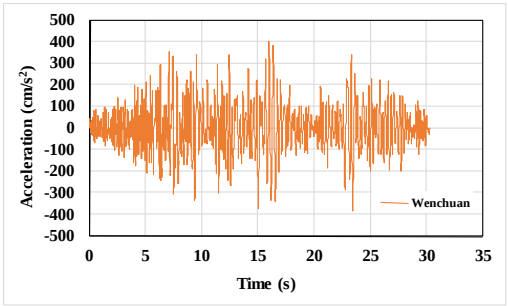


**Fig. 14** Time history curve of Wenchuan

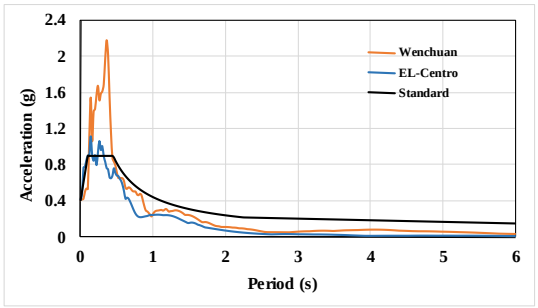


**Fig. 15** Response spectrum

### *3.5. Measurement set-up*

#### *3.5.1. Cable force and bolt load*

Pressure sensors (Fig. 16 (a)) are placed at one ends of the steel strands to record variations of cable forces ranging up to 500 kN during the loading process. The bolted forces of CD are measured by pressor sensors ranging up to 300 kN (Fig. 16 (c)).

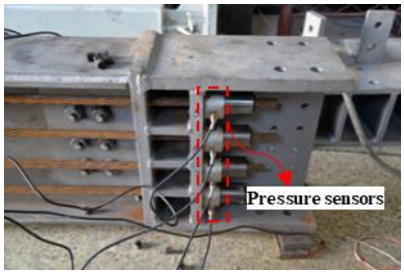


(a) Force sensor

(b) Pressure sensor

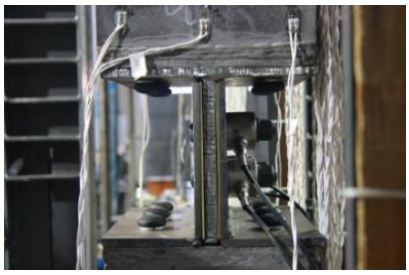

(c) Bolt sensor

**Fig. 16** The setup and appearance of sensors

*3.5.2. Displacement*

The measurement of displacement mainly includes the following aspects, and the layout diagrams are presented in Fig. 17.

(1) Displacements of frames: the displacement sensors of the horizontal actuator measures the lateral displacements of the model structures. The displacement meters ranging up to 150 cm are placed at the left/right upper flanges of the columns. The displacements of the top of the column are measured. The other displacement meters are placed at the base of the columns and measure the slippages.

(2) Gap-openings: the gap-opening of connections are monitored by the resistance displacement meters whose range is up to 40 mm. The meters were installed at the inner sides of upper and lower flanges of the long beam.

(3) Displacements of the CD: the displacement meters ranging up to 50 cm are allocated at the base of the CD. The horizontal slippages at the bottom of the lower column are measured. Two displacement meters are placed at the upper and lower columns of CD, adjacent to the friction damper. The ranges of these meters are up to 150 cm. The distance of gap opening of the friction damper thus is calculated as the difference between displacements of the upper and lower columns.

*3.5.3. Strain*

Strain gauges are installed on the various positions of the specimens (Fig. 18): flanges and bases of columns, flanges of the beam, upper and lower columns of the CD (Fig.18 (b)). Three-way strain gauges are used to measure the web of frame columns and that of the CD.

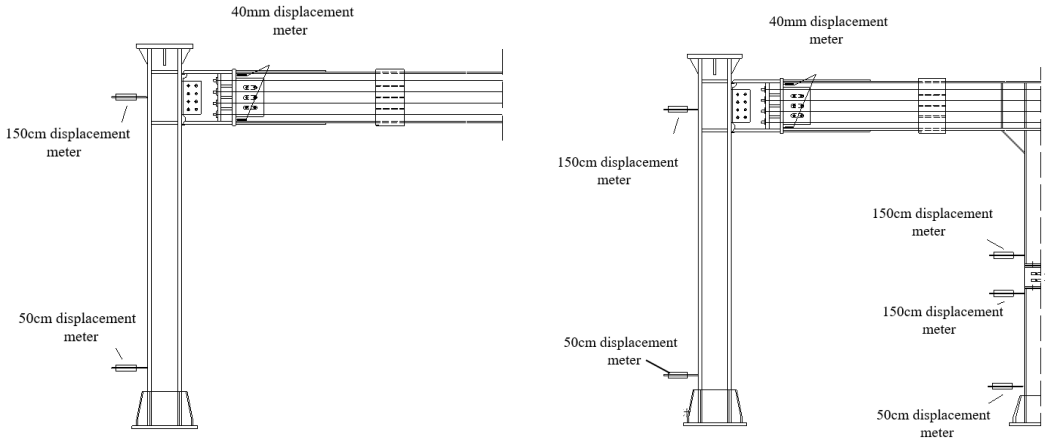


(a) Layout of displacement meter for PSC

(b) Layout of displacement meter for PSC-CD

**Fig. 17** Layout diagrams of displacement meter

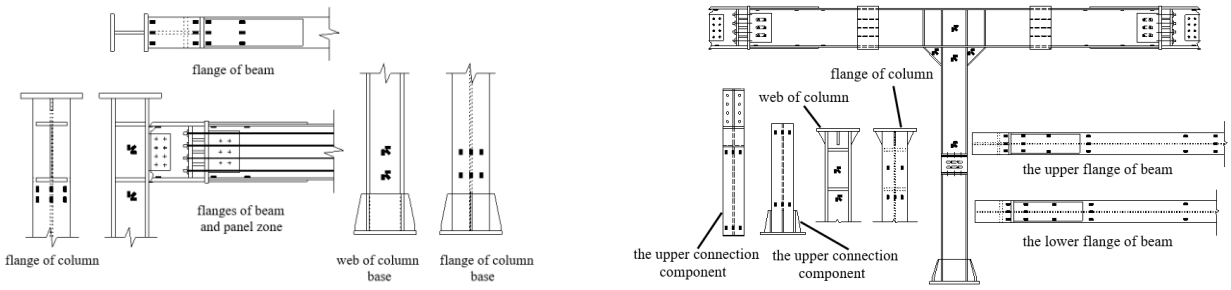


(a) Arrangement of strain gauges for PSC

(b) Arrangement of strain gauges for PSC-CD

**Fig. 18** The detailed arrangement of strain gauges

**Table 5**
The variation of maximum displacement response

| | Items | 0.07g | 0.20g | 0.40g | 0.51g | 0.62g | 0.80g |
|---|---|---|---|---|---|---|---|
| PSC | + (mm) | 5.22 | 15.50 | 34.50 | 46.30 | 46.70 | 66.70 |
| | Interstory drift (1/rad) | 563 | 190 | 85 | 63 | 63 | 44 |
| | - (mm) | 7.81 | 23.02 | 35.12 | 45.10 | 58.05 | 65.02 |
| | Interstory drift (1/rad) | 376 | 129 | 84 | 65 | 51 | 45 |
| PSC-CD | + (mm) | 7.00 | 19.60 | 29.30 | 32.40 | 45.40 | 61.80 |
| | Interstory drift (1/rad) | 420 | 150 | 100 | 91 | 65 | 48 |
| | - (mm) | 8.20 | 16.80 | 26.90 | 31.50 | 30.80 | 39.80 |
| | Interstory drift (1/rad) | 359 | 175 | 109 | 93 | 95 | 74 |

## 4. Experimental study

### 4.1. Displacement response

The time history curves of the variation of displacement response for PSC and PSC-CD under the action of Wenchuan wave is shown in Fig. 19. The displacement response under Wenchuan wave is greater than that under EL-Centro wave. The analysis presented in this paper mainly focus on the Wenchuan wave. The maximum horizontal displacements are listed in Table. 5.

The inter-story drifts of both PSC and PSC-CD were less than the elastic limits, i.e. 1/250 required by the specification [25], under the attack of 8-degree frequent earthquake. However, the drifts of both systems were beyond the elastic inter-story limits but within the plastic inter-story drift (1/50) when the amplitudes of Wenchuan wave were as strong as 8-degree fortification and rare earthquakes.

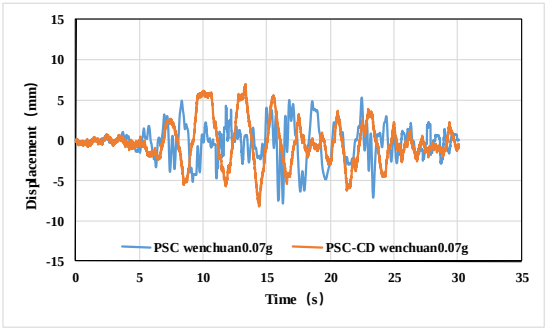


(a) In the condition of frequent earthquake(0.07g)

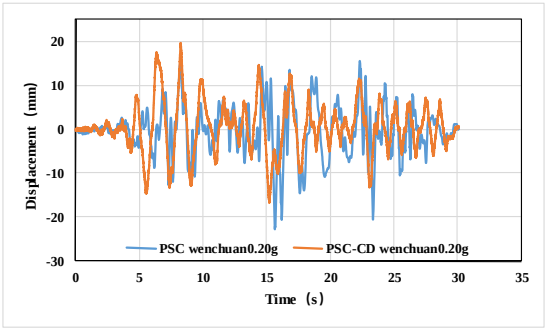


(b) In the condition of fortification earthquake (0.02g)

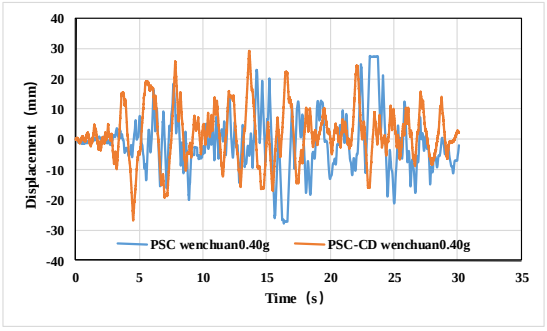


(c) In the condition of rare earthquake (0.40g)

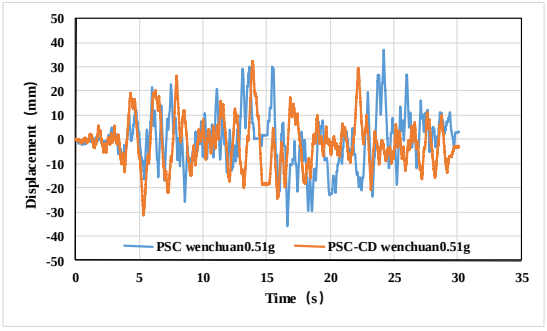


(d) In the condition of 8-degree rare earthquake (0.51g)

**Fig. 19** Displacement time history curves for PSC and PSC-CD under the action of Wenchuan wave

(a) Column interstory at 1/84 for PSC

(b) Column interstory at 1/100 for PSC-CD

**Fig. 20** Photographs of lateral displacement for columns under the actions of Wenchuan (PGA=0.04g)

(a) Column interstory at 1/63 for PSC

(b) Column interstory at 1/91 for PSC-CD

**Fig. 21** Photographs of lateral displacement for columns under the actions of Wenchuan (PGA=0.51g)

### 4.2. Gap-opening

The gap openings of beam-column connections demonstrate the structural performances of the systems. The values of gap-opening for PSC and PSC-CD are listed in Table. 6. The beam-column connections remained stills during the 8-degree frequent earthquake. Small gaps showed when the amplitudes of the Wenchuan wave reached 8-degree fortification earthquake.

The gap openings developed as the amplitudes of Wenchuan wave increased from 0.2g to 1.0g (Table. 6). The maximum rotations are 0.514% for PSC and 0.344% for PSC-CD when the acceleration is 0.51g. The rotations reach 1.547% for PSC and 0.933% for PSC-CD as the acceleration is 1.0g. The PSC-CD show its advantages as the earthquake go stronger.

On the other hand, the residual gap-opening rotations of the PSC-CD remain smaller compared to that of the PSC. The residual gap-openings are 0.033% for the PSC but 0% for the PSC-CD at acceleration 0.51g. The PSC has 0.029% residual gap-opening when the acceleration is 1.0g. The PSC-CD is only 0.011%. The CD provides the additional lateral stiffness and damping to protect the beam-column connections thus strengthen the overall steel frames eventually.

**Table 6**
The maximum and residual gap-opening

| Items | PGA | | Maximum gap-opening | | Residual gap-opening | | Maximum gap-opening rotation | | Residual gap-opening rotation | |
|---|---|---|---|---|---|---|---|---|---|---|
| | | | - | + | - | + | - | + | - | + |
| | | | mm | mm | mm | mm | rad% | rad% | rad% | rad% |
| PSC | 0.20g | EL-Centro | 0.31 | 0.23 | 0.040 | 0.008 | 0.068 | 0.052 | 0.009 | 0.002 |
| | | Wenchuan | 0.41 | 0.35 | 0.013 | 0.025 | 0.090 | 0.078 | 0.003 | 0.006 |
| | 0.40g | Wenchuan | 1.30 | 0.82 | 0.130 | 0.135 | 0.289 | 0.181 | 0.029 | 0.030 |
| | 0.51g | Wenchuan | 2.32 | 0.86 | 0.150 | 0.090 | 0.514 | 0.192 | 0.033 | 0.020 |
| | 0.62g | Wenchuan | 4.63 | 1.21 | 0.030 | 0.013 | 1.028 | 0.268 | 0.007 | 0.003 |
| | 0.80g | Wenchuan | 5.60 | 2.03 | 0.020 | 0.023 | 1.243 | 0.451 | 0.004 | 0.005 |
| | 1.0g | Wenchuan | 6.96 | 2.87 | 0.075 | 0.133 | 1.547 | 0.637 | 0.017 | 0.029 |
| PSC-CD | 0.20g | EL-Centro | 0.5 | 0.15 | 0 | 0 | 0.111 | 0.033 | 0 | 0 |
| | | Wenchuan | 0.6 | 0.3 | 0 | 0 | 0.133 | 0.067 | 0 | 0 |
| | 0.40g | Wenchuan | 1.3 | 0.5 | 0 | 0.05 | 0.289 | 0.111 | 0 | 0.011 |
| | 0.51g | Wenchuan | 1.55 | 0.7 | 0 | 0 | 0.344 | 0.156 | 0 | 0 |
| | 0.62g | Wenchuan | 1.9 | 1.1 | 0 | 0 | 0.422 | 0.244 | 0 | 0 |
| | 0.80g | Wenchuan | 2.8 | 1.95 | 0.05 | 0.1 | 0.622 | 0.433 | 0.011 | 0.022 |
| | 1.0g | Wenchuan | 4.2 | 2.15 | 0 | 0.05 | 0.933 | 0.478 | 0 | 0.011 |

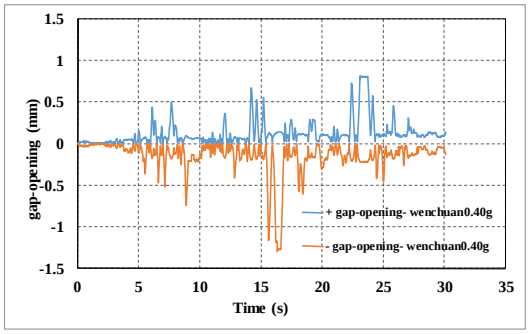


(a) Gap-opening of PSC (Wenchuan 0.40g)

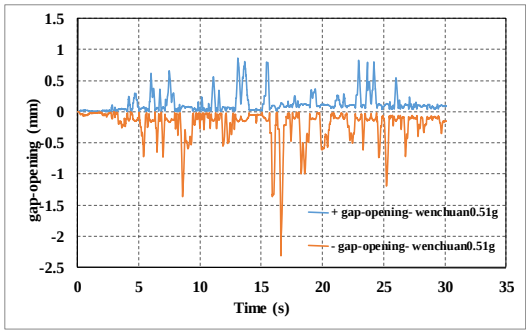


(b) Gap-opening of PSC (Wenchuan 0.51g)

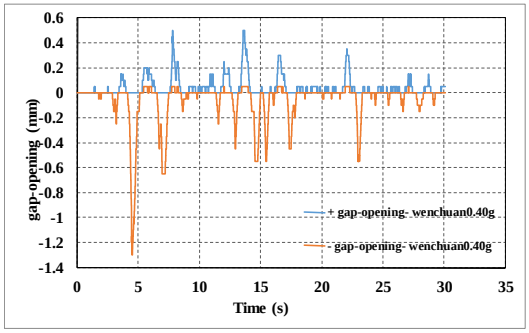


(c) Gap-opening of PSC-CD (Wenchuan 0.40g)

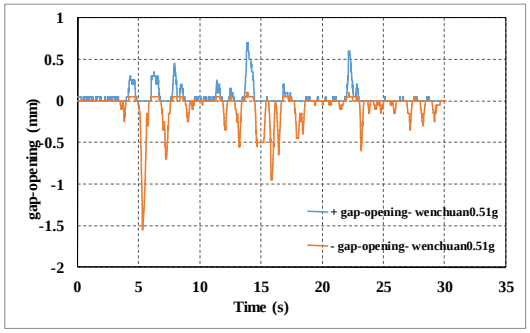


(d) Gap-opening of PSC-CD (Wenchuan 0.51g)

**Fig. 22** Time history curves of gap-opening for PSC and PSC-CD

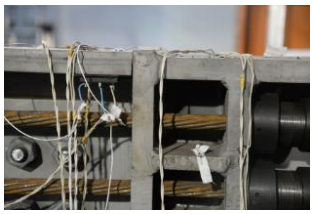

(a) Gap-opening of PSC (0.40g)

(a) Gap-opening of PSC (0.51g)

(c) Gap-opening of PSC-CD (0.40g)

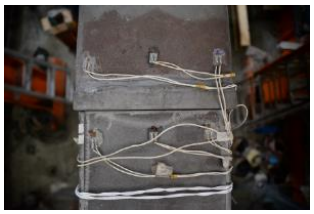

(d) Gap-opening of PSC-CD (0.51g)

**Fig. 23** The photographs of gap-opening for PSC and PSC-CD under Wenchuan waves

### *4.3. Cable force*

Table. 7 presents the variations of cable force in different seismic accelerations. It lists the initial values, maximum values, minimum values during the testing and the final values at the end. The ultimate tensile strength of steel strands $T_u$ is 591kN presented in the previous section. In the condition of 8-degree frequent earthquake, the cable force is unchanged as no openings at the connections. In the condition of 8-degree fortification earthquake, cable force increases slightly. In the condition of rare earthquake, the maximum cable forces for PSC and PSC-CD are $0.266T_u$ and $0.277T_u$ respectively. The cable forces recover to the initial values after loading in each case of the seismic accelerations as shown in Table. 7. Under the action of seismic waves whose peak acceleration is in the range of 0.62g to 1.0g, the increases of cable forces for PSC are greater than that of PSC-CD as the greater gap-openings are generated. The variations of cable force have the same tendency with gap openings. The systems are resilient after earthquake as PT steel strands are used. After the test, the maximum accumulative decreases for PSC and PSC-CD were 9.79% and 4.98%. The remained PT cable forces demonstrates that the systems, especially the PSC-CD can function and withstand aftershocks in the reality.

**Table 7**
Variation of cable force

| Items | Moment | 0.07g | 0.20g | 0.40g | 0.51g | 0.62g | 0.80g | 1.0g |
|---|---|---|---|---|---|---|---|---|
| | | $T_{ave}/T_u$ | $T_{ave}/T_u$ | $T_{ave}/T_u$ | $T_{ave}/T_u$ | $T_{ave}/T_u$ | $T_{ave}/T_u$ | $T_{ave}/T_u$ |
| PSC | Initial | 0.249 | 0.248 | 0.246 | 0.244 | 0.238 | 0.233 | 0.229 |
| | Maximum | 0.250 | 0.257 | 0.266 | 0.275 | 0.309 | 0.318 | 0.335 |
| | Minimum | 0.246 | 0.244 | 0.241 | 0.237 | 0.231 | 0.227 | 0.221 |
| | End | 0.249 | 0.248 | 0.244 | 0.243 | 0.236 | 0.231 | 0.225 |
| PSC-CD | Initial | 0.247 | 0.256 | 0.252 | 0.251 | 0.250 | 0.247 | 0.245 |
| | Maximum | 0.261 | 0.267 | 0.277 | 0.282 | 0.282 | 0.293 | 0.316 |
| | Minimum | 0.244 | 0.242 | 0.241 | 0.241 | 0.235 | 0.235 | 0.227 |
| | End | 0.255 | 0.250 | 0.251 | 0.251 | 0.247 | 0.245 | 0.236 |

**Table 8**
Cumulative decreases of cable force

| PGA | PSC | | | | PSC-CD | | | |
|---|---|---|---|---|---|---|---|---|
| | EL-Centro | | Wenchuan | | EL-Centro | | Wenchuan | |
| | Percentage | Force/kN | Percentage | Force/kN | Percentage | Force/kN | Percentage | Force/kN |
| 0.07g | 0.11% | 0.16 | 0.13% | 0.19 | 0.58% | 0.83 | -2.70% | -3.9 |
| 0.20g | 0.44% | 0.63 | 0.39% | 0.56 | -3.16% | -4.57 | -0.62% | -0.9 |
| 0.40g | 1.31% | 1.9 | 1.91% | 2.77 | - | - | -1.01% | -1.47 |
| 0.51g | 2.01% | 2.92 | 2.55% | 3.69 | - | - | -1.01% | -1.47 |
| 0.62g | 4.52% | 6.55 | 5.32% | 7.71 | - | - | 0.69% | 1 |
| 0.80g | 6.35% | 9.2 | 7.10% | 10.29 | - | - | 1.57% | 2.27 |
| 1.0g | 8.24% | 11.94 | 9.79% | 14.19 | - | - | 4.98% | 7.2 |

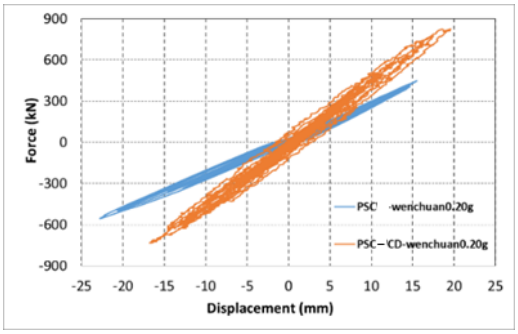


(a) Hysteresis loops of PSC and PSC-CD (0.20g)

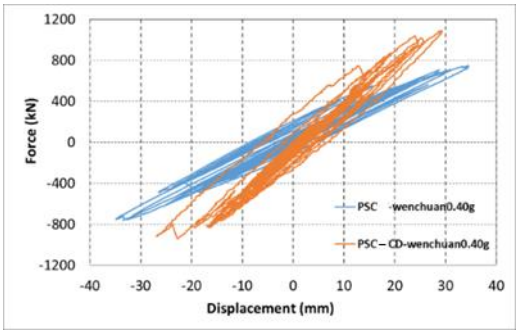


(b) Hysteresis loops of PSC and PSC-CD (0.40g)

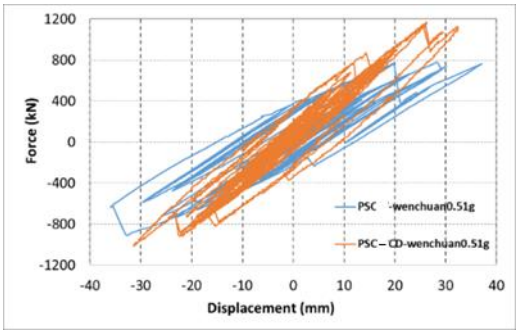


(c) Hysteresis loops of PSC and PSC-CD (0.51g)

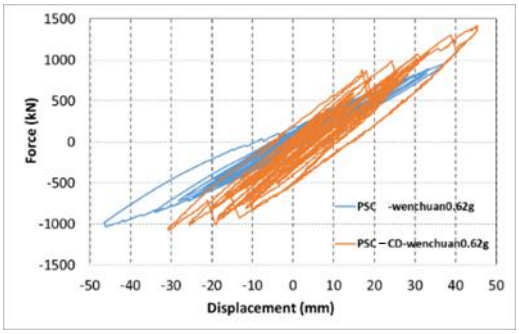


(d) Hysteresis loops of PSC and PSC-CD (0.62g)

**Fig. 24** Force-displacement curves of PSC and PSC-CD under the actions of different earthquake (Wenchuan wave)

### 4.4. Hysteretic behavior

The force-displacement curves of the two frames show the linearity in the elastic states before the 8-degree fortification earthquake. The initial PSC-CD system shows higher initial lateral stiffness compared to the PSC system, 48.20 kN/mm and 30.95 kN/mm respectively.

The hysteresis behaviors of the systems start as the PGA reaches 0.2g (the fortification earthqauake) (Fig. 24 (a)). The inside areas of the hysteresis loops further increase as the PGA increases (Fig. 24). The areas inside the curves of PSC-CD are greater than that of PSC. The energy dissipation capacity of PSC-CD is better than that of PSC. The loading capacity of PSC-CD is much higher than that of PSC in the same condition. Hysteresis loops of PSC-CD appear 'zigzag' shapes due to the discontinuous slippage of friction damper. The existence of CD provides the additional damping. Thus the energy consumption capacity of the PSC-CD improves the steel frame are protected in turn.

### 4.5. Strain analysis

The maximum values of the strain for some typical locations under the different ground motions are shown in Table. 9. In the condition of 8-degree frequent earthquake and fortification earthquake, PSC and PSC-CD are both in the elastic state. The maximum strains exist in panel zones for frames and flanges for the CD. The main structure is safe.

In the condition of 8-degree rare earthquake, the values of strain increase continuously. Both panel zones of PSC and PSC-CD reach to the plastic stage. The value of PSC is larger than that of PSC-CD over $2\varepsilon_y$ ($\epsilon_y = 2000\mu\epsilon$). The maximum strains locate at the flange of column bases as well as at the beam of the PSC reaching to the plastic stages.

Though the PSC is resilient, the PSC-CD shows better seismic performance with greater lateral stiffness and energy-dissipation capacities. The panel zones of both systems need to be improved and carefully checked. The stiffening ribs can be installed and the thickness of the panel zones can increase.

**Table 9**
Maximum values of the strain at some typical locations

| PGA | Text component | Seismic wave | Flange of column base | Web of column base | Panel zone | Flange of long beam | Flange of short beam | Flange of intermediate column | web of intermediate column |
|---|---|---|---|---|---|---|---|---|---|
| 0.07g | PSC | Wenchuan | 430 | 88 | 909 | 326 | 200 | 0 | 0 |
| | PSC-CD | Wenchuan | 373 | 180 | 377 | 110 | 65 | 497 | 338 |
| 0. 20g | PSC | Wenchuan | 1006 | 164 | 1875 | 927 | 851 | 0 | 0 |
| | PSC-CD | Wenchuan | 393 | 356 | 495 | 199 | 206 | 1171 | 724 |
| 0.40g | PSC | Wenchuan | 1279 | 129 | 4898 | 1219 | 1132 | 0 | 0 |
| | PSC-CD | Wenchuan | 1003 | 901 | 3428 | 714 | 667 | 1599 | 964 |

**Table 10**
Slippage of intermediate column

| Seismic action | Slippage | |
|---|---|---|
| | +/mm | -/mm |
| EL-C0.07g | 1.213 | -0.817 |
| Wenchuan0.07g | 1.357 | -0.522 |
| EL-C0.20g | 0.774 | -1.316 |
| Wenchuan 0.20g | 4.382 | -1.484 |
| Wenchuan 0.40g | 8.991 | -12.157 |
| Wenchuan 0.51g | 8.6 | -10.5 |
| Wenchuan 0.62g | 24.58 | -12.64 |
| Wenchuan 0.80g | 41.36 | -8.54 |
| Wenchuan 1.0g | 34.21 | -33.65 |

### 4.6. Analysis of intermediate column friction damper

#### 4.6.1. Slippage analysis of friction damper

The slippage variations under the action of ground motion are shown in Table. 10 and Fig. 25. The test pictures of slippage of intermediate column under different ground motions are shown in Fig. 27. It can be found that the slippage is too small before 8-degree fortification earthquake. The friction damper of CD provides additional stiffness at this stage and small amount of damping function. The maximum slippage is 4.328 mm. The slippage increases to 12.157 mm under the rare earthquakes (PGA = 0.40g). The friction damper reached to 24.58 mm slippage at large under the PGA = 0.62g seismic wave. The slippage of friction damper increases with the enhance of earthquake effect. The time history of slippage of CD displays in Fig. 26. It can be concluded that the CD originally provides additional lateral stiffness when the intensity of earthquake is small. The friction damper starts working as the seismic energy increase and the displacements of CD arise.

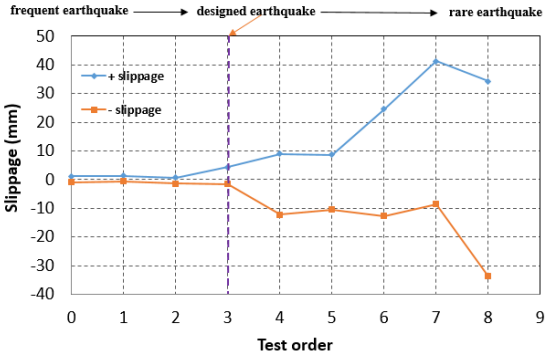


**Fig. 25** Slippage under the action of different conditions of ground motion

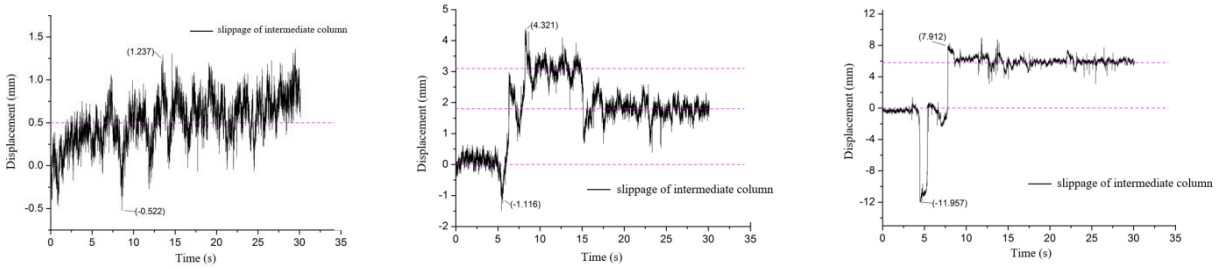


(a) Slippage of CD (0.07g) (b) Slippage of CD (0.20g) (f) Slippage of CD(0.40g)

**Fig. 26** Slippage time histories of intermediate column damper

(a) 0.07g

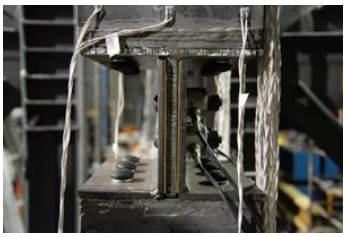

(a) 0.20g

(a) 0.40g

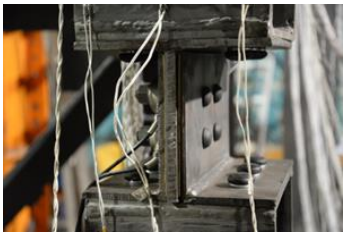

(a) 0.51g

(a) 0.62g

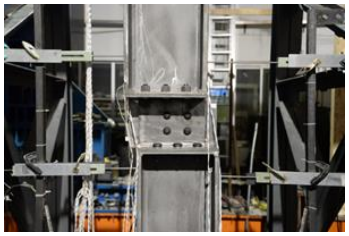

(a) 0.80g

**Fig. 27** Slippage of intermediate column under different ground motions

**Table 11**
Bolt force variations

| Seismic action | Moment | 0.07g $P_{los}/P_{ave}$ | 0.20g $P_{los}/P_{ave}$ | 0.40g $P_{los}/P_{ave}$ | 0.51g $P_{los}/P_{ave}$ | 0.62g $P_{los}/P_{ave}$ | 0.80g $P_{los}/P_{ave}$ | 1.0g $P_{los}/P_{ave}$ |
|---|---|---|---|---|---|---|---|---|
| EL-Centro | Initial | 0.00% | 5.03% | - | - | - | - | - |
| | Maximum | 3.01% | 8.63% | - | - | - | - | - |
| | Minimum | -0.43% | 3.35% | - | - | - | - | - |
| | End | 2.40% | 6.49% | - | - | - | - | - |
| Wenchaun | Initial | 2.40% | 6.49% | 14.97% | 12.98% | 17.32% | 21.20% | 27.89% |
| | Maximum | 4.27% | 14.56% | 16.25% | 17.32% | 23.58% | 29.25% | 36.93% |
| | Minimum | 0.77% | 5.03% | 4.78% | 4.27% | 5.16% | 3.30% | 17.34% |
| | End | 3.30% | 12.49% | 12.98% | 15.91% | 21.20% | 27.89% | 35.12% |

**Table 12**
Bolt force loss

| PGA | EL-Centro | | Wenchuan | |
|---|---|---|---|---|
| | Percentage | Force/kN | Percentage | Force/kN |
| 0.07g | 2.40% | 2.35 | 0.89% | 0.88 |
| 0.20g | 1.46% | 1.43 | 6.00% | 5.88 |
| 0.40g | - | - | -1.99% | -1.95 |
| 0.51g | - | - | 2.94% | 2.88 |
| 0.62g | - | - | 3.88% | 3.80 |
| 0.80g | - | - | 6.69% | 6.55 |
| 1.0g | - | - | 7.23% | 7.07 |

**Table 13**
Cumulative losses of bolt force

| PGA | EL-Centro | | Wenchuan | |
|---|---|---|---|---|
| | Percentage | Force/kN | Percentage | Force/kN |
| 0.07g | 2.40% | 2.35 | 3.30% | 3.23 |
| 0.20g | 6.49% | 6.35 | 12.49% | 12.23 |
| 0.40g | - | - | 12.98% | 12.70 |
| 0.51g | - | - | 15.91% | 15.58 |
| 0.62g | - | - | 21.20% | 20.75 |
| 0.80g | - | - | 27.89% | 27.30 |
| 1.0g | - | - | 35.12% | 34.38 |

*4.6.2 Bolt forces of the intermediate column friction damper*

The average initial bolt force, $P_{ave}$, is 98.785kN. The variations of average bolt force are listed on Table. 11. Positive values represent the decrease of bolt forces and negative values represent the increase of bolt forces. The losses of bolt forces at the beginning and end moments of each loading stage are listed in Table. 12. The accumulative losses of bolt force at the end of each loading stage are listed in Table. 13. The losses of bolt force are probably from the testing noises and installation errors as the CD only provides the lateral stiffness under 8-degree frequent earthquake (PGA = 0.07g). The friction damper in the CD slipped and the loss of bolt forces accumulates as the PGA is 0.2g. The maximum loss of bolt forces (PGA = 0.4g) is 16.25%, i.e. 12.70 kN at the end of testing. It can be found from Table.12 that the maximum loss was 6.0% in the conditions of as the PGA is 0.2g. The bolt force increase by 1.99% in the condition of 8-degree rare earthquake (PGA = 0.4g). The bolts provide stable and continuous pressure for the friction damper. Losses of bolt force are acceptable for the stability of CD under the 8-degree rare earthquake (PGA=0.51g). This implies that the friction damper is applicable in practical engineering. As shown in Table.13, the accumulative loss of bolt force is 12.98% decrease by 12.7kN after the action of 8-degree rare earthquake (PGA = 0.4g). It indicates that the friction damper of CD can withstand multiple aftershocks and the structural system functions properly.

## 5. Conclusions

A resilient prefabricated steel frame, PSC-CD, is innovatively developed from the PSC frame. The performance of the PSC-CD is compared to that of the PSC through carefully designed pseudo-dynamic testing. Conclusions are summarized as follows:

(1) The structural design and theoretical analysis of the PSC-CD are

conducted in the paper. The theoretical force-displacement curve of the PSC-CD is carefully proposed and validated through the testing. The testing specimens and experimental conditions are thoroughly discussed. The structural design method of the PSC-CD is feasible for the actual project.

(2) In the condition of 8-degree frequent earthquake (PGA = 0.07g), the interlayer drifts of both frames are less than the elastic interlayer limit (1/250). No gap-openings appear in the beam-column connections. The CD provides additional lateral stiffness to the steel frame. The friction damper of the CD in PSC-CD frame remain still. The force-displacement curves of the two systems are linear.

(3) In the condition of 8-degree fortification earthquake (PGA = 0.2g), the maximum inter-story drifts of PSC and PSC-CD are 1/129 and 1/150, beyond the elastic interlayer limit (1/250) but less than the plastic interlayer limit (1/50). Slight gap-opening occurs without residual rotation once unloading. The panel zones of PSC and PSC-CD reach the plastic state. The overall frames of both systems remain elastic states.

(4) In the condition of rare earthquake (PGA = 0.4g), the enclosed areas of the hysteresis curves further developed. The curve of PSC-CD is zigzag contributed by the friction damper of the CD. The energy-dissipation capacity and bearing capacity of PSC-CD is better than that of PSC. The beam-column connections are almost self-closed once unloading after the testing. The PSC-CD has much less residual gap-opening compared to that of the PSC. The losses of cable forces of the PSC-CD are smaller than that of the PSC as well.

(5) Before the fortification earthquake, the friction damper of the CD provides additional lateral stiffness to the frame without slippage. The CD provides damping function through the slippage of the friction damper as the seismic acceleration increases. The frictional blots of the friction damper increase the stability of the CD. Minor losses of bolt forces accumulate with the increase of seismic acceleration. The PSC-CD thus performs better than the PSC considering its stiffness and damping functions. This design of frame is applicable in the practical engineering.

## References

The work presented in paper is supported by the Joint Program of Beijing Natural Science Foundation and Education Commission (Grant No. KZ201910016018) and Program for Changjiang Scholars and Innovative Research Team in University (IRT-17R06) .

## References

[1] James M. Ricles,Richard Sause, Maria M. Garlock,Chen Zhao. Posttensioned seismic-resistant connections for steel frames. Journal of Structural Engineering, Vol. 127, No. 2, February, 2001.\

[2] J. M. Ricles, M. ASCE; R. Sause, S. W. Peng; and L. W. Lu. Experimental Evaluation of Earthquake Resistant Posttensioned Steel Connections. Journal of Structural Engineering, Vol. 128, No. 7, July 1, 2002.

[3] Ricles JM, Sause R, Peng SW, Lu LW. Experimental evaluation of earthquake resistant post-tensioned steel connections. J Struct Eng 2002;128(7): 850–9.

[4] Maria M. Garlock, James M. Ricles, Richard Sause. Experimental Studies of Full-Scale Posttensioned Steel Connections. Journal of Structural Engineering, Vol. 131, No. 3, March 1, 2005.

[5] Garlock M. Full-scale testing, seismic analysis, and design of post-tensioned seismic resistant connections for steel frames. Ph.D. dissertation, Civil and Environmental Engineering Dept., Lehigh Univ., Bethlehem, PA; 2002.

[6] Constantin Christopoulos; Andre Filiatrault, Chia-Ming Uang, and Bryan Folz. Posttensioned Energy Dissipating Connections for Moment-Resisting Steel Frames. Structural Engineering, Vol. 128, No. 9, September 1, 2002.

[7] P. Rojas; J. M. Ricles, R. Sause. Seismic Performance of Post-tensioned Steel Moment Resisting Frames With Friction Devices. Journal of Structural Engineering, Vol. 131, No. 4, April 1, 2005.

[8] Ying-Cheng Lin, James Ricles, Richard Sause, Choung-Yeol Seo. Earthquake simulations on a self-centering steel moment resisting frame with web friction devices. Structures 2009: Don't Mess with Structural Engineers © 2009 ASCE.

[9] Lin YC, Sause R, Ricles JM. Seismic performance of steel self-centering, moment-resisting frame: hybrid simulations under design basis earthquake. J Struct Eng 2013;139(11):1823–32.

[10] Federal Emergency Management Agency (FEMA)450. NEHRP recommended provisions for seismic regulations for new buildings and other structures. Part 1-provisions and Part 2-commentary. Washington, D.C.; 2003.

[11] Michael Wolski, A.M. ASCE, James M. Ricles, Richard Sause. Experimental Study of a Self-Centering Beam–Column Connection with Bottom Flange Friction Device. Journal of Structural Engineering, Vol. 135, No. 5, May 1, 2009.

[12] Feng X. Performance of research and engineering applications of the intermediate cylindrical friction damper. Southweat Jiaotong University.2012.

[13] Zhang Pengbo. Study on historical characteristics and evaluation method of shear damper (in Japanese).

[14] Suzui Kangzheng, satono Gangzhi, Nomura runnei hailianhe. Development and practicality of 4-sided friction. Dalin group technical research institute report no.752011 (in Japanese).

[15] Zhang AL, Zhang YX, Li R, Wang ZY. Cyclic behavior of a prefabricated self-centering beam–column connection with a bolted web friction device.Eng Struct 2016;111:185-198.

[16] Zhang YX, Wang ZY, Zhao W, Zhao WZ. A pseudo-dynamic test study on a self-centering prefabricated steel frame with a column base connected by semi-rigid joints. Adv Steel Const 2016;12(3):296-315.

[17] Zhang YX, Li QG, Zhuge Y, Liu AR, Zhao WZ. Experimental study on spatial prefabricated self-centering steel frame with beam-column connections containing bolted web friction devices. Eng Struct 2019;195:1-21.

[18] ZHANG Ailin, ZHANG Yanxia, ZHAO Wei, et al. Pseudo dynamic tests for a resilient prefabricated steel frame [J].Journal of Vibration and Shock, 2016, 35(05) : 207-215(in Chinese).

[19] ZHANG Yanxia, FEI Chenchao, NING Guang, et al. Dynamic elasto-plastic analysis on resilient prefabricated steel frame [J]. Journal of Vibration and Shock, 2016, 35( 18) : 101 − 110 (in Chinese).

[20] ZHANG Ailin, ZHANG Yanxia, CHEN Yuanyuan, et al. Static pushover test on resilient prestressed steel frame with intermediate column containing friction dampers [J]. Journal of Building Structures, 2016, 37(3): 125-133 (in Chinese).

[21] GB 50011-2010 Code for seismic design of buildings. Beijing: China Architecture &Building Press, (in Chinese); 2016.

[22] Kumar S, Itoh Y, Saizuka K, Usami T. Pseudodynamic testing of scaled models. J Struct Eng 1997;123(4):524-6.

[23] JGJ82-2011, Technical specifications for high strength bolt connections of steel structures. Beijing: China Architecture & Building Press (in Chinese).

[24] GB50017-2017, Standard for design of steel structures. Beijing: China Architecture & Building Press. [in Chinese].

[25] GB50019-2017, Standards for design of steel buildings. Beijing: China Architecture & Building Press; 2016 (in Chinese).

**Advanced Steel Construction** – Vol. 18 No. 3 (2022) 728–735
**DOI:**10.18057/IJASC.2022.18.3.10


# EFFICIENCY OF DIFFERENT CONNECTIONS ON THE BEHAVIOUR OF COLD-FORMED SINGLE-ANGLE STEEL MEMBERS CONNECTED THROUGH ONE LEGUNDER AXIAL LOADING

R. Saleema begum [1, *] and P. Suresh Kumar [2]

[1] *Research Scholar, Department of Civil Engineering, University college of Engineering. Panruti, India*
[2] *Professor, Department of Civil Engineering, University college of Engineering. Panruti, India*
**(Corresponding author: E-mail: saleemabegum30@gmail.com)*

**ABSTRACT**

A detailed experimental program was performed using 36 cold-formed steel (CFS) single-angle column members attached by one leg was investigated subjected to axial compression loads. The key purpose of this research is to investigate the effect of slenderness ratio and different connection types on the load-carrying capacity of CFS angle sections under axial compression. The parameters investigated via the test program includes (a) angle sections with and without lipped profile, (b) sectional thicknesses (2 mm and 3mm), (c) slenderness ratios ($\lambda$ = 20, 50, 80) from short to slender columns, and (d) type of connections i.e. two-bolt, three-bolt and welded connections. Results shown that the angle sections had a significant reduction in the load-carrying capacity when the slenderness ratio was increased from 20 to 80. Moreover, the mode of failure for short columns was changed from local buckling mode to combined local and flexural buckling for intermediate columns ($\lambda$ = 50) and torsional-flexural buckling mode for long columns ($\lambda$ = 80). Also, a detailed analytical study was carried out comparing the predictability of existing equations from different standards for angle sections under axial compression.

**ARTICLE HISTORY**

Received: 31 May 2022
Revised: 14 June 2022
Accepted: 19 June 2022

**KEYWORDS**

Cold-formed steel;
Bolted single-angle;
Welded single-angle;
Axial compression;
Local buckling;
Flexural-local buckling;
Flexural- torsional buckling



## 1. Introduction

The use of cold-formed steel (CFS) members especially in developing countries like India has significantly increased for the construction of residential, commercial and industrial buildings. Angle sections fabricated using CFS are predominantly used in different structural steel sections. Moreover, the fabrication of angle sections is relatively easier because of their simplified cross-section. Angle sections are usually connected to the other members through a single leg and are usually designed for predominant compression loads. It is worth mentioning that the effect of additional moments created due to eccentric connections and the shift of the effective centroid is neglected. The behaviour of axially loaded CFS angles sections with different end conditions has been previously investigated [1-7]. Popovic et al. [3]carried out the experimental investigations on CFSin-line galvanized equal angle sections. They concluded that theultimateload-carrying capacity of the stub column predicted by AS 4600 was found to conservative when compared to the experimental results. Young [9] performed tests on cold-formed steel plain angle columns with fixed end conditions. The test results were used as a benchmark for comparing the predictability of existing design equations suggested by American specifications and Australian/New Zealand standards for CFS sections. Ellobody and Young [11] developed a detailed finite element (FE) model for predicting thebehaviour of plain angle CFS columns. The developed model considered the effect of initial and geometric imperfections. The experimental results of 21 columns tested by Young [9] showed a good correlation with their FE model. Detailed experimental behaviour ofCFScolumns with unequal angles and non-symmetric lipped angle sections were also investigated [12-14]. Vishnuvardhan and Samuel knight [15] investigated thecompression behavior of CFS columns connected through single and compound plain angles. The load-carrying capacity and failure modes of CFS angles with different end conditions (i.e. ball, bolted and welded) were consideredas the test parameters to understand the overall behaviour of stub and short columns with single, double and starred angles. Zhou et al. [16] developed a non-linear FE model for predicting the ultimate compression strength of CFS angle sections connected through a single bolt. In the developed model, the contact between the angle section and gusset plate was also provided to achieve a conservative estimate of ultimate strength.

Several previous research papers have focused on the finite element modelling of CFS angle sections under axial loading which is used further for understanding the validity of existing equations from design standards [17-21]. Landesmann et al [20] carried outa detailed experimental behaviour to understand the slenderness effects (Short, intermediate and slender sections) of steel equal-leg angle columns with pin end conditions. The authors carried out the experimental investigation along with the nonlinear FEmodelling and analytical calculations (DSM equations). They concluded that the predictions from the validated FE model and improved analytical equations showed a close correlation with the test results of CFS columns with different slenderness limits. Silvestre et al. [22] documented a detailed design procedure for fixed and pin-ended columns with equal-leg angles. The height of the columns was varied in a range of short-to-intermediate level.The modified DSM approach showed a good ability to capture the ultimate strength of columns with short as well as intermediate lengths.Reviewing the existing literature, it is clear that only a handful of works have focused on the type of connections used for connecting the angle section to the column under axial compression. In specific, no studies have focussed on the effect of different connections (two bolted, three bolted and welded) and slenderness effects (short, intermediate and long) on the overall behavior ofCFS single-angle column members subjected to axial compression loading.The current work contributes towards filling the existing knowledge gap by presenting the experimental study on thebehaviour of 36single-angle CFS columns connected using two bolts, three bolts and welded connections for different column lengths (short, intermediate and long). Also, detailed analytical study was performed using the existing design equations to understand their predictability by comparison with the experimental results.

## 2. Research significance

From the critical review of existing studies, it is clear that only a few research works have focussed on understanding the axial behavior of single-angle CFS members. In specific, a knowledge gap can be witnessed to understand the effect of different connection types on the CFS columns subjected to axial compression loads. This study evaluates the effectiveness of different connection types on the compression behaviour of short, intermediate and slender CFS single-angle column members. The following are the specific objectives of the work:

(a) To quantify the effect of different connection types (two bolted, three bolted and welded) used for connecting the angle section to the column under axial compression.

(b) To understand the effect of slenderness ratio on the compression behaviour of CFS single- angle column members subjected to axial compression.

(c) To evaluate the validity of existing design equations for predicting the behaviour of CFS single-angle column members subjected to axial compression.

## 3. Experimental program

### *3.1. Details of test matrix*

The test specimens were prepared from the cold-formed steel (CFS) material and connected using the gusset plates at both the ends, by bending, press braking and suitable welding procedures. Table 1 shows the overall details of the test program adopted in this work. The cold-formed sheets were supplied without holes and each specimen was tailor-made to the required lengths. Four different types of angels namely A 100 x 100 x 2, LA 82 x 82 x 20 x 2, A 100 x 100 x 3 and LA 83 x 83 x 20 x 3 were tested as a part of this work. Three different slenderness ratios ($\lambda_v$) were considered for each angle section such as 20, 50, and 80, where $\lambda_v$ is the slenderness ratios about the minor principal axis and controlled the length of members. For the members connected using bolts, a single-angle section was bolted to a tee section at each end. The calculation length can bedefined as the design length which includes two times the end-plate thickness i.e., $L=L_0 +2t+2 L_g$ Where L is calculation length, $L_0$ is the net length between two end-plates; $L_g$ is the unconnected length, tis the gusset plate thickness of T-plate. For the welded connection of CFS angle section, the experimental angles are CFS T-stubs which are arc-weldedusing two hot-rolled steel plates. The specimens tested as a part of this experimental program is shown in Fig. 1. Thisincludes a CFS column which is connected at the base by a single-angle with and without lipped profile.Two different thickness of CFS sections are used namely 2.0 mm and 3.0 mm. The specimen identification is denoted as P-CON-SL-t where, P- profile type (section with or without lippedprofile), CON – the type of connection (bolted or welded), SL –slenderness ratio (20 or 50 or 80) and t – thickness of CFS section. Example: In the nomenclature A-B2-20-2.0, A refers to the plain angle section without Lip; B2 refers to two bolted connection types; 20 refers to the value of slenderness ratio and 2.0 refers to the thickness of CFS section.

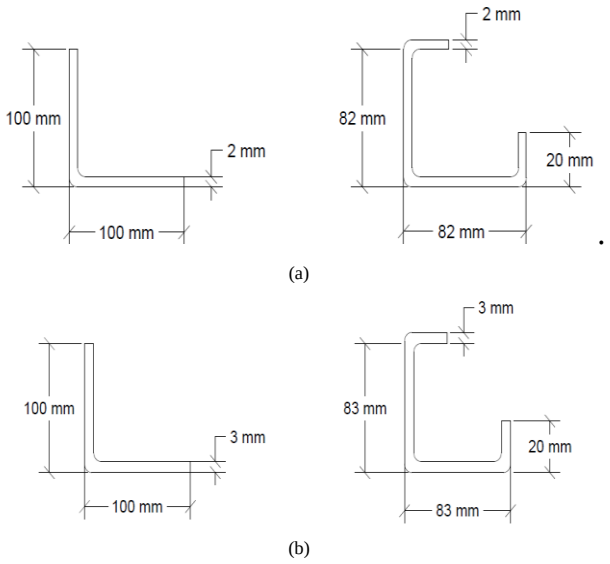


**Fig. 1** Sectional details of plain and lipped section. (a) 2.0 mm thick and (b) 3.0 mm thick

### *3.2. Material characterisation*

The coupon samples were prepared from the fabricated specimens as per the guidelines provided in ASTM 2013 [24]. The dimensions of the coupon samples are shown in Fig. 2(a). From each thickness of the test specimens (2.0 mm and 3.0 mm), six coupon samples were prepared and am average values were considering for reporting the mechanical properties of CFS sections. During sample preparation, the coupons were cut from the centre of the angle section as shown in Fig. 2(b). The stress-strain behaviour obtained for 2.0 mm and 3.0 mm CFS sections are shown in Fig. 2(c). Table 2 shows the mechanical properties of CFS section. For CFS sections with 2 mm thickness, the average yield strength and ultimate strain were found to be 268 MPa and 0.35 respectively. In the case of CFS sections with 3 mm thickness, the average yield strength and the ultimate strain were found to be 230 MPa and 0.44 respectively.

**Table 1**
Details of test specimen

| S. No | Specimen Size (mm) | Specimen ID | Area ($mm^2$) | Total length (mm) | Slenderness ratio ($\lambda$) | Connection Type |
|---|---|---|---|---|---|---|
| 1 | 100 x 100x 2 (Plain Angle) | A-B2-20-2.0 | 396 | 594 | 20 | 2Bolts |
| | | A-B3-20-2.0 | | 644 | | 3Bolts |
| | | A-W-20-2.0 | | 559 | | Weld |
| 2 | 82 x 82 x 20 x 2 (Lipped Angle) | LA-B2-20-2.0 | 396 | 594 | | 2 Bolts |
| | | LA-B3-20-2.0 | | 644 | | 3 Bolts |
| | | LA-W-20-2.0 | | 559 | | Weld |
| 3 | 100 x 100 x 2 (Plain Angle) | A-B2-50-2.0 | 396 | 1200 | 50 | 2 Bolts |
| | | A-B3-50-2.0 | | 1250 | | 3 Bolts |
| | | A-W-50-2.0 | | 1165 | | Weld |
| 4 | 82x82x20x2 (Lipped Angle) | LA-B2-50-2.0 | 396 | 1200 | | 2 Bolts |
| | | LA-B3-50-2.0 | | 1250 | | 3 Bolts |
| | | LA-W-50-2.0 | | 1165 | | Weld |
| 5 | 100 x 100 x 2 (Plain Angle) | A-B2-80-2.0 | 396 | 1807 | 80 | 2 Bolts |
| | | A-B3-80-2.0 | | 1857 | | 3 Bolts |
| | | A-W-80-2.0 | | 1772 | | Weld |
| 6 | 82 x 82 x 20x2 (Lipped Angle) | LA-B2-80-2.0 | 396 | 1807 | | 2 Bolts |
| | | LA-B3-80-2.0 | | 1857 | | 3 Bolts |
| | | LA-W-80-2.0 | | 1772 | | Weld |
| 7 | 100 x 100 x 3 (Plain Angle) | A-B2-20-3.0 | 591 | 592 | 20 | 2 Bolts |
| | | A-B3-20-3.0 | | 642 | | 3 Bolts |
| | | A-W-20-3.0 | | 557 | | Weld |
| 8 | 83x83x20x3 (Lipped Angle) | LA-B2-20-3.0 | 591 | 592 | | 2 Bolts |
| | | LA-B3-20-3.0 | | 642 | | 3 Bolts |
| | | LA-W-20-3.0 | | 557 | | Weld |
| 9 | 100 x 100 x 3 (Plain Angle) | A-B2-50-3.0 | 591 | 1195 | 50 | 2 Bolts |
| | | A-B3-50-3.0 | | 1245 | | 3 Bolts |
| | | A-W-50-3.0 | | 1160 | | Weld |
| 10 | 83x83x20x3 (Lipped Angle) | LA-B2-50-3.0 | 591 | 1195 | | 2 Bolts |
| | | LA-B3-50-3.0 | | 1245 | | 3 Bolts |
| | | LA-W-50-3.0 | | 1160 | | Weld |
| 11 | 100 x 100 x 3 (Plain Angle) | A-B2-80-3.0 | 591 | 1799 | 80 | 2 Bolts |
| | | A-B3-80-3.0 | | 1849 | | 3 Bolts |
| | | A-W-80-3.0 | | 1764 | | Weld |
| 12 | 83 x 83 x 20x3 (Lipped Angle) | LA-B2-80-3.0 | 591 | 1799 | | 2 Bolts |
| | | LA-B3-80-3.0 | | 1849 | | 3 Bolts |
| | | LA-W-80-3.0 | | 1764 | | Weld |

**Table 2**
Mechanical Properties of CFS

| S. No | Thickness of CFS | Elastic Modulus | Yield Strength (fy) | Ultimate Strength (fu) | fu/fy | Elongation |
|---|---|---|---|---|---|---|
| 1. | 2.0 mm | 200 GPa | 268.0 MPa | 362.0 MPa | 1.35 | 35.85% |
| 2. | 3.0 mm | 200 GPa | 229.8 MPa | 306.1 MPa | 1.33 | 44.24% |

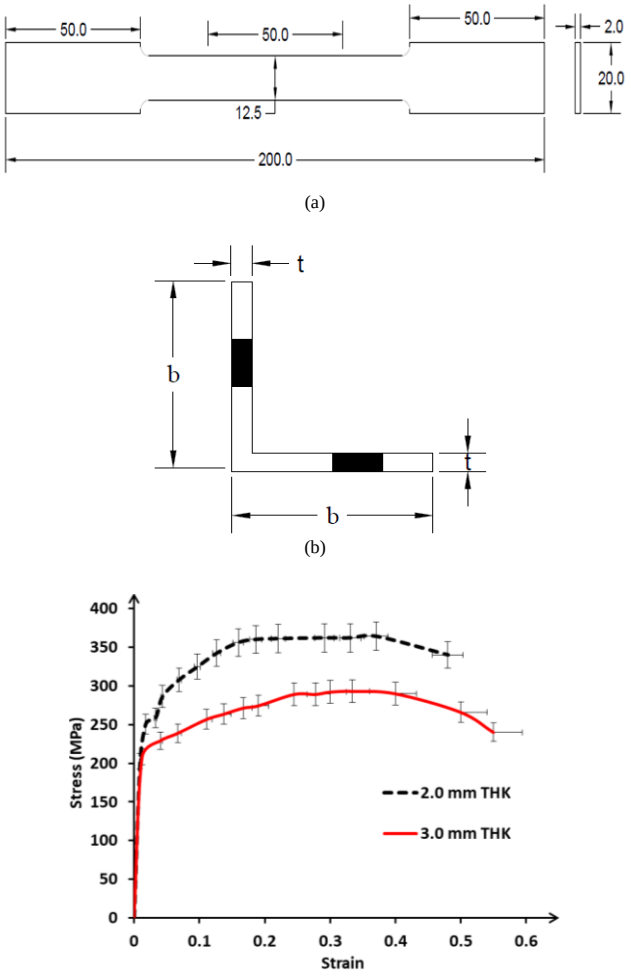


**Fig. 2** Coupon details and stress – strain behaviour of CFS with different thickness

### *3.3. Test setup and instrumentation details*

The specimens are tested using theuniversal testing machine (UTM) of 1000 kN capacity. In total, thirty-six single angle column members connected to the tee section were tested under axial compression to determine their ultimate strength and corresponding failure modes. The web of the tee sections is connectedusing either bolted or welded type as shown in Fig. 3. Three different slenderness ratios are evaluated by testing short, intermediate and long columns.A 10 mm thick end plates of size 100 x 100 mm and 150 x 100 mm are welded and made as T-stub gusset plates attached to the specimens at each end for bolted and welded connection. The specimens were fixed vertically by gripping the gusset plates and were tested to failure. For each test, the load was increased at a faster rate in the elastic range (5 kN/sec) and a slower range in the plastic range till the specimen failed. To understand the post-buckling behaviour of test specimens, the measurements were also done beyond the peak load. The procedure is repeated till the failure stage is reached for all the specimens.

The details of the test setup and instrumentations used during the application of compression loads are shown in Fig. 4. Carehas been taken to load the specimen vertically using the gusset plate. Dial gauges of least count 0.01 mm were used to measure the axial shortening of the member and lateral deflections. Dial gauges were placed at the mid-height of the angle section and at one-fourth of the height of the angle section with their end touching the web and flange of the specimens for measuring the lateral deflections. To measure the axial shortening of the test specimen,two dial gauge was placed with its end touching the movable head of the column testing machine. Electrical resistance strain gauges were used to measure the strains at mid-height of the angle section. A strain indicator with 5 channels was used to record the strain measurements. Strain gauge and dial gauge readings were measured at every increment of load and the load was increased until the specimen attains failure.

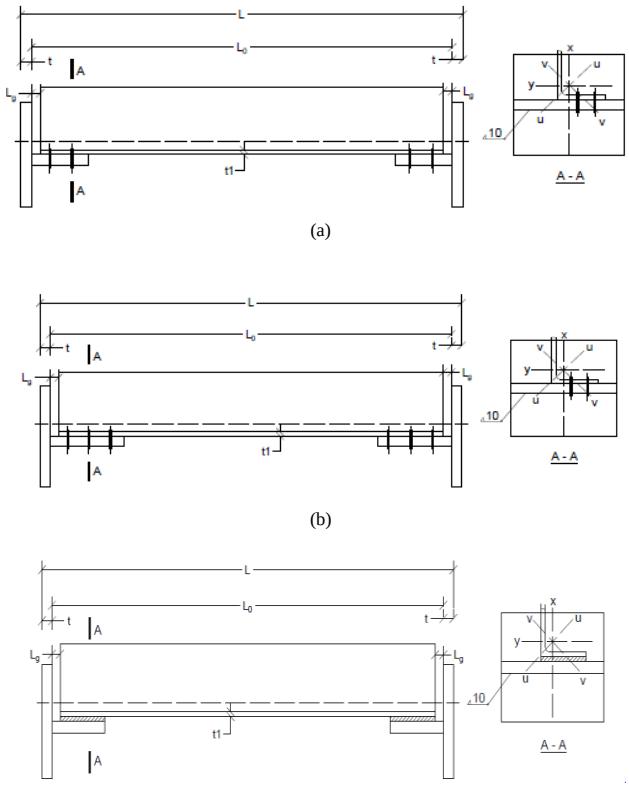


**Fig. 3** Schematic representation of different end connections used.

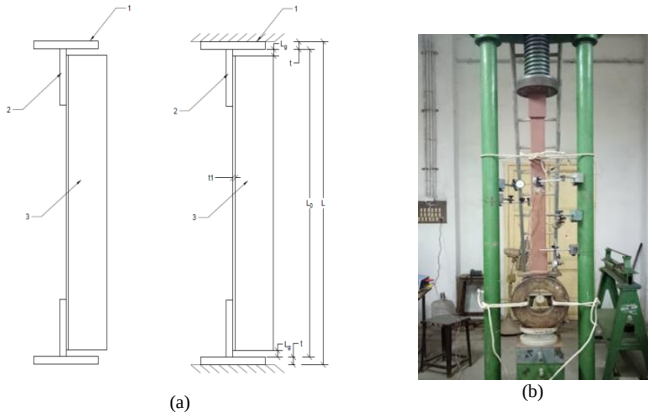


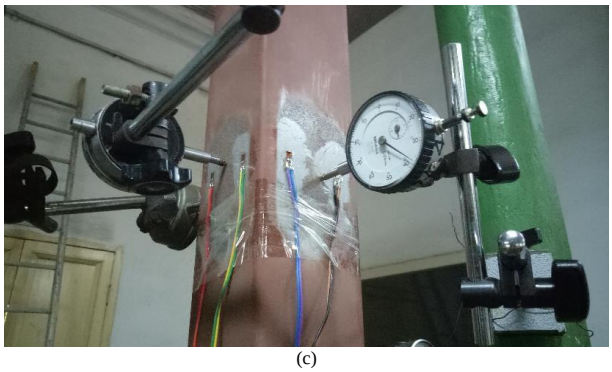


**Fig. 4** Test setup and instrumentation details

## 4. Results and discussion

The test results obtained for single –angle column members with different slenderness ratio, sectional thickness and type of connections are discussed in the following section to understand the axial capacity and the change in failure mode.

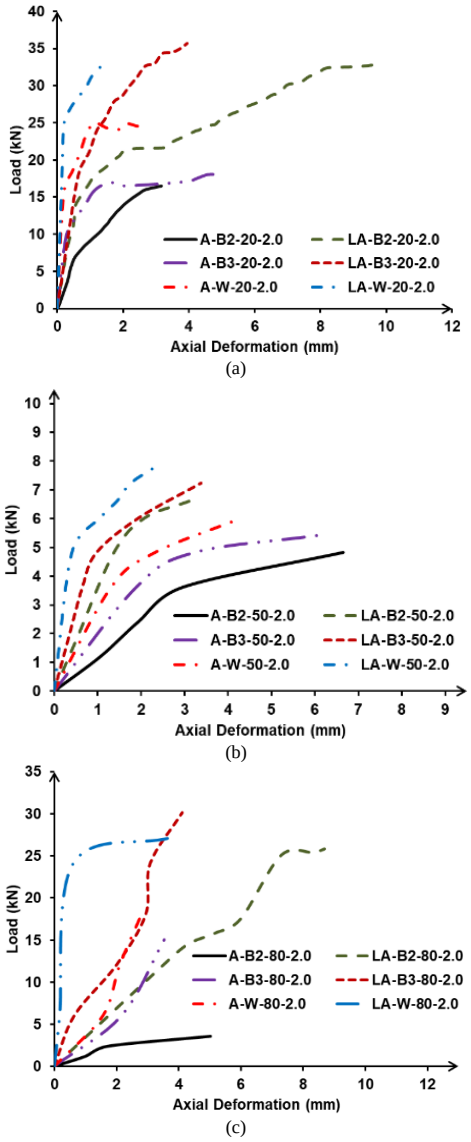


**Fig. 5** Overall behavior of specimens with 2.0 mm sectional thickness

### *4.1. Single-angle column members with 2.0 mm thickness*

Table 3 highlights the peak load for different specimens and their corresponding failure modes. The load-displacement behaviour obtained for single angle columns with different connections is shown in Fig. 5. It is clear that the axial load carrying capacity of specimens reduced significantly with the increase in slenderness ratio. Single-angle column members with a slenderness ratio of 20 and connected using 2 bolts had an axial load of 16.50 kN. With the increase in slenderness ratio, the axial capacity of columns reduced significantly by 70.7% and 85.3% compared to A-B2-20-2.0. However, for the same specimen (A-B2-20-2.0), the axial load capacity increased by 9.4% and 50.6% when the column and single angle is connected using 3 bolts and welded connection, respectively. Similarly, for the specimen A-B3-20-2.0, the peak load was found to be 18.05 kN. When the slenderness ratio is increased to 50 and 80, the peak load reduced by 69.9% and 83.5% respectively compared to A-B3-20-2.0. For the specimens connected through the welded section (A-W-20-2.0), the axial load capacity was found to be 24.86 kN which is more than 50% for the similar specimen with 2 bolt connection (A-B2-20-2.0). When the slenderness ratio was increased to 50 and 80, the axial load capacity reduces by 73.4% and 80.7% respectively compared to the specimen A-W-20-2.0.

Use of a lipped profile instead of plain angles helped in increasing the axial capacity of members with different connections. Comparison for the specimen with a slenderness ratio of 20 and 2 bolted connections, the peak strength of the lipped section increased by 98.8% when compared to the specimen without lip. Similar results were observed for lipped profile when the slenderness ratio is increased more than 20. With the increase in slenderness ratio (LA-B2-50-2.0 and LA-B2-80-2.0), the lipped angle sections were more effective under axial loading and helped in enhancing the overall load capacity by 24.82% and 106.6% when compared to similar specimens without lip (A-B2-50-2.0 and A-B2-80-2.0). For the specimen connected using 3 bolts (LA-B3-20-2.0), the peak load was found to be 35.67 which is more than 97.6% compared to a similar specimen without lipped angle. When the slenderness ratio is increased, the lipped angle section also shows a significant reduction in axial resistance due to the secondary effects and the reduction was found to be 79.8% and 83.1% respectively. For lipped angles connected by welding, the peak load increased by 58.6% compared toasimilar specimen without lipped profile. Moreover, the specimens LA-W-80-2.0 and LA-W-80-2.0 had axial load reduction of about 80.2% and 84.2% respectively when compared to the specimen with low slenderness ratio (LA-W-20-2.0).

**Table 3**
Test results for specimens with 2.0 mm thickness

| Specimen ID | Angle size (mm) | b/t ratio | Slenderness ratio (λ) | Peak load ( PEXP ) kN | Failure mode |
|---|---|---|---|---|---|
| A-B2-20-2.0 | 100 x 100 x 2.0 | 50 | 20 | 16.50 | L |
| A-B2-50-2.0 | | | 50 | 4.82 | L+F |
| A-B2-80-2.0 | | | 80 | 2.42 | F+T |
| A-B3-20-2.0 | 100 x 100 x 2.0 | 50 | 20 | 18.05 | L |
| A-B3-50-2.0 | | | 50 | 5.42 | L+F |
| A-B3-80-2.0 | | | 80 | 3.01 | F+T |
| A-W-20-2.0 | 100 x 100 x 2.0 | 50 | 20 | 24.86 | L |
| A-W-50-2.0 | | | 50 | 6.62 | L+F |
| A-W-80-2.0 | | | 80 | 4.81 | F+T |
| LA-B2-20-2.0 | 82 x 82 x 20 x2.0 | 41 | 20 | 32.80 | L |
| LA-B2-50-2.0 | | | 50 | 6.02 | L+F |
| LA-B2-80-2.0 | | | 80 | 5.00 | F+T |
| LA-B3-20-2.0 | 82 x 82 x 20 x 2.0 | 41 | 20 | 35.67 | L |
| LA-B3-50-2.0 | | | 50 | 7.22 | L+F |
| LA-B3-80-2.0 | | | 80 | 6.02 | F+T |
| LA-W-20-2.0 | 82 x 82 x 20 x 2.0 | 41 | 20 | 39.45 | L |
| LA-W-50-2.0 | | | 50 | 7.83 | L+F |
| LA-W-80-2.0 | | | 80 | 6.62 | F+T |

Note: L – Local Buckling; L+F – Combination of local and flexural buckling and T – Flexural- torsional buckling

### *4.2. Single-angle column members with 3.0 mm thickness*

Table 4 highlights the peak load for specimens with 3.0 mm thickness. Moreover, the overall load-displacement behaviour obtained for single angle columns with different connections is shown in Fig. 6. In this section, the comparison is made highlighting the effect of different slenderness ratios and types of connections. For the control specimen with a slenderness ratio of 20 and connected by two bolts (A-B2-20-3.0), the peak load was found to be 34.87 kN.Increase in the slenderness ratio by 50 and 80, the axial capacity reduced by 77.5% and 82.7% respectively. For the specimen with 3 bolted connections and slenderness ratio 20 (A-B3-20-3.0), the axial load increased marginally by 6.1% when compared to 2 bolted sections (A-B2-20-3.0).When the slenderness ratio is increased by 50 and 80, the axial strength reduced by 77.2% and 80.5% respectively. The use of a welded connection was more effective compared to the other two connections used. For specimen A-W-20-3.0, the peak compressive strength increased by 21.7% when compared to the specimen with two bolted connections (A-B2-20-3.0). For similar specimen, the peak strength reduced by 75.9% and 80.1% for specimens with slenderness ratio of 50 and 80 respectively.

For the specimens with 3.0 mm thickness, the use of a lipped section profile helps in enhancing the peak compressive strength. Comparing the behaviour of single angled column members with lipped profile, the peak strength increased by 51.3%, 70.4% and 54.1% respectively when compared to the similar specimens A-B2-20-3.0, A-B3-20-3.0, A-W-20-3.0 respectively without a lipped profile. Considering the effect of different connections, the lipped angle sections connected using 3 bolts showed better performance when compared to the 2 bolt and welded connection. The effect of slenderness ratio also played a significant role in the compressive strength of lipped angle column sections. For the 2 bolt connection, the peak compressive strength reduced by 81.7% and 82.9% for specimens with slenderness ratio 50 (LA-B2-50-3.0) and 80 (LA-B2-80-3.0) respectively.Similarly, for the welded

specimens with lipped angles, the peak load reduced by 82.5% and 84.4% for specimens with slenderness ratio 50 (LA-W-50-3.0) and 80 (LA-W-80-3.0) respectively

**Table 4**
Test results for specimens with 3.0 mm thickness

| Specimen ID | Angle size (mm) | b/t ratio | Slenderness ratio (λ) | Peak load ( PEXP) kN | Failure mode |
|---|---|---|---|---|---|
| A-B2-20-3.0 | 100 x 100 x 3.0 | 33.33 | 20 | 34.87 | L |
| A-B2-50-3.0 | | | 50 | 7.83 | L+F |
| A-B2-80-3.0 | | | 80 | 6.02 | F+T |
| A-B3-20-3.0 | 100 x 100 x 3.0 | 33.33 | 20 | 37.00 | L |
| A-B3-50-3.0 | | | 50 | 8.43 | L+F |
| A-B3-80-3.0 | | | 80 | 7.23 | F+T |
| A-W-20-3.0 | 100 x 100 x 3.0 | 33.33 | 20 | 42.43 | L |
| A-W-50-3.0 | | | 50 | 10.24 | L+F |
| A-W-80-3.0 | | | 80 | 8.43 | F+T |
| LA-B2-20-3.0 | 82 x 82 x 20 x3.0 | 27.66 | 20 | 52.75 | L |
| LA-B2-50-3.0 | | | 50 | 9.63 | L+F |
| LA-B2-80-3.0 | | | 80 | 9.03 | F+T |
| LA-B3-20-3.0 | 82 x 82 x 20 x 3.0 | 27.66 | 20 | 63.03 | L |
| LA-B3-50-3.0 | | | 50 | 10.84 | L+F |
| LA-B3-80-3.0 | | | 80 | 9.63 | F+T |
| LA-W-20-3.0 | 82 x 82 x 20 x 3.0 | 27.66 | 20 | 65.38 | F |
| LA-W-50-3.0 | | | 50 | 11.45 | L+F |
| LA-W-80-3.0 | | | 80 | 10.24 | F+T |

Note: L – Local Buckling; F – Flexural Buckling; L+F – Combination of local and flexural buckling and T – Flexural torsional buckling

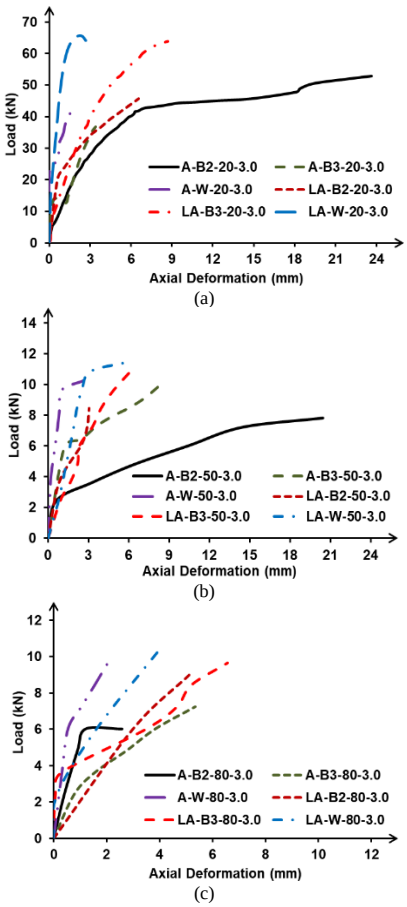


**Fig. 6** Overall behavior of specimens with 3.0 mm sectional thickness

*4.3. Load – strain behaviour*

The load - strain behaviour of single-angle column members with different slenderness ratio and connections are shown in Figs. 7 and 8. The negative values indicate the compressive strain and the positive value indicates the tensile strain. For the specimens with a slenderness ratio of 20, the welded section showed better performance interns of excessive compressive and tensilestrain values. The compressive strength showed a value close to 1400 µm/m exhibiting a large ductile response before failure. Also, the stiffness of the specimen improves with the change in connection type. The single-angle column members with welded connection showed a higher value of initial stiffness followed by the members with 3 bolt connection and then the 2 bolt connection. With the increase in slenderness ratio, the compressive strain reduced significantly. However, the tensile strain values showed some increase due to the increased secondary effect i.e., large lateral deflections before failure. For the single-angle column members without a lipped profile and having a slenderness ratio of 80, the compressive strain was close to 1600 µm/m showing good axial resistance irrespective of the large lateral deflections.

Similar behavior was observed for the sections with 3.0 mm thickness except for the fact that most of them were subjected to predominate compressive strain. This behaviour also indicates an increase in overall effectiveness with the increase in sectional thickness. In the case of sections with 3 mm thickness, the welded connection exhibited a better performance in resisting excessive compressive strains. For the slenderness ratio of 20, the maximum compressive strain resistance of 1400 µm/m is exhibited by the specimen A-W-20-3.0.Similarly, a compressive strain value of 1600 µm/m was attained by specimen A-W-80-3.0 showing their ability to take excessive axial strain irrespective of the large secondary effects (lateral deformation) due to the slenderness ratio of 80. Provision of lipped profile did not significantly enhance the performance in terms of compressive strain resistance. Nevertheless, the peak compressive strength increased when compared to the specimens without a lipped profile.

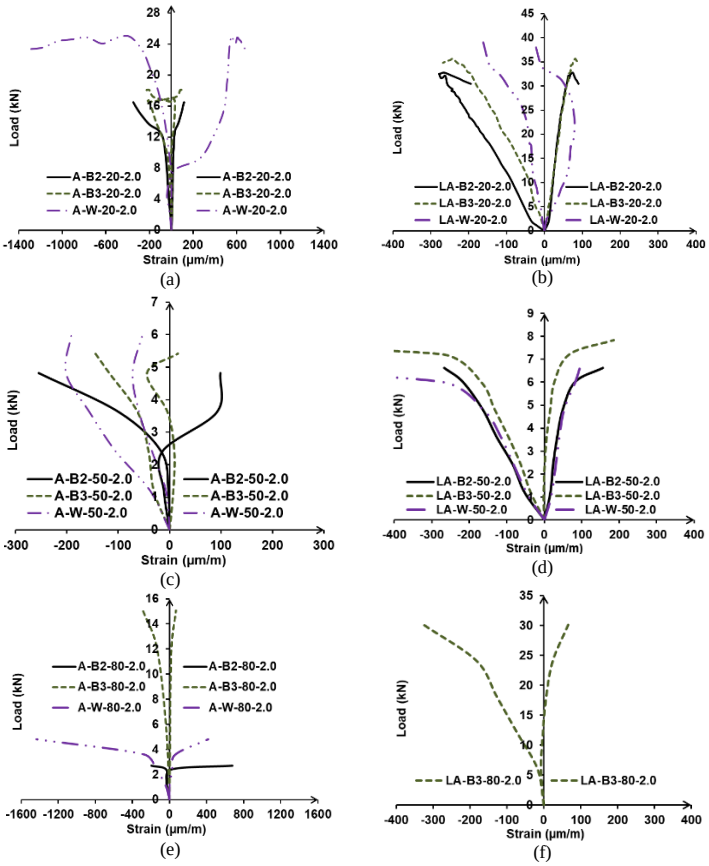


**Fig. 7** Overall Load – Strain Behavior with 2.0 mm sectional thickness

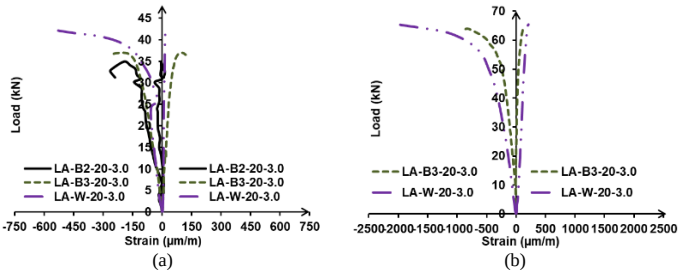

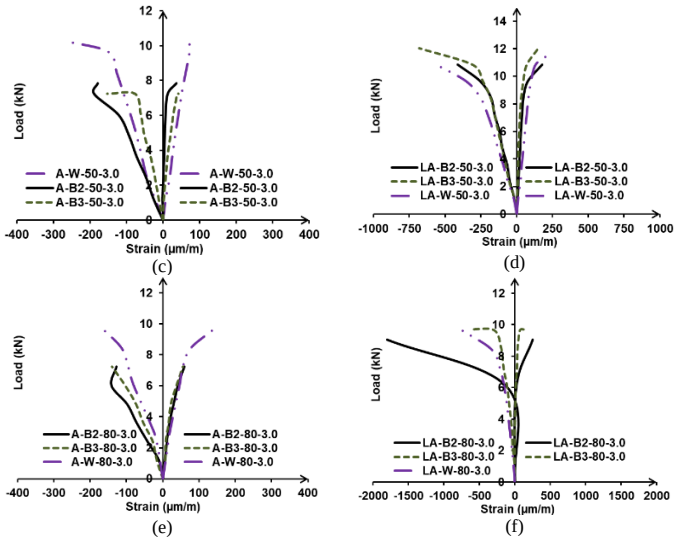


**Fig. 8** Overall load – strain behavior with 3.0 mm sectional thickness

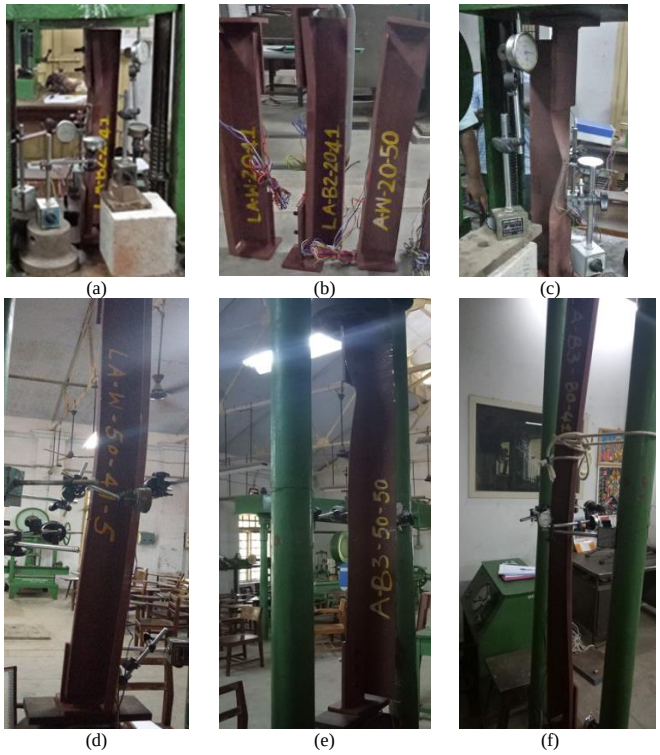


**Fig. 9** Failure of specimens with different slenderness ratio and connections

### *4.4. Failure mode comparison*

The failure mode of single-angle column sections with different thickness and slenderness ratio is shown in Fig. 9. All the angle sections with and without lipped profile and connected using two bolts had failure due to local buckling. The occurrence of local buckling failure is characterised by the presence of flexural deformation of the plate initiated either at the one-third or mid-height of the column. With the increase in number of bolts used for connecting the column and the single-angle, the occurrence of local buckling alone is prevented and the failure is due to a combination of flexural and local buckling. No single-angle column members had failure due to flexural buckling only i.e., the rigid body movement or global movement of the entire column members. For all the members connected using 3 bolts, the local-flexure buckling failure mode occurred which is characterised by the occurrence of global movement of the entire member along with the localised plate deformation either at the mid-height or one-third height of the section. The interaction between the local and flexural buckling relies largely on the slenderness ratio of the section and the dominance of flexural buckling can be witnessed significantly with the increase in slenderness ratio. For the single-angle welded column section, the failure mode is due to flexural-torsional buckling. This failure mode involves a combination of member bending and twisting as well as any local buckling of slender elements. Due to the low-torsional rigidity of thin walled members, the compression flange tends to buckle in the inward direction. The failure mode type of flexural torsional buckling is different from the lateral torsional buckling which involve a twisting of the entire cross section about its shearcentre. When the connection type for single-angle column sections are changed from two or three bolted connection, the failure mode is converted from local buckling or flexural-local buckling into flexural-torsional buckling irrespective of the slenderness ratio and sectional thickness.

## 5. Prediction analysis of existing design standards

### *5.1. IS 801: 2005 [26]*

Singly symmetric shapes or intermittently fastened singly- symmetric components of built-up shapes Having Q =1.0 which may be subject to Torsional Flexural Buckling-singly symmetric shapes subject to both axis compression and bending applied in the plane of symmetry shall be proportioned to meet the following four requirements as applicable.

$$\sigma_{ex} = \pi^2 E/(KL/r_x)^2 \quad (1)$$

For $F_a/F_{a1} + f_{b1}C_m/F_{b1}(1-F_a/F') \leq 1$

$$F_a/F_{ao} + f_{b1}/F_{b1} \leq 1 \quad (2)$$

For $f_a/F_{a1} \leq 0.15$

$$F_a/F_{a1} + f_{b1}/F_{b1} \leq 1.0 \quad (3)$$

If the point of application of the eccentric load is located on the side of the centroid opposite from that of the shear centre, that is if e is positive, then the average compression stress fa shall not also not exceed Fa given below

For $\sigma_{TF} \geq 0.5F_y$

$$Fa = 0.522\ F_y - F_y^2/7.67\sigma_{TF} \quad (4)$$

For $\sigma_{TF} < 0.5F_y$

$$Fa = 0.522\ \sigma_{TF} \quad (5)$$

Where $\sigma_{TF}$ shallbe determined according to the formula:

$$\sigma_{TF}/\ \sigma_{TFo} + C_{TF}\sigma_{b1}/\sigma_{bt}(1-\ \sigma_{TF}/\sigma_e) = 1.0 \quad (6)$$

From the mean compressive stress values, the peak strength of the CFS columnscan be estimated by multiplying the effective area value and the calculatedaverage allowablestress from the above mentioned equation.

### *5.2. American iron and steel institute AISI 2016*

The design rules of the current AISI design code is based on the research work by Popovic et al. [1].The nominal axial strength ($P_n$) is calculated using equation (9).

$$P_n = A_e F_n \quad (9)$$

The ultimate design strengthcan be estimated using equation (10)

$$P_u = P_n/1.80 \quad (10)$$

Considering the Allowable Stress Design (ASD), the peak load of the CFS column members can be estimated as given in equation (11)

$$P_u = 0.85 \times Pn \quad (11)$$

$F_n$is determined as per the below equations (12) or (13)

For $\boldsymbol{\lambda}_c \leq 1.5$

$$F_n = [0.658\boldsymbol{\lambda}_c^2]\ F_y \quad (12)$$

For $\boldsymbol{\lambda}_c > 1.5$

$$F_n = [0.877/\ \boldsymbol{\lambda}_c^2\ ]F_y \quad (13)$$

Where

$\lambda_c = \sqrt{F_y/Fe}$

WhereFe= least of the elastic flexural, torsional and torsional- flexural buckling stresses determined appropriately.For the sections subjected to flexural-torsional buckling or torsional buckling, the elastic flexural buckling stress can be calculated using the following formula

$$F_{cre} = \frac{\pi^2 E}{(KL/r)^2} \quad (14)$$

E = Modulus of elasticity of steel
K = Effective length factor
L = laterally unbraced length of member
R = Radiusofgyrationoffullunreducedcross-sectionaboutaxisofbuckling

The load capacity in combined axial and bending is determined using the following equation.

$$\frac{\bar{P}}{P_a} + \frac{\overline{M_x}}{M_{ax}} + \frac{\overline{M_y}}{M_{ay}} \leq 1.0 \quad (15)$$

*5.3. British standard BS:5950 (Part 5)-2002*

For CFS column sections with at least one axis of symmetry and subjected to torsional – flexural buckling mode, the peak compressive strengthcan be estimatedusing the provisions ofBS:5950 (Part 5)-2002 [27]. The stress corresponding to the torsional–flexural buckling can be calculated using equation (15) where the effective length (LE)is substituted by a factored effective length α are calculatedusing the following conditions below.

$$F_C/P_{CS} + M_x/M_{cx} + M_y/M_{CY} \leq 1 \quad (16)$$

For beams not subject to lateral buckling the following relationship should be satisfied.

$$F_C/P_C + M_x/C_{bx}M_{cx}(1-F_C/P_{EX}) + M_Y/C_{by}M_{cy}(1-F_C/P_{EY}) \leq 1 \quad (17)$$

For beams subject to lateral buckling the following relationship should be satisfied.

$$F_C/P_C + M_x/M_b + M_y/C_{by}M_{cy}(1-F_c/P_{cy}) \leq 1 \quad (18)$$

The magnitudes of moments $M_x$ and $M_y$ should take in to account any moment induced by the change in neutral axis position of the effective cross-section caused by the axial load. In the determination of $C_{bx}$ and $C_{by}$ the effects of change in the neutral axis position of the effective cross section caused by the axial load. In the determination of $C_{bx}$and $C_{by}$ the effects of change in the neutral axis position on the moment variation may be neglected.

*5.4. Comparison of predictions with the test results*

Table 5 and Table 6 highlights the comparison of test results with the peak strength predictions obtained from the analytical calculations for different sectional thickness. It can be witnessed that the results obtained from the analytical calculations under-predicted the tests. The variation of the ultimate strength ratio of experiments and analytical studies ($P_{EXP}$ / $P_{Code}$) for single angle column members with 2.0 mm sectional thickness was found to be 1.07, 1.40 and 3.92 for IS 801: 2005, AISI 2016 and BS 5950: 2002 respectively. Similarly, the variation of the ultimate compression strength ratio of tests and analytical predictions ($P_{EXP}$ / $P_{Code}$) for single angle column members with 3.0 mm sectional thickness was found to be 0.63, 1.85 and 13.90 for IS 801: 2005, AISI 2016 and BS 5950: 2002 respectively. From the above prediction range, it is very clear that the values obtained from IS 801-2005 were conservative and close when compared to the test results of specimens with 2.0 mm sectional thickness. However, when the sectional thickness is increased to 3.0 mm, the analytical predictions over-predicted the experimental results by more than 35%. For both the sectional thickness, the BS code and AISI code were found to provide a conservative estimate of compression load. It is worth mentioning that the analytical predictions obtained from the British standards were too-much conservative. The prediction range increases (COV = 13.92) drastically when the sectional thickness is increased to 3.0 mm. The predictions from AISI 2016showed a close and conservative estimate of test results.

**Table 5**
Test results for specimens with 2.0 mm thickness

| Specimen ID | Test ( PEXP ) kN | IS 801: 2005 ( PIS ) kN | AISI 2016 ( PAISI ) kN | BS 5950:2002 ( PBS ) kN | PIS/PEXP | PAISI/PEXP | PBS/PEXP |
|---|---|---|---|---|---|---|---|
| A-B2-20-2.0 | 16.5 | 4.23 | 4.15 | 4.15 | 0.26 | 0.25 | 0.25 |
| A-B2-50-2.0 | 4.82 | 3.47 | 4.10 | 1.35 | 0.72 | 0.85 | 0.28 |
| A-B2-80-2.0 | 2.42 | 3.45 | 4.01 | 0.58 | 1.43 | 1.66 | 0.24 |
| A-B3-20-2.0 | 18.05 | 4.23 | 4.16 | 5.97 | 0.23 | 0.23 | 0.33 |
| A-B3-50-2.0 | 5.42 | 3.48 | 4.13 | 2.27 | 0.64 | 0.76 | 0.42 |
| A-B3-80-2.0 | 3.01 | 3.47 | 4.07 | 0.99 | 1.15 | 1.35 | 0.33 |
| A-W-20-2.0 | 24.86 | 4.23 | 4.16 | 9.63 | 0.17 | 0.17 | 0.39 |
| A-W-50-2.0 | 6.62 | 3.48 | 4.14 | 3.55 | 0.53 | 0.63 | 0.54 |
| A-W-80-2.0 | 4.81 | 3.47 | 4.11 | 1.22 | 0.72 | 0.85 | 0.25 |
| LA-B2-20-2.0 | 32.8 | 10.08 | 17.85 | 4.16 | 0.31 | 0.54 | 0.13 |
| LA-B2-50-2.0 | 6.02 | 5.24 | 4.92 | 1.35 | 0.87 | 0.82 | 0.22 |
| LA-B2-80-2.0 | 5 | 3.45 | 2.85 | 0.59 | 0.69 | 0.57 | 0.12 |
| LA-B3-20-2.0 | 35.67 | 10.91 | 19.85 | 5.97 | 0.31 | 0.56 | 0.17 |
| LA-B3-50-2.0 | 7.22 | 7.17 | 6.24 | 2.27 | 0.99 | 0.86 | 0.31 |
| LA-B3-80-2.0 | 6.02 | 4.42 | 5.25 | 0.99 | 0.73 | 0.87 | 0.17 |
| LA-W-20-2.0 | 39.45 | 11.69 | 21.85 | 8.82 | 0.30 | 0.55 | 0.22 |
| LA-W-50-2.0 | 7.83 | 6.59 | 5.49 | 3.56 | 0.84 | 0.70 | 0.45 |
| LA-W-80-2.0 | 6.62 | 5.51 | 4.25 | 1.48 | 0.83 | 0.64 | 0.22 |
| Mean COV | | | | | 0.65 | 0.71 | 0.28 |

**Table 6**
Test results for specimens with 3.0 mm thickness

| Specimen ID | Test ( PEXP ) kN | IS 801: 2005 ( PIS ) kN | AISI 2016 ( PAISI ) kN | BS 5950:2002 ( PBS ) kN | PIS/PEXP | PAISI/PEXP | PBS/PEXP |
|---|---|---|---|---|---|---|---|
| A-B2-20-3.0 | 34.87 | 14.22 | 6.77 | 4.99 | 0.41 | 0.19 | 0.14 |
| A-B2-50-3.0 | 7.83 | 3.15 | 6.73 | 1.54 | 0.40 | 0.86 | 0.20 |
| A-B2-80-3.0 | 6.02 | 2.99 | 6.67 | 0.67 | 0.50 | 1.11 | 0.11 |
| A-B3-20-3.0 | 37 | 14.22 | 6.77 | 7.25 | 0.38 | 0.18 | 0.20 |
| A-B3-50-3.0 | 8.43 | 3.19 | 6.75 | 2.57 | 0.38 | 0.80 | 0.31 |
| A-B3-80-3.0 | 7.23 | 3.11 | 6.72 | 1.13 | 0.43 | 0.93 | 0.16 |
| A-W-20-3.0 | 42.43 | 14.22 | 6.77 | 11.91 | 0.34 | 0.16 | 0.28 |
| A-W-50-3.0 | 10.24 | 3.22 | 6.76 | 4.02 | 0.31 | 0.66 | 0.39 |
| A-W-80-3.0 | 8.43 | 3.16 | 6.74 | 1.68 | 0.37 | 0.80 | 0.20 |
| LA-B2-20-3.0 | 52.75 | 47.21 | 35.59 | 4.30 | 0.89 | 0.67 | 0.08 |
| LA-B2-50-3.0 | 9.63 | 3.38 | 2.79 | 1.33 | 0.35 | 0.29 | 0.14 |
| LA-B2-80-3.0 | 9.03 | 2.63 | 2.34 | 0.58 | 0.29 | 0.26 | 0.06 |
| LA-B3-20-3.0 | 63.03 | 50.20 | 37.39 | 6.25 | 0.80 | 0.59 | 0.10 |
| LA-B3-50-3.0 | 10.84 | 3.88 | 3.07 | 2.22 | 0.36 | 0.28 | 0.20 |
| LA-B3-80-3.0 | 9.63 | 3.10 | 2.62 | 0.98 | 0.32 | 0.27 | 0.10 |
| LA-W-20-3.0 | 65.38 | 53.28 | 39.26 | 10.27 | 0.81 | 0.60 | 0.16 |
| LA-W-50-3.0 | 11.45 | 4.29 | 3.31 | 3.47 | 0.37 | 0.29 | 0.30 |
| LA-W-80-3.0 | 10.24 | 3.46 | 2.83 | 1.43 | 0.34 | 0.28 | 0.14 |
| Mean COV | | | | | 0.45 | 0.51 | 0.18 |

## 6. Summary and conclusions

The following major conclusions can be drawn from the limited results presented in this work:

- Use of two bolt connection showed a negative effect with the increase in slenderness ratio i.e., with the increase in slenderness ratio from 20 to 80, the peak compression load reduced significantly by more than 80%. All the single-angle column members connected with 2 bolts had failure due to local buckling mode.
- In the case of single-angle column members with three bolted connections, the peak strength increased in a range of 10% when compared to the specimens with two bolted connections. Moreover, the failure mode converted from local buckling mode (2 bolted connection) to flexural-local buckling mode (3 bolted connection).
- Use of welded connection was found to most efficient among the three investigated as a part of this study. The welded connection used for connecting the angle section to the column section helped in significantly enhancing the peak strength and strain. Moreover, the specimens were found to fail under flexural-torsional buckling mode.
- Increase in the value of slenderness ratio showed a considerable reduction in the ultimate compressive strength of single-angle column members. However, the slenderness ratio didn't have any effect of the failure mode of members which were more dependent on the type of connections used.
- The analytical procedure used in this study showed a good predictability for the ultimate compressive strength of single-angle column members with and without lipped profile. Only, the predictions obtained from the AISI code were conservative and close to the test results.

## References


[1] Madugula MKS, Prabhu TS, Temple MC. Ultimate strength of concentrically loaded cold-formed angles. Canadian J. Civ. Eng. 1983; 10(1): 60-68.

[2] Madugula MKS, Ray SK. Ultimate strength of eccentrically loaded cold -formed angles. Canadian J. Civ. Eng. 1984; 10(1): 225-233.

[3] Popovic D, Hancock HJ, Rasmussen KJR. Axial compression tests of cold formed angles. J. Struct. Eng. 1999; 125(5): 515-52

[4] Dhanalakshmi M, Shanmugam, NE. Stub column tests on cold-formed steel angle sections. International Specialty Conference on Cold-Formed Steel Structures, Missouri U.S.A, October 19th - 20th, 2000.

[5] Popovic D, Hancock HJ, Rasmussen KJR. Compression tests on cold formed angles loaded parallel with a leg. J. Struct. Eng. 2001; 127(6):600-607.

[6] Dubina D, Ungureanu V. Effect of imperfections on numerical simulation of instability Behaviour of Cold-formed steel members. Thin Walled Struct. 2002; 40(3): 239-262.

[7] Narayanan S, Mahendran M. Ultimate capacity of innovative cold-formed steel columns. J.Constr. Steel Res. 2003; 59(4): 489-508.

[8] AS 4600. Cold Formed Steel Structures. Australia/New Zealand Standards 2005.

[9] Young B. Tests and design of fixed-ended cold-formed steel plain angle columns. J. Struct. Eng. 2004; 130(12).

[10] AISI Manual. Cold-formed Steel Design Manual. American Iron and Steel Institute 2016.

[11] Ellobody E, Young B. Behavior of cold-formed steel plain angle columns. J. Struct. Eng. 2005; 131(3).

[12] Young B, Ellobody E. Design of cold-formed steel unequal angle compression members. Thin-Walled Struct. 2007; 45(3): 330-38.

[13] Chantel YL. Experimental study of steel single unequal-leg under eccentric compression. J. Constr. Steel Res. 2011; 67(6): 919-928.

[14] Young B, Chen J. Column tests of cold-formed steel non-symmetric lipped angle sections. J. Constr. Steel Res. 2008; 64(7-8): 808-15.

[15] Vishnuvardhan S, Samuel Knight GM. Behavior of cold-formed steel single and compound plain angles in compression. Adv. Steel Constr. 2008; 4(1): 46-58.

[16] Zhou F, James B, Lim P, Young B. Ultimate compressive strength of cold-formed steel angle struts loaded through a single bolt.Adv. Struct. Eng. 2012; 15(9): 1586-95.

[17] Maia WF, Vieira LCM, Schafe BW, Malite M. Numerical and experimental investigation of cold-formed steel double angle members under compression. International Specialty Conference on Cold-Formed Steel Structures, Missouri, USA, October 24th– 25th, 2012.

[18] MacDonald M, Kulatunga MP. Finite element analysis of cold-formed steel structural members with perforations subjected to compression loading. Mech. Mechanical Eng. 2013; 17(2): 127-139.

[19] Shifferaw Y, Schafer BW. Cold-formed steel lipped and plain angle columns with fixed ends. Thin-Walled Struct. 2014; 80: 142-52.

[20] Landesmann A, Camotim D, Dinis PB, Cruz R. Short-to intermediate slender pin-ended cold-formed steel equal-leg angle columns: Experimental investigation, numerical simulations and DSM design. Eng. Struct. 2017; 132(1) 471-93.

[21] Ananthi GBG, Vishnuvardhan S, Samuel Knight GM. Experimental and numerical investigation on thin-walled single and starred angle sections under compression. Arab. J. Sci. Eng. 2015; 40: 3417–27.

[22] Silvestre N, Dinis P.B, Camotim D. Development on the design of cold formed steel angles. J. Struct. Eng. 2013; 139(5).

[23] Ananthi GBG. A study on cold-formed steel compound angle section subjected to axial compression. KSCE J. Civ. Eng. 2018; 22(5): 1803–18.

[24] Georgieva I, Schueremans L, Pyl L, Vandewalle L. Numerical study of built-up Double-Z members in bending and compression. Thin walled Struct. 2012; 60: 85-97.

[25] ASTM E8/E8M-13a. Standard test methods for tension testing of metallic materials. West Conshohocken, PA, 2013.

[26] IS 801: Code of Practice for Use of Cold Formed Light Gauge Steel Structural Members in General Building Construction. 2005.

[27] BS 5950 Part 5. Structural use of steelwork in building - Code of practice for design of cold formed thin gauge sections. 2002.